
# Computer Simulation Methods to study Interfacial Tensions: From the Ising Model to Colloidal Crystals

Dissertation

zur Erlangung des Grades

*Doktor der Naturwissenschaften*

am Fachbereich Physik, Mathematik und Informatik

der Johannes Gutenberg-Universität Mainz

vorgelegt von

**Fabian Schmitz**

geboren in Andernach

Mainz, Oktober 2014

*Erster Berichterstatter:*
*Zweiter Berichterstatter:*
*Tag der Promotion:* 26.11.2014

*It's not that I'm so smart, it's just that I stay with problems longer.*

Albert Einstein

Fabian Schmitz

**Computer Simulation Methods to study Interfacial Tensions: From the Ising Model to Colloidal Crystals**

In condensed matter systems, the interfacial tension plays a central role for a multitude of phenomena. It is the driving force for nucleation processes, determines the shape and structure of crystalline structures and is important for industrial applications. Despite its importance, the interfacial tension is hard to determine in experiments and also in computer simulations. While for liquid-vapor interfacial tensions there exist sophisticated simulation methods to compute the interfacial tension, current methods for solid-liquid interfaces produce unsatisfactory results.

As a first approach to this topic, the influence of the interfacial tension on nuclei is studied within the three-dimensional Ising model. This model is well suited because despite its simplicity, one can learn much about nucleation of crystalline nuclei. Below the so-called roughening temperature, nuclei in the Ising model are not spherical anymore but become cubic because of the anisotropy of the interfacial tension. This is similar to crystalline nuclei, which are in general not spherical but more like a convex polyhedron with flat facets on the surface. In this context, the problem of distinguishing between the two bulk phases in the vicinity of the diffuse droplet surface is addressed. A new definition is found which correctly determines the volume of a droplet in a given configuration if compared to the volume predicted by simple macroscopic assumptions.

To compute the interfacial tension of solid-liquid interfaces, a new Monte Carlo method called "ensemble switch method" is presented which allows to compute the interfacial tension of liquid-vapor interfaces as well as solid-liquid interfaces with great accuracy. In the past, the dependence of the interfacial tension on the finite size and shape of the simulation box has often been neglected although there is a nontrivial dependence on the box dimensions. As a consequence, one needs to systematically increase the box size and extrapolate to infinite volume in order to accurately predict the interfacial tension. Therefore, a thorough finite-size scaling analysis is established in this thesis. Logarithmic corrections to the finite-size scaling are motivated and identified, which are of leading order and therefore must not be neglected. The astounding feature of these logarithmic corrections is that they do not depend at all on the model under consideration. Using the ensemble switch method, the validity of a finite-size scaling ansatz containing the aforementioned logarithmic corrections is carefully tested and confirmed. Combining the finite-size scaling theory with the ensemble switch method, the interfacial tension of several model systems, ranging from the Ising model to colloidal systems, is computed with great accuracy.

Fabian Schmitz

**Computersimulationsmethoden zur Untersuchung von Grenzflächenspannungen: Vom Isingmodell bis hin zu kolloidalen Kristallen**

Die Oberflächenspannung ist von zentraler Bedeutung für viele Phänomene im Bereich der Festkörperphysik, beispielsweise bei Keimbildungsprozessen, bei der Struktur von Kristallen und in vielen verschiedenen industriellen Anwendungen. Trotz ihrer Bedeutung ist die Oberflächenspannung in Experimenten und Computersimulationen schwer zu bestimmen. Während für Grenzflächenspannungen zwischen Flüssigkeiten und Gasen etablierte Simulationsmethoden existieren, sind die Ergebnisse im Falle von Grenzflächen zwischen Kristallen und Flüssigkeiten nicht zufriedenstellend.

Einen ersten Zugang zu diesem Thema bietet die Untersuchung des Einflusses der Oberflächenspannung auf Nuklei im dreidimensionalen Isingmodell, welches konzeptionell einfach ist und dennoch die Beobachtung von Nukleationsprozessen erlaubt. Unterhalb der sogenannten Aufrauungstemperatur ist ein Nukleus im Isingmodell nicht sphärisch sondern würfelförmig mit flachen Facetten und abgerundeten Ecken und Kanten. Dies ist zurückzuführen auf die Anisotropie der Oberflächenspannung. Dasselbe Phänomen tritt auch bei kristallinen Nuklei auf, sodass deren Form im Allgemeinen eher einem konvexen Polyeder entspricht als einer Kugel. In diesem Zusammenhang wird auch die Frage diskutiert, wie man die flüssige und gasförmige Phase nahe der typischerweise sehr diffusen Grenzfläche unterscheiden kann. Die Antwort bietet ein neues Kriterium, mit dem das Volumen des Nukleus in einer gegebenen Konfiguration korrekt bestimmt werden kann.

Um die Oberflächenspannung für Grenzflächen zwischen Kristallen und Flüssigkeiten bzw. Flüssigkeiten und Gasen mit hoher Genauigkeit zu bestimmen, wird eine neue Simulationsmethode namens "ensemble switch method" benutzt. In der Vergangenheit wurde die Abhängigkeit der Oberflächenspannung von der endlichen Größe und Form der Simulationsbox oft vernachlässigt, obwohl eine nichttriviale Abhängigkeit besteht. Daher muss man die Boxgröße systematisch variieren, um durch Extrapolation auf eine unendlich große Box die Grenzflächenspannung zu bestimmen. In dieser Arbeit wird aus diesem Grund eine gründliche Analyse der Finite-Size-Effekte durchgeführt. Die in führender Ordnung auftretenden universellen logarithmischen Korrekturen, die erstaunlicherweise nicht vom untersuchten Modell abhängen, werden motiviert und mit verschiedenen Effekten in Verbindung gebracht, unter anderem dem bisher nicht dokumentierten "domain breathing"-Effekt. Die Richtigkeit der Finite-Size-Analyse wird mithilfe der ensemble switch method sorgfältig überprüft und bestätigt. Die Kombination der Finite-Size-Analyse und der ensemble switch method erlaubt es, die Oberflächenspannung für verschiedene Modelle, vom Isingmodell bis hin zu kolloidalen Systemen, mit hoher Präzision zu bestimmen.

## Parts of this work were published in:


[1] F. Schmitz, P. Virnau, and K. Binder, Phys. Rev. E **87**, 053302 (2013)

[2] B. Block, D. Deb, F. Schmitz, A. Statt, A. Tröster, A. Winkler, T. Zykova-Timan, P. Virnau, and K. Binder, EPJST **223**, 347 (2014)

[3] F. Schmitz, P. Virnau, and K. Binder, Phys. Rev. Lett. **112**, 125701 (2014)

[4] F. Schmitz, P. Virnau, and K. Binder, Phys. Rev. E **90**, 012128 (2014)

# Contents

# Chapter 1

# Introduction

Physics is a challenging endeavor, aiming at understanding the fundamental principles of the whole universe and the interaction between the elementary constituents of matter and energy. This is a bold and ambitious challenge, but especially in the last century, there were quite a few breakthroughs changing our understanding of the universe. For me, there is one branch of physics which is especially attractive because it is much closer to our everyday life than any other field of physics. This branch is condensed matter physics, which focuses on understanding the interplay of condensed phases of matter, ranging from weather phenomena over industrial processes, magnetic systems, superconducting phases and Bose-Einstein condensates to everyday things like ice tea and refrigerators.

Condensed matter physics is a vast field with many handshakes to other fields in chemistry, materials science, nanotechnology, atomic physics and biophysics. Therefore it is no surprise that a large fraction of physicists are active researchers in this field. Nevertheless, condensed matter physics is a complicated subject to deal with. This is due to the fact that the physical systems typically contain a large number of particles, e.g. electrons in metals or colloidal particles in solution or particles to study hydrodynamic behavior of liquids in certain geometries etc.

In order to study phase transitions and similar phenomena, colloidal systems are especially attractive. Contrary to atomistic systems, colloids are mesoscopic particles with sizes ranging from several nanometers to micrometers. They are also fascinating systems in their own right, being important for cosmetics, food industry, colloidal ink or enamels. Furthermore, they form an interlink between microscopic and macroscopic systems, since they behave in many aspects like atoms or molecules. The main advantages of studying colloidal systems rather than atomic systems are as follows:

- The colloid-colloid interaction can be tuned by changing the colloids' material, surface structure or charge and by changing the suspension in which the colloids are suspended. Hence, a wide range of pair potentials can be modeled.
- Being a factor $10^3$ to $10^4$ times larger than atoms, colloids are much easier to track, e.g. via optical methods like confocal microscopy.
- The timescales in colloidal systems are also much slower compared to atoms. Hence, processes like crystallization and melting can be observed in real-time.

This makes colloidal systems perfect model systems to study phase transitions and similar phenomena.

One major topic in condensed matter physics is nucleation. Nucleation phenomena are ubiquitous in nature, industry and our personal life. To describe them, a theory nowadays known as classical nucleation theory (CNT) came up in the 1930s [Volmer and Weber, 1926; Volmer, 1929; Becker and Döring, 1935; Zeldovich, 1943]. This theory projects macroscopic properties to mesoscopic length scales to describe the nucleation process for general liquid-vapor transitions. The theory has now been examined very closely for a long time and still remains valid today, despite being applied to crystalline nuclei and to microscopical nuclei which violate the simplifying assumptions of the CNT [Kashchiev, 2000].

The examinations in this work are based on computer simulations. The use of computer simulations in the field of statistical physics began in the 1950s, when the Monte Carlo method was introduced [Metropolis et al., 1953]. It allowed to calculate averages of physical observables in many-body systems by creating a series of Boltzmann weighted configurations. This simple technique has led to powerful algorithms and much insight during the past 60 years. Over the years, computer simulations have become an accepted approach to problems where experiments cannot be executed and exact theories are missing or incomplete. Computer simulations are also used to complement experiments or theories by offering a third perspective. One major advantage of computer simulations is that pair interactions can be set as desired and effects like polydispersity or impurities can be turned on and off and therefore be analyzed individually. Also, all the particle trajectories are known, so precise measurements of properties like pair correlation functions or local density fluctuations are possible. Another major advantage is that the physical system represented within the computer does not need to be physical at all. For example, there exist algorithms to slowly shift from one physical state into another via a path of unphysical states. Of course, one has to be very careful to ensure that the output of such a simulation is sensible.

The challenge of computer simulations is twofold. On the one hand, one needs to

think of new, more efficient algorithms to solve the problems at hand. On the other hand, new hardware offers new possibilities, and hence a computer physicist is always keen to gain access to supercomputers with a large number of CPUs. Since the speed of a single CPU (or core) is limited, the industry has started to use parallel architectures where a large number of cores work together to solve a given problem, using parallelization standards like MPI or OpenMP.

This thesis centers on the interfacial tension of an interface between two bulk phases, studying liquid-vapor coexistence and solid-liquid coexistence. The interfacial tension is a quantity of tremendous importance as it governs fundamental processes like formation of ice crystals in the atmosphere or crystallization in industrial applications and technical processes. Hence it has a wide interest in the scientific community and allows to test the classical nucleation theory (CNT) for crystalline nuclei [Block et al., 2014]. Since the computation of the interfacial tension is a difficult task, the use of supercomputers is absolutely necessary.

The ambition of this work is to compute the interfacial tension of several physical systems via computer simulations. The interfacial tensions of solid-liquid interfaces are of special interest, as they are particularly hard to compute. To this end, a new Monte Carlo algorithm is invented and applied to various systems. Over the course of this thesis, it was found that the resulting interfacial tension is not independent of the size of the physical system in the computer, even if it is continued in all spatial directions by using periodic boundary conditions. Therefore, a rigorous finite-size scaling analysis is done in order to identify the relevant effects when varying the size of the simulation box. The resulting finite-size scaling ansatz, which takes these effects into account, enables us to greatly improve the predictions of interfacial tensions.

The outline of this thesis is as follows. Chapter 2 contains a short introduction to Monte Carlo simulations and also covers some more advanced topics like pseudorandom number generators and sophisticated algorithms like thermodynamic integration. Also, the model systems considered in this work are introduced as well as classical nucleation theory. After this, chapter 3 addresses the problems of classical nucleation theory in environments with crystalline phases. Since the interfacial tension is not isotropic (unlike in fluid systems), the shape of crystalline nuclei is not spherical but rather faceted. Therefore, chapter 3 investigates whether classical nucleation theory is applicable in such systems. The simplest system where the interfacial tension is anisotropic is the Ising model in three dimensions, where droplets are only spherical at high temperatures (below the model's critical point) but become more and more cubic at lower temperatures. In this context, we discuss a method to separate a nucleus from its surroundings unambiguously.

After this investigation, chapter 4 introduces a new method to calculate interfacial

tensions. This "ensemble switch method" is based on the idea of thermodynamic integration and allows to compute the interfacial tension between two bulk phases for arbitrary model systems. Chapter 5 then presents a theory of finite-size scaling for the interfacial tension. Although the derivation uses the language of the Ising model, the resulting finite-size scaling ansatz is of general validity because the underlying effects are independent of details of the model. The second part of the chapter contains thorough tests of the finite-size scaling ansatz for the two- and three-dimensional Ising model using the ensemble switch method.

The ensuing chapter 6 pursues the aim of computing the interfacial tension for solid-liquid interfaces. The first step in this chapter is to consider conceptually simpler liquid-vapor interfaces and show that the ensemble switch method and the finite-size scaling ansatz are not restricted to discrete model systems like the Ising model. The second step is to compute the interfacial tension directly for two common models, namely hard spheres and the Asakura-Oosawa model. The thesis ends with some concluding remarks.

# Chapter 2

# Theoretical Background

*Ludwig Boltzmann, who spent much of his life studying statistical mechanics, died in 1906, by his own hand. Paul Ehrenfest, carrying on the work, died similarly in 1933. Perhaps it will be wise to approach the subject cautiously.*

David L. Goodstein [Goodstein, 1985]

This chapter introduces the concepts and necessary tools used in the later chapters. It begins with a short introduction to Monte Carlo simulations. The next two sections cover the relevant models for this thesis, namely the Ising model (or lattice gas model) and several continuous models like Lennard-Jones particles, hard spheres and the Asakura-Oosawa model. Sections 2.4 and 2.5 sum up the necessary facts about classical nucleation theory (CNT) and capillary wave theory. While the former provides the basis for chapter 3, the latter plays a role in the whole thesis, as it is a central concept in the study of interfaces. After this, some technical details about Monte Carlo simulations will be covered, for example pseudorandom numbers, optimization schemes and algorithms to measure quantities like the pressure or the chemical potential. The final section presents some of the methods to compute free energies. The methods discussed there are the basis for the ensemble switch method in chapter 4, which will then be used in the later chapters to compute interfacial tensions for the various models introduced in this chapter.

## 2.1 Basic Concepts

### 2.1.1 On Monte Carlo Simulations

If a small physical system with a given volume $V$ and particle number $N$ is coupled to a large system, referred to as the *heat bath*, the temperature of the small system is determined by the heat bath. It follows that the probability of the small system to be in a state $i$ with energy $E_i$ is given by a Boltzmann distribution

$$P(E_i) = \frac{\exp(-\beta E_i)}{Z} \,, \tag{2.1}$$

where $Z(N,V,T)$ is the partition function of the canonical ensemble

$$Z(N,V,T) = \sum_i \exp(-\beta E_i) \,. \tag{2.2}$$

Here and in the following, $\beta = 1/(k_\mathrm{B}T)$ denotes the inverse temperature and $k_\mathrm{B}$ is the Boltzmann constant. The free energy of the system is then given by

$$\beta F(N,V,T) = -\ln[Z(N,V,T)] \,. \tag{2.3}$$

Knowing the thermodynamic potential of a system implies knowledge over all equilibrium properties of the system, e.g.

$$E(N,V,T) = \left.\frac{\partial \beta F(N,V,T)}{\partial \beta}\right|_{N,V} \qquad S(N,V,T) = -\left.\frac{\partial F(N,V,T)}{\partial T}\right|_{N,V}$$

$$\mu(N,V,T) = \left.\frac{\partial F(N,V,T)}{\partial N}\right|_{V,T} \qquad P(N,V,T) = -\left.\frac{\partial F(N,V,T)}{\partial V}\right|_{N,T}$$

$$C_V(N,V,T) = \frac{\partial E(N,V,T)}{\partial T} = \left.\frac{\partial^2 F(N,V,T)}{\partial T^2}\right|_{N,V}$$

Therefore, knowledge about the partition function of a given system is desirable. However, it is impossible to analytically derive or compute it apart from some simple systems like the ideal gas or the one- and two-dimensional Ising model.

The aim of statistical mechanics is to predict mean values of physical observables of a given physical system. The expectation value of an observable $A$ is defined by

$$\langle A \rangle = \int A(\Gamma) p(\Gamma) \mathrm{d}\Gamma \,, \tag{2.4}$$

where the points in phase space are denoted with $\Gamma$. The integral ranges over the whole phase space and is weighted with a probability distribution $p$. On the other hand, there is the time average

$$\overline{A} = \lim_{T\to\infty} \frac{1}{T} \int_0^T A(\Gamma(t))\mathrm{d}t \ , \tag{2.5}$$

where the mean value is taken along the trajectory of the system through phase space. The equality of these two averages is absolutely non-trivial. If $\langle A \rangle = \overline{A}$ holds, then the system is called *ergodic*. There are some examples of ergodic and non-ergodic systems but in general it is still impossible to tell if a given system is ergodic. Therefore, one typically assumes that the system under consideration is ergodic until the opposite is proven. Ergodicity is an important concept for Monte Carlo simulations because it predicts observables by approximating Eq. (2.4) while Molecular Dynamics uses a different approach based on approximating Eq. (2.5).

Monte Carlo simulations are a means to solve a problem by using random numbers. One traditional example is the calculation of $\pi$. One draws a circle with diameter 1 within a square of side length 1. By drawing $N$ random points within the square and counting the number $N_{\text{hit}}$ of points within the circle, one can approximate $\pi$ using the fact that $N_{\text{hit}}/N \approx A_{\text{circle}}/A_{\text{square}} = \pi/4$. Provided the points are on average evenly distributed on the square, then one can get a good estimate for $\pi$ for large $N$.

Monte Carlo simulations can also be used in statistical physics by translating the concept of phase space into a Markov chain. Every state the physical system can be in is represented by a knot $\boldsymbol{x}$ in a network and every transition from one state to another has a certain transition probability $W(\boldsymbol{x}_i \to \boldsymbol{x}_j)$. These transition probabilities depend on the current knot but not on the history of previously visited knots. A Markov chain is a path in this network of knots

$$\boldsymbol{x}_0 \xrightarrow{W(\boldsymbol{x}_0\to\boldsymbol{x}_1)} \boldsymbol{x}_1 \xrightarrow{W(\boldsymbol{x}_1\to\boldsymbol{x}_2)} \boldsymbol{x}_2 \xrightarrow{W(\boldsymbol{x}_2\to\boldsymbol{x}_3)} \boldsymbol{x}_3 \to \dots \ . \tag{2.6}$$

Consider one knot $\boldsymbol{x}_i$ in this network. There is a flow of probability from and to this knot, so that the probability $P(\boldsymbol{x}_i, t)$ of being at the knot $\boldsymbol{x}_i$ at time $t$ changes as

$$P(\boldsymbol{x}_i, t+1) - P(\boldsymbol{x}_i, t) = \sum_{\boldsymbol{x}_j \neq \boldsymbol{x}_i} P(\boldsymbol{x}_j, t) W(\boldsymbol{x}_j \to \boldsymbol{x}_i) - \sum_{\boldsymbol{x}_j \neq \boldsymbol{x}_i} P(\boldsymbol{x}_i, t) W(\boldsymbol{x}_i \to \boldsymbol{x}_j) \ . \tag{2.7}$$

This equation is called *master equation*, as it governs the overall probability distribution across the network of knots. The *Theorem of Markov* states that

> If a Markov chain is ergodic, which means that one can go from any knot to any other knot in a finite number of steps, then the Markov chain has

a unique stationary probability distribution

$$P(\boldsymbol{x}) = \lim_{t\to\infty} P(\boldsymbol{x}, t) \tag{2.8}$$

for all knots $\boldsymbol{x}$. This stationary probability distribution is approached for $t \to \infty$, regardless which initial state $\boldsymbol{x}_{\text{start}}$ is chosen.

The proof can be found in [Feller, 1968]. If one initializes the system in a state $\boldsymbol{x}_{\text{start}}$, then the probability is concentrated on this point at $t = 0$. As time proceeds, the probability will spread across the network. The Theorem of Markov ensures that the probability distribution of the system will "forget" the initial state and approach an equilibrium distribution. For the stationary distribution, Eq. (2.7) becomes

$$\sum_{\boldsymbol{x}_j \neq \boldsymbol{x}_i} P(\boldsymbol{x}_j) W(\boldsymbol{x}_j \to \boldsymbol{x}_i) = \sum_{\boldsymbol{x}_j \neq \boldsymbol{x}_i} P(\boldsymbol{x}_i) W(\boldsymbol{x}_i \to \boldsymbol{x}_j) \ . \tag{2.9}$$

This equation is fulfilled if the following stricter equation is fulfilled

$$P(\boldsymbol{x}_j) W(\boldsymbol{x}_j \to \boldsymbol{x}_i) = P(\boldsymbol{x}_i) W(\boldsymbol{x}_i \to \boldsymbol{x}_j) \ . \tag{2.10}$$

This requirement is called *detailed balance*. It states that the probability to be at one knot $\boldsymbol{x}_i$ and move to a neighboring knot $\boldsymbol{x}_j$ is equal to the probability to be in the neighboring knot $\boldsymbol{x}_j$ and go back to the original knot $\boldsymbol{x}_i$.

The concept of Markov chains translates to problems of statistical physics easily. The network of knots $\{\boldsymbol{x}\}$ represents the phase space $\{\Gamma\}$ of a given physical system if the equilibrium probability $P(\boldsymbol{x})$ represents thermal equilibrium, namely

$$P(\boldsymbol{x}) = \frac{1}{Z} \exp\left[-\beta E(\boldsymbol{x})\right] \tag{2.11}$$

where $\beta = 1/(k_{\text{B}}T)$ is the inverse temperature and $E(\boldsymbol{x})$ is the energy of the state (or configuration), given by the system's Hamiltonian $\mathcal{H}(\boldsymbol{x})$. The transition probability $W(\boldsymbol{x}_i \to \boldsymbol{x}_j)$ can be split into two parts

$$W(\boldsymbol{x}_i \to \boldsymbol{x}_j) = W_{\text{choose}}(\boldsymbol{x}_i \to \boldsymbol{x}_j) W_{\text{accept}}(\boldsymbol{x}_i \to \boldsymbol{x}_j) \tag{2.12}$$

The first part $W_{\text{choose}}$ is the probability to choose a state $\boldsymbol{x}_j$ for the transition and the second part $W_{\text{accept}}$ is the probability to make the move. Usually one takes $W_{\text{choose}}(\boldsymbol{x}_i \to \boldsymbol{x}_j) = W_{\text{choose}}(\boldsymbol{x}_j \to \boldsymbol{x}_i)$. Then from the detailed balance (2.10), one can conclude

$$\frac{W_{\text{accept}}(\boldsymbol{x}_i \to \boldsymbol{x}_j)}{W_{\text{accept}}(\boldsymbol{x}_j \to \boldsymbol{x}_i)} = \frac{P(\boldsymbol{x}_j)}{P(\boldsymbol{x}_i)} = \exp\left(-\beta[E(\boldsymbol{x}_j) - E(\boldsymbol{x}_i)]\right) \ . \tag{2.13}$$

Note that if $W(\boldsymbol{x}_i \to \boldsymbol{x}_j)$ is zero, then $W(\boldsymbol{x}_j \to \boldsymbol{x}_i)$ is also zero, so there is no division by zero taking place here. This equation tells how the transition probabilities between points in phase space have to be chosen to yield the thermal equilibrium distribution of states. To fulfill Eq. (2.13), many choices are possible, but the most common one is the Metropolis criterion [Metropolis et al., 1953]

$$W_{\text{accept}}(\boldsymbol{x}_i \to \boldsymbol{x}_j) = \min\left[1, \exp\left(\beta[E(\boldsymbol{x}_j) - E(\boldsymbol{x}_i)]\right)\right] \tag{2.14}$$

where a Monte Carlo move is accepted with the probability $\exp\left(\beta[E(\boldsymbol{x}_j) - E(\boldsymbol{x}_i)]\right)$, but always if the total energy is lowered.

Monte Carlo simulations offer a simple way to calculate mean values of physical observables via Eq. (2.4). One simply has to follow a Markov chain through phase space and measure $A$ along the way. Then

$$\langle A \rangle \approx \sum_{i=1}^{N} A(\boldsymbol{x}_i) \; . \tag{2.15}$$

To proceed from one configuration to the next, Monte Carlo moves are made. A Monte Carlo move consists of the following steps

1. Create from the current configuration $\boldsymbol{x}_i$ a new configuration $\boldsymbol{x}'$.
2. Calculate the energy difference $\Delta E = E(\boldsymbol{x}') - E(\boldsymbol{x}_i)$ between the new and the old configuration.
3. Draw a random number $r \in [0, 1]$.
4. If $r < \mathrm{e}^{-\beta \Delta E}$, accept the new configuration $\boldsymbol{x}_{i+1} = \boldsymbol{x}'$, otherwise restore the old configuration and set $\boldsymbol{x}_{i+1} = \boldsymbol{x}_i$.

The second step is an attempt to move from one point in phase space to another point in phase space. If the jump is too large, the move will be declined. Therefore, one has to think of moves which change the configuration significantly and, at the same time, have a high acceptance ratio. For example, in an Ising model, one can attempt to flip one spin, or a whole cluster of spins at the same time. In continuous models, one can try to add or remove a particle, or translate a particle over a small distance. Note also that the system can remain in one configuration for several steps if all moves are declined. This is due to the probabilistic nature of the Markov chain reflecting the thermal fluctuations in the physical system.

When using Monte Carlo techniques, some aspects have to be kept in mind.

- After initializing the system, one has to wait until the initial configuration is forgotten and equilibrium is reached. Then one can start to measure $A$ to get the equilibrium value. If one immediately starts to measure $A$, there is a systematic error in the resulting value.
- The way in which the transition moves are chosen greatly influences the performance of the simulation. If the Monte Carlo moves have little acceptance probabilities or the changes of the configuration by a move is very small, it can take a very long time to reach equilibrium and get meaningful results. Therefore, a lot of research focuses on thinking of new and better Monte Carlo moves, especially in polymer physics.
- It must be ensured that the detailed balance is fulfilled. It should be emphasized that in this context, $W_{\text{choose}}(\boldsymbol{x}_i \to \boldsymbol{x}_j) = W_{\text{choose}}(\boldsymbol{x}_j \to \boldsymbol{x}_i)$ is sometimes forgotten.

### 2.1.2 The Interfacial Tension

If two phases are in contact with each other, for example a crystal and some surrounding liquid, the system creates an interface between the two phases, which costs free energy. This is the reason why heterogeneous structures are unstable in computer simulations, as the system can usually lower its free energy by eliminating the interfaces and becoming homogeneous[1].

In general, the interfacial tension $\gamma$ is defined as the amount of free energy $\Delta F$ needed to create an interface, divided by the area $A$ of the interface

$$\gamma = \lim_{V \to \infty} \frac{\Delta F}{A} \,. \tag{2.16}$$

While with growing volume $V$, the free energy and the interfacial area diverge, the interfacial tension $\gamma$ is finite and well-defined in the thermodynamic limit. In computer simulations, one can use advanced Monte Carlo techniques to compute $\Delta F$ directly, but only with limited success [cf. section 4.2]. As explained in chapter 1, the interfacial tension is of great importance in condensed matter physics. Hence, the whole thesis focuses on this quantity, which is known exactly only for some specific model systems like the Ising model in two dimensions.

[1] There are exceptions to this rule: In the one-dimensional Ising model, the system is heterogeneous for $T > 0$. Instead of aligning all spins, it creates domains in which spins are parallel. This is due to the fact that the free energy cost to create domain walls is outweighed by the entropy gained by having the freedom to place the domain walls anywhere in the system. This is an important effect discussed in chapter 5, as it is not restricted to the Ising model.

## 2.2 Discrete Model Systems

If one wishes to study nucleation phenomena with computer simulations, there are two major challenges. First, due to limited resources, one can typically only access a small number of decades in time, which corresponds to barriers much smaller than what is needed to monitor relevant nucleation barriers which are about 30 $k_\mathrm{B}T$. Second, it is in general difficult and still an unsolved problem to decide whether an atom belongs to a droplet or to the environment, for the interfaces are in general diffuse and fluctuating. For these reasons, it is a very advantageous to study nucleation in a simplistic model, which contains nucleation phenomena but can be simulated easily. The Ising model does not only provide a link to the past studies of nucleation phenomena [Binder and Stauffer, 1972; Binder and Müller-Krumbhaar, 1974; Binder and Stauffer, 1976; Binder, 1987], where the computing power has much more limited than today, but also to quite recent studies [Pan and Chandler, 2004; Winter et al., 2009b; Ryu and Cai, 2010; Prestipino et al., 2013], showing that the Ising model is a valuable and established model. Later, in this thesis, a link between worlds will be established by using the Ising model, the simplicity of which allows to study a huge variety of system sizes with acceptable computational effort, to understand much more complicated systems, namely colloidal model systems like hard spheres and the Asakura-Oosawa model, which are introduced in section 2.3.

In this section, the Ising model and the similar lattice gas model will be introduced. Also, the finite-size phases will be shown, since they play an important role when defining droplet volumes in chapter 3.

### 2.2.1 The Ising (lattice gas) Model

The Ising model one of the central models in statistical physics. On a $d$-dimensional simple cubic lattice, where each lattice site is occupied by a spin $\sigma_i$ (which can take the values $\pm 1$) and has $q = 2d$ next neighbors, $q$ being the coordination number of the lattice, the Hamiltonian $\mathcal{H}$ is given by

$$\mathcal{H} = -J \sum_{\langle i,j \rangle} \sigma_i \sigma_j - H \sum_i \sigma_i \ , \tag{2.17}$$

$H$ being a global magnetic field and $J$ being the coupling constant between next neighbors $\langle i, j \rangle$. Note that we set $J = 1$ in the whole thesis, as it is the natural energy scale in this model.

For homogeneous nucleation, one usually considers the three-dimensional Ising model on a simple cubic lattice with linear dimension $L$ and volume $V = L^3$,

using periodic boundary conditions in all three directions. At high temperatures, the interaction between the spins is much weaker than the thermal fluctuations, so that the magnetization per volume $m = \sum_i \sigma_i / V$ is zero on average. At low temperatures, the interaction enables the system to become ordered, thereby gaining a net magnetization $m_{\mathrm{sp}}(T)$. The phase transition of second order occurs at the critical temperature $k_{\mathrm{B}} T_c / J = 4.5115$ [Ferrenberg and Landau, 1991; Baillie et al., 1992].

The Ising model is closely related to the lattice gas model [Lee and Yang, 1952], where physical quantities can be mapped from one model to the other, as will be explained below. For the lattice gas model, consider a simple cubic lattice, where each lattice site $i$ can either be occupied ($c_i = 1$) or empty ($c_i = 0$). The particles interact via an interaction constant $J$ if they are next to each other on the lattice. Within the grandcanonical ensemble $(\mu, V, T)$, i.e. at constant chemical potential $\mu$, volume $V$ (number of lattice sites) and temperature $T$, the Hamiltonian is given by

$$\mathcal{H}_{\mathrm{LG}} = -J \sum_{\langle i,j \rangle} c_i c_j - \mu \sum_i c_i \, . \tag{2.18}$$

This lattice gas Hamiltonian can be mapped onto the Ising Hamiltonian (2.17) via the transformation

$$\sigma_i = 2c_i - 1 \quad \Leftrightarrow \quad c_i = \frac{1 + \sigma_i}{2} \, . \tag{2.19}$$

The important properties between the two models translate as follows

$$J = \frac{J_{AA}}{4} \, , \qquad \varrho = \frac{1+m}{2} \, , \qquad H = \frac{\mu - \mu_{\mathrm{coex}}}{2} \, , \tag{2.20}$$

with $\mu_{\mathrm{coex}} = q J_{AA}/2$, $q$ being the coordination number of the lattice, which is $2d$ in $d$ dimensions. The interpretation is that an Ising system in a magnetic field $H$ is equivalent to a lattice gas model at the corresponding chemical potential. Further information can be found in [Binder and Kalos, 1980; Lee and Yang, 1952]. In this thesis, the two models will be used side by side, depending on the point of view. The magnetization $m$ of the Ising model corresponds to the density of spins pointing upwards via $\varrho = (1+m)/2$.

The two-dimensional Ising model on a square lattice is exactly soluble [Onsager, 1944] for vanishing magnetic field $H$. Setting $J$ to unity, the critical temperature $T_c$ is the solution of the equation $\sinh(2\beta)^2 = 1$, which is

$$T_c = \frac{2}{\operatorname{arcsinh}(1)} = \frac{2}{\ln(1+\sqrt{2})} \approx 2.26919 \tag{2.21}$$

The interfacial tension (for the definition, see section 2.1.2) is given by

$$\gamma = \begin{cases} 2\beta + \ln(\tanh(\beta)) & T < T_c \\ 0 & T \geq T_c \end{cases} \, . \tag{2.22}$$

This is important for chapter 5, where numerical calculations of $\gamma$ can be compared to the exact result. In three dimensions, the interfacial tension $\gamma$ and the critical temperature $T_c$ are only known numerically.

### 2.2.2 Finite-Size Phases in the Lattice Gas Model

In computer simulations, the systems under consideration are always finite. Using periodic boundary conditions in order to extract the system's bulk properties, one can observe different geometries [Schrader et al., 2009a,b] of the system, depending on the density $\varrho$ of occupied lattice sites, respectively. Figure 2.1 shows that there are seven different geometries in a homogeneous system with periodic boundary conditions in all three directions. In the following, a phase with low density will be referred to as vaporous while a system with high density will be called liquid. Of course, due to the spin exchange symmetry, it could as well be the other way around. The different geometries only appears in a finite box. In the thermodynamic limit, the chemical potential dependency on density is much simpler, for it is completely flat in the two-phase region.

If the density is very low, there are only small fluctuating liquid clusters in a vaporous surrounding. Unlike in the thermodynamic limit, where the chemical potential is zero in the two-phase region $\varrho_{v,\mathrm{coex}} < \varrho < \varrho_{l,\mathrm{coex}}$, the vaporous state in a finite geometry is also stable also at slightly higher densities than $\varrho_{v,\mathrm{coex}}$. At some point however, the system performs the droplet evaporation-condensation transition [Binder, 2003; MacDowell et al., 2004; Schrader et al., 2009a], at which the liquid phase coagulates to form a compact (spherical) shape. At this point, the system is decomposed into a liquid region and a vaporous region, separated by an interface with an interface tension $\gamma_{vl}$.

Increasing the density even more leads to a second transition, where the droplet becomes so large that it connects to itself via the periodic boundary condition and thereby assumes a cylindrical shape. This behavior is motivated by the increased volume-to-interface ratio of the cylindrical shape compared to a spherical shape. The next transition occurs when the liquid phase connects to itself via two periodic boundaries. Such a geometry is called a slab [Schrader et al., 2009a; Block et al., 2010; Tröster et al., 2012]. Since the interface area does not change with varying density, the chemical potential is flat in this geometry. Because of the spin exchange symmetry, the different geometries occur now with exchanged roles of positive and negative spins, namely a cylindrical vaporous bubble, a compact (spherical) bubble and a liquid with small fluctuating vaporous clusters.

It should be emphasized that the exact shape of the minority phase depends on the

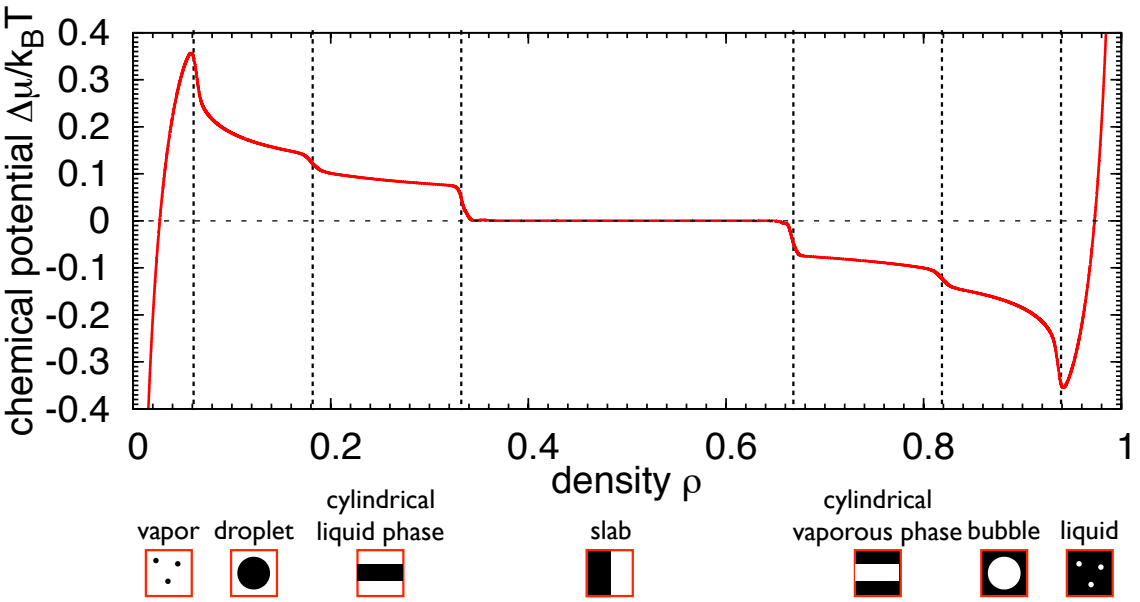


Figure 2.1: The chemical potential $\beta\Delta\mu$ against the density $\varrho$ for a three-dimensional Ising system at a temperature below the critical temperature. The transitions between two geometries is accompanied by a phase transition and therefore a jump in the chemical potential. This jump is blurred because in a finite system, the partition function is always analytical and hence cannot have a jump. In larger systems, the jumps become steeper. The data shown here is from a system with $L = 20, k_\mathrm{B}T/J = 3.0$. For $L \to \infty$, the structure in the two-phase region vanishes and the chemical potential is zero for $\varrho_{v,\mathrm{coex}} < \varrho < \varrho_{l,\mathrm{coex}}$.

model and the temperature. In general, the minority phase tries to minimize its free energy by minimizing the interface, which naturally leads to spherical or cylindrical shapes. However, in the Ising model and any other model where the interface tension $\gamma$ depends on the orientation (especially crystals), the shape will deviate from the spherical form. This will be discussed in section 3.2.

### 2.2.3 Connection to the Random-Cluster Model

There exist quite a few advanced simulation methods to efficiently sample the Ising model. One of these is the Swendsen-Wang algorithm [Swendsen and Wang, 1987], where instead of single spin flips, a whole cluster of spins is flipped in one step. It has been shown that this is an accurate sampling which is dramatically faster than single spin flip algorithms, especially in the vicinity of the critical point. However, it

plays an important role in chapter 3 for a different reason.

An ordinary Monte Carlo move in an Ising system is to choose one spin randomly and attempt to flip it using the Metropolis criterion Eq. (2.14). The Swendsen-Wang algorithm attempts to flip whole clusters instead of single spins. A cluster is determined by creating bonds between all spins of equal orientation. Those spins, which are connected to each other, belong to the same cluster. This procedure divides the system in a number of clusters (each cluster consisting of at least one spin), where each spin belongs to exactly one cluster. Then one of these clusters is chosen and an attempt is made to flip all spins belonging to this cluster, again using the Metropolis criterion Eq. (2.14). At high temperatures this procedure is much faster, i.e. the auto-correlation function vanishes much more quickly, if compared to ordinary single spin flips.

When creating bonds, a bond between two spins with the same orientation must be set only with a temperature-dependent probability

$$p = 1 - \exp(2\beta) \ , \tag{2.23}$$

where $\beta = 1/(k_\mathrm{B}T)$ is the inverse temperature and the interaction constant $J$ is set to 1. The following calculation motivates this Swendsen-Wang probability $p$. A mathematically rigorous derivation is found in chapter 4 of [Fortuin and Kasteleyn, 1972].

The partition function of the Ising model with vanishing magnetic field $H$ is given by

$$Z = \sum_\sigma \exp\left(\beta \sum_{\langle ij\rangle} \sigma_i \sigma_j\right) \ , \tag{2.24}$$

where $\sum_\sigma$ sums over all configurations of spins and $\sum_{\langle ij\rangle}$ sums over all next neighbors. The partition function can be rewritten as

$$\begin{aligned} Z &= \sum_\sigma \exp\left(\beta \sum_{\langle ij\rangle} \sigma_i \sigma_j\right) \\ &= \sum_\sigma \prod_{\langle ij\rangle} \exp\left(\beta \sigma_i \sigma_j\right) \\ &= \sum_\sigma \prod_{\langle ij\rangle} \mathrm{e}^{\beta} \left(\delta_{\sigma_i,\sigma_j} + \mathrm{e}^{-2\beta} \delta_{\sigma_i,-\sigma_j}\right) \ . \end{aligned}$$

Now we add a zero and rearrange the terms

$$\begin{aligned} Z &= \sum_{\sigma} \prod_{\langle ij \rangle} \mathrm{e}^{\beta} \left( \delta_{\sigma_i,\sigma_j} + \mathrm{e}^{-2\beta} \delta_{\sigma_i,-\sigma_j} + \mathrm{e}^{-2\beta} \delta_{\sigma_i,\sigma_j} - \mathrm{e}^{-2\beta} \delta_{\sigma_i,\sigma_j} \right) \\ &= \sum_{\sigma} \prod_{\langle ij \rangle} \mathrm{e}^{\beta} \left( (1 - \mathrm{e}^{-2\beta}) \delta_{\sigma_i,\sigma_j} + \mathrm{e}^{-2\beta} ) \right) \ . \end{aligned}$$

Introducing the probability $p = 1 - \mathrm{e}^{-2\beta}$, one obtains

$$Z = \sum_{\sigma} \prod_{\langle ij \rangle} \mathrm{e}^{\beta} \left( p \delta_{\sigma_i,\sigma_j} + (1-p) \right) \ . \tag{2.25}$$

Now using the relation $a + b = \sum_{k=0}^{1} (a\delta_{k,0} + b\delta_{k,1})$, the final result is

$$Z = \sum_{\sigma} \prod_{\langle ij \rangle} \sum_{n_{ij}} \mathrm{e}^{\beta} \left( p \delta_{\sigma_i,\sigma_j} \delta_{n_{ij},1} + (1-p) \delta_{n_{ij},0} \right) \ . \tag{2.26}$$

The $n_{ij}$ establish the connection to the random cluster model. The bond between the next neighbors $\langle i, j \rangle$ is active with a probability $p = 1 - \mathrm{e}^{-2\beta}$, but only if $\sigma_i = \sigma_j$. So there can only be bonds between spins with equal sign.

In a simulation, one can sample this partition function by initializing inactive bonds between all neighbors. Then one activates the bond between each pair of spins with $\sigma_i = \sigma_j$ with the probability $p$. In the end, one has subdivided the configuration into a number of clusters. At high temperatures, flipping these clusters instead of single spins generate uncorrelated configurations with much less computational effort. However, this is not relevant for this work. Instead, the physical relevance of these clusters will be discussed in chapter 3.

## 2.3 Continuous Model Systems

### 2.3.1 The Lennard-Jones Model

The Lennard-Jones potential $U(r)$ for two atoms with distance $r$ was proposed by John Lennard-Jones [Jones, 1924] for the description of vaporous Argon. The potential consists of short-ranged repulsive term $\propto r^{-n}$, describing Pauli repulsion forces, and an attractive term $\propto r^{-m}$ with $m = 6$, representing the London dispersion forces. Although the repulsive part of real atoms is better described by other functions of $r$, the great benefit of the following representation is its computational efficiency, when the repulsive term is just the square of the attractive term

$$U(r) = 4\varepsilon \left[ \left( \frac{\sigma}{r} \right)^{12} - \left( \frac{\sigma}{r} \right)^{6} \right] \tag{2.27}$$

Here, $\sigma$ is the natural length scale of the potential and can be interpreted as the diameter of the particles. The constant $\varepsilon$ sets the depth of the potential minimum of the potential. The critical temperature of a full Lennard-Jones potential is $k_\mathrm{B}T/\varepsilon = 1.326(2)$ [Caillol, 1998]. The phase diagram is shown in Fig. 2.2.

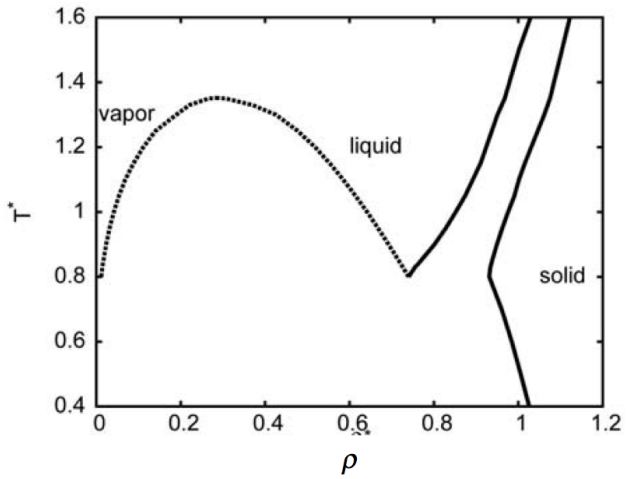


Figure 2.2: Phase diagram for the Lennard-Jones potential (2.27). The horizontal axis shows the reduced density $N/V$ and the vertical axis the reduced temperature $T^* = k_\mathrm{B}T/\varepsilon$. The dashed line corresponds to the liquid-vapor coexistence and the solid lines to solid-liquid and solid-vapor coexistence. The triple line, where all three phases coexist at one temperature, is at $T^* \approx 0.8$. This picture is taken from [Bizjak et al., 2009].

From a computational physicist's point of view, this interaction is long-ranged. Therefore the Lennard-Jones potential is often truncated at a distance $r_\mathrm{cut}$ and shifted so that the potential approaches zero smoothly:

$$U(r) = \begin{cases} 4\varepsilon \left[ \left(\frac{\sigma}{r}\right)^{12} - \left(\frac{\sigma}{r}\right)^{6} + Y \right] & , r \leq r_\mathrm{cut} \\ 0 & , r > r_\mathrm{cut} \end{cases} \tag{2.28}$$

with $Y = (2^7 - 1)2^{-14}$. The cutoff radius is chosen to be $r_\mathrm{cut} = 2 \cdot 2^{1/6}$ in this work. The truncation decreases the computational effort while maintaining the overall behavior of the particles. Both potentials are plotted in Fig. 2.6.

Although for the truncated potential, the phase diagram looks similar, the choice of $r_\mathrm{cut}$ (and also whether the potential is shifted or not) effectively defines a different model [Smit, 1992], e.g. the critical temperature is lower, because the interaction range is decreased. For our choice $r_\mathrm{cut} = 2 \cdot 2^{1/6}$, the critical temperature is $k_\mathrm{B}T/\varepsilon = 0.999$ [Virnau, 2003].

### 2.3.2 A short Introduction to Crystallography

A solid phase is characterized by the arrangement of its constituents. One can distinguish three kinds of solids:

- Crystals: The constituents are arranged with a periodic order. A crystal can have two-, three-, four- or sixfold symmetry.
- Incommensurable structures and quasi-crystals: These structures consist of two or more sub-lattices whose lattice constants are incommensurable. A quasi-crystal has a long-range order and can have five-, eight-, ten- or twelvefold symmetry.
- Amorphous structures: There is no order in these structures. The disorder can be positional (colloidal glasses, metallic glasses) or topological (amorphous semiconductors).

The lattice structure of a crystal is described by a Bravais lattice, which is a discrete set of all points of the form

$$\boldsymbol{R}_{j,m,n} = j\boldsymbol{a}_1 + m\boldsymbol{a}_2 + n\boldsymbol{a}_3 \tag{2.29}$$

where $j, m, n$ are integers and the $\boldsymbol{a}_i$ are three fixed linearly independent vectors called the primitive vectors of the lattice. They are not unique, so one can describe the same lattice by several sets of $\{\boldsymbol{a}_i\}$. Instead of a set of primitive vectors, one can also characterize the lattice by a unit cell. A unit cell is a volume which, if translated by all $\boldsymbol{R}_{j,m,n}$, completely fills the entire space without overlaps or empty spaces. One can always find a so-called primitive unit cell which contains only one point of the Bravais lattice. A unit cell can contain one or several constituents.

A crystal structure is fully characterized by the structure of the unit cell and the lattice structure. There are 14 Bravais lattices in total. In this work, the simple cubic (sc), the body-centered cubic (bcc), the face-centered cubic (fcc) and the hexagonal close-packed (hcp) are of importance. The unit cell of the sc lattice is a cube with one particle in each corner. If one takes the sc lattice and adds one atom in the center of the unit cell, one obtains the bcc lattice. The fcc structure is obtained from the sc lattice by adding one atom in the center of each of the six sides of the cube.

An important quantity of crystal structures is the coordination number $q$, which is the number of next neighbors of an atom. Due to the periodicity of the lattice, this number is the same for all particles in a lattice. The fcc lattice plays a special role because it has the highest coordination number possible, corresponding to a

close-packing of equal spheres[2]. The hcp structure differs from the fcc structure only by the way in which the close-packed lattice planes are stacked. Whereas hcp has an ABAB structure, the fcc structure corresponds to a stacking in an ABCABC fashion. The volume packing fraction $\eta = \frac{\pi}{6}\frac{N\sigma^3}{V}$, $\sigma$ being the diameter of the spheres, of both close-packed structures is

$$\eta_{\max} = \frac{\sqrt{2}\pi}{6} \approx 0.740480 \tag{2.30}$$

which is the highest packing fraction one can achieve with equal spheres.

| crystal | $q$ | $\eta_{\max}$ |
|---|---|---|
| sc | 6 | $\pi/6 \approx 0.5236$ |
| bcc | 8 | $\sqrt{3}\pi/8 \approx 0.6802$ |
| fcc | 12 | $\sqrt{2}\pi/6 \approx 0.7405$ |
| hcp | 12 | $\sqrt{2}\pi/6 \approx 0.7405$ |

Table 2.1: Coordination number $q$ and maximal volume packing fraction $\eta_{\max}$ of various crystal structures. The fcc and hcp structures have the highest volume packing fraction one can produce with equal spheres.

The reciprocal lattice is a very important way to study lattice structures. It is defined to be the set of points satisfying

$$\mathrm{e}^{\mathrm{i}\boldsymbol{K}\cdot\boldsymbol{R}_{j,m,n}} = 1 \tag{2.31}$$

for all Bravais lattice points $\boldsymbol{R}_{j,m,n}$. The set of vectors $\{\boldsymbol{K}_{h,k,l}\}$ having this property characterize a Bravais lattice in reciprocal space, and the reciprocal primitive vectors can be calculated from the ones of the original lattice by

$$\boldsymbol{b}_1 = 2\pi\frac{\boldsymbol{a}_2 \times \boldsymbol{a}_3}{\boldsymbol{a}_1 \cdot (\boldsymbol{a}_2 \times \boldsymbol{a}_3)} \quad \boldsymbol{b}_2 = 2\pi\frac{\boldsymbol{a}_3 \times \boldsymbol{a}_1}{\boldsymbol{a}_1 \cdot (\boldsymbol{a}_2 \times \boldsymbol{a}_3)} \quad \boldsymbol{b}_3 = 2\pi\frac{\boldsymbol{a}_1 \times \boldsymbol{a}_2}{\boldsymbol{a}_1 \cdot (\boldsymbol{a}_2 \times \boldsymbol{a}_3)} \,. \tag{2.32}$$

The reciprocal lattice points are then given by

$$\boldsymbol{K}_{h,k,l} = h\boldsymbol{b}_1 + k\boldsymbol{b}_2 + l\boldsymbol{b}_3 \tag{2.33}$$

The reciprocal lattice of the reciprocal lattice is again the original lattice. The Brillouin zone is a possible unit cell of the reciprocal lattice. It contains all unique vectors in reciprocal space, since

$$\mathrm{e}^{\mathrm{i}(\boldsymbol{q}+\boldsymbol{K}_{h,k,l})\cdot\boldsymbol{R}_n} = \mathrm{e}^{\mathrm{i}\boldsymbol{q}\cdot\boldsymbol{R}_{j,m,n}} \,. \tag{2.34}$$

[2]Therefore it is also referred to as cubic close-packed.

This reflects the periodicity of the crystal. One can use the reciprocal lattice to characterize the lattice planes of the original lattice because the normal vector to a lattice plane is always a reciprocal lattice vector. The vector $\boldsymbol{K}_{h,k,l}$ is a normal to the plane that intercepts the points $\boldsymbol{a}_1/h, \boldsymbol{a}_2/k, \boldsymbol{a}_3/l$ or a multiple thereof. The integers $h, k$ and $l$ are called Miller indices and the set of planes with normal $\boldsymbol{K}_{h,k,l}$ is then denoted by $(hkl)$. To denote a direction rather than a set of planes, the notation $[jmn]$ is commomly used, which stands for the vector $j\boldsymbol{a}_1 + m\boldsymbol{a}_2 + n\boldsymbol{a}_3$. Note that it is a special case that in cubic lattices, $[hkl]$ is a normal to the planes described by $(hkl)$.

In computer simulations, if a crystal is said to be in (111) orientation, this means that the (111) planes are parallel to the $xy$ plane of the simulation box, which usually has the shape of a rectangular cuboid. As the interfacial tension between a crystalline structure and a fluid depends on which side of the crystal is exposed to the liquid, the interfacial tension has to be calculated for each orientation separately.

### 2.3.3 The Hard Sphere Model

Hard spheres (or hard disks in two dimensions) are a very fundamental model system. While the interaction between hard spheres is trivial, this model shows a rich variety of interesting phenomena. Because the model is independent of temperature, its properties are determined purely by entropy. Often, hard spheres can serve as a first approximation to other models with short ranged interactions. The hard spheres are spheres with a diameter $\sigma$ and the pair potential

$$U_{\mathrm{HS}}(r) = \begin{cases} \infty & r \in [0, \sigma] \\ 0 & r \in (\sigma, \infty) \end{cases} . \tag{2.35}$$

There is no interaction between hard spheres except for the fact that they cannot overlap, for this would require an infinite amount of energy. The phase diagram of hard spheres is one-dimensional, as shown in Fig. 2.3. The only parameter is the packing fraction

$$\eta = \frac{\pi}{6} \frac{N\sigma^3}{V} , \tag{2.36}$$

where $N$ is the particle number and $V$ the volume.

There are two important points in the phase diagram, namely at $\eta_l = 0.494$ and $\eta_c = 0.545$. At packing fractions below $\eta_l$, the hard spheres form an unordered phase, which is referred to as liquid or fluid phase. When crossing $\eta_l$, the system consists into two separate phases, namely a fluid phase at $\eta_l$ and a crystal phase at $\eta_c$. The

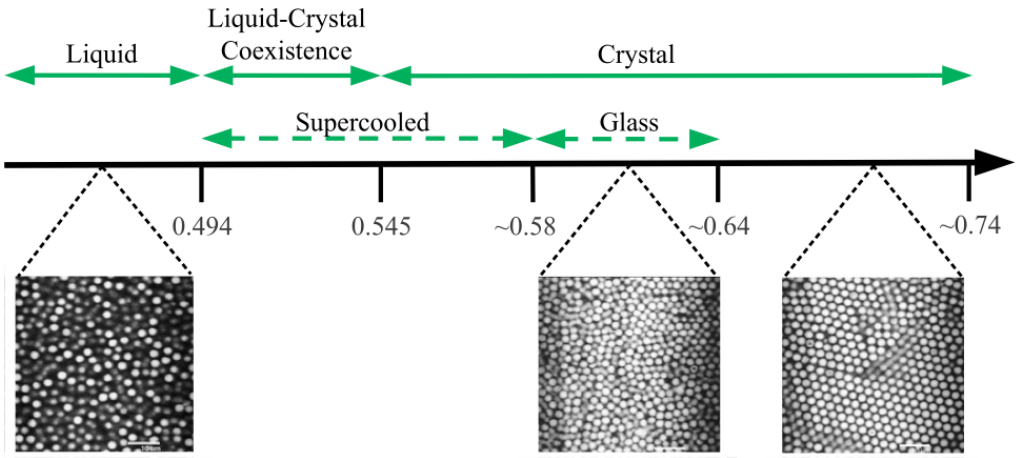


Figure 2.3: Phase diagram of hard spheres. For $\eta < 0.494$, the hard sphere is in the disordered liquid (or fluid) phase. For $\eta > 0.545$, the hard spheres form a crystalline phase. The packing fraction $\eta = \sqrt{2}\pi/6 \approx 0.74$ is the maximum packing fraction, for then the hard spheres are close-packed. For $0.494 < \eta < 0.545$, the system separates into two coexisting phases. In polydisperse colloidal suspensions, the boundaries between liquid and crystal are shifted, and also a glassy state can occur. On the bottom, confocal micrographs of analogous phases in a colloidal suspensions with 5% polydispersity are shown. This picture is taken from [Hunter and Weeks, 2012].

volume of each phase is given by a simple lever rule

$$V_l = \frac{\eta_c - \eta}{\eta_c - \eta_l} V \qquad V_c = \frac{\eta - \eta_l}{\eta_c - \eta_l} V \ . \tag{2.37}$$

At $\eta_c$, the whole volume is in the crystalline phase. If $\eta$ is further increased, the crystal will become denser until at $\eta_{\max} = \sqrt{2}\pi/6 \approx 0.74$, the hard spheres become close-packed.

In experiment, hard spheres do not occur. Instead, one can use colloidal suspensions with interaction potentials similar to hard spheres. However, due to the fabrication process, the spheres do not have a fixed diameter $\sigma$ but are typically polydisperse and non-uniform. Polydispersity introduces new phenomena and is therefore not considered in this work. Hard spheres can have various crystal shapes, for example fcc, hcp or bcc. The bcc lattice is unstable because its free energy is higher than for a liquid of the same density [Colot and Baus, 1985]. The free energy difference between fcc and hcp is very small, but it was found to be positive [Mau and Huse, 1999; Pronk and Frenkel, 1999], so fcc is preferred slightly, because it has the highest entropy.

### 2.3.4 The Asakura-Oosawa Model

The Asakura-Oosawa model (or AO model) offers a simple description of a binary mixture of colloids and polymers [Oosawa and Asakura, 1954; Asakura and Oosawa, 1958]. Despite its simplicity, it catches the basic properties of binary mixtures [Vrij, 1976]. The colloids are represented by hard spheres with diameter $\sigma$ whereas the polymers are represented by ideal gas particles whose diameter $\sigma_p$ is twice radius of gyration of the polymers. Thereby the conformational degrees of freedom of the polymers are neglected; they are assumed to be in a globular state. Hence the polymers do not interact with each other, i.e. they can penetrate each other without energy cost, but they interact with the colloids via a hard sphere interaction.

The AO model is a purely entropic model. It is characterized by the diameter ratio $q = \frac{\sigma_p}{\sigma}$, which is usually between 0 and 1, and the particle concentrations. The polymers give rise to an effective interaction between the colloids. This interaction is a depletion interaction [Ilett et al., 1995] and can be understood as follows, see also Fig. 2.4. A polymer can approach a colloid to a minimum distance $(\sigma + \sigma_p)/2$, so the colloids have a so-called depletion zone with the shape of a spherical shell around them, which is inaccessible by polymers. Now if two colloids approach each other, their depletion zones overlap, so that the total depletion volume of all colloids is reduced. The increase of volume accessible by polymers corresponds to an increase of entropy. Therefore, the polymers give rise to an attractive interaction between the colloids, which is of entropic origin.

If the diameter ratio $q = \frac{\sigma_p}{\sigma}$ is small enough, the polymers' degrees of freedom can be integrated out and contribute via an effective potential between the colloids [Asakura and Oosawa, 1958; Dijkstra et al., 1999]. Therefore the AO model is fully equivalent to a model containing no polymers but only colloids, where the hard sphere interaction is replaced by the following effective potential [for a plot, see Fig. 2.6]

$$U_{\mathrm{effAO}}(r) = \begin{cases} \infty & r \in [0, \sigma) \\ -\eta_p^r \frac{(1+q)^3}{q^3} \left(1 - \frac{3r}{2(1+q)\sigma} + \frac{r^3}{2(1+q)^3\sigma^3}\right) & r \in [\sigma, \sigma(1+q)] \\ 0 & r \in (\sigma(1+q), \infty) \end{cases} , \quad (2.38)$$

where $\eta_p^r = \pi\sigma_p^3 z_p/6$ is the polymer reservoir packing fraction, which serves as a temperature-like parameter[3] in this model, and $z_p$ being the polymer fugacity. The diameter ratio $q$ changes the interaction range. For the effective potential to be exact,

[3] If $\eta_p^r$ is increased, the difference between the densities of the fluid and crystalline phase decreases. This resembles the Ising model or the Lennard-Jones model, where the same happens if the temperature is increased. At the critical temperature, the difference becomes zero.

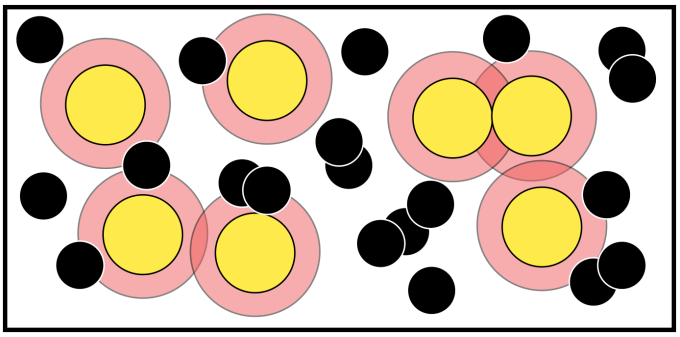

Figure 2.4: Visualization of the origin of the depletion force in the AO model. There are large colloids (yellow) and small polymers (black). The colloid-colloid and the colloid-polymer interaction is hard-sphere-like, while the polymers can move through each other without energetic cost (like ideal gas particles). The depletion zones, i.e. the volumes where the polymers' center of mass cannot be due to the colloid-polymer interaction, are shown in red. If two colloids approach each other, their depletion zones overlap (darker red), increasing the total volume accessible to polymers. Hence, moving colloids together increases the entropy of the system, which results in an effective attractive force between colloids.

$q$ must fulfill

$$q < q^* = \frac{2}{\sqrt{3}} - 1 \approx 0.1547 \tag{2.39}$$

for only then the effective AO model is an exact single particle species representation of the original AO model[4]. The reason is that the polymers can then only interact with two colloids at a time. This can be seen by simple geometric arguments, for if a polymer is trapped between close-packed colloids, $q^*$ corresponds to the minimal diameter where the polymer can touch all three colloids.

The effective AO model becomes a hard sphere model for $q \to 0$. For $q > 0$, the coexistence region broadens [Lekkerkerker et al., 1992], as can be seen in Fig. 2.5. In this work, we focus on $\eta_p^r = 0.1$ and $q = 0.15$, where the coexistence packing fractions are $\eta_c = 0.6357$ and $\eta_l = 0.4955$ [Statt, 2015][5].

There exists an extension of this effective AO model which remedies the fact that the potential is not differentiable and divergent. It is called soft effective AO model

[4]For $q > q^*$, there exist approximate effective potentials [Dijkstra et al., 2006].
[5]Note that this reference is work in progress.

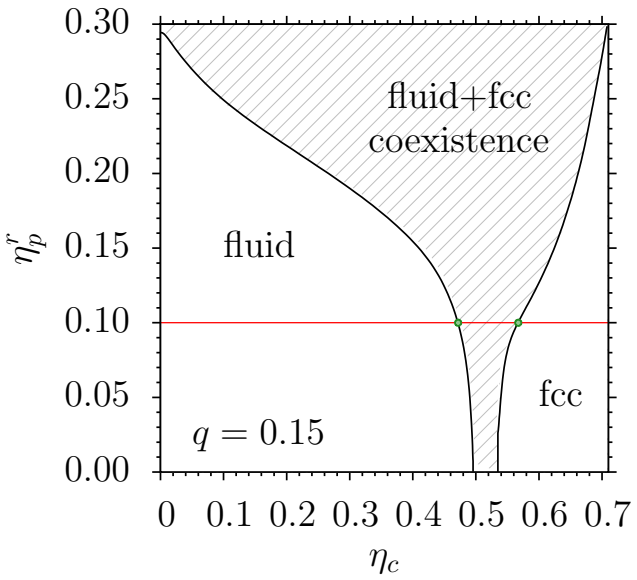


Figure 2.5: Phase diagram for the AO model at $q = 0.15$. The $x$-axis shows the packing fraction $\eta_c = \pi N\sigma^3/(6V)$ and the $y$-axis the polymer reservoir packing fraction $\eta_p^r$. The simulations in this work are entirely done at $\eta_p^r = 0.1$. Note that for $\eta_p^r \to 0$, the hard sphere case is recovered.

and is defined by

$$U_{\text{softEffAO}}(r) = \begin{cases} 100\ k_\text{B}T & r \in [0, \sigma_\text{core}) \\ 4\left[\left(\frac{b\sigma}{r-e\sigma}\right)^{12} + \left(\frac{b\sigma}{r-e\sigma}\right)^{6} - \left(\frac{b}{1+q-e}\right)^{12} - \left(\frac{b}{1+q-e}\right)^{6}\right] & r \in [\sigma_\text{core}, \sigma) \\ -\eta_p^r \frac{(1+q)^3}{q^3}\left(1 - \frac{3r}{2(1+q)\sigma} + \frac{r^3}{2(1+q)^3\sigma^3}\right) & r \in [\sigma, \sigma(1+q)) \\ 0 & r \in (\sigma(1+q), \infty) \end{cases}, \tag{2.40}$$

where $b$ and $e$ control the shape of the potential[6], respectively. This potential is a continuous fit to the effective Asakura-Oosawa model [Dijkstra et al., 1999]. It has been shown that the phase diagram of this model is similar to the original effective AO model [Statt, 2015].

[6]Within this thesis, the parameters are $b = 0.01$, $e = 0.988571$ in order to fulfill the (arbitrarily chosen) constraint $U(r = \sigma) = 1$, while $\sigma_\text{core}$ is fixed by the constraint that the potential should be continuous, i.e. $U(\sigma_\text{core}) = 100\ k_\text{B}T$. The value is $\sigma_\text{core} = 0.9960187400451774$.

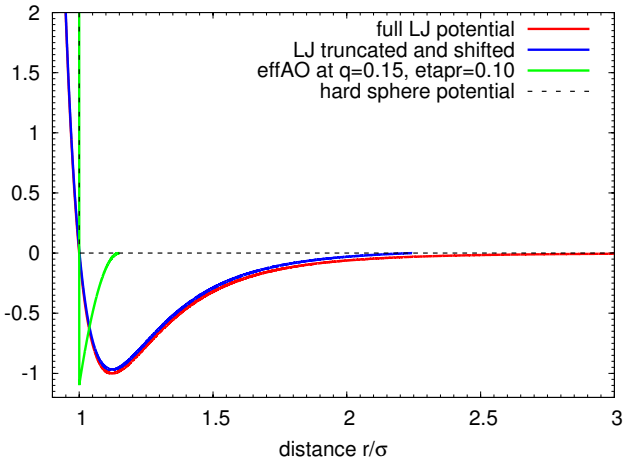


Figure 2.6: Plots of various pair potentials, as indicated. The dashed line shows the hard sphere potential, which is infinite for $r < \sigma$ and zero else. The effective AO model is similar, except for a short-ranged attractive part between $r = \sigma$ and $r = (1 + q)\sigma$. For $q \to 0$ and $\eta_p^r \to 0$, the effective AO model is equal to the hard sphere model. The figure also shows the Lennard-Jones potential (2.27) as well as the truncated and shifted variant. A potential of the soft effective AO model is not shown, as it is equal to the effective AO model's potential apart from the fact that the sharp edge at $r/\sigma = 1$ is smooth (the larger the parameter $b$ the smoother the edge).

## 2.4 Classical Nucleation Theory

The classical nucleation theory goes back to Volmer, Zeldovich, Becker and Döring [Volmer and Weber, 1926; Becker and Döring, 1935; Zeldovich, 1943]. One considers a one-component fluid, in which a new domain (nucleus) consisting of a minority phase is formed via thermal fluctuations out of a majority phase. This process is called homogeneous nucleation. The formation of such a nucleus is a rare event, due to the high free energy associated to it. The nucleation rate $j$, being the number of newly formed nuclei per unit volume and unit time, is therefore given by an Arrhenius law

$$j = \omega \exp\left(-\frac{\Delta F^*}{k_\mathrm{B}T}\right) . \tag{2.41}$$

Here, $\Delta F^*$ is the free energy barrier needed to form a critical nucleus, while $\omega$ is a kinetic prefactor. To explain CNT, we will consider the case of a supersaturated vapor (majority phase), in which a liquid droplet (minority phase) forms. One can make a simple ansatz for the formation free energy of a macroscopic droplet in a

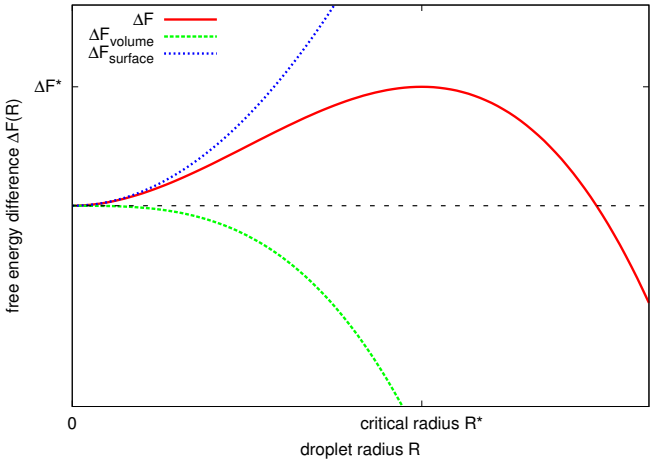


Figure 2.7: The free energy barrier results from two competing contributions to the free energy. The surface term is positive because the surface of the droplet costs free energy. The volume term, however, is negative and favors the growth of a nucleus. These two contributions balance each other at the critical radius $R^*$, where the height of the free energy barrier is $\Delta F(R^*) = \Delta F^*$.

vaporous surrounding, taking into account a surface and a volume contribution [see also Fig. 2.7]:

$$\Delta F_{\mathrm{hom}} = 4\pi\gamma_{vl}R^2 - \frac{4\pi}{3}\Delta\mu(\varrho_l - \varrho_v)R^3 \ . \tag{2.42}$$

Note that the shape of the droplet is assumed to be spherical with a radius $R$. Because the droplet can exchange particles with its surrounding, it is natural to choose the chemical potential $\mu$ and the temperature $T$ as variables for the thermodynamical potential. The difference in thermodynamic potentials of liquid and vapor at is expanded at the coexistence curve, $\Delta\mu = \mu - \mu_{\mathrm{coex}}$, the droplet having the density $\varrho_l$ and the surrounding $\varrho_v$. In this simple ansatz, according to the capillarity approximation, the interfacial tension $\gamma_{vl}$ is taken to be independent of the droplet size. So instead of $\gamma_{vl}(R)$ one inserts the interfacial tension $\gamma_{vl}(R = \infty)$ of a macroscopically large, flat interface. To find the critical free energy and the corresponding droplet size, one simply differentiates the expression (2.42) by $R$, which yields

$$R^* = \frac{2\gamma_{vl}}{\Delta\mu(\varrho_l - \varrho_g)} \tag{2.43}$$

This is the critical droplet radius corresponding to the free energy barrier $\Delta F^*_{\mathrm{hom}} = \Delta F_{\mathrm{hom}}(R^*)$. The height $\Delta F^*_{\mathrm{hom}}$ of the free energy barrier can be written with respect

to the surface or volume terms as

$$\Delta F^*_{\text{hom}} = \frac{4\pi}{3}\gamma_{vl}(R^*)^2 = \frac{\gamma_{vl}}{3}A^* \tag{2.44a}$$

$$\Delta F^*_{\text{hom}} = \frac{4\pi}{3}\Delta\mu(\varrho_l - \varrho_g)(R^*)^3 = \frac{1}{2}\Delta\mu(\varrho_l - \varrho_v)V^* \tag{2.44b}$$

or with respect to the properties of the two phases

$$\Delta F^*_{\text{hom}} = \frac{16\pi}{3}\frac{\gamma^3_{vl}}{(\Delta\mu(\varrho_l - \varrho_g))^2}\ . \tag{2.44c}$$

The question, to which extend this macroscopic theory is applicable to small droplets with several hundred particles and free energy barriers below 100 $k_BT$, has been in the focus of research for a long time. This will be covered in chapter 3. Note that the interfacial tension enters in Eq. (2.44c) with a power of three! Therefore, precise knowledge of the interfacial tension is absolutely necessary. In the Ising language, the expression $\Delta\mu(\varrho_l - \varrho_g)$ translates into

$$\Delta\mu(\varrho_l - \varrho_v) = 2H\left(\frac{1+m''}{2} - \frac{1+m'}{2}\right) = H(m'' - m') \approx 2m_{\text{coex}}H \tag{2.45}$$

where the approximation close to the coexistence curve

$$m'' - m' = 2m_{\text{coex}} + \mathcal{O}(H^3) \tag{2.46}$$

has been used.

The generalization to crystalline nuclei surrounded by a metastable liquid can also be treated by the same ansatz if the corresponding interfacial tension is used. However, the assumption of a spherical nucleus is only a first approximation. As will be shown, even in simple systems with anisotropy effects like the Ising model, the shape of the nucleus is quite non-trivial: At low temperatures the surface of the nucleus is facetted and more like a cube than like a sphere, changing the volume-to-surface ratio. The situation is similar but also more complicated for crystalline nuclei, where the facets belong to a certain crystalline orientation. Nevertheless, classical nucleation theory has been used to describe crystal nucleation with some success (for a mini-review, see [Block et al., 2014]).

Classical nucleation theory can also be extended to two-dimensional systems. Assuming droplets with a circular shape, instead of (2.42) one has

$$\Delta F_{\text{hom,2d}} = 2\pi\gamma_{vl}R - \pi\Delta\mu(\varrho_l - \varrho_v)R^2\ . \tag{2.47}$$

The same procedure as above leads then to

$$R^* = \frac{\gamma_{vl}}{\Delta\mu(\varrho_l - \varrho_v)} , \tag{2.48}$$

$$\Delta F^*_{\mathrm{hom,2d}} = \pi \frac{\gamma_{vl}^2}{\Delta\mu(\varrho_l - \varrho_g)} = \gamma_{vl}(2\pi R^*) = \Delta\mu(\varrho_l - \varrho_g)(\pi R^{*2}) . \tag{2.49}$$

Apart from the homogeneous nucleation discussed above, there is also heterogeneous nucleation [Turnbull, 1950a,b]. Here, a droplet is not created out of the bulk but on a wall. Since the wall effectively reduces the surface of the droplet, the free energy barrier $\Delta F^*_{\mathrm{het}}$ is much smaller than $\Delta F^*_{\mathrm{hom}}$. In fact, many nucleation phenomena in nature are rather attributed to heterogeneous nucleation, e.g. nucleation of water droplets on dust particles in the atmosphere. The shape of a droplet on a wall is that of a sphere cap, which minimizes the surface and maximizes the volume. The sphere cap has a certain contact angle $\theta$, which is the angle between the wall and the tangent at the point where the surface touches the wall.

To discuss heterogeneous nucleation, we need Young's equation [Young, 1805]

$$\gamma_{wv} - \gamma_{wl} = \gamma_{lv} \cos\theta \tag{2.50}$$

with the before-mentioned contact angle $\theta$ and the interfacial tensions between vapor ($v$), liquid ($l$) and wall ($w$). This equation is a result of a balance of forces acting on the droplet. If this equation was not fulfilled, there would be a net force and the droplet would move along the wall. Using Young's equation, it can be shown that both the volume and the surface term are reduced in the same way by a function $f(\theta)$ so that the free energy is given by

$$\Delta F_{\mathrm{het}} = f(\theta) \left[ 4\pi\gamma_{vl} R^2 - \frac{4\pi}{3} \Delta\mu(\varrho_l - \varrho_v) R^3 \right] . \tag{2.51}$$

Compared to Eq. (2.42), the only difference is the function $f(\theta)$ given by

$$f(\theta) = \frac{1}{4}(1 - \cos\theta)^2(2 + \cos\theta) \tag{2.52}$$

and only depending on the contact angle $\theta$. Consequently, the free energy barrier is reduced by this factor

$$\Delta F^*_{\mathrm{het}} = f(\theta) \Delta F^*_{\mathrm{hom}} , \tag{2.53}$$

e.g. for a contact angle of 90°, the barrier is half as high. Of course, for crystalline nuclei, the assumption that the nuclei have the shape of a sphere cap is arguable [Block et al., 2014].

## 2.5 Capillary Wave Theory

Capillary waves are oscillations of an interface due to thermal fluctuations [Buff et al., 1965; Weeks, 1977], see also [Privman, 1992; Binder et al., 1995]. Consider a flat horizontal one-dimensional interface in two-dimensional space. Thermodynamic fluctuations roughen the interface and create long-wavelength modulations as well as short-wavelength fluctuations. The latter cause overhangs, bubbles and other non-trivial effects. Therefore, one usually coarse-grains the system to a point where these short-wavelength effects disappear. Then the interface can be described by a function $h(x)$, giving the height of the interface at each point relative to the equilibrium position (reference plane). The deviation from the equilibrium position implies a gain of entropy, but at the same time, there is also a cost of energy proportional to the bending of the interface. The total energy of an interface is therefore given by

$$\Delta E = \int \mathrm{d}x\, \gamma(\theta) \sqrt{1 + \left(\frac{\mathrm{d}h(x)}{\mathrm{d}x}\right)^2}\,, \tag{2.54}$$

where $\gamma$ is the interfacial tension of the interface and $\theta = \arctan(\mathrm{d}h/\mathrm{d}x)$ is the angle relative to the reference plane. If $|\mathrm{d}h(x)/\mathrm{d}x| \ll 1$ for all $x$, i.e. the interface is relatively flat, one can expand the integrand up to second order

$$\gamma(\theta) \approx \gamma(0) + \gamma'(0)\frac{\mathrm{d}h(x)}{\mathrm{d}x} + \frac{\gamma''(0)}{2}\left(\frac{\mathrm{d}h(x)}{\mathrm{d}x}\right)^2 + \mathcal{O}\left(\left(\frac{\mathrm{d}h(x)}{\mathrm{d}x}\right)^3\right)$$

$$\sqrt{1 + \left(\frac{\mathrm{d}h(x)}{\mathrm{d}x}\right)^2} \approx 1 + \frac{1}{2}\left(\frac{\mathrm{d}h(x)}{\mathrm{d}x}\right)^2 + \mathcal{O}\left(\left(\frac{\mathrm{d}h(x)}{\mathrm{d}x}\right)^3\right)$$

$$\gamma(\theta)\sqrt{1 + \left(\frac{\mathrm{d}h(x)}{\mathrm{d}x}\right)^2} = \gamma(0) + \gamma'(0)\frac{\mathrm{d}h(x)}{\mathrm{d}x} + \\ + \frac{1}{2}(\gamma(0) + \gamma''(0))\left(\frac{\mathrm{d}h(x)}{\mathrm{d}x}\right)^2 + \mathcal{O}\left(\left(\frac{\mathrm{d}h(x)}{\mathrm{d}x}\right)^3\right)$$

leading to the capillary wave Hamiltonian

$$\mathcal{H} = \frac{\kappa}{2}\int \mathrm{d}x \left(\frac{\mathrm{d}h(x)}{\mathrm{d}x}\right)^2\,, \tag{2.55}$$

where

$$\kappa = \gamma(0) + \gamma''(0) \tag{2.56}$$

is the interfacial stiffness. The linear term in $\mathrm{d}h/\mathrm{d}x$ yields boundary terms and can be omitted, as well as constant terms. Because the interfacial stiffness $\kappa$ decreases with growing temperature, the interface becomes more and more diffuse.

Higher dimensions can be treated analogously [Privman, 1992], because the different directions decouple when using the above approximations. In three dimensions the result is

$$\mathcal{H} = \frac{\kappa}{2} \int \mathrm{d}x \int \mathrm{d}y \left[ \left( \frac{\partial h(x,y)}{\partial x} \right)^2 + \left( \frac{\partial h(x,y)}{\partial y} \right)^2 \right] . \tag{2.57}$$

The above discussion is only valid in the regime of rough interfaces, i.e. above the roughening transition and below the critical point. For the Ising model in two dimensions, $T_R = 0$, but in three dimensions, $k_\mathrm{B} T_R / J \approx 2.454$ [Bürkner and Stauffer, 1983; Mon et al., 1989, 1990; Hasenbusch and Pinn, 1994; Hasenbusch et al., 1996; Hasenbusch and Pinn, 1997]. A discussion of the behavior of the interfacial properties around $T_R$ can be found in [Binder et al., 1995].

Above the roughening transition, the Hamiltonian can be written as

$$\mathcal{H}_\mathrm{cw} = \frac{\kappa}{2} \frac{L^{d-1}}{(2\pi)^{d-1}} \int \mathrm{d}^{d-1}q \; q^2 |h_{\boldsymbol{q}}|^2 \tag{2.58}$$

where $h_{\boldsymbol{q}}$ is the Fourier transform of the function $h(\boldsymbol{x})$, respectively, which has been restricted to a box of volume $L^d$ with periodic boundary conditions. The equipartition theorem yields

$$\frac{k_\mathrm{B} T \kappa}{2} \frac{L^{d-1}}{(2\pi)^{d-1}} q^2 |h_{\boldsymbol{q}}|^2 = \frac{1}{2} k_\mathrm{B} T \; . \tag{2.59}$$

This relation can be used to determine $\kappa$ in computer simulations [cf. section 4.2]. One can also derive the mean interfacial width $w(L)$ of an interface in a periodic box of linear dimension $L$ as follows

$$\begin{aligned} w^2(L) = \langle h^2(\boldsymbol{x}) \rangle - \langle h(\boldsymbol{x}) \rangle^2 = \frac{L^{d-1}}{(2\pi)^{d-1}} \int \mathrm{d}^{d-1}q \; q^2 \langle |h_{\boldsymbol{q}}|^2 \rangle \propto \frac{1}{\kappa} \int \mathrm{d}^{d-1}q \; q^2 \\ \propto \frac{1}{\kappa} \int \mathrm{d}q \; q^{d-4} \; . \end{aligned} \tag{2.60}$$

From this, it follows

$$w^2(L) \propto \kappa^{-1} \int_{2\pi/L}^{0} \mathrm{d}q\, q^{-2} \propto \kappa^{-1} L \qquad (d = 2)\,, \tag{2.61a}$$

$$w^2(L) \propto \kappa^{-1} \int_{2\pi/L}^{2\pi/\xi} \mathrm{d}q\, q^{-1} \propto \kappa^{-1} \ln\left(\frac{L}{\xi}\right) \qquad (d = 3)\,, \tag{2.61b}$$

$$w^2(L) \propto \kappa^{-1} \int_{2\pi/L}^{0} \mathrm{d}q\, q^{d-4} \propto \kappa^{-1} L^{3-d} \qquad (d > 3)\,. \tag{2.61c}$$

In two dimensions the fluctuations are strong, so that the interfacial fluctuations are of the order of $\sqrt{L}$, while in 4 and higher dimensions, the fluctuations are of the order of 1. The three-dimensional case is special: The interfacial fluctuations are of the order $\sqrt{\ln L}$. Note that a cutoff length $\xi$ for the short wavelength spectrum needs to be introduced for the result to be finite. This cutoff is of unknown physical relevance. Usually, one takes the correlation length $\xi$ as the cutoff, because the capillary wave picture does not apply at short length scales, where the interface cannot be described by a function $h(x, y)$ but is a rather fuzzy object with bubbles and droplets [Parry and Boulter, 1994; Mecke and Dietrich, 1999; Milchev and Binder, 2002; Vink et al., 2005].

From a convolution approximation it can be shown [Binder et al., 2001], that the mean interfacial width can also be written as

$$\langle w^2 \rangle = w_0^2 + \frac{1}{4\beta\kappa} \ln(L/\xi) \tag{2.62}$$

Unfortunately, $\xi$ cannot be distinguished from the intrinsic width $w_0^2$.

## 2.6 More about Monte Carlo Simulations

### 2.6.1 Boundary Conditions

The everlasting problem of computer simulations is that the resources are limited. Therefore one has to focus on small system sizes. If one considers a simulation box with free boundaries, the particles feel the box boundaries so that layering and other phenomena occur. So to study the bulk properties of a given model, one would have to use a huge box and focus on the center of this box, where the influence of the boundaries is minimal. On the other hand, periodic boundaries provide a straightforward solution to mimic an infinite system by a finite box. If a particle leaves the simulation box, it enters the same box on the opposite side. One can

think of the box being copied in all spatial dimensions infinitely many times, thereby emulating an infinitely large system.

Periodic boundary conditions are very adequate for bulk simulations or systems with planar surfaces. Unfortunately, there are also some disadvantages. There are artifacts from long-range forces like electromagnetic forces. Crystals exhibit a strain field if the box dimensions are not compatible with the lattice spacings. Also capillary waves and correlation lengths cannot become greater than the linear dimensions of the box. Therefore, finite-size scaling is necessary to analyze these effects.

In order to implement periodic boundary conditions, one needs to take care of two aspects. First, if a particle leaves the box, it needs to enter it at the corresponding point on the other side of the box. Furthermore, the distance between two particles must be calculated using the minimum image convention, meaning that the distance from a given particle to another particle is defined as the distance to the closest image of the particle.

There are also other useful types of boundary conditions in the context of discrete models like the Ising model, namely antiperiodic boundary conditions and fixed-spin boundary conditions. For antiperiodic boundary conditions in an Ising model, the exchange constant $J$ is reversed for the interactions across the boundary. If two spins of opposite orientation are on either side of the boundary, they will "see" each other as being parallel. This antiperiodic boundary condition favors slab configurations with one interface, so one can study an interface without having to constrain the density (or magnetization, respectively). A different possibility is to just fix the spins next to the boundary to $+$ on one side and $-$ on the other[7]. This is applied in a more general way in [Svrakic et al., 1988], where the interface is also clamped and tilted. Alternatively one can introduce strong surface fields in the layers next to the boundaries. For strong fields, this is obviously equivalent to the fixed-spin boundary condition.

### 2.6.2 Pseudorandom Number Generators

Any Monte Carlo simulation heavily depends on the quality of the random numbers. Because many random numbers are needed, one usually uses pseudorandom number generators, which take as input a seed $s$ and create a sequence $\{r_i\}_i$ of pseudorandom numbers via a deterministic algorithm. One example of such an algorithm is the linear congruential random generator:

$$r_{i+1} = (ar_i + b) \mod \mathrm{M} \tag{2.63}$$

[7]Such Dirichlet boundary conditions lead to rather large finite-size effects and are therefore not used in this thesis.

with $r_0 = s$. This algorithm creates pseudorandom integer numbers in the interval $[0, \mathrm{M} - 1]$, where $M$ is usually $2^{32}$ or $2^{64}$. The values

$$a = 1103515245 \quad , \quad b = 12345$$

are used in ISO/IEC 9899:1999, also known as the C99 standard. It can be shown that the quality of the pseudorandom numbers depend on the choices of $a, b$ and $M$. The period length is at most $M$, but it can be much shorter if $a$ and $b$ are poorly chosen. The highest period lengths can be achieved if

- $b$ and $M$ are relatively prime (their greatest common divisor is 1).
- $a - 1$ is divisible by all prime factors of $M$.
- $a - 1$ is a multiple of 4 if $M$ is a multiple of 4.

These requirements are called Hull-Dobell Theorem [Severance, 2001]. However, throughout this work, a more sophisticated algorithm is used, which is called Mersenne[8] Twister algorithm. This algorithm is fast, has a very long period of $2^{19937} - 1$ iterations and is proven to generate equidistributed 32-bit pseudorandom numbers. It also passes the so-called diehard tests, a series of statistical tests to measure the quality of pseudorandom numbers. One disadvantage is that if the seed of two instances is close to each other, it can take a long time until the pseudorandom number sequences diverge from each other. Nevertheless, it is among the best pseudorandom number generators currently known.

### 2.6.3 Optimization Techniques

There exist a number of practices to enhance the performance of Monte Carlo simulations. One important aspect is the reduction of computing time for the calculation of the energy of the whole system. Since one has to take all pairs of particles into account, the computing time is of order $N^2$. This can be reduced to the order $N$ if one decomposes the simulation box into cells of diameter $d_{\mathrm{cell}}$. Then, one needs to keep book of which particle resides in which cell. Of course, if particles move around, they leave one cell and move to another, so the information has to be kept up-to-date. If one wants to calculate the energy of one particle, the cells provide knowledge about which particles are in the vicinity so that only these particles can have a non-zero interaction with the current particle. If the cell diameter $d_{\mathrm{cell}}$ is chosen so that it is at least as large as the maximum interaction range,

[8] The name originates from the period length which is chosen to be a Mersenne prime.

e.g. the particle diameter $\sigma$ for hard spheres or $r_{\text{cut}}$ for the truncated and shifted Lennard-Jones fluid [cf. section 2.3.1], then one has to check only the particle's cell and the 26 cells surrounding it. This improves performance significantly, as one saves a lot of calculations of distances and potentials. Therefore, it is a standard technique in modern Monte Carlo simulations.

The optimal cell size $d_{\text{cell}}$ is slightly larger than the maximum interaction range. However, if studying crystalline structures, the simulation box must fit to the crystalline structure in order to avoid any stress or strain to the crystal. Therefore, the cell system cannot be optimal and the performance benefit is slightly reduced. However, using cells is still advantageous also in this case, especially for larger box sizes.

### 2.6.4 The Chemical Potential in Computer Simulations

The Widom particle insertion method [Widom, 1963, 1982; Frenkel and Smit, 2001; Landau and Binder, 2009] is a straight-forward method to measure the chemical potential in a simulation box. If the Hamiltonian of a system can be written in the form $\mathcal{H}(\{\boldsymbol{p}_k\},\{\boldsymbol{r}_k\}) = T(\{\boldsymbol{p}_k\}) + U(\{\boldsymbol{r}_k\})$ in a cubic box with volume $V = L^3$ with $N$ identical particles, one can integrate the kinetic part to obtain

$$Z(N,V,T) = \frac{V^N}{\Lambda^{3N} N!} \int \mathrm{d}^{3N}\boldsymbol{s}\, \exp(-\beta U(\boldsymbol{s}_1,\ldots,\boldsymbol{s}_N,L)) \,, \tag{2.64}$$

where $\Lambda = h/\sqrt{2\pi m k_{\text{B}} T}$ is the thermal de Broglie wavelength and $\boldsymbol{s}_i = \boldsymbol{r}_i/L$ are the normalized coordinates of the particles in the box. The factor $N!$ takes into account the fact that the particles are indistinguishable. The free energy can then be written as

$$F(N,V,T) = -k_{\text{B}}T \ln Z_{\text{can}}(N,V,T) = F_{\text{id}}(N,V,T) + F_{\text{ex}}(N,V,T) \tag{2.65}$$

with

$$F_{\text{id}}(N,V,T) = -k_{\text{B}}T \ln\left(\frac{V^N}{\lambda^{3N} N!}\right) \tag{2.66}$$

$$F_{\text{ex}}(N,V,T) = -k_{\text{B}}T \ln\left(\int \mathrm{d}^{3N}s\, \exp(-\beta U(\boldsymbol{s}_1,\ldots,\boldsymbol{s}_N,L))\right) \tag{2.67}$$

Now since the chemical potential $\mu$ is the first derivative of the free energy by the number of particles, one can write (for large $N$)

$$\mu = \left.\frac{\partial F}{\partial N}\right|_{V,T} = -k_{\text{B}}T \ln\left(\frac{Z_{\text{can}}(N+1,V,T)}{Z_{\text{can}}(N,V,T)}\right) = \mu_{\text{id}} + \mu_{\text{ex}} \tag{2.68}$$

with

$$\mu_{\mathrm{id}} = -k_{\mathrm{B}}T \ln\left(\frac{V/\lambda^3}{N+1}\right) \tag{2.69}$$

$$\mu_{\mathrm{ex}} = -k_{\mathrm{B}}T \ln\left(\frac{\int \mathrm{d}^{3N+3}s \exp(-\beta U(\boldsymbol{s}_1,\ldots,\boldsymbol{s}_{N+1},L))}{\int \mathrm{d}^{3N}s \exp(-\beta U(\boldsymbol{s}_1,\ldots,\boldsymbol{s}_N,L))}\right) \tag{2.70}$$

The first term $\mu_{\mathrm{id}}$ corresponds to the ideal gas term, while the excess term $\mu_{\mathrm{ex}}$ contains the interaction of the particles. The quotient in the expression of the excess chemical potential is an ensemble average of $\Delta U = U(\boldsymbol{s}_1,\ldots,\boldsymbol{s}_{N+1},L) - U(\boldsymbol{s}_1,\ldots,\boldsymbol{s}_N,L)$ over the coordinates of the $(N+1)$th particle. Therefore $\mu_{\mathrm{ex}}$ can be measured simply by inserting an $(N+1)$th "testparticle" and measure the energy difference:

$$\mu_{\mathrm{ex}} = -k_{\mathrm{B}}T \ln \int \mathrm{d}^3 s \langle \exp(-\beta\Delta U)\rangle_N \approx -k_{\mathrm{B}}T \ln\left(\frac{1}{M}\sum_{i=1}^{M} \exp(-\beta(\Delta U)_i)\right) \tag{2.71}$$

The last expression shows how approach can easily be applied to Monte Carlo simulations by randomly inserting a particle, calculate the energy difference and removing it again.

Although this method works well for gas and liquid phases, it fails at high densities, i.e. in glass and crystalline phases, since the particle insertion always creates overlaps, leading to extremely high predictions for the chemical potential. There are some proposed methods to circumvent this problem [Boulougouris et al., 1999]. Another idea is to create a low density volume within the simulation box and measure the chemical potential there [Powles et al., 1994]. Because the chemical potential is constant throughout the whole simulation box in thermal equilibrium, the chemical potential in the low density volume equals the chemical potential in the whole system.

In chapter 3, a lattice version of the Widom particle insertion method [Murch and Thorn, 1978; Winter et al., 2009a] is used to measure the chemical potential $\Delta\mu_L(T,\varrho)$ in the framework of the lattice gas model. It works as follows. Consider a lattice with $V$ lattice sites and $N$ particles. The partition function is

$$Z_{\mathrm{can}}(N,V,T) = \frac{1}{N!} \sum_{N\text{-particle states } j} \exp(-\beta E_j(N,V)) \ , \tag{2.72}$$

where the summation includes all states with $N$ particles and $E_j(N,V)$ is the energy of the $j$th state. Similarly to the continuous case, one can write

$$\beta\mu = \beta \left.\frac{\partial F}{\partial N}\right|_{V,T} = -\ln\left(\frac{Z_{\mathrm{can}}(N+1,V,T)}{Z_{\mathrm{can}}(N,V,T)}\right) \tag{2.73}$$

$$= -\ln\left(\frac{1}{N+1}\frac{\sum_{(N+1)\text{-particle states } k} \exp(-\beta E_k(N+1,V))}{\sum_{N\text{-particle states } j} \exp(-\beta E_j(N,V))}\right) \ . \tag{2.74}$$

Now define $\Delta E_j = E_j(N+1,V) - E_j(N,V)$ as the change of energy upon adding a particle to an $N$-particle configuration $j$. Then one can rewrite the summation over all $(N+1)$-particle configurations as a sum over all $N$-particle configurations, where each $N$-particle configuration can produce $V-N$ $(N+1)$-particle configurations, since the added particle can only occupy one of the $V-N$ empty lattice sites. Hence

$$\beta\mu = -\ln\left(\frac{V-N}{N+1}\frac{\sum_{N\text{-particle states } k}\exp(-\beta E_k(N,V))\exp(-\beta\Delta E_k)}{\sum_{N\text{-particle states } j}\exp(-\beta E_j(N,V))}\right) \tag{2.75}$$

$$= -\ln\left(\frac{V-N}{N+1}\left\langle\exp(-\beta\Delta E_k)\right\rangle_{N\text{-particle states k}}\right) . \tag{2.76}$$

Like in the continuous case, one can distinguish between ideal and excess part:

$$\beta\mu = \beta\mu_{\text{id}} + \beta\mu_{\text{ex}} \tag{2.77}$$

$$\beta\mu_{\text{id}} = -\ln\left(\frac{V-N}{N+1}\right) \tag{2.78}$$

$$\beta\mu_{\text{ex}} = -\ln\left(\left\langle\exp(-\beta\Delta E_k)\right\rangle_{N\text{-particle states k}}\right) . \tag{2.79}$$

Similarly, one can calculate the chemical potential by removing a particle. Then the result is

$$\beta\mu_{\text{id}} = \ln\left(\frac{N}{V-N+1}\right) \tag{2.80}$$

$$\beta\mu_{\text{ex}} = \ln\left(\left\langle\exp(-\beta\Delta E_k)\right\rangle_{N\text{-particle states k}}\right) . \tag{2.81}$$

In this work, the chemical potential will always be the average of both values, because they can easily be computed in one run.

### 2.6.5 The Pressure in Computer Simulations

In statistical mechanics, the pressure is defined as the partial derivative of the free energy:

$$P = -\left(\frac{\partial F(N,V,T)}{\partial V}\right)\Bigg|_{N,T} \tag{2.82}$$

If the potential $U(\{\boldsymbol{r}\}) = U(\{L\boldsymbol{s}_k\})$ is differentiable, one can get an expression which is very handy for computation of the pressure in a simulation. Combining the

thermodynamic relation Eq. (2.82) with Eq. (2.64), the calculation is as follows

$$\begin{aligned} P &= -\left.\frac{\partial F(N,V,T)}{\partial V}\right|_{N,T} \\ &= k_\mathrm{B}T \left.\frac{\partial \ln Z(N,V,T)}{\partial V}\right|_{N,T} \\ &= k_\mathrm{B}T \left( \frac{\partial \ln(V^N)}{\partial V} + \frac{\partial \ln \int \mathrm{d}^{3N}\boldsymbol{s} \exp(-\beta U(\boldsymbol{s}_1,\ldots,\boldsymbol{s}_{N+1},L))}{\partial V} \right) . \end{aligned}$$

The derivative can be computed explicitly as follows

$$\begin{aligned} &= \frac{Nk_\mathrm{B}T}{V} + k_\mathrm{B}T \frac{\int \mathrm{d}^{3N}\boldsymbol{s} \sum_{j=1}^{N} (-\beta \frac{\partial U(\{L\boldsymbol{s}_k\})}{\partial V}) \exp(-\beta U(\{L\boldsymbol{s}_k\}))}{\int \mathrm{d}^{3N}\boldsymbol{s} \exp(-\beta U(\{L\boldsymbol{s}_k\}))} \\ &= \frac{Nk_\mathrm{B}T}{V} + \frac{\int \mathrm{d}^{3N}\boldsymbol{s} \sum_{j=1}^{N} (-\frac{\partial U(\{\boldsymbol{r}_k\})}{\partial \boldsymbol{r}_i} \frac{\partial \boldsymbol{r}_i}{\partial V}) \exp(-\beta U(\{L\boldsymbol{s}_k\}))}{\int \mathrm{d}^{3N}\boldsymbol{s} \exp(-\beta U(\{L\boldsymbol{s}_k\}))} \\ &= \frac{Nk_\mathrm{B}T}{V} + \frac{\int \mathrm{d}^{3N}\boldsymbol{s} \sum_{j=1}^{N} (-\frac{\partial U(\{\boldsymbol{r}_k\})}{\partial \boldsymbol{r}_i} \frac{\boldsymbol{r}_i}{3V}) \exp(-\beta U(\{L\boldsymbol{s}_k\}))}{\int \mathrm{d}^{3N}\boldsymbol{s} \exp(-\beta U(\{L\boldsymbol{s}_k\}))} \\ &= \frac{Nk_\mathrm{B}T}{V} + \frac{1}{3V} \sum_{j=1}^{N} \left\langle -\frac{\partial U(\{\boldsymbol{r}_k\})}{\partial \boldsymbol{r}_i} \cdot \boldsymbol{r}_i \right\rangle . \end{aligned}$$

For the case of a pairwise potential, which depends only on the distance of the particles, this reduces to

$$P = \frac{Nk_\mathrm{B}T}{V} + \frac{1}{3V} \sum_{i=1}^{N} \sum_{j=i+1}^{N} \langle \boldsymbol{f}_{ij} \cdot \boldsymbol{r}_{ij} \rangle \tag{2.83}$$

with $\boldsymbol{r}_{ij} = \boldsymbol{r}_i - \boldsymbol{r}_j$ and $\boldsymbol{f}_{ij} = -\left.\frac{\partial U(r)}{\partial r}\right|_{r_{ij}}$. The first term is the ideal gas term, while the second term takes into account the interaction of the particles.

The expression (2.83) can only be applied if the pair potential $U(r)$ is differentiable. This excludes hard spheres or any potential with a hard core. There exist other methods to deal with this, for example [Deb et al., 2012a].

## 2.7 Free Energy Computation using Monte Carlo

Often, the free energy is considered as a function of a reaction coordinate. For example, for the Ising model, the free energy as a function of the magnetization

(or density of spins pointing upwards) allows to gain much insight about interfacial tensions or nucleation processes. In general, free energy landscapes are rather complex and contain minima separated by large barriers, so that the system is often trapped in one minimum and one cannot sample properly without spending huge amounts of time. A straightforward example is the Ising model, where the two minima at $\pm m_{\text{coex}}$ are separated by a large free energy barrier. If the system is small enough, the system can traverse through the barrier, but for larger systems, the system is trapped in one minimum and will never explore the other minimum in reasonable time periods.

The first idea to overcome this problem is multicanonical sampling. Later, other techniques have been invented. We will focus on multicanonical sampling and successive umbrella sampling here.

### 2.7.1 Multicanonical Sampling

Multicanonical sampling [Berg and Neuhaus, 1992] is a simple method to allow a system to explore the full range of the reaction coordinate. The idea is to introduce an effective Hamiltonian, which is the sum of the model's Hamiltonian and a weight function. The weight function is chosen so that the minima and maxima of the true free energy landscapes are compensated so that the resulting effective free energy landscape is flat. If the weight function is the free energy landscape itself, the system can explore the whole reaction coordinate range and will return a flat histogram. If the weight function differs slightly from the true free energy landscape, the true free energy landscape can be extracted by combining the original weight function and the output histogram. However, if the weight function differs significantly from the true free energy landscape, the free energy barriers are not compensated and one does not gain anything from the simulation.

The advantage of this technique is that it obeys detailed balance [cf. Eq. (2.10)]. An important disadvantage is obvious: One needs some educated guess for the "weight function". Nowadays, there are other algorithms which create the weighting function on-the-fly during the simulation[9] or using the idea of thermodynamic integration, e.g. successive umbrella sampling (for references, see section 2.7.3).

Nevertheless, multicanonical sampling provides a good check whether a free energy landscape represents the true free energy of a system. Any free energy algorithm only works well if the reaction coordinate explores the whole range. If there are entropic barriers, so that the simulation stays on one side for a long time, there is little information in the histogram, because the whole sampling depends on the

[9] The most popular algorithm of this kind is Wang-Landau sampling [Wang and Landau, 2001a,b].

sampling of the barrier. The criteria for the quality of the histogram are

- The histogram is flat.
- The reaction coordinate behaves like a random walk over the whole reaction coordinate range. There are no entropic barriers.

### 2.7.2 Thermodynamic Integration

Thermodynamic integration is a method to compute the free energy by integrating one of its derivatives, like energy $E = \partial(\beta F)/\partial\beta|_{N,V}$ or pressure $E = \partial F/\partial V|_{N,T}$. The integration starts at a reference state 0, characterized by a Hamiltonian $\mathcal{H}_0$, and ends at a state 1 with Hamiltonian $\mathcal{H}_1$. To connect these states by a path, one can define the mixed states via

$$\mathcal{H}(\kappa) = \mathcal{H}_0 + \kappa(\mathcal{H}_1 - \mathcal{H}_0) \tag{2.84}$$

The free energy difference between the two states can then be written as

$$F_1 - F_0 = \int_0^1 \frac{\partial F}{\partial \kappa} \mathrm{d}\kappa = -k_\mathrm{B}T \int_0^1 \frac{\partial \ln(Z(\kappa))}{\partial \kappa} \mathrm{d}\kappa \tag{2.85}$$

where $Z(\kappa)$ is the partition function which depends on the reaction coordinate $\kappa$.

$$F_1 - F_0 = -k_\mathrm{B}T \int_0^1 \mathrm{d}\kappa \frac{1}{Z(\kappa)} \frac{1}{\Lambda^{3N} N!} \int \mathrm{d}^{3N} r \exp(-\beta U(\kappa)) \frac{\partial(-\beta\,\mathcal{H}(\kappa))}{\partial \kappa} \tag{2.86}$$

$$= \int_0^1 \mathrm{d}\kappa \left\langle \frac{\partial\,\mathcal{H}(\kappa)}{\partial \kappa} \right\rangle \tag{2.87}$$

$$= \int_0^1 \mathrm{d}\kappa \left\langle \mathcal{H}_1 - \mathcal{H}_0 \right\rangle \tag{2.88}$$

To compute the free energy, one has to divide the interval $[0, 1]$ into $M + 1$ values $\kappa_i$, sample the quantity $\langle \mathcal{H}_1 - \mathcal{H}_0 \rangle$ at each $\kappa_i$ and then integrate numerically.

### 2.7.3 Successive Umbrella Sampling

The successive umbrella sampling [Virnau and Müller, 2004; Virnau et al., 2004], see also [Virnau, 2003], is similar to thermodynamic integration but takes a slightly different approach. Instead of sampling $\langle U_1 - U_0 \rangle$, it makes the ansatz

$$\beta(F_1 - F_0) = \int_0^1 \frac{\partial \ln(Z(\kappa))}{\partial \kappa} \mathrm{d}\kappa \tag{2.89}$$

and then estimates this derivative directly by discretizing the integration path $[0,1]$ into $M+1$ values $\kappa_i$, so that one has $M$ windows, where each window contains two neighboring values $\kappa_i, \kappa_{i+1}$. Then for each window, one conducts a simulation where the system can jump back and forth between $\kappa_i$ and $\kappa_{i+1}$ and counts the number of occurrences $P$ in state $i$ and $i+1$. Because of

$$\left.\frac{\partial \ln(Z(\kappa))}{\partial \kappa}\right|_{\kappa_i} \approx \frac{\ln(Z(\kappa_{i+1})) - \ln(Z(\kappa_i))}{\kappa_{i+1} - \kappa_i} = \frac{\ln(P(i+1)/P(i))}{1} = \ln\left(\frac{P(i+1)}{P(i)}\right) \tag{2.90}$$

one can express the integrand by the number of occurrences.

After setting up the simulation in a window $\{\kappa_i, \kappa_{i+1}\}$, the successive umbrella move makes an attempt to change $\kappa$ and counts the number of occurrences as follows:

1. Draw a random number $p_1$. In case $\kappa = \kappa_i$, if $p_1 < 0.5$, $\kappa' = \kappa_{i-1}$. If $p_1 \geq 0.5$, $\kappa' = \kappa_{i+1}$. In case $\kappa = \kappa_{i+1}$, if $p_1 < 0.5$, $\kappa' = \kappa_i$. If $p_1 \geq 0.5$, $\kappa' = \kappa_{i+2}$.
2. If $\kappa'$ is not within the window $\{\kappa_i, \kappa_{i+1}\}$, reject the move by setting $\kappa_{\text{next}} = \kappa$. Otherwise, calculate the energy difference $\Delta E = E(\kappa') - E(\kappa)$ of the current configuration for $\kappa$ and $\kappa'$. Draw a random number $p_2$. If $p_2 < \exp(-\beta \Delta E)$, accept the move by setting $\kappa_{\text{next}} = \kappa'$, else reject the move by setting $\kappa_{\text{next}} = \kappa$.
3. The new value of $\kappa$ is $\kappa_{\text{next}}$. Count the current state to $P(i)$ or $P(i+1)$, depending on whether the new $\kappa$ is $\kappa_i$ or $\kappa_{i+1}$.

This Monte Carlo move is done with a certain frequency during the simulation. It is important to count in the last step whether $\kappa$ has changed or not, especially if a move to leave the window is rejected. This can be understood as follows. If there was no window restriction, $\kappa$ could leave the window and return later. Upon entering the window again, this would have to be counted. Hence one must not simply count if $\kappa$ jumps within the window but also if an attempt is made to leave the window. Only then, (2.90) is correctly estimated.

An advantage of successive umbrella sampling is that it fulfills detailed balance (unlike Wang-Landau sampling [Wang and Landau, 2001a,b]) and can be applied even for very steep free energy landscapes. It is very robust and a valuable tool for the work in this thesis.

## 2.8 How to behave on Supercomputers

Usually, advanced Monte Carlo methods require tremendous computing power, which can only be delivered by current generation supercomputers. Often, a large number

of cores (or CPUs) is combined via MPI to tackle a problem. This number can range from about 100 cores to up to 100 000 cores or even more. It is clear that supercomputers capable of delivering large numbers of cores with lots of memory and fast communication between the cores are complex machines and therefore expensive and hard to maintain.

For the simulations of this thesis, a massive use of the Mainz supercomputer Mogon was necessary[10]. Needless to say, such massive use of a machine creates some friction both for the team running the machine and for other users. Future users might benefit from the following remarks.

My work on supercomputers led to the impression that the administrators of supercomputers usually have a librarian's mentality:

- Every book must be at its proper place in the bookshelf.
- The users must not read books or even remove them from the library.
- If a book is missing or damaged, it is always the users' fault.

The user, of course, has quite the opposite opinion. He believes that every book is just for him to read, so he just keeps the books he likes in his office for as long as possible. If he returns a book with some damage, he is entirely sure that the book was in this condition when he borrowed it.

For supercomputing, similar things apply. The ideal user from the viewpoint of the administrator does not use the supercomputer at all. If otherwise, no output is created and no communication between cores or nodes is needed, and the program is of course well-written and contains no bugs. The ideal supercomputer from the viewpoint of a typical user is infinitely large with incredible performance and communication speed, so that there is no limit to I/O and the jobs do not have to wait more than a second to start computing. Of course, his program is free of bugs, so any crash is due to bad configuration of the supercomputer. Furthermore, other users than oneself should be banned.

There is no easy way to reconcile opposing standpoints, but as a user I suggest to adapt to a supercomputer's features and try to be a good citizen, e.g. by following some Golden Rules:

1. Read the supercomputer's manual, even if it is boring and cumbersome.

[10] This project was by far the largest effort on this machine, taking about 40 million core hours on Interlagos Opteron 6272 processors in 2013. In 2014, the intensive use has been continued.

2. Test your code on your local machine before any production run.

3. Produce as little output as possible into as few files as possible.

4. Minimize the disk space needed on the supercomputer by downloading finished calculations.

5. Try to minimize communication between different ranks. Use non-blocking receives (MPI_Irecv) to create time windows in which an expected message can be received. This will avoid one rank waiting for other ranks.

6. Login nodes are for logging in, not for running your programs.

7. In the dictionary, “to deliberate” comes before “to submit”.

# Chapter 3

# Anisotropy of the Surface Tension and its Effects on Nucleation in the Ising Model

This chapter considers the classical nucleation theory within the Ising model, questioning the simplifying assumption of spherical droplets. After a short introduction, section 3.2 will deal with the temperature dependence of shapes of macroscopical droplets in the Ising/lattice gas model. Afterwards, several ways to define droplet volumes are discussed and tested. It will be shown that a microscopical definition of physically sensible droplets is possible. The final section will summarize the results and give an outlook to further applications. Note that parts of the results of this chapter appeared in [Schmitz et al., 2013].

## 3.1 Introduction

Classical nucleation theory (CNT), which was introduced in section 2.4, has been tested and refined over several decades [Feder et al., 1966; Reiss et al., 1968; Langer, 1969; Abraham, 1974; Binder and Stauffer, 1976; Binder, 1987; Oxtoby and Evans, 1988; Dillmann and Meier, 1989; Reiss et al., 1990; Oxtoby, 1992; Laaksonen et al., 1995; ten Wolde and Frenkel, 1998; Kashchiev, 2000; Pan and Chandler, 2004; Winter et al., 2009a]. However, the question of accuracy has not been satisfactorily answered, especially for free energy barriers $\lesssim 100 k_\mathrm{B} T$. On the experimental side [Vilsanen et al., 1993; Fladerer and Strey, 2006; Iland et al., 2007], there are still discussions on the validity of the CNT or on possible improvements. Since critical droplets occur very seldom, often only the combined effects of nucleation and growth can

be observed. Also, the results often suffer from heterogeneous nucleation processes because impurities of the samples (dust, ions, etc.) serve as surfaces for heterogeneous nucleation. Another problem is that the nucleation rate varies exponentially with the supersaturation, there is only a narrow window of sensible parameters to test CNT.

Computer simulations are a well-suited approach to this kind of challenge [Abraham, 1974; Binder and Müller-Krumbhaar, 1974; Binder and Stauffer, 1976; Binder, 1987; ten Wolde and Frenkel, 1998; Schrader et al., 2009a; Block et al., 2010; Ryu and Cai, 2010; Tröster et al., 2012]. However, there are also two major problems. Since computing time and algorithm efficiency is always limited, only the simulation of small nucleation barriers is possible, whereas larger ones are desired for comparison with experiments. The other problem is the question how to distinguish between a nucleus and the environment on an atomistic scale, because the interfaces are broad and fluctuating [Binder and Stauffer, 1972; Rowlinson and Widom, 1982].

This chapter will mainly deal with the second problem, showing that the definition of physical clusters leads to consistent predictions of the droplet volume no matter how diffuse the interface is.

## 3.2 The Shape of Droplets in the Ising Model

In this section, the properties of macroscopical droplets will be studied without using any droplet definition. Here, and in the following sections, the magnetization of the system is kept constant and the interaction constant $J$ is set to unity throughout. Otherwise, the inhomogeneous state of a droplet surrounded by vapor would quickly decay into a homogeneous state. The Monte Carlo move to flip spins therefore randomly chooses two spins with opposing orientation and attempts to flip them simultaneously. The droplets in the box consist of between $10^4$ and $10^5$ lattice sites. These volumes correspond to very high nucleation barriers far beyond observation in simulation and experiment. But the study of such large droplets is useful to clarify some general conceptual questions.

To reveal the typical shape of droplets, it is useful to consider these macroscopical droplets first. Therefore, we proceed as follows: The droplets are equilibrated within a cubic box of length $L$ with periodic boundary conditions in all directions. From each equilibrated configuration, the center of mass of the droplet is computed and a two-dimensional density histogram $\varrho(u, v)$ is produced, where $u, v$ can be $(x, y), (x, z)$ or $(y, z)$ and the histogram's origin is the droplet's center of mass. This is due to the symmetric shape the droplet will have in order to minimize its free energy. This procedure will give an average density distribution in the plane cutting through the droplet's center of mass.

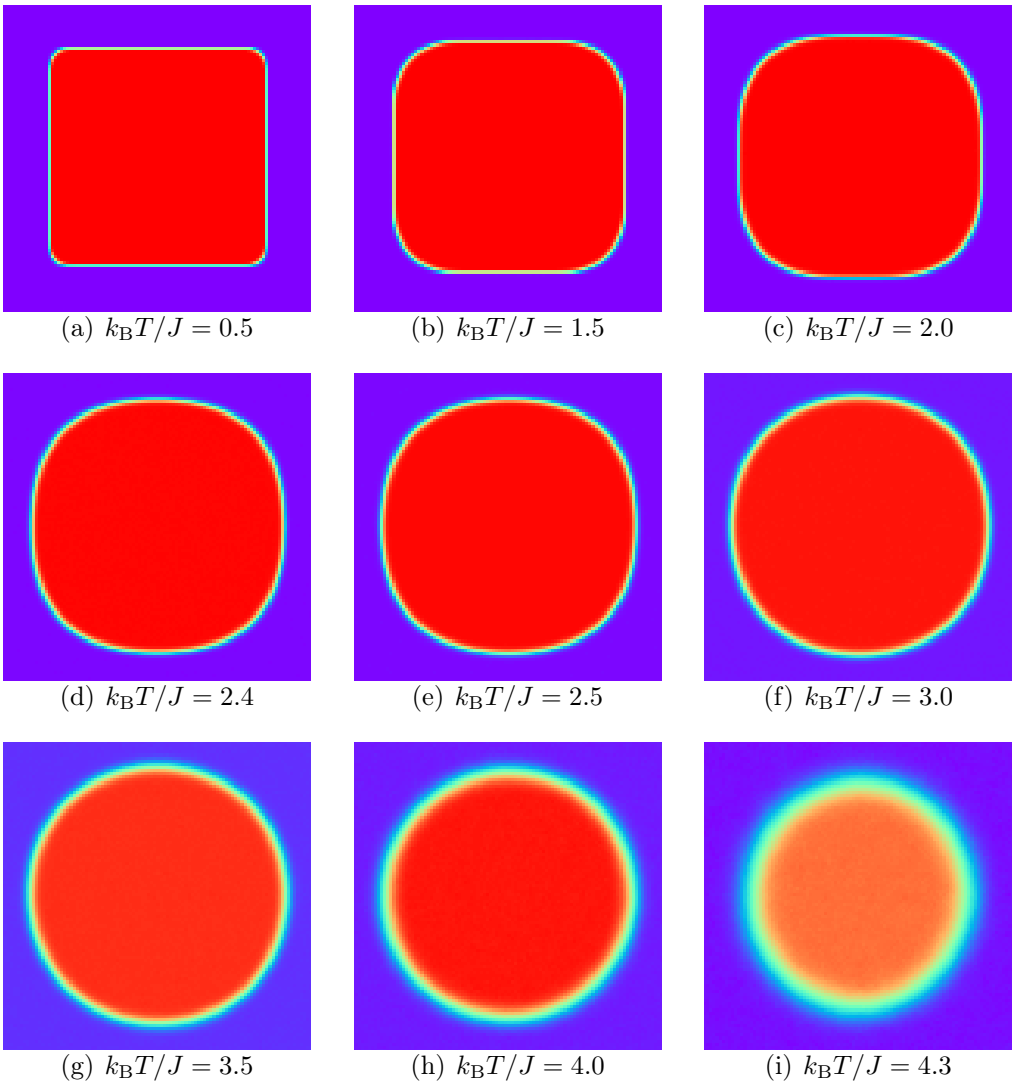

(a) $k_\mathrm{B}T/J = 0.5$ (b) $k_\mathrm{B}T/J = 1.5$ (c) $k_\mathrm{B}T/J = 2.0$

(d) $k_\mathrm{B}T/J = 2.4$ (e) $k_\mathrm{B}T/J = 2.5$ (f) $k_\mathrm{B}T/J = 3.0$

(g) $k_\mathrm{B}T/J = 3.5$ (h) $k_\mathrm{B}T/J = 4.0$ (i) $k_\mathrm{B}T/J = 4.3$

Figure 3.1: Average droplet shape at various temperatures. A cubic system with $L = 100$ is equilibrated at a fixed density. In regular intervals, the density relative to the droplet's center of mass is measured in each direction. The color coding is as follows: red areas have density $\varrho = 1$ while purple areas have density $\varrho = 0$. One can see the cubic shape for low temperatures and the spherical shape at high temperatures. At the same time, the interface width increases with temperature. As expected, with increasing temperature, the difference $\varrho_l - \varrho_g$ decreases.

The results are shown in Fig. 3.1 at a fixed density $\varrho = 0.33$ for all temperatures[1]. At the lowest temperature, the interface is clearly faceted, but the corners are already rounded. With increasing temperature, the six facets of the cube become smaller and smaller. Just below the so-called roughening temperature $k_\mathrm{B}T_R/J \approx 2.454$, which will be discussed later in this section, the facets can hardly be seen in this picture due to finite-size effects at the points where the facets and the round surface merge. Above the roughening temperature, the surface is curved everywhere, but the droplet's contour still appears non-circular if looked at closely. Upon further increase of temperature, the droplets eventually become perfectly round. Along with this transition of shape goes an increase of the interfacial width, especially in the vicinity of the critical point.

These effects can be understood as follows. The shape of the droplet is determined by the interfacial tension $\gamma(\theta, \varphi)$ and can be determined in principle from the Wulff construction [Wulff, 1901]. However, this requires precise knowledge of $\gamma(\theta, \varphi)$, which is in general hard to compute [Bittner et al., 2009].

As was pointed out in section 2.2.2, the geometry in a box with periodic boundary condition depends strongly on the density. Here, the focus is on the case with a droplet in a vaporous surrounding. The shape of the droplet is given by the interfacial stiffness $\kappa$ [cf. section 2.5], which is connected to the interfacial tension $\gamma$ by [Hasenbusch and Pinn, 1993]

$$\kappa = \gamma + \left.\frac{\mathrm{d}^2\gamma}{\mathrm{d}\theta^2}\right|_{\theta=0} \tag{3.1}$$

where $\theta$ is the angle between the interface and a reference axis (e.g. the z-axis). The interfacial tension for a flat wall is defined by [cf. section 2.1.2]

$$\gamma = \lim_{L\to\infty} \frac{\Delta F}{L^2} \tag{3.2}$$

where $L^2$ is the area of the interface and $\Delta F$ is the free energy needed to form the interface. As has been shown [Hasenbusch and Pinn, 1993], in the lattice gas model the interfacial tension and the interfacial stiffness are equal only for high temperatures, i.e. for temperatures above $k_\mathrm{B}T/J = 3.8$. This explains why the spherical shape is only seen above this temperature while the shape deviates from a sphere more and more if the temperature is lowered.

[1] At low temperatures, the stable state at this density would be a cylindrical droplet connected to itself by the periodic boundary conditions. However, for the system sizes used here, a compact droplet is perfectly metastable for the time of the measurements. This choice of density was made in the interest of an economical use of computer resources.

Apart from the critical temperature $k_\mathrm{B}T_c/J \approx 4.5115$, there is a second important temperature in this context called the roughening temperature $T_R$. At $k_\mathrm{B}T/J = 0$, the droplet is perfectly cubic. As one increases the temperature, first the corners, then the edges and eventually the facets of the droplet begin to disappear. A transition takes place at $k_\mathrm{B}T_R/J \approx 2.454$ [Bürkner and Stauffer, 1983; Mon et al., 1989, 1990; Hasenbusch and Pinn, 1994; Hasenbusch et al., 1996; Hasenbusch and Pinn, 1997]. At this temperature, the curvature of the surface is non-zero everywhere. However, this does not mean that the droplet has a spherical shape, in which case the curvature would be constant. Above the roughening transition, the shape of the droplet becomes rounder and rounder, since $\gamma \to \kappa$ for $T \to T_c$. At the critical temperature, the droplets would be perfectly round. However, at the same time, the interface width diverges, which can be understood by the concept of capillary waves.

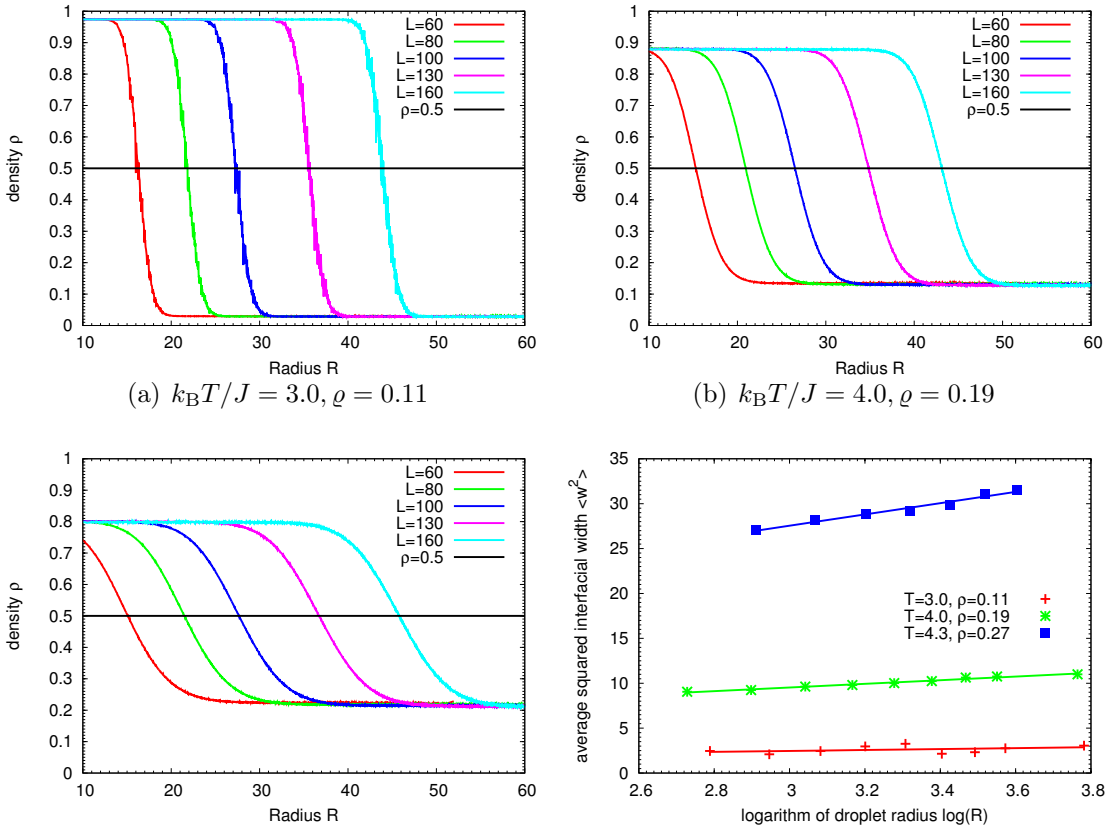


(a) $k_\mathrm{B}T/J = 3.0, \varrho = 0.11$

(b) $k_\mathrm{B}T/J = 4.0, \varrho = 0.19$

(c) $k_\mathrm{B}T/J = 4.3, \varrho = 0.27$

(d) interfacial width vs. droplet radius

Figure 3.2: Density profiles of droplets at various temperatures in cubic boxes of volume $L^3$. The interface broadening is clearly visible. The shape of the interface does not depend on the droplet size, if the droplet is large enough. However, there is a logarithmic dependency, shown in (d).

The CWT result (2.62), that the interfacial width diverges logarihmically, is expected to carry over to macroscopical droplets, since for large droplets, the interface is locally flat and most of the capillary wave spectrum is not affected by the curvature. Therefore, the result for the broadening of a planar interface of linear dimension $L$ [cf. section 2.5] can be taken as a first approximation for the case of macroscopical droplets, replacing $L$ by the droplet radius $R$:

$$\langle w^2 \rangle = w_0^2 + \frac{k_\mathrm{B}T}{4\kappa} \ln \frac{R}{\lambda_\mathrm{min}} \; . \tag{3.3}$$

Here, $w_0$ is the intrinsic width of the interface while $\lambda_\mathrm{min}$ is the short wavelength cutoff of the capillary wave spectrum. From Eq. (3.3), it is clear that the interfacial width diverges, as $\kappa \to 0$ for $T \to T_c$. So while the droplet becomes rounder with increasing temperature, its interface becomes more diffuse at the same time.

This approach can be tested for temperatures above the roughening transition, where it makes sense to measure a radial density profile. The results are shown in Fig. 3.2, where the density of the system is again fixed at $\varrho = 0.33$. The volumes of the droplets considered here range from 15.000 to 500.000 spins, corresponding to huge nucleation barriers far beyond observation in computer simulations. The density profiles show that the interfacial width grows with temperature and droplet radius. From these density profiles, the droplet radius is estimated to be the radius where the density is 0.5, while the surface width $w$ is measured by fitting

$$\varrho(r) = \frac{\varrho_l + \varrho_g}{2} - \frac{\varrho_l - \varrho_g}{2} \arctan(r/w) \tag{3.4}$$

to the profile. Instead, a linear fit around the radius with $\varrho(R) = 0.5$, where the profile is linear, is made. Since $\arctan(x/w) = x/w + \mathcal{O}((x/w)^3)$, this is also valid to estimate $w$. The results are shown in Fig. 3.2(d), asserting the qualitative agreement with (3.3). Using the interfacial tension of Hasenbusch and Pinn [Hasenbusch and Pinn, 1993], the slope of (3.3) is expected to be $\frac{1}{4\kappa} \approx 2.5$ for $k_\mathrm{B}T/J = 4.0$ and $\frac{1}{4\kappa} \approx 8.0$ for $k_\mathrm{B}T/J = 4.3$. From the data, the slopes are $\frac{1}{4\kappa} \approx 2.1$ for $k_\mathrm{B}T/J = 4.0$ and $\frac{1}{4\kappa} \approx 5.8$ for $k_\mathrm{B}T/J = 4.3$, which is distinctly lower but of the same order of magnitude.

## 3.3 Microscopical Cluster Definitions

The effect of interface broadening is what makes a microscopical definition of droplets difficult, since it is a priori not clear whether a lattice site in the interface belongs to the droplet or to the surroundings. In this section, several definitions are tested for

their validity in the thermodynamic limit. Also, macroscopical definitions will be presented for comparison.

The appeal of a microscopical definition is evident. Such a definition allows to analyze a given configuration and immediately distinguish the two phases from each other. Then one could try to carry over such a definition to subcritical droplets and gain a better understanding of nucleation events. Here, two definitions will be compared, namely geometrical droplets, which have been used in the literature frequently for the study of nucleation, and physical droplets, which are also known under the name Swendsen-Wang droplets.

The fact that droplets at low temperatures have cubic shape with planar facetted interfaces (cf. Fig. 3.1) also holds for microscopical droplets [Wonczak et al., 2000]. For the study of a vapor-liquid transition, where the droplets are spherical and have rough, curved interfaces, one needs to work at high temperatures, namely distinctly above the roughening transition and well below the critical point (cf. section 3.2). Round droplets occur only for temperatures above $k_{\mathrm{B}}T/J = 3.8$, where the difference between interfacial tension and interfacial stiffness becomes negligible [Privman, 1988; Hasenbusch and Pinn, 1993]. As will be shown in this section, the geometrical droplet definition is appropriate only at low temperatures and leads to systematically wrong results when applied to droplets at high temperature. However, many studies of nucleation have been carried out at about $T/T_c = 0.6$, which is only slightly above $T_R$. Consequently, the surface term in the free energy barrier (2.42) is enhanced by the rather cubic shape. On the other hand, it is known that the interfacial tension depends on the interfacial curvature and that $\gamma_{vl}(R) < \gamma_{vl}$, i.e. the interfacial tension for small spheres is smaller than for a planar interface. This means that the surface term is decreased, and it is hard to answer whether the two effects cancel each other or if one of the two is dominant. In the literature, nucleation barriers where reported to be too high, too low or in agreement with classical nucleation theory. Therefore, this section aims at showing that only physical droplets lead to conclusive statements about properties of droplets for all temperatures, while geometrical droplets fail above the roughening temperature.

### 3.3.1 The Lever Rule Method

The lever rule method [Winter et al., 2009a; Schrader et al., 2009b; Block et al., 2010; Tröster et al., 2012] is a means to predict the droplet volume via simple thermodynamic considerations and without any assumptions about the droplet's shape. Therefore it is well-suited to test the accuracy of microscopical droplet definitions. Note that the lever rule method does not only apply in the lattice gas model but also in Lennard-Jones fluids and other models.

Consider a finite box of volume $V = L^3$ at fixed temperature. Then there exists an effective thermodynamic potential

$$f_L(T, \varrho) = \frac{F(N, V, T) - F(N = V\varrho_l, V, T)}{V} \,. \tag{3.5}$$

This is the free energy per lattice site relative to the free energy of the system at density $\varrho_l$. See section 2.2.1 for the terminology and the translation between the Ising model and the lattice gas model. One can then also define a chemical potential as the derivative of the free energy by the particle number

$$\widetilde{\mu}(N, V, T) = \left.\frac{\partial F(N, V, T)}{\partial N}\right|_{V,T} \tag{3.6}$$

$$\Delta\mu_L(T, \varrho) = \widetilde{\mu}(N, V, T) - \mu_{\text{coex}} \,, \tag{3.7}$$

where $\mu_{\text{coex}}$ is the coexistence chemical potential. As one can see in Fig. 3.3, the isotherms $\Delta\mu_L(T, \varrho)$ exhibit a loop with respect to $\varrho$. This has already been discussed in section 2.2.2. The important point is that for a range of values of $\Delta\mu$, there are three states sharing the same chemical potential, i.e. can exist in equilibrium next to each other. The two homogeneous states at low density $\varrho_g > \varrho_{g,0}$ and high density $\varrho_l > \varrho_{l,0}$, and a third state in the two-phase coexistence of a droplet and a supersaturated vapor. The fact that the state share the same chemical potential, the liquid phase forming the droplet must have the same physical properties as the pure liquid while the same holds for the vapor. Provided $L$ is large enough, the system can be decomposed into independent subsystems, where the volume $V_l$ contains the droplet while the volume $V_g$ contains the vapor. Then

$$V = V_l + V_g \,, \tag{3.8}$$

$$N = \varrho V = \varrho_l V_l + \varrho_v (V - V_l) + N_{\text{exc}} \,, \tag{3.9}$$

$$V f_L(T, \varrho) = V_l f_L(T, \varrho_l) + (V - V_l) f_L(T, \varrho_g) + \Delta F \,, \tag{3.10}$$

where $N_{\text{exc}}$ takes into account particles belonging to the interface rather than to one of the two sub-volumes. $\Delta F$ is the surface free energy, which can be computed via (3.10) if the droplet volume $V_l$ and the free energy isotherm $f_L(T, \varrho)$ is known. In this decomposition, it is assumed that the interaction between particles belonging to the liquid and particles in the vapor is restricted to the interface and can thereby be accounted for in the surface free energy term $\Delta F$. This is a reasonable assumption for short-ranged interactions.

It should be mentioned that the computation of the free energy of a system is a complicated matter, especially for large systems. The reason is that the free energy (like entropy for example) cannot be expressed as an average of an observable over

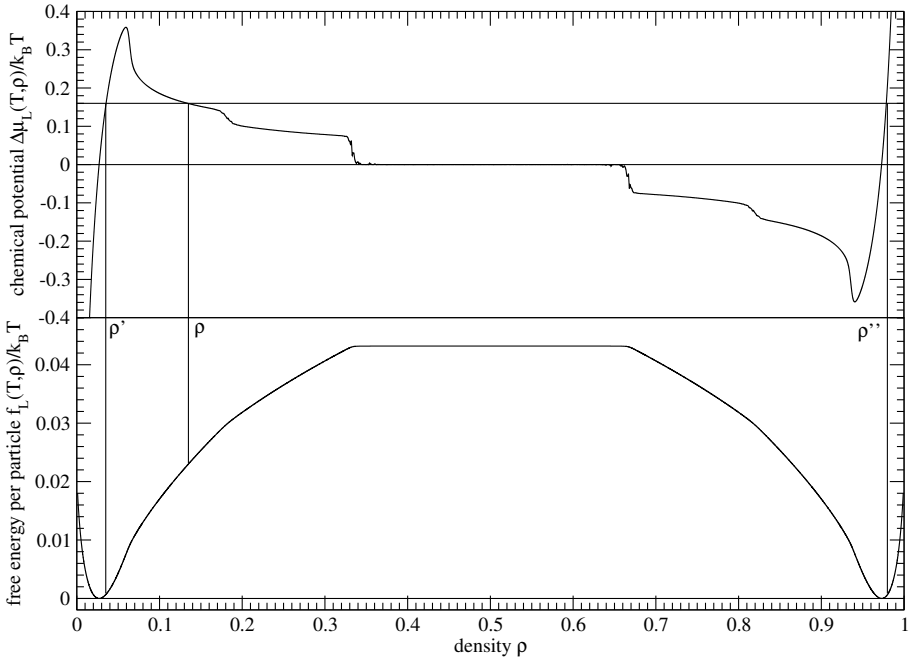


Figure 3.3: Illustration of the lever rule method in a comparatively small system ($L = 20$) at $k_BT/J = 3.0$. At the top, there is the chemical potential $\beta\Delta\mu_L(T, \varrho)$, at the bottom the free energy $\beta f_L(T, \varrho)$. One can choose any density $\varrho$ between the droplet evaporation-condensation transition and the transition from the droplet phase to the cylinder phase (see also Fig. 2.1). For each of these densities $\varrho$, one can find two other densities $\varrho'$ and $\varrho''$ with equal chemical potential. They are the corresponding vaporous and liquid densities $\varrho_g$ and $\varrho_l$, respectively.

phase space ("mechanical quantities"), but the free energy is a quantity depending on the phase space volume accessible to the system ("thermal quantities"). Many advanced simulation methods allow to compute the free energy efficiently, like successive umbrella sampling [Virnau and Müller, 2004; Virnau et al., 2004], multicanonical sampling [Berg and Neuhaus, 1992] or Wang-Landau sampling [Wang and Landau, 2001b,a; Shell et al., 2002; Landau et al., 2004]. See also [Landau and Binder, 2009; Binder and Heermann, 2010] for general information on these sampling methods. In this study, a different approach is chosen. Instead of computing the chemical potential as a derivative of the free energy via (3.6), the chemical potential $\Delta\mu(T, \varrho)$ is computed directly using a lattice version of the Widom particle insertion method (see section 2.6.4 for details). This allows to work with box sizes that are orders of magnitude larger.

To determine the droplet volume, one can use (3.9). This leads to the lever rule

prediction of the droplet volume

$$V_{\mathrm{LR}} = V \frac{\varrho - \varrho_g}{\varrho_l - \varrho_g} \,. \tag{3.11}$$

Here, the excess number of particles is assumed to vanish: $N_{\mathrm{exc}} = 0$. This is the notion of equimolar dividing surface between the two phases [Rowlinson and Widom, 1982], which states that it is possible to separate the two phases by an infinitely thin interface[2]. Since surface effects become negligible for large droplets, (3.11) is correct for $L \to \infty$. Therefore by reading off $\varrho$, $\varrho_l$ and $\varrho_g$ in Fig. 3.3, one immediately extracts the droplet volume. Note that unlike classical nucleation theory, there is no assumption about the shape of the droplet[3] in (3.11).

Figure 3.4 shows the curves $\Delta\mu_L(T, \varrho)$ which have to be measured very carefully in order to apply (3.11) accurately. Because of the spin inversion symmetry, it is sufficient to measure $f_L(T, \varrho)$ only for $\varrho < 0.5$. Furthermore, only the pure phase region and the droplet region need to be sampled, as shown in Fig. 3.4.

The lever rule method has some disadvantages. It is not possible to apply this method to arbitrarily small droplets, because the simulation boxes must not be so small that the inhomogeneous state of a droplet with supersaturated vapor around it becomes unstable [Binder and Kalos, 1980]. On the other hand, very large droplets also become increasingly difficult to analyze, because the computational effort of sampling $f_L(T, \varrho)$ grows with $L^3$. Therefore, a different approach needs to be found, whose correctness can be tested in the thermodynamic limit via the lever rule method.

### 3.3.2 Microscopically defined Clusters

The question is how to define the cluster size of a droplet when the number of particles it consists of become less than some thousand. This is the regime where clusters are not round anymore. A microscopical cluster definition, by which a particle (or a lattice site) can determine if it belongs to the droplet or not only by looking at its local environment, would be very convenient.

The simplest microscopical droplet definition is the geometrical droplet definition. The idea is that neighboring occupied lattice sites belong to the same droplet [Binder

[2] In [Tröster et al., 2012], this assumption is not made. Instead of the equimolar dividing surface, they define the surface of tension, which allows for a non-vanishing excess particle number. This is important for small droplets in particular.

[3] If one assumes a sphere, i.e. $V_l = 4\pi R^3/3$, then the surface free energy in Eq. (3.10) takes the form $\Delta F = 4\pi\gamma_{vl}(R)R^2$.

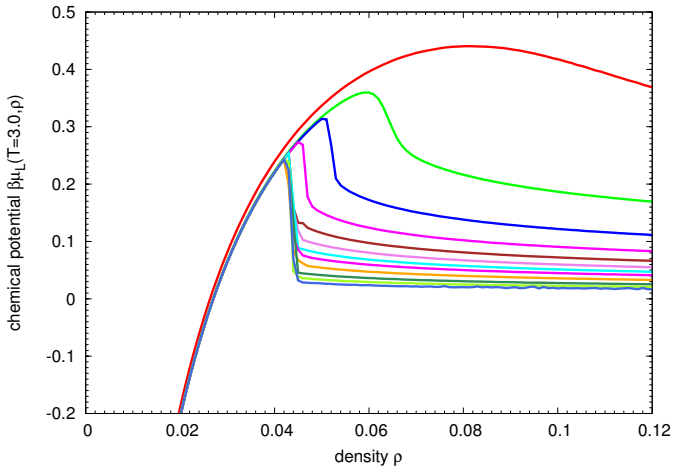


Figure 3.4: Chemical potential $\Delta\mu_L(T, \varrho)$ at $k_\mathrm{B}T/J = 3.0$ and several cubic boxes ($L = 10, 20, 30, 40, 50, 60, 70, 80, 100, 130, 160, 200$, from top to bottom). Only the droplet area and the evaporation-condensation transition is shown here [cf. Fig. 2.1]. Due to the symmetry of the Ising model, which implies $\Delta\mu(\varrho) = -\Delta\mu(1-\varrho)$, it suffices to sample the densities below 0.5. Again, the homogeneous phases have very little dependence on the system size $L$, whereas the heterogeneous parts strongly depend on $L$. Note that the evaporation-condensation transition is very smooth in small boxes and becomes sharper for larger box sizes.

and Müller-Krumbhaar, 1974]. The droplet volume is then obtained by counting all occupied lattice sites belonging to the cluster, $\ell_\mathrm{geom}$. Assuming that the density within a macroscopical droplet equals the density $\varrho_l$ of a bulk liquid phase, the volume of the droplet can be calculated as

$$V_\mathrm{geom} = \frac{\ell_\mathrm{geom}}{\varrho_l} \,. \tag{3.12}$$

It has been shown [Coniglio and Klein, 1980; Swendsen and Wang, 1987; De Meo et al., 1990] that this definition does not contain much physical significance: There exists a percolation transition line in the phase diagram (Fig. 3.5), where a geometrical cluster of infinite size appears [Müller-Krumbhaar, 1974; Binder, 1980]. This percolation transition does not have any significance from a thermodynamic point of view [Coniglio, 1975; Coniglio et al., 1977; Binder, 1980; Hayward et al., 1987]. As a consequence, the droplet shown in Fig. 3.1(i) cannot be detected by the geometrical definition, because the density of the environment is so high that the whole system percolates and $V_\mathrm{geom} \approx V$.

Fortuin and Kasteleyn [Kasteleyn and Fortuin, 1969; Fortuin and Kasteleyn, 1972] worked on mapping a $q$-state Potts model to a correlated bond-percolation problem. They found out that the Ising model ($q = 2$) corresponds to a correlated percolation problem with the probability

$$p(T) = 1 - \exp\left(\frac{2J}{k_\mathrm{B}T}\right) \tag{3.13}$$

of "active" bonds between parallel spins. Therefore, neighboring occupied lattice sites only belong to the same cluster if they are connected by an active bond [cf. section 2.2.3]. It has been shown [Coniglio and Klein, 1980; Swendsen and Wang, 1987; De Meo et al., 1990], that the percolation transition of these physical clusters coincides with the critical point of the Ising model or lattice gas model. If for a given configuration, the cluster contains $\ell_\mathrm{phys}$ occupied lattice sites, then the volume of the droplet is given by

$$V_\mathrm{phys} = \frac{\ell_\mathrm{phys}}{m_l} = \frac{\ell_\mathrm{phys}}{2\varrho_l - 1} \,. \tag{3.14}$$

It is obvious that the geometrical definition is recovered in the limit $T \to 0$, when all bonds become active. Hence it is to be expected that the geometrical cluster definition works at low temperatures, while at high temperatures, one geometrical cluster consists of one or several physical clusters. In this study, the geometrical droplet definition is only used to show the systematical errors that arise for medium and high temperatures.

The physical clusters have been used in the literature in the context of critical phenomena, where they are also referred to as Swendsen-Wang clusters [Swendsen and Wang, 1987; Wolff, 1989], their significance in the context of nucleation has been ignored almost completely [Acharyya and Stauffer, 1998; Shneidman et al., 1999b; Ramos et al., 1999; Shneidman et al., 1999a; Vehkamaki and Ford, 1999; Wonczak et al., 2000; Pan and Chandler, 2004; Ryu and Cai, 2010]. It should be noted though that the definition of physical clusters is of stochastic nature, since the bonds between neighboring spins of equal orientation are activated only with a certain probability. So given a fixed configuration, the geometrical cluster definition always yields the same clusters while the physical clusters will fluctuate. In the following static analysis, this is not important because the predicted volume is taken as the average over many configurations. If one wishes to apply physical clusters to dynamic simulations, one might want to analyze one configuration several times to get a mean cluster distribution.

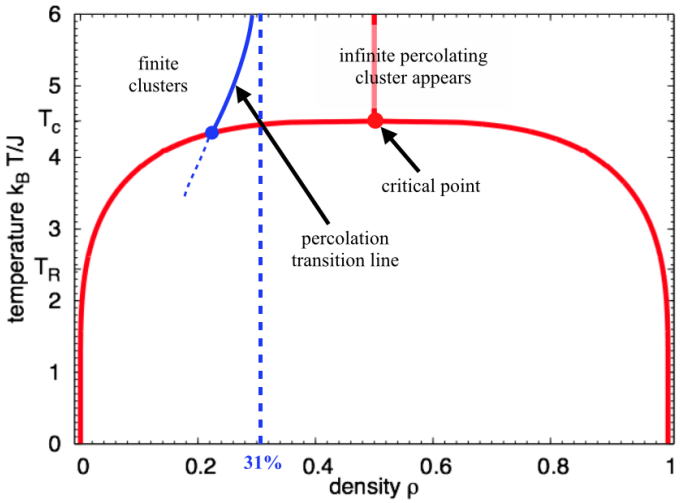


Figure 3.5: Phase diagram of the Ising/lattice gas model. There is a transition line [Binder, 1980] where the system has a transition from not being percolated to having a large cluster percolating the whole system. If there is no interaction (corresponding to high temperature), the system percolates at a density $\varrho_{\text{perc}} = 31\%$. The interaction decreases this percolation threshold, so the transition line approaches $\varrho_{\text{perc}}$ from lower densities. Geometrical clusters diverge at this transition line and cannot detect the physically relevant droplets which diverge at $T_c$ and not at the percolation transition line.

Both the geometrical and the physical droplet definition can be implemented by an efficient algorithm called Hoshen-Kopelman[4] algorithm [Hoshen and Kopelman, 1976]. It follows a brief summary of the concept. The aim is to go though the lattice only once, labeling all lattice sites one after another. If the lattice site does not contain a particle, its label is set to zero. If a neighbor of the current lattice site has a label already, then one stores the information that both labels belong to the same cluster in an array. By convention, the label with the lowest label is the proper label of the cluster. So in the end one has a number of clusters, each cluster having one or more labels, one of them (by convention the smallest label) being the proper label. The structure of the labels corresponds to a tree graph where the proper label is the root and all other labels point directly or indirectly towards the root.

To compute the volume of physical or geometrical droplets via (3.12) or (3.14), respectively, one has to know the relation $\varrho_l(T, \Delta\mu)$. This, however, is an easy task, compared to measuring the whole curve $\Delta\mu_L(T, \varrho)$ needed for the lever rule

[4]There also exists a more efficient "enhanced" Hoshen-Kopelman algorithm [Hoshen et al., 1997].

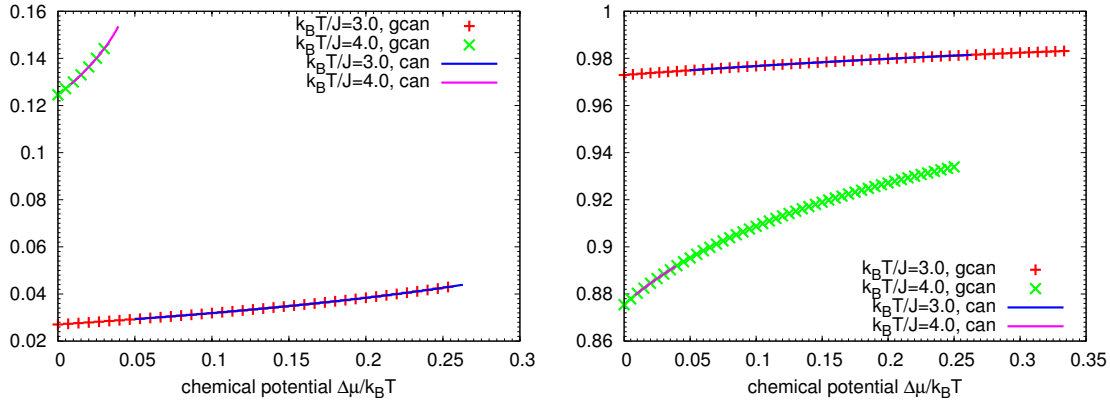


(a) $\varrho_g(T, \Delta\mu)$ (b) $\varrho_l(T, \Delta\mu)$

Figure 3.6: Dependence of the density of the homogeneous phases on the chemical potential in a cubic box of linear dimension $L = 60$ at temperatures $k_\mathrm{B}T/J = 3$ and 4. The symbol belong to grand-canonical ensemble simulations while the curves correspond to measuring $\Delta\mu_L(T, \varrho)$ in the canonical ensemble via the Widom particle insertion method (see chapter 2.6.4).

method (3.11). Fig. 3.6 shows the results of measuring $\varrho_l$ and $\varrho_g$ in a grand-canonical ensemble with various $\Delta\mu$, as well as in a canonical ensemble using the Widom particle insertion method. The finite-size effects, which differ for the two ensembles considered [Landau and Binder, 2009; Binder and Heermann, 2010], are not seen at all in the pure phases.

### 3.3.3 Finite-Size Scaling

In order to test the physical droplet definition, simulations in the canonical ensemble in a cubic box of linear dimension $L$ are carried out. The density is fixed at various values $\varrho$ in the droplet range [see Fig. 2.1]. A small droplet is put in the box to serve as a starting point for a nucleus to form. The system is then carefully equilibrated so that the initial size and shape of the droplet do not influence the outcome. The simulation of a lattice gas in the canonical ensemble (or equivalently, the Ising model with conserved magnetization) is the spin exchange algorithm [Landau and Binder, 2009; Binder and Heermann, 2010]. However, the standard nearest-neighbor exchange method causes a hydrodynamic slowing-down because any local excess density can only relax diffusively. Therefore, in this context a single-spin-flip algorithm is used, in which the total number of occupied lattice sites is restricted to an interval $[N-1, N]$. Any spinflip that would leave this interval is automatically rejected. The difference

between this almost-conserved density and a strictly canonical simulation is of order $L^{-3}$ and therefore negligible.

Because the prediction of the lever rule method is true in the thermodynamic limit, it is useful to normalize the predictions of the physical droplet definition (3.14) to the lever rule prediction (3.11). Fig. 3.7 shows that the ratio $V_{\mathrm{phys}}/V_{\mathrm{LR}}$ converges to unity for $L \to \infty$ for all temperatures and densities. The physical droplet definition turns out to work at all temperatures, especially below the roughening temperature as well as close to the critical point.

Also shown in Fig. 3.7 is the prediction using geometrical droplets. At low temperatures, this definition is very similar to the physical droplet definition, for the bond probability (3.13) is close to unity. Therefore, it is to be expected that the geometrical droplets also extrapolate to the correct volume predicted by the lever rule method. However, at higher temperatures the deviations become noticeable. The predicted volumes lie systematically above and yield completely unreasonable results at $k_{\mathrm{B}}T/J = 4.3$, where the volume is overestimated even asymptotically by up to 80%, while the actual volumes the error is up to 400%. This is a consequence of the percolation transition of the geometrical droplets [Müller-Krumbhaar, 1974], which is why the predicted volume approaches the box volume instead of the droplet's volume. This emphasizes that geometrical droplets should not be used for temperatures around $k_{\mathrm{B}}T/J = 2.6$ or higher.

The data needed to apply the lever rule method can also serve to give a volume prediction based on classical nucleation theory. At given temperature $T$ and chemical potential $\Delta\mu_L(T, \varrho)$, the critical droplet has the volume

$$V_{\mathrm{CNT}} = \frac{4\pi}{3} R^{*3} = \frac{4\pi}{3} \left( \frac{2\gamma_{vl}}{\Delta\mu(\varrho_l - \varrho_g)} \right)^3 , \tag{3.15}$$

where (2.43) has been used. Using the interfacial tension $\gamma_{vl}$ by Hasenbusch & Pinn [Hasenbusch and Pinn, 1993, 1994], there are no free parameters at all. The data is also shown in Fig. 3.7. In contrast to the microscopical predictions, the dependence on $1/L$ is very weak, so the data converges horizontally against the limit of infinite box size. Apart from that, the ratio $V_{\mathrm{CNT}}/V_{\mathrm{LR}}$ converges to unity only for temperatures $k_{\mathrm{B}}T/J \geq 4.0$, whereas CNT underestimates the volume systematically for lower temperatures. This behavior can be attributed to the fact that CNT is based on spherical droplets. However, it can clearly be seen in Fig. 3.1 that the droplets below $k_{\mathrm{B}}T/J = 4.0$ and especially below $k_{\mathrm{B}}T/J = 2.5$ are nonspherical. Therefore, CNT underestimates the surface area of a droplet at low temperature. This observation is consistent with the findings of Hasenbusch & Pinn [Hasenbusch and Pinn, 1993] that the anisotropy of the interfacial tension becomes important for temperatures below $k_{\mathrm{B}}T/J = 3.8$.

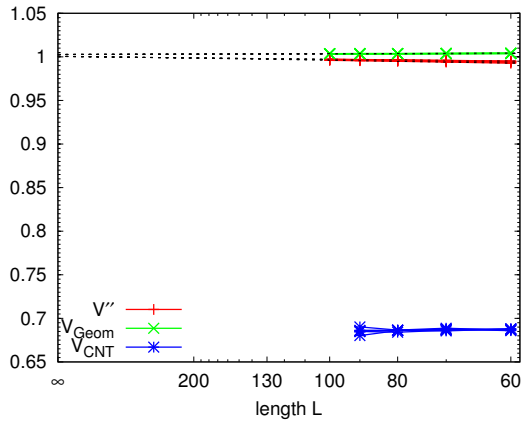


(a) $k_{\mathrm{B}}T/J = 2.0$

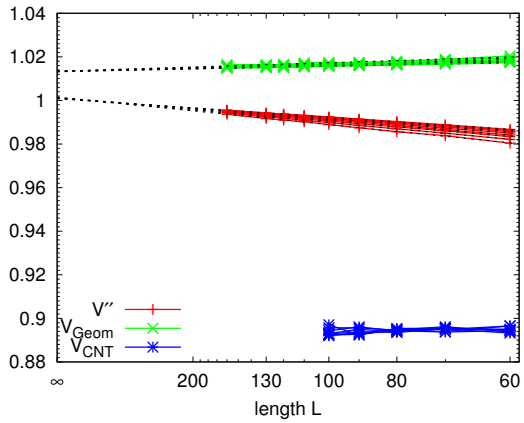


(b) $k_{\mathrm{B}}T/J = 2.6$

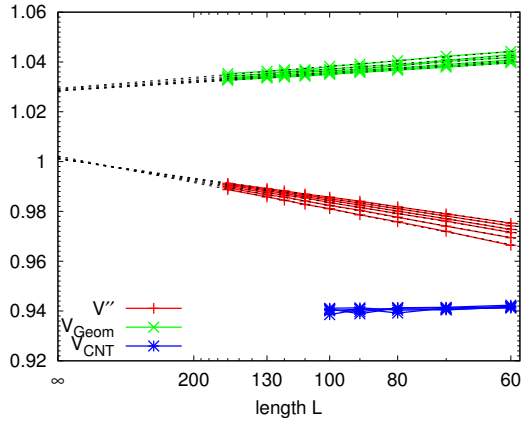


(c) $k_{\mathrm{B}}T/J = 3.0$

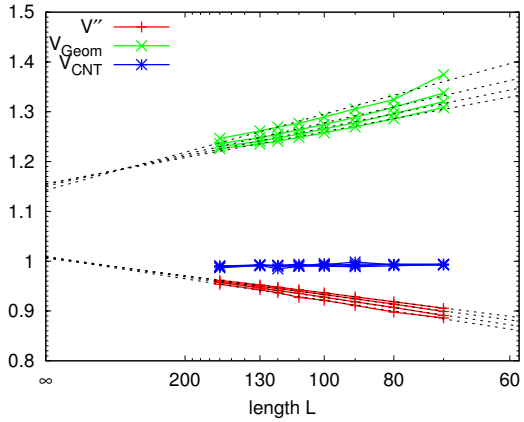


(d) $k_{\mathrm{B}}T/J = 4.0$

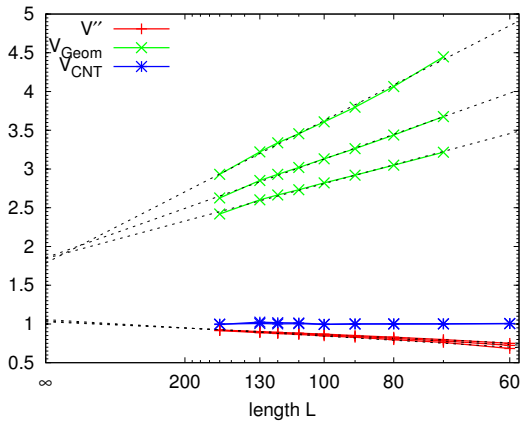


(e) $k_{\mathrm{B}}T/J = 4.3$

Figure 3.7: Finite-size scaling of the ratio $V_{\mathrm{phys}}/V_{\mathrm{LR}}$ [red data] against $1/L$ for various densities and temperatures. The ratios $V_{\mathrm{geom}}/V_{\mathrm{LR}}$ [green data] and $V_{\mathrm{CNT}}/V_{\mathrm{LR}}$ [blue data] are also included. The volumes are computed using (3.11), (3.12) and (3.14), while for the classical nucleation theory, a spherical droplet with radius $R^*$ (see (2.43)) and volume $4\pi R^{*3}/3$ is assumed. The densities are chosen to be in the range where the droplet is not aware of the finiteness of the box, as explained in section 2.2.2.

At first sight, the finding that $V_{\mathrm{CNT}}/V_{\mathrm{LR}}$ is independent of $R^*$ seems to disagree with the results in [Winter et al., 2009a; Schrader et al., 2009a; Winter et al., 2009b; Block et al., 2010; Das and Binder, 2011; Tröster et al., 2012], where the interfacial tension $\gamma_{vl}(R)$ is shown to have a curvature-dependency. In these references, evidence is provided that

$$\gamma_{vl}(R) = \frac{\gamma_{vl}}{1 + 2\left(\frac{l}{R}\right)^2} , \tag{3.16}$$

where $\gamma_{vl} = \gamma_{vl}(R = \infty)$ is the interfacial tension of a flat wall and $l$ is a length proportional to the correlation length in the bulk [Das and Binder, 2011]. Tolman [Tolman, 1949] introduced the idea of a curvature-dependent interfacial tension for small droplets

$$\gamma_{vl}(R) = \frac{\gamma_{vl}}{1 + 2\frac{\delta}{R}} , \tag{3.17}$$

but it has been shown [Fisher and Wortis, 1984] that such a correction does not appear for $R \to \infty$, i.e. $\delta = 0$, because of the spin reversal symmetry of the Ising model. A straightforward calculation using (2.42) and (3.16) shows that

$$\begin{aligned} \frac{R^* \Delta\mu(\varrho_l - \varrho_g)}{2\gamma_{vl}} &= \frac{1 + 4\left(\frac{l}{R}\right)^2}{\left(1 + 2\left(\frac{l}{R}\right)^2\right)^2} \\ &\approx 1 - 4\left(\frac{l}{R}\right)^4 + \mathcal{O}\left(\left(\frac{l}{R}\right)^6\right) . \end{aligned} \tag{3.18}$$

Clearly, these corrections are negligible for $l \ll R^*$. Since the correlation length is less than one lattice spacing for temperatures below $k_{\mathrm{B}}T/J = 4.0$, this correction cannot explain the discrepancy shown in Fig. 3.7. Instead it must be fully due to the anisotropy of the interfacial tension, resulting in a non-spherical shape of the droplet.

The droplet shape is spherical only at high temperatures, while at zero temperature, the shape is cubic. For intermediate temperatures, the shape is in principle given by the Wulff construction [Wulff, 1901]. To get an expression for the free energy barrier, which does not explicitly depend on the droplet shape but only on the droplet's volume, one can use general expressions for the droplet's volume $V = \widetilde{V}R^3$ and surface $A = \widetilde{A}R^2$, given the droplet's linear dimension[5] is $R$. The extreme cases of a spherical ($\widetilde{V} = 4\pi/3$; $\widetilde{A} = 4\pi$) and a cubic ($\widetilde{V} = 8$; $\widetilde{A} = 24$) droplet shape are also included in this approach. Note however, that other corrections like a radius

[5] Due to symmetry, one can exclude shapes which need more than one parameter. For example, a droplet will always be rather cubic or spherical than elongated in one direction like a cuboid or an ellipsoid.

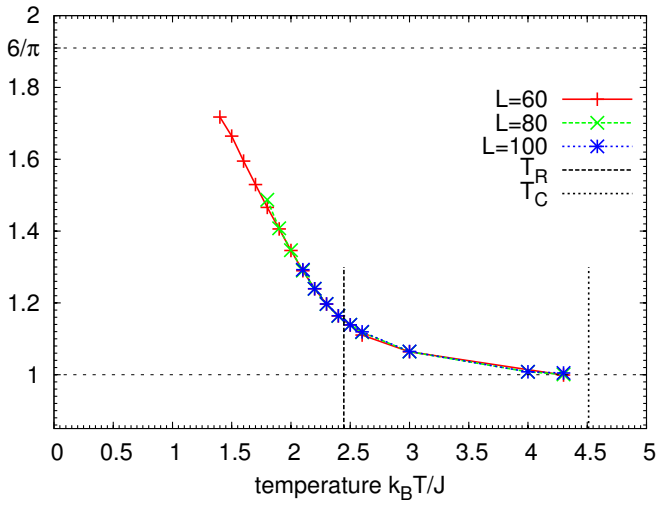


Figure 3.8: Ratio $V_{\mathrm{LR}}/V_{\mathrm{CNT}}$ of the droplet volume according to the lever rule and the volume predicted by CNT. While they agree at high temperatures, the classical nucleation theory systematically underestimates the volume because of the assumption of spherical droplets. A dependence of this effect on the box size $L$ is not found.

dependent interfacial tension $\gamma(R)$ are neglected, as they are negligible for large droplets [Tröster et al., 2012]. The free energy barrier $\Delta F_{\mathrm{hom}} = \gamma_{vl} A - \Delta\mu(\varrho_l - \varrho_g)V$ can then be written as

$$\Delta F_{\mathrm{hom}} = \gamma_{vl} \widetilde{A} \widetilde{V}^{-2/3} V^{2/3} - \Delta\mu(\varrho_l - \varrho_g)V \ . \tag{3.19}$$

Minimizing the free energy barrier with respect to $V$ yields the critical volume

$$V^* = \left( \frac{2}{3} \frac{\gamma_{vl}}{\Delta\mu(\varrho_l - \varrho_g)} \widetilde{A} \widetilde{V}^{-2/3} \right)^3 \tag{3.20}$$

and the free energy barrier height

$$\Delta F^*_{\mathrm{hom}} = \frac{1}{3} \gamma_{vl} \widetilde{A} \widetilde{V}^{-2/3} (V^*)^{2/3} = \frac{1}{2} \Delta\mu(\varrho_l - \varrho_g) V^* \tag{3.21}$$

This equation states that the free energy barrier is proportional to the droplet's volume and furthermore depends on the densities and the chemical potential. In the simulation, where the overall density $\varrho$ and the temperature $T$ are fixed, the chemical potential $\Delta\mu(T, \varrho)$ and the densities are determined and of course independent of the droplet's shape. Therefore one can conclude for the limit $T \to 0$

$$\left. \frac{V^*}{V^*_{\mathrm{CNT}}} \right|_{T=0} = \left. \frac{\Delta F^*}{\Delta F^*_{\mathrm{CNT}}} \right|_{T=0} = \frac{\widetilde{A}^3_{\mathrm{cube}} \widetilde{V}^{-2}_{\mathrm{cube}}}{\widetilde{A}^3_{\mathrm{sphere}} \widetilde{V}^{-2}_{\mathrm{sphere}}} = \frac{6}{\pi} \ , \tag{3.22}$$

where the first expression in (3.21) was used[6]. Since the droplet's volume can be expressed by the lever rule method regardless of temperature and droplet shape, it is to be expected that $V_{\mathrm{LR}}/V_{\mathrm{CNT}} \to 1$ for $T \to T_c$ and $V_{\mathrm{LR}}/V_{\mathrm{CNT}} \to 6/\pi$ for $T \to 0$. Fig. 3.8 indeed confirms this expectation.

### 3.3.4 Excess Effects

Having a closer look at the finite-size scaling of physical droplets in Fig. 3.9, which shows the same data as in Fig. 3.7, there a a asymptotic correction of order $1/L$. From this one can conclude that the assumption $N_{\mathrm{exc}} = 0$ [cf. section 3.3.1] does not hold for physical droplets. Assuming that the excess particle number is proportional to the surface area of the droplet, with $\varrho_{\mathrm{exc}}$ being the excess density corresponding to the interface,

$$N_{\mathrm{exc}} = \varrho_{\mathrm{exc}} A = C \varrho_{\mathrm{exc}} V_l^{2/3} \ , \tag{3.23}$$

where $C = \widetilde{A}\widetilde{V}^{-2/3}$ depends on the droplet's shape, e.g. $C = (36\pi)^{1/3}$ for a sphere and $C = 6$ for a cube, then one can insert (3.11) as a first-order approximation to obtain

$$N_{\mathrm{exc}} = C \varrho_{\mathrm{exc}} L^2 \frac{(\varrho - \varrho_g)^{2/3}}{(\varrho_l - \varrho_g)^{2/3}} \ . \tag{3.24}$$

Instead of (3.11), the expected volume of the droplet is

$$\begin{aligned} V_{\mathrm{LR,\,exc}} &= V \frac{\varrho - \varrho_g}{\varrho_l - \varrho_g} - C \varrho_{\mathrm{exc}} L^2 \frac{(\varrho - \varrho_g)^{2/3}}{(\varrho_l - \varrho_g)^{5/3}} \\ &= V_{\mathrm{LR}} \left[ 1 - \frac{C \varrho_{\mathrm{exc}}}{L} (\varrho_l - \varrho_g)^{-2/3} (\varrho - \varrho_g)^{-1/3} \right] \ . \end{aligned} \tag{3.25}$$

There is indeed a $1/L$ correction of the volume predicted by the lever rule method, yielding smaller estimates for the volume in a finite box of volume $V = L^3$. To test this, Fig. 3.10 shows the data contained in Fig. 3.9 plotted against $(\varrho_l - \varrho_g)^{-2/3}(\varrho - \varrho_g)^{-1/3}$. The data collapses onto universal curves for each temperature.

## 3.4 Conclusion

In this chapter, the properties of macroscopical droplets in the Ising (lattice gas) model were considered. To this end, the droplets' transition from cubic to spherical

[6] Note that $\gamma_{vl}$ is also equal, since CNT just takes the value for flat walls, while the interface of a cubic droplet consists of flat walls by definition.

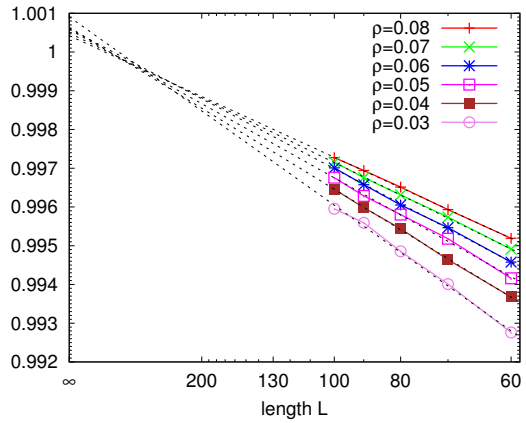


(a) $k_{\mathrm{B}}T/J = 2.0$

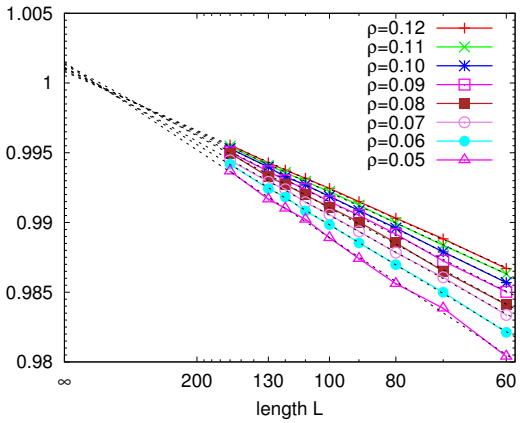


(b) $k_{\mathrm{B}}T/J = 2.6$

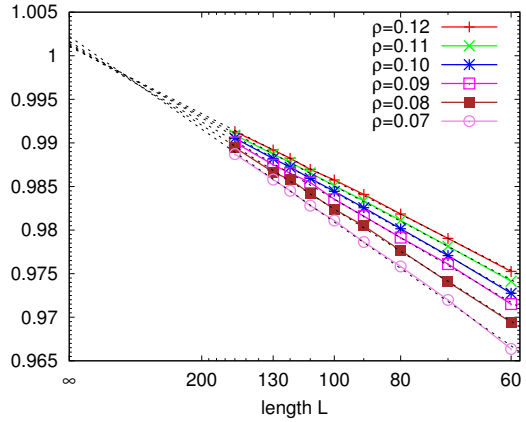


(c) $k_{\mathrm{B}}T/J = 3.0$

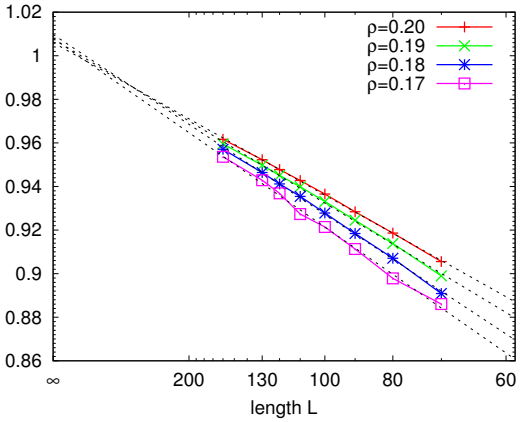


(d) $k_{\mathrm{B}}T/J = 4.0$

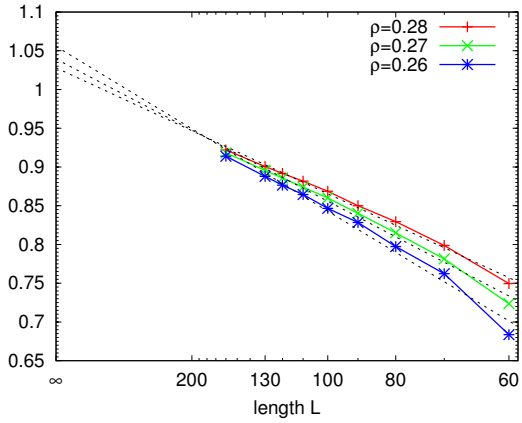


(e) $k_{\mathrm{B}}T/J = 4.3$

Figure 3.9: Finite-size scaling of the ratio $V_{\mathrm{phys}}/V_{\mathrm{LR}}$ against $1/L$ for various densities and temperatures. The volumes are computed using (3.11) and (3.14). The densities are chosen to be in the range where the droplet is not aware of the finiteness of the box, as explained in section 2.2.2. The extrapolation is not perfect due to the fact both $V_{\mathrm{phys}}$ and $V_{\mathrm{LR}}$ suffer from statistical errors in the estimation of $\varrho_l$ and $\Delta\mu$.

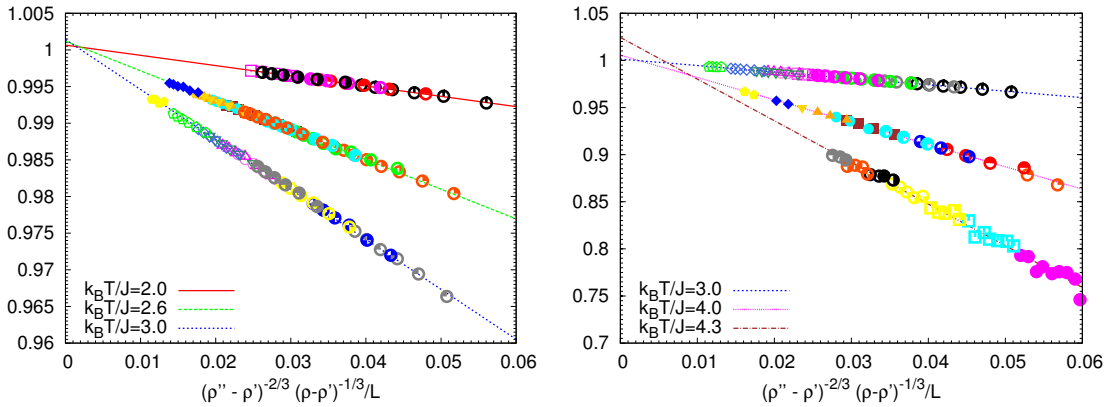


(a) $k_{\mathrm{B}}T/J = 2.0, 2.6, 3.0$ (b) $k_{\mathrm{B}}T/J = 3.0, 4.0, 4.3$

Figure 3.10: Plot of $V_{\mathrm{LR,\,exc}}/V_{\mathrm{LR}}$ versus $(\varrho_l - \varrho_g)^{-2/3}(\varrho - \varrho_g)^{-1/3}$ in order to test (3.25). All data from Fig. 3.9 is also used here, each density $\varrho$ is shown with a separate color. Linear fits to the data are included.

shapes were discussed (Fig. 3.1). It was shown that droplets below the roughening transition have facets, while droplets at high temperatures are perfectly spherical. However, although the facets disappear at the roughening temperature $T_R$, the droplets are round but not spherical at intermediate temperatures, giving rise to an enhanced nucleation barrier (Fig. 3.8). The enhancement of the free energy barrier due to the anisotropy of the droplet shape was discussed in detail. It was shown that the correction due to the non-spherical shape vanishes near the critical point but rises gradually with decreasing temperature and growing steeply below the roughening temperature to reach $6/\pi$ for $T \to 0$. The enhancement at the temperature $k_{\mathrm{B}}T/J = 0.6$, commonly used in the literature, is about 10% and should therefore not be ignored.

While the droplet shape changes from cube to sphere with increasing temperature, the interfacial width increases, making the distinction between lattice sites belonging to the droplet or the environment a delicate matter. An increase of the interfacial width with the size of the droplet was also discovered (Fig. 3.2(d)), which is compatible with the prediction for planar interfaces.

The problem of properly defining droplets in the Ising model was also discussed thoroughly. There has been much work about nucleation in the Ising (lattice gas) model, but it was often inconclusive due to the use of geometrical clusters. In this chapter, evidence was presented that this cluster definition fails at commonly studied temperatures and should therefore be avoided (Fig. 3.7). At low temperatures, the geometrical and physical clusters coincide, but the temperature range below the

roughening temperature is not attractive for the study of nucleation phenomena because of the anisotropy effects (Fig. 3.1). At intermediate temperatures just above the roughening transition, the overestimation ranges from 1 to 3%, even in the thermodynamic limit. In the temperature range where droplets are found to be spherical, i.e. above $k_{\mathrm{B}}T/J = 3.8$, the geometrical clusters overestimate the size of droplets dramatically because of the percolation transition (Fig. 3.5). In contrast, the physical droplet definition leads to consistent results with the lever rule method if applied to macroscopic droplets in a homogeneous surrounding, although there is an unexpected surface excess in the particle number (Fig. 3.10).

All these considerations can also be carried out in $d = 2$ dimensions, where both the lever rule method and the physical droplet definition can be carried over literally. Note that the roughening temperature in two dimensions is $k_{\mathrm{B}}T_R/J = 0$, which means that the transition from a circular shape to a square occurs without any singularity. However, the overestimation of the geometrical droplet definition will be similar to the three-dimensional case.

An extension of the physical droplet definition to off-lattice systems is very desirable, but it is unknown to date how to extend (3.13) to continuous models.

# Chapter 4

# The Ensemble Switch Method

In this chapter, the ensemble switch method, which has been used in the past [Deb et al., 2011, 2012a,b] to compute wall tensions between colloidal systems and various walls , is extended to be able to compute interfacial tensions. After a short introduction about the difficulties of computing interfacial tensions for solid-liquid interfaces [sections 4.1 and 4.2], the ensemble switch method is presented in section 4.3. The ensuing sections are devoted to discussions of the results and their interpretation for liquid-vapor interfaces [section 4.4] and solid-liquid interfaces [section 4.5].

## 4.1 Introduction

The interfacial tension plays a central role in condensed matter and materials science. Not only does it determine the shape of nuclei as shown in section 3.2 and is a central ingredient to classical nucleation theory [cf. section 2.4], but also in many other areas where interfaces occur: nucleation of liquid droplets in an oversaturated vapor [e.g. in the atmosphere [Kashchiev, 2000; Balibar and Villain, 2006]], formation of nematic or smectic droplets in fluids which can form liquid crystal phases, nucleation of ferroelectric or ferromagnetic domains, mesophases of strongly segregated block copolymers [Hamley, 1998], hadron condensation from the quark-gluon plasma [Meyer-Ortmanns, 1996], nanosystems [Dietrich et al., 2013], wetting phenomena [Domb and Lebowitz, 1988; Bonn and Ross, 2001; de Gennes et al., 2003], stable heterogeneous structures, and many other applications in biological systems. These phenomena are fascinating problems of statistical mechanics and have important applications (in nanoscopic devices, materials science of thin films and surfactant layers (e.g. [Narayanan, 2008]), extracting oil and gas from porous rocks [Gelb et al., 1999], etc.).

Since it is difficult to measure interfacial tensions in experiment, computer simulations are the means of choice to determine them. Over the years, a variety of methods came into existence, each having some advantages and drawbacks. Mean-field-type approaches are widely used [Cahn and Hilliard, 1958; Evans, 1979; Oxtoby, 1992; Bier et al., 2005] but build upon arguable assumptions: A necessary input is the free-energy density of homogeneous states in the two-phase coexistence region [Binder et al., 2012]. Such a concept is only valid for long-range forces and not well-defined in the short-range case [Lebowitz and Penrose, 1966; Penrose and Lebowitz, 1971; Langer, 1974; Binder, 1984, 1987; Puri and Wadhavan, 2009]. Furthermore the existence of a well-defined "intrinsic interfacial profile" is doubted[1]. Mean-field-type theories are able to simulate bulk phase behavior, they face severe problems when studying interfaces: Interfaces have fluctuations on all length scales, and the short wavelength spectrum interferes with bulk fluctuations in a non-trivial way. The long-wavelength part of the spectrum, however, can be accounted for by the concept of capillary waves [cf. section 2.5], but a cutoff wavelength has to be introduced, the physical significance of which is not clear.

In the case of a liquid-vapor coexistence, some methods are able to produce satisfactory results with reasonable computational effort, but for crystal-liquid coexistence, there are merely rough estimates which do not agree within their respective error bars. The reason might be that the finite-size scaling of the methods has not been discussed thoroughly enough [see chapter 5].

## 4.2 An Overview of existing Methods to compute the Interfacial Tension

There exists a number of methods to compute the interfacial tension. In the case of vapor-liquid interfacial tensions, many of these methods yield reliable results. For the crystal-fluid interface of hard spheres, however, the methods are not applicable or disagree with each other. This subsection provides an overview over some of the methods, making no claim to be complete. Table 4.1 shows results for hard sphere interfaces from various methods. It is striking to see that they contradict each other by several standard deviations. To give a better impression of the challenge, Fig. 4.1 shows the results from Table 4.1 versus time. It is obvious that computing the interfacial tension for hard spheres is a major open problem.

[1] See for example the article of B. Widom in [Domb and Green, 1972] and also [Jasnow, 1984; Binder et al., 2011] for further remarks.

| source | method | $\beta\sigma^2\gamma_{100}$ | $\beta\sigma^2\gamma_{110}$ | $\beta\sigma^2\gamma_{111}$ |
|---|---|---|---|---|
| [Davidchack and Laird, 2000] | MD-C | 0.62(1) | 0.64(1) | 0.58(1) |
| [Mu et al., 2005] | MC-CWT | 0.64(2) | 0.62(2) | 0.61(2) |
| [Davidchack and Laird, 2005] | MD-C | 0.592(7) | 0.571(6) | 0.557(7) |
| [Davidchack et al., 2006] | MD-C | 0.574(17) | 0.557(7) | 0.546(16) |
| [Davidchack, 2010] | MD-C | 0.5820(19) | 0.5590(20) | 0.5416(31) |
| [Härtel et al., 2012] | DFT | 0.687(1) | 0.665(1) | 0.636(1) |
| [Härtel et al., 2012] | MC-CWT | 0.639(11) | 0.616(11) | 0.600(11) |
| [Fernandez et al., 2012] | MC-T | 0.636(11) | | |

Table 4.1: Collection of interfacial tensions computed by various methods. $\beta = 1/(k_\mathrm{B}T)$ is the inverse temperature and $\sigma$ the hard sphere diameter. MD-C stands for molecular dynamics using the cleaving method (see below), MC-CWT stands for Monte Carlo simulations with an analysis of the capillary wave spectrum (see below). DFT is the abbreviation for density functional theory and MC-T stands for "tethered" Monte Carlo, which is a recent approach. This is of course not a comprehensive list of results for hard spheres.

### 4.2.1 The Probability Distribution Method

The probability distribution method [Binder, 1982] is one of the most commonly used techniques to compute the interfacial tension of liquid-vapor interfaces. We first describe it for the Ising model, where the relevant distribution is the distribution of the magnetization $m$. Recall that there is a one-to-one correspondence between the Ising model and the lattice gas model, where the magnetization corresponds to the density of particles [cf. section 2.2.1]. The method makes use of the fact that one can measure the probability $P_L$ of homogeneous states $m = \pm m_\mathrm{coex}$ and heterogeneous states $m = 0$ with two planar interfaces via Monte Carlo simulations (e.g. using multicanonical sampling, see section 2.7.1). Here, we consider a $d$-dimensional system with linear dimension $L$ of the (hyper-)cubic simulation box and periodic boundary conditions in all directions. The treatment sketched below refers to Ising models (or other systems in the Ising universality class with a symmetry between the coexisting phases).

The method makes use of the fact that the free energy can be written in terms of the probability distribution $\ln P_L(m) = -\beta F(m)$ and that the states at $m = 0$ and $m = \pm m_\mathrm{coex}$ differ only by the presence and absence of two interfaces [see Fig. 4.2], so that

$$\ln\left(\frac{P_L(m_\mathrm{coex})}{P_L(0)}\right) = \beta F(0) - \beta F(m_\mathrm{coex}) = 2L^{d-1}\beta\gamma_L \,, \tag{4.1}$$

where $\gamma_L$ is the interfacial tension and $2L^{d-1}$ is the interfacial area in a box with a

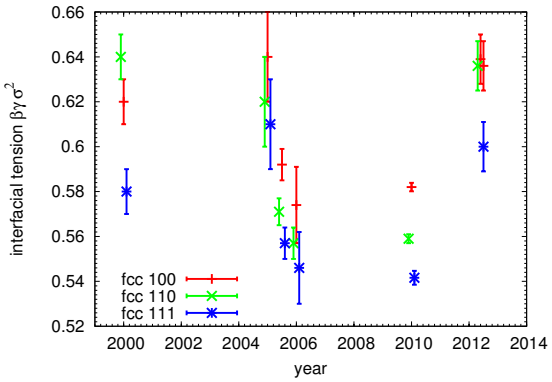


Figure 4.1: Graphical overview of some selected results since the year 2000 for computer simulations to determine the interfacial tension of hard sphere crystal-fluid interfaces, for three different orientations of the fcc crystal.

slab geometry. The interfacial tension in the thermodynamic limit can be obtained via

$$\beta\gamma = \lim_{L\to\infty} \frac{1}{2L^{d-1}} \ln\left(\frac{P_L(m_{\text{coex}})}{P_L(0)}\right) \tag{4.2}$$

Note that $P_L(m_{\text{coex}})$ depends on the box geometry, for in the vicinity of the maxima, $P_L(m)$ can be expressed by a Gaussian

$$P_L(m) = \frac{1}{\sqrt{2\pi\sigma_\varrho^2}} \exp\left(-\frac{1}{2}\frac{(m-\langle m\rangle)^2}{\sigma_\varrho^2}\right) \qquad \sigma^2 = \frac{k_{\text{B}}T\chi_{\text{coex}}}{L^d}\,, \tag{4.3}$$

where $\langle m\rangle = \pm m_{\text{coex}}$. Therefore, $P_L(m_{\text{coex}}) \propto L^{d/2}$.

Although this method to estimate the interfacial tension works extremely well in the Ising model and has also been applied to Lennard-Jones fluid-vapor coexistence with success (see e.g. [Hunter III and Reinhardt, 1995; Potoff and Panagiotopoulos, 2000]), it cannot straightforwardly be used to calculate solid-liquid interfacial tensions.

Alternatively to (4.2), one can obtain the interfacial tension via another limiting process, namely [Binder, 1982]

$$\beta\gamma = \lim_{L\to\infty} \frac{1}{2L^{d-1}} \ln\left(\frac{1}{P_L(0)}\right)\,. \tag{4.4}$$

Here, the dependence of $P_L(m_{\text{coex}})$ can be avoided altogether.

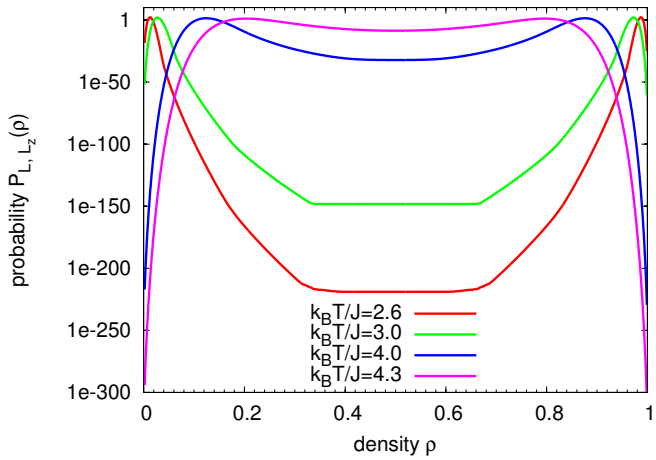


Figure 4.2: Probability distribution of an Ising model for $d = 3$ with $L = 20 = L_z$ and various temperatures as indicated. At low temperatures, the heterogeneous states ($\varrho = 0.5$) are strongly suppressed. One can also see kinks, where the chemical potential has a discontinuity in the limit $L \to \infty$. In a finite system, the discontinuities are smeared out, hence the kinks are slightly rounded (for more information cf. section 2.2.2). The probability ratio between the minimum at $\varrho = 0.5$ and the maxima can be used to measure the interfacial tension.

### 4.2.2 Pressure Anisotropy

If one can compute the pressure of a system, e.g. using the virial expression (2.83) or other methods, the interfacial tension can be derived from the anisotropy of the pressure tensor across an interface [Tolman, 1948; Walton et al., 1983; Frenkel and Smit, 2001].

In a homogeneous fluid at equilibrium, the pressure components in all directions must be equal. If one considers an inhomogeneous system which contains interfaces, then the pressure $p_z$ normal to the interfaces must be constant for the system to be stable. The tangential components $p_x, p_y$, however, which are equal to $p_z$ in the bulk, change near the interfaces. It can be shown [Tolman, 1948; Walton et al., 1983], that the interfacial tension can be computed by integrating the pressure difference between the normal pressure $p_z$ and the tangential pressure $p_t = (p_x + p_y)/2$ through the system

$$\beta\gamma = \frac{\beta}{2} \int_{-L_z/2}^{L_z/2} \mathrm{d}z \, [p_z(z) - p_t(z)] \ . \tag{4.5}$$

The factor 1/2 arises from the fact that one usually has two interfaces in a box with periodic boundary conditions. Unfortunately, the definition of $p_x(z), p_y(z), p_z(z)$ is

ambiguous, and different definitions lead to slightly but significantly different results [Walton et al., 1983]. Fortunately, the above expression (4.5) for $\gamma$ does not suffer from this, since it actually reduces to

$$\beta\gamma = \frac{\beta L_z}{2}\left(P_z - P_t\right) \tag{4.6}$$

so that one only needs the components of the total pressure $\boldsymbol{P}$.

To calculate $p_x(z), p_y(z), p_z(z)$, one divides the system into $b$ slabs perpendicular to the interfaces. Assuming a pair potential $U(r)$ which only depends on the distance $r$ between the particles, the pressure components in each slab $k$ can be calculated by

$$p_\alpha(k) = k_\mathrm{B}T\langle\varrho(k)\rangle - \frac{1}{V(k)}\left\langle \sum_{(ij)\in k} U'(r_{ij})\frac{\alpha_{ij}^2}{r_{ij}} \right\rangle \tag{4.7}$$

with $\alpha = x, y, z$ and $k = 1, \ldots, b$. The sum runs over all pairs $(ij)$ of particles belonging to the slab $k$, i.e. if the line connecting the two particles is partially or completely within the slab. To get the correct pressure, one has to divide the contribution to the pressure by the number of slabs, the line intersects, e.g. if both particles are in the same slab, the slab gets the full contribution, while if there is a slab between the particles' slab, then each slab gets one third of the contribution. This follows the Kirkwood-Buff convention [Nijmeijer et al., 1988], but there are also other sensible conventions[2].

The disadvantage of this method is that it cannot be applied straightforwardly to discontinuous potentials like hard spheres or the AO model. The technique also becomes difficult to apply for vapor-liquid interfaces near criticality because then the signal to noise ratio is very unfavorable.

### 4.2.3 Thermodynamic Integration with cleaving Potentials

Based on the cleaving method of Broughton and Gilmer [Broughton and Gilmer, 1986], Davidchack computes the interfacial tension of hard sphere coexisting phases using molecular dynamics simulations [Davidchack and Laird, 2003]. The idea is to use cleaving potentials to perform a reversible integration from a system with two separated boxes to a system with one box and two coexisting phases with an interface. Instead of "real" hard spheres, they use a potential

$$u(r) = \varepsilon\left(\frac{\sigma}{r}\right)^n \tag{4.8}$$

[2]For a comparison of two conventions, see e.g. [Walton et al., 1983].

where $\sigma$ is the hard sphere diameter and $\varepsilon$ defines the energy scale. Obviously, for $n \to \infty$ this potential approaches the hard-sphere limit. The procedure to compute $\gamma$ consists of four steps:

1. Start with a crystal with some orientation in a box with periodic boundary conditions in all directions. Set up an external cleaving potential and move it gradually into the box. After this step, the periodic boundary condition in one direction is replaced by the cleaving potential, for the particles cannot traverse the cleaving potential.

2. Equilibrate a fluid in a box. Then use the same cleaving potential as for the crystal and move it into the box.

3. Combine the two boxes and replace the boundary conditions of the separate boxes by periodic boundary conditions for the combined box. The two phases are then still separated by the cleaving potentials, so there is no interface yet.

4. Gradually move the cleaving potentials out of the two boxes, thereby allowing contact between the phases.

The interfacial tension $\gamma$ is the sum of free energy differences of these 4 steps divided by the total area of interfaces.

To apply this method to hard-sphere-like systems [Davidchack and Laird, 2005], one has to replace the cleaving potentials by cleaving walls, which consist of particles arranged in the crystal structure corresponding to the crystal in the system. Instead of increasing the intensity of the potential, the walls are set up a certain distance $z_i$ outside the box and then slowly moved into the box to $z_f$.

There are some challenges in this approach. First, one works at finite $n$ and has to extrapolate to the hard-sphere case. Furthermore, the cleaving potentials have to be chosen very carefully. They induce crystalline layers to the liquid in step 2 and prohibit contact of the two phases during step 3. Step 2 is a great source of hysteresis. In order to reduce it, the box containing the fluid is first stretched to decrease the density below coexistence density, before step 2 is executed. After step 2, the box is compressed again. These additional steps help to decrease hysteresis. Alternatively to this stretching and compressing, one can introduce a well potential to decrease the density only near the cleaving walls [Davidchack, 2010].

Another problem in this approach is that the translational freedom of the interface is suppressed. If the interface moves "too far" away from the initial position, the whole run is thrown away, which usually happens for 10 to 60% of the simulation runs. Apart from the wasted simulation time, there is some undesirable arbitrariness

in what "too far away" means. Also, there is no finite-size scaling done. Instead, a rather large system (15000 to 30000 particles) is considered and it is claimed that this is sufficiently large to compute the value of the interfacial tension in the thermodynamic limit.

### 4.2.4 Capillary Wave Spectrum

An introduction to capillary wave theory (CWT) can be found in section 2.5. Here, we briefly discuss how the interfacial tension $\gamma$ can be obtained from the capillary wave spectrum.

In capillary wave theory, the interface is represented by a function $h(\boldsymbol{x}) = z(x, y) - \langle z(x, y)\rangle$, describing the distance of the local interface to the equilibrium position. It is more convenient to work with the Fourier transform of $h(\boldsymbol{x})$, which is given by

$$h_{\boldsymbol{q}} = \sum_{\boldsymbol{q}} h(\boldsymbol{x}) \mathrm{e}^{\mathrm{i}\boldsymbol{q}\cdot\boldsymbol{x}} \tag{4.9}$$

where $\boldsymbol{q} = (q_x, q_y)^\top$ is the two-dimensional wave vector. In the long-wavelength limit, CWT can relate the interfacial stiffness $\kappa$ to the height fluctuation spectrum

$$\langle h_{\boldsymbol{q}}^2 \rangle = \frac{k_\mathrm{B}T}{L^2 q^2 \kappa} \,. \tag{4.10}$$

Therefore one can compute the interfacial stiffness from simulations [Weeks, 1977] by conducting a numerical Fourier transform of the height profile $h(\boldsymbol{x})$ and use (4.10). This was used in molecular dynamics simulations by [Hoyt et al., 2001; Rozas and Horbach, 2011] to determine the interfacial tension of nickel. Alternatively, one can measure the interfacial width and use [cf. (2.62)]

$$\langle w^2 \rangle = w_0^2 + \frac{1}{4\beta\kappa} \ln(L/\lambda_{\min}) \tag{4.11}$$

This is however only possible if the interfacial stiffness is isotropic in the directions parallel to the surface. This method has been used in [Rozas and Horbach, 2011] and also in [Zykova-Timan et al., 2010] for the study of the effective AO model.

## 4.3 Description of the Ensemble Switch Method

To study interfaces, it is useful to consider a cuboid simulation box of length $L_z$ and cross-section area $A = L_x L_y$, in which two coexisting phases are set up. The lengths

$L_x, L_y$ and $L_z$ are always given in units of a natural length (usually the particle diameter $\sigma$).

The interfacial tension $\gamma$ between two coexisting phases, e.g. crystal and liquid or liquid and vapor, is defined as the amount of free energy $\Delta F$ per area $A$ needed for the creation of such an interface:

$$\gamma = \frac{\Delta F}{A} \ . \tag{4.12}$$

The computation of the free energy is a complicated task, especially if crystalline structures are involved. The reason is that the free energy cannot be expressed as an average of an observable over phase space, but the free energy is a quantity depending on the phase space volume accessible to the system. Therefore, a sophisticated Monte Carlo technique is required. The idea of the ensemble switch method is to calculate the free energy difference between a reference state 0 and a final state 1 by connecting these states by a continuous path parametrized by a parameter $\kappa$. This technique has been successfully applied to compute wall tensions [Deb et al., 2012a,b].

In order to compute the interfacial tension, one proceeds as follows. State 0 ($\kappa = 0$) with Hamiltonian $\mathcal{H}_0$ consists of two separate boxes with cross-section area $A = L_x L_y$ and length $L_z/2$, each having periodic boundary conditions in all directions [cf. Fig. 4.3(a)]. Each box contains one of the coexisting phases. This geometry does not have any interfaces, for the phases are only connected to themselves and do not interact with each other. The thermodynamic integration connects these two boxes and combines them into one [Fig. 4.3(b)]. The final state ($\kappa = 1$) with Hamiltonian $\mathcal{H}_1$ consists of one box with cross-section area $A = L_x L_y$ and length $L_z$, in which the two phases are in coexistence and have thereby formed two interfaces (because of the periodic boundary conditions one always has an even number of interfaces). The free energy difference $\Delta F = F(\kappa = 1) - F(\kappa = 0)$ between the initial state and the final state is given by

$$\Delta F = (F_{\text{bulk},1} + F_{\text{bulk},2} + 2\gamma L_x L_y) - (F_{\text{bulk},1} + F_{\text{bulk},2}) = 2\gamma L_x L_y \ , \tag{4.13}$$

where $\gamma$ is the interfacial tension to be measured. The bulk contributions cancel each other in this difference if one carefully sets up the phases with coexistence properties. Hence

$$\gamma(L_x, L_y, L_z) = \frac{\Delta F(L_x, L_y, L_z)}{2L_x L_y} \ . \tag{4.14}$$

Note that the interfacial tension $\gamma(L_x, L_y, L_z)$ depends on the box dimensions. This will become important in the next chapters.

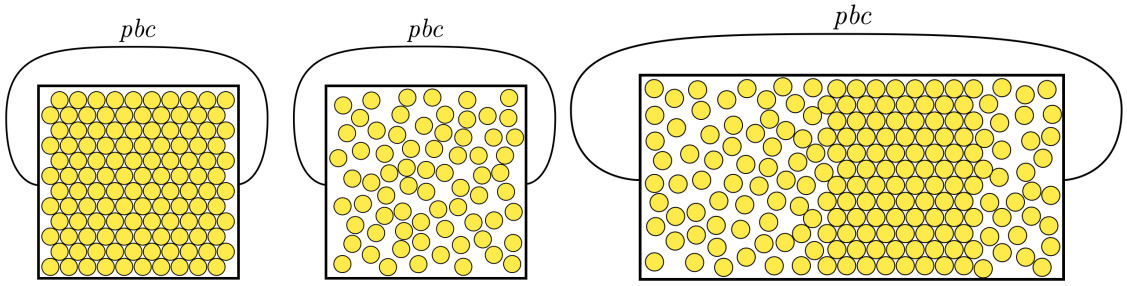


(a) $\kappa = 0$ (b) $\kappa = 1$

Figure 4.3: Schematic diagram of the initial state (a) and the final state (b). The initial state consists of two separate boxes, each filled with a homogeneous phase (in this case crystal and fluid). There are no interfaces present. In the final state, the two boxes have been connected, so that the phases are in direct coexistence and form two interfaces. The connection is achieved by continuously changing the periodic boundary conditions at the boundaries of the two boxes. The free energy difference between the initial and final state is equal to $2\gamma L_x L_y$, where $L_x L_y$ is the cross-section area of one interface.

The initial and final states have exactly the same degrees of freedom and differ only by the applied boundary conditions. For the intermediate states, it is useful to introduce a mixed Hamiltonian

$$\mathcal{H}(\kappa) = \kappa\,\mathcal{H}_1 + (1-\kappa)\,\mathcal{H}_0\ , \qquad 0 \le \kappa \le 1\ . \tag{4.15}$$

Of course, such a mixed state cannot occur in experimental setups, which is why we refer to them as "unphysical" states, but within the framework of Monte Carlo simulations, this is a perfectly valid Hamiltonian giving rise to the free energy

$$\beta F(\kappa) = -\ln\left(\mathrm{Tr}\{\exp[-\beta\,\mathcal{H}(\kappa)]\}\right) \tag{4.16}$$

where $\beta = 1/(k_\mathrm{B}T)$ is the inverse temperature. A special role in this Monte Carlo method is played by the boundaries of the two boxes which create the periodic boundary conditions in $z$-direction. From the viewpoint of the two separate boxes, there are two periodic boundary conditions, connecting the left side of each box with the right side. The two boxes are hence completely separated from each other. From the perspective of the large box, the left boundary is connected with the right boundary via periodic boundary conditions while in the center of the large box, there is boundary anymore. The two states $\kappa = 0, 1$ and their respective Hamiltonians $\mathcal{H}_0, \mathcal{H}_1$ hence differ only by their periodic boundary conditions. For the intermediate states, the energy of a particle is computed by weighting the contributions of the two viewpoints with $\kappa$ and $1-\kappa$, respectively, according to Eq. (4.15).

In order to sample the integration path efficiently, it is necessary to divide the interval $[0, 1]$ into a discrete set $\{\kappa_k\}$ of $M$ values. Then one can use successive umbrella sampling [cf. section 2.7.3] by creating a set of overlapping windows[3] $\{[\kappa_0, \kappa_1], [\kappa_1, \kappa_2], \ldots, [\kappa_{M-1}, \kappa_M]\}$. Within each window, apart from particle movements, one has to implement an additional move, which attempts to change $\kappa_k \leftrightarrow \kappa_{k+1}$. Such a move is accepted with the standard Metropolis criterion. If the internal energies $E_0, E_1$ and $E(\kappa)$ are kept up-to-date during the simulation, the computational cost of this move is completely negligible, as one only has to compute Eq. (4.15) for the new $\kappa_k$ and apply the Metropolis criterion.

The free energy difference within that window is given by $\beta\Delta F_k = \ln[P(\kappa_k)/P(\kappa_{k+1})]$ where $P(\kappa_k)$ is the probability that $\kappa = \kappa_k$ and $P(\kappa_{k+1})$ is the probability that $\kappa = \kappa_{k+1}$. The total free energy difference between the initial and final states is then given by $\Delta F = \sum_{k=0}^{M-1} \Delta F_k$. The ensemble switch method is very easy to parallelize. Since each window can be treated separately, one can use $M$ cores to sample the whole integration path at the same time[4].

Another means to improve the results is to choose the set $\{\kappa_k\}$ so that the step within a window is smaller where necessary and larger elsewhere. Since most of the interesting physics takes place near $\kappa = 0$ and $\kappa = 1$, one can obtain better results by choosing

$$\kappa_k = \sin^2\left(\frac{\pi k}{2M}\right) \tag{4.17a}$$

$$\kappa_k = \begin{cases} \frac{(2k/M)^a}{2} & k < M/2 \\ 1 - \frac{[2(1-k/M)]^a}{2} & k \geq M/2 \end{cases}, \tag{4.17b}$$

or something with a similar shape. The parameter $a$ changes the shape of (4.17b) from a linear shape ($a = 1$) to the extreme case of a step function ($a \to \infty$). We found $a = 6$ to be useful for the crystal-liquid case. As we will switch between $\kappa$ and $k/M$ where appropriate, please note that in this work, the parametrization Eq. (4.17a) will be used for the liquid-vapor case discussed in section 4.4, chapter 5 and section 6.1, while Eq. (4.17b) will be used for the solid-liquid case in sections 4.5 and 6.2. One important aspect is that the pair potential between the particles should be bounded. If the pair potential diverges, the transition from $\kappa = 0$ to $\kappa > 0$ is rejected if there is only one overlap created by mixing the boundary conditions. As this is virtually always the case, there is no way to smoothly combine the two boxes.

[3] Each window contains only two values of $\kappa$ here. It is also possible to use larger windows, but the statistical error depends on the statistics of the least probable state of the window, so that the results are not guaranteed to be better if using larger windows.

[4] Initially, one can perform a run on one core over the whole range of $\kappa$ and write out the equilibrated configurations, which are then used to sample all windows at once.

If the potential is bounded at some high value, so that the bulk properties only have a negligible difference compared to the original model, the results do not depend on this boundary. The question whether this has any effect on the results will be postponed to later in this chapter, namely section 4.5.

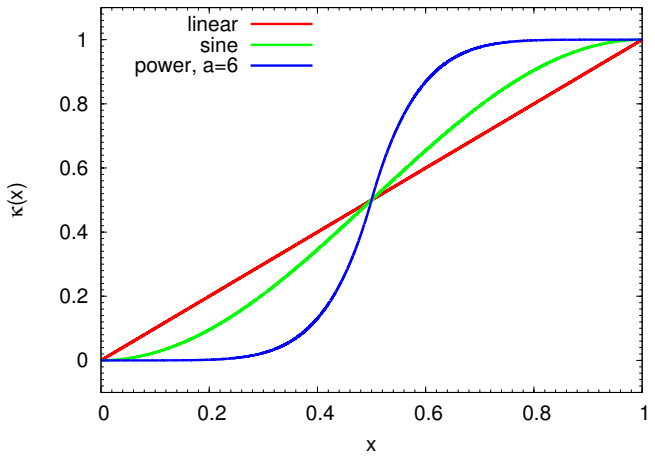


Figure 4.4: Some choices for the mapping $k \to \kappa_k$. Instead of a linear mapping, one can make smaller windows where more accuracy is needed. The curve labeled sine shows Eq. (4.17a) while the curve labeled power shows Eq. (4.17b) with $a = 6$. Both functions have smaller steps near 0 and 1, while the step size is larger near $x = k/M = 0.5$.

The particle movements can be local canonical moves, where an attempt is made to move a particle to a position within some small volume around it, or nonlocal moves, where the new particle position can be everywhere in the box. Although the latter moves typically have a much lower acceptance probability, the autocorrelation of successive configurations is much smaller, as one virtually traverses the phase space with seven-league boots. However, in systems with high density, the acceptance probability of nonlocal moves goes to zero and one has to use local moves. This applies to solid-liquid coexistence in particular.

Furthermore, the particles must be able to move anywhere in the whole simulation box. Then, one still has a physically well-defined state at $\kappa = 0$, corresponding to a "Gibbs ensemble like" ensemble [Frenkel and Smit, 2001], although the boxes containing homogeneous phases may exchange particles. On the contrary, if one prohibits any particle exchange between the two boxes, which will obviously fix the interfaces created during the thermodynamic integration to the volume where the two boxes are connected, then the results will be systematically wrong because the interfaces created are unphysical, as their capillary waves and other fluctuations are

suppressed. Furthermore, the chemical potential can have a gradient, which does not occur if one allows an exchange of particles between the two boxes. To test this, one can measure the chemical potential using the method discussed in section 2.6.4.

## 4.4 Liquid-Vapor Interfaces

In this section, we will discuss the results of the ensemble switch method using a variant of the well-known Lennard-Jones fluid [cf. section 2.3.1]. We modify the potential so that it does not exceed $\varepsilon_0 = 100\ k_\mathrm{B}T$. This modification hardly changes the bulk properties of the particles, as the probability for two particles to approach each other is proportional to $\mathrm{e}^{-100}$. The potential is therefore given by

$$U(r) = \begin{cases} \varepsilon_0 & , r < r_\mathrm{core} \\ 4\varepsilon \left[ \left(\frac{\sigma}{r}\right)^{12} - \left(\frac{\sigma}{r}\right)^{6} + Y \right] & , r_\mathrm{core} \leq r < r_\mathrm{cut} \\ 0 & , r > r_\mathrm{cut} \end{cases} \tag{4.18}$$

The radius $r_\mathrm{core}$ is determined by $U(r_\mathrm{core}) = \varepsilon_0$, making the potential continuous. The explicit formula for this radius is given by

$$r_\mathrm{core} = \left( 1 + \sqrt{k_\mathrm{B}T\varepsilon_0 + \left[ 1 - \frac{2\sigma^6}{r_\mathrm{cut}^6} \right]^2} \right)^{-1/6} 2^{1/6}\sigma \ . \tag{4.19}$$

The critical temperature of this model is $k_\mathrm{B}T_c/\varepsilon = 0.999$, [Virnau, 2003]. Below this temperature, a phase separation into a denser phase called liquid and a less dense phase called gas takes place. In the following, we fix the temperature at $k_\mathrm{B}T/\varepsilon = 0.78$ and set $\varepsilon$ to unity. Furthermore, the particle diameter $\sigma$ is set to unity and the box dimensions $L, L_z$ are given in units of $\sigma$. At the chosen temperature, the coexistence densities for the liquid and vaporous phase are $\varrho_l = 0.706$ and $\varrho_g = 0.027$.

Figure 4.5 shows a typical result for $\Delta F(\kappa) = F(\kappa) - F(\kappa = 0)$ as a function of the index $k$, divided by the number of successive umbrella windows $M = 1024$. Following the integration path from $k/M = 0$, the free energy difference increases until a maximum is reached at about $k/M = 0.7$. Then the free energy decreases again to reach the final value. The curve starts with vanishing slope from the initial state and ends the same way at $\kappa = 1$. This is due to the choice of the set $\{\kappa_i\}$ according to Eq. (4.17a), which increases the number of windows near both ends of the curve.

At first glance, one could ask why the curves are non-monotonic, for according to the interpretation of thermodynamic integration, the two interfaces are continuously formed while $\kappa$ goes from 0 to 1. This maximum can be understood if one considers

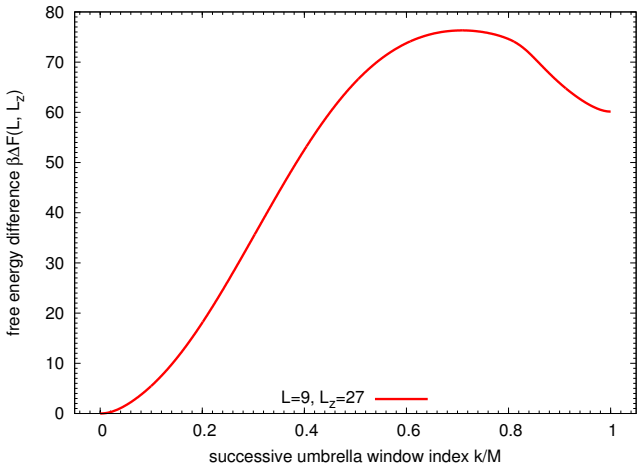


Figure 4.5: Free energy $\Delta F(\kappa)$ versus $\kappa$ for the Lennard-Jones model introduced above. The box dimensions are $L = 9$ and $L_z = 27$.

filling both boxes at $\kappa = 0$ with the same phase, e.g. a liquid. Then, during the thermodynamic integration there are no interfaces introduced and the free energy difference between the initial and final state should be zero. Figure 4.6(a) shows what happens if one brings equal phases together. As expected, the free energy difference between the two states of interest is zero, but for the intermediate states, the free energy rises to about 75 $k_{\mathrm{B}}T$.

To understand this, it is interesting to look at density profiles at the boundary regions, i.e. the vicinity of the boundaries where the two boxes are joint. Figure 4.6(b) shows the density profile for various states during the thermodynamic integration, averaged over a number of configurations. At $k = 0$, the boxes are completely disjoint and therefore the density profile is completely flat. As soon as they are brought into contact, the particles begin to avoid the volume between the two boxes. This effect is strongest exactly at $k/M = 1/2$. At the same time, the density profile shows a layering behavior.

These two effects originate from the fact that particles in the boundary region face an interpolation of two independent configurations. On the one hand, they interact with particles on the other side of their respective box, via the periodic boundary condition, and on the other hand they interact with the particles at the border of the other box. If one particle aligns according to one boundary condition, its position is most likely energetically unfavorable with respect to the other boundary condition. Therefore, to minimize their energy, particles tend to avoid this volume altogether and instead form layers next to it. According to Eq. (4.15), this behavior

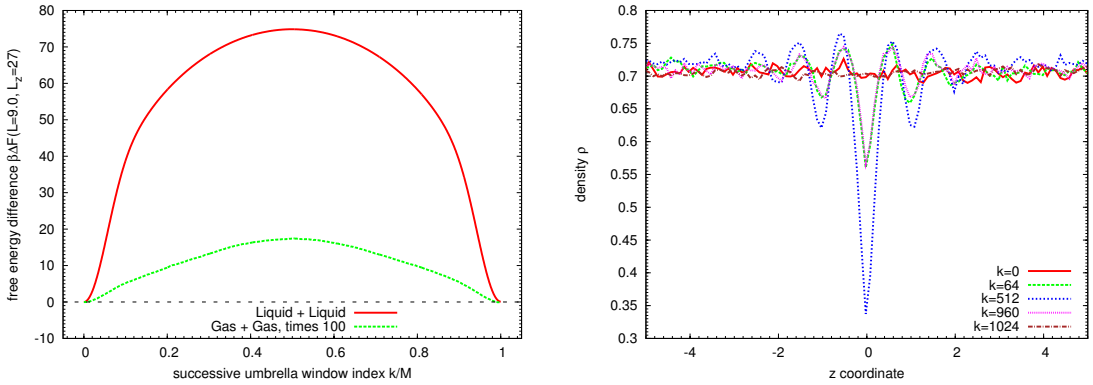


(a) (b)

Figure 4.6: (a) Free energy $\Delta F(\kappa)$ versus $\kappa$ for a liquid-liquid coexistence and a gas-gas coexistence ($L = 9, L_z = 27$). In both cases, $\Delta F = 0$ as expected. Note that the gas-gas curve is magnified by 100. The maxima are at 0.017 $k_\mathrm{B}T$ for the gas-gas case and 75 $k_\mathrm{B}T$ for the liquid-liquid case. The curves are perfectly symmetrical around $k/M = 1/2$. (b) Density profiles for the liquid-liquid coexistence ($L = 9, L_z = 27$) at various $k$, as indicated ($L = 9, L_z = 27$). For $0 < k/M < 1$, there are depletion zones around the boundary region where the two boxes are connected. This depletion is most pronounced exactly at $k/M = 1/2$ and vanishes for $\kappa \to 0$ or $\kappa \to 1$, where the density is homogeneous in the whole system.

is expected to be maximal at $\kappa = 0.5$, where both kinds of interactions have equally strong weight. Therefore, the magnitude of the depletion zone is highest at this point. After the maximum, these effects diminish symmetrically, so that the density profile looks the same at $\kappa$ and $1 - \kappa$. At $\kappa = 1$, the thermodynamic integration is complete and any effect of this depletion is gone. This shows that the integration path between two physical states via "unphysical" states is meaningful. Figure 4.7 illustrates with snapshots how the systems look like at various $k/M$. One can clearly see the depletion zone in the snapshot near $\kappa = 0.5$.

Now we return to the case where one box contains a liquid and the other vapor. Fig. 4.8 shows the corresponding density profiles. Note that only the right half of the whole simulation box is shown, containing one of the two boundaries[5] in the center. At $k/M = 0$, the density in both boxes is completely flat. As the thermodynamic integration proceeds to $k/M = 0.375$, the two phases begin to interact. While the density of the liquid decreases at the boundary similarly to the liquid-liquid case,

[5]Recall that from the viewpoint of the small boxes ($\kappa = 0$), there are periodic boundary conditions at the boundaries so that the two boxes do not interact. For $\kappa > 0$, particles can interact across the boundaries with the particles in the other box.

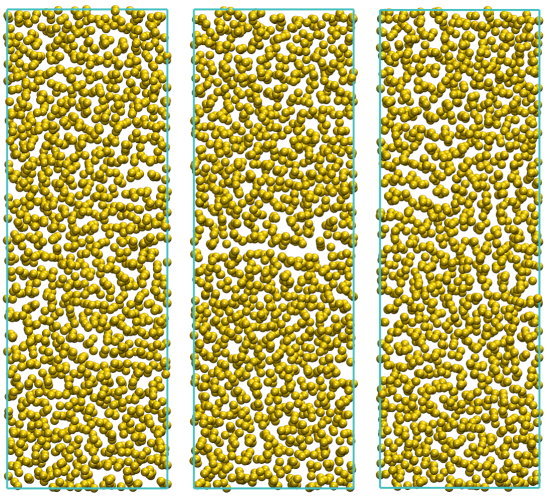

Figure 4.7: Snapshots of the liquid-liquid coexistence at $k/M = 1/1024$ (left), $k/M = 507/1024$ (center) and $k/M = 1023/1024$ (right). While particles can penetrate each other near the boundary at $k/M = 0$ (because there is no interaction across the boundaries at $\kappa = 0$), they are repelled by a frustration effect for $0 < \kappa < 1$, which is strongest at $\kappa = 0.5$. For $k/M \to 1$, the system becomes homogeneous again.

the density of the vapor increases in the vicinity of the boundary. As soon as the density becomes continuous, the interface is fully formed, which takes place at about $k/M = 0.8$.

The fact that the depletion effect is explicitly seen on the liquid side in the liquid-vapor case gives further confidence that the formation of depletion zones is an additional effect during the thermodynamic integration, which does not influence the total free energy $F(\kappa = 1) - F(\kappa = 0)$. To further analyze the behavior of the system during the thermodynamic integration, Fig. 4.9 documents the behavior of the pressure and the chemical potential along the integration path. Since these quantities are typically inaccessible in systems involving crystalline structures, it is illuminating to study the effects of the mixing of boundary conditions during the thermodynamic integration on these quantities for the liquid-vapor case. For the chemical potential, the Widom particle insertion method is applied [cf. section 2.6.4], while the pressure is evaluated using a virial expression [cf. section 2.6.5]. Note that for $P_z$ and $\mu$, the absolute values at $\kappa = 0$ and $\kappa = 1$ agree, while the value for $P_x$ differs significantly. This is due to the fact that the pressure parallel to the interfaces is sensitive to the presence or absence of interfaces. Hence, the difference in $P_x$ shows that indeed, interfaces are added. This difference can be used to compute the interfacial tension [for more

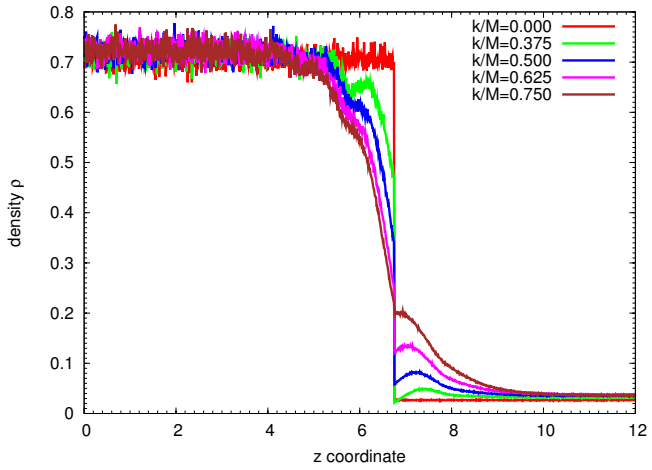


Figure 4.8: Density profiles in $z$-direction for a LJ fluid-vapor coexistence at various $k/M$, as indicated. While at $k/M = 0$ the two boxes are separated and the densities are constant, this changes as the mixing commences.

information, please refer to section 4.2].

The most striking feature about Fig. 4.9 is that the values of the chemical potential $\mu$ and the pressure $P_z$ are not constant along the path from $\kappa = 0$ to $\kappa = 1$. With the knowledge from the previous discussions about the depletion zones, this is not surprising. However, one should be concerned about whether this indicates that the method is not well-defined.

A good criterion to check the validity of the simulations is the constancy of the chemical potential in the box at a given $\kappa$. If the chemical potential is not constant, particles cannot move freely through the whole system. Therefore we proceed to measure these physical quantities with spatial resolution, in order to see whether they are constant throughout the whole system, especially in the vicinity of the interface. To this end, the system is subdivided into $N_B$ bins. In each bin, the energy $U(z)$, the density $\varrho(z)$, the pressure $\boldsymbol{P}(z)$ and the chemical potential $\mu$ are measured.

When applying the virial method for the measurement with spatial resolution, one needs to pay special attention if the particles are in different bins. As stated in [Frenkel and Smit, 2001], we count the pressure contribution of two particles into all bins containing the line connecting the two particles. Please refer to the pressure anisotropy method in section 4.2 for more information about the ambiguity of assigning the virial pressure expression between particles to bins.

Also, because it is expected that the interface moves along the $z$-direction, at least if

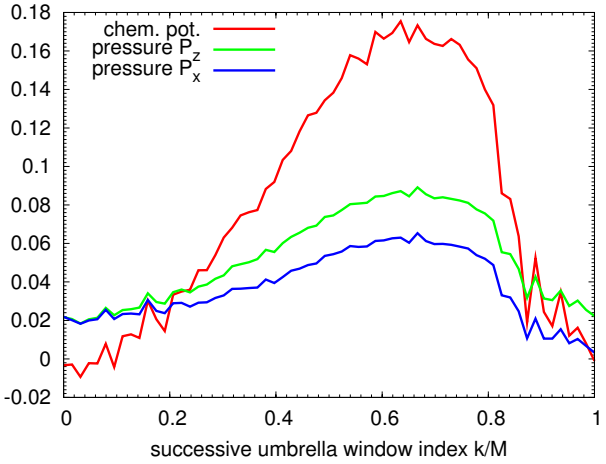


Figure 4.9: Plot of the chemical potential $\mu$ and the pressure components $P_x$ and $P_z$ versus the reaction coordinate $\kappa$. The chemical potential was measured using the Widom method (see section 2.6.4), while the pressure was calculated using the virial expression (see section 2.6.5). These observables are not constant along the integration path. It is important to note that they have the same values for $\kappa = 0$ and $\kappa = 1$. $P_x$ is an exception because it is influenced by the presence or absence of interfaces. The data shown is from a LJ vapor-fluid coexistence in a rather large box with $L = 13.5$ and $L_z = 40.4$.

$\kappa$ is close to 1, the spatial distributions are measured with respect to the center of mass of the system. This is convenient, for in most types of coexistence, the center of mass is typically in the center of the more dense phase, which can then serve as a good reference point.

Figure 4.10 shows how the chemical potential changes during the thermodynamic integration. Note that the chemical potential $\beta\Delta\mu = \beta\mu - \beta\mu_{\text{coex}}$ is plotted, where $\beta\mu_{\text{coex}} = -3.929$. At all values of $k/M$ shown, the chemical potential is constant. In fact, one cannot tell from the figure whether the liquid is on the left or on the right[6]. The whole chemical potential rises about 0.2 as $k/M$ increases and then goes back to its equilibrium value.

Having discussed this, one could expect that the Free energy differences $\Delta F(\kappa)$ seen in Fig. 4.5 are actually superpositions of two effects. On the one hand, there are two interfaces formed, which is why the free energy difference is nonzero, and on the other hand, depletion zones are reversibly created and annihilated during the thermodynamic integration. To check this, we assume that the presence of the

[6]Actually it is in the center, between -6.75 to +6.75.

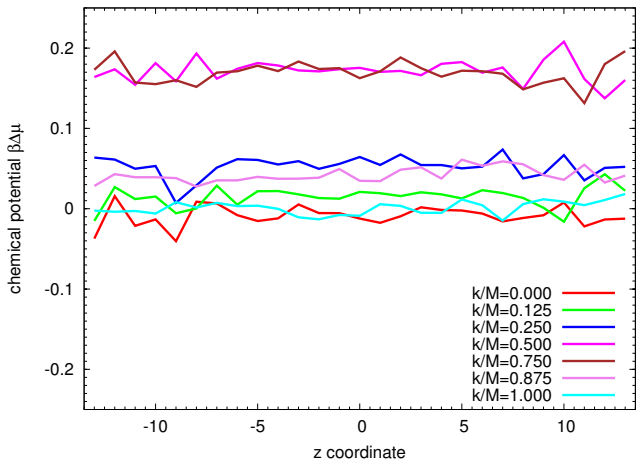


Figure 4.10: Spatial distributions of the chemical potential for a liquid-vapor coexistence of Lennard-Jones particles at temperature $k_{\mathrm{B}}T/\varepsilon = 0.78$. The box dimensions are $L = 9$ and $L_z = 27$. While the chemical potential changes along the integration path, it is spatially constant at all times. The fluctuations are of statistical nature.

interfaces is proportional to the reaction coordinate $\kappa$, so that this contribution to the free energy can be approximated as

$$\beta\Delta F_{\mathrm{interfaces}} = 2\gamma L^2 \kappa \ , \tag{4.20}$$

where the factor 2 comes from the fact that the box contains two interfaces with area $L^2$ each. If one subtracts this contribution from the free energy differences $\Delta F(\kappa)$, one obtains a curve as in Fig. 4.11.

The shape of the resulting curve labeled K1 resembles the curve from the liquid-liquid case (also shown). The height of the maximum is about one half and the position of the maximum is roughly at 0.55. The shape is not as perfectly symmetric around $\kappa = 0.5$ as in the liquid-liquid case, but it shows that this consideration captures the main idea: The free energies $\Delta F(\kappa)$ obtained from the ensemble switch method are a superposition of two effects, namely the formation of interfaces and additionally the formation and annihilation of the depletion zones. This is the reason why the free energies $\Delta F(\kappa)$ are not monotonic.

There is another important issue when applying our method. As mentioned in section 4.3, one can use local or nonlocal canonical moves to translate particles within the box. In the following, the difficulties with local moves will be discussed. As can be shown easily, the mobility of the interfaces, which is proportional to the interfacial area $L^{-2}$, is of the order $10^2$ higher [cf. Fig. 6.3] than with local moves [if

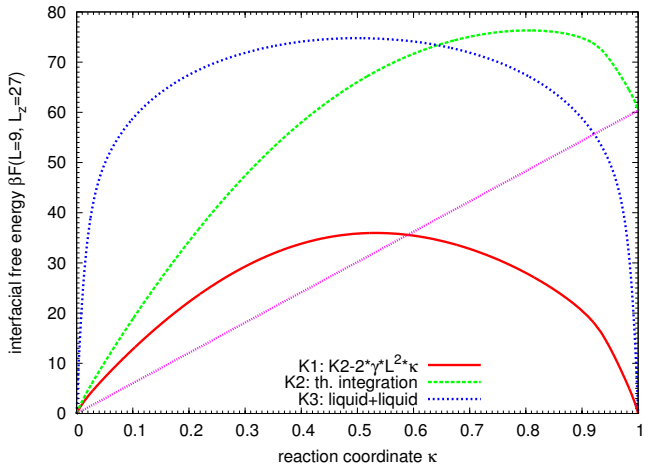


Figure 4.11: Free energy $\Delta F(\kappa)$ versus $\kappa$ for a liquid-vapor coexistence. If one subtracts a term as in Eq. (4.20) from the original curve K2, the remaining curve K1 is very similar to the liquid-liquid case K3, where the only contribution to the free energy originates from the depletion zone.

interpreting time as Monte Carlo time, where one time step is complete if one Monte Carlo step has been attempted per particle (on average)]. Therefore, the algorithm takes a lot more time to sample the relevant configurations, so that the free energies $\Delta F(\kappa)$ take more time to equilibrate. Figure 4.12 shows this for one specific case for a rather large box.

The convergence is very fast as long as the interfaces cannot move, i.e. for $k/M \leq 0.75$, or $\kappa \leq 0.85$. At some point, however, the interfaces, which are always created in the boundary region where the two boxes are connected, begin to explore the whole box volume, so that their mobility determines the speed of convergence. Therefore, this last part of $\Delta F(\kappa)$ has to be sampled with more care. These problems do not occur if nonlocal moves can be used, as Fig. 4.12 shows.

If one is restricted to local moves, e.g. when crystalline structures are involved, one is tempted to pin the interface to one position, but this can have undesirable side effects. Therefore, we do not constrain the system but let it fluctuate freely. Although this can lead to more computing time, we do not have to deal with uncontrolled effects caused by interfering with the system. See section 6.3 for some techniques to constrain or even encourage translational degrees of freedom.

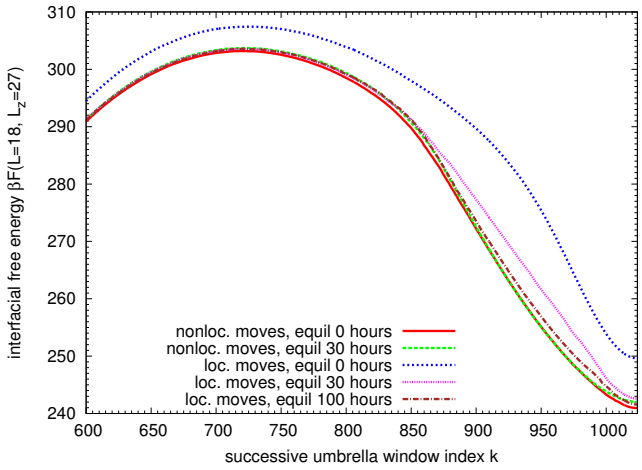


Figure 4.12: Dependence of the free energy $\Delta F(\kappa)$ on the type of particle movement and equilibration time for a system with $L = 18$ and $L_z = 27$. In case of nonlocal moves, the curve immediately equilibrates, while the local moves make the curve converge from above to the final result. This convergence is slow only in the last part of the integration, especially for $k/M > 0.75$.

## 4.5 Solid-Liquid Interfaces

In this section, a typical example of a solid-liquid interface is discussed, as it behaves slightly differently compared to the liquid-vapor case discussed in the previous section. As an example we use the well-known hard sphere model, where particles interact via the pair potential

$$U(r) = \begin{cases} \varepsilon_0 & , r \leq \sigma \\ 0 & , r > \sigma \end{cases} , \tag{4.21}$$

where $\varepsilon_0$ is the potential strength and $\sigma$ is the particle diameter. In our case $\varepsilon_0 = 100\ k_\mathrm{B}T$, whereas the original hard sphere model uses $\varepsilon_0 = \infty$. As discussed previously, this modification is necessary but does not change the initial and final states of the thermodynamic integration significantly. In this section, we will test this. The coexistence densities for the solid and fluid phase are $\eta_s = 0.545$ and $\eta_f = 0.494$ [Hunter and Weeks, 2012], where $\eta = \pi N\sigma^3/(6V)$ is the particle packing fraction. In our simulations, $\sigma = 0.902875$ while the lattice spacing is set to unity.

Note that the lengths are always given in units of the hard sphere diameter $\sigma$. To set up a crystal properly in a box with constant volume, one has to carefully adjust the box size to the crystalline structure. For example, for a fcc structure with (100) orientation, $L_x, L_y$ and $L_z$ have to be multiples of $2\sqrt{2}$. Therefore, the given

numerical values are not the actual box sizes but only rounded values. In this section, we use a medium sized box with $L_x = L_y = 6\sqrt{2} \approx 8.5$ and $L_z = 24\sqrt{2} \approx 33.9$. In the following, we focus on fcc crystals with (100) orientation. For other orientations, $L_x = L_y$ is not always possible.

Figure 4.13 shows a typical result for $\Delta F(\kappa)$ as a function of the index $k$, divided by the number of successive umbrella windows $M = 1024$. Similarly to the curve shown in Fig. 4.5, the curve is not monotonic. Instead, it rises steeply, then has a plateau and finally drops again to reach the final value. Note that the $\{\kappa_k\}$ are chosen according to Eq. (4.17b).

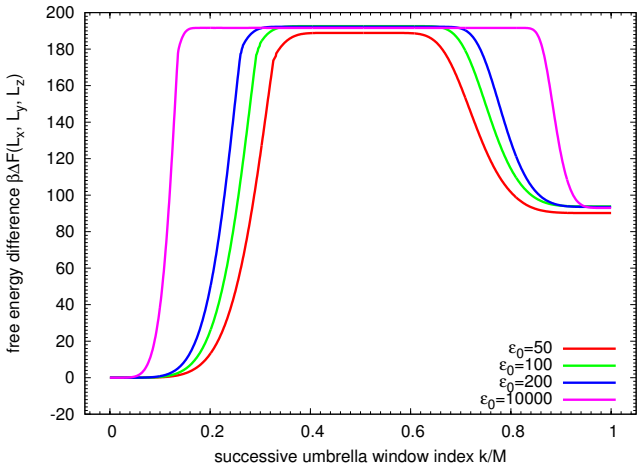


Figure 4.13: Free energy $\Delta F(\kappa)$ versus $\kappa$ for the solid-fluid coexistence of the hard spheres model introduced above. The box dimensions are $L_x = 8.5 = L_y$ and $L_z = 33.9$. The shape differs significantly from that in Fig. 4.5. Note that the choice of $\varepsilon_0$ does not change the curves significantly. With a proper $\varepsilon_0$-dependent rescaling of the $x$-axis, one could make all curves collapse onto each other.

In Fig. 4.13, the integration has been carried out for various $\varepsilon_0$, ranging from 50 to 10000. Obviously, the result does not depend on the chosen value $\varepsilon_0$, as long as it is not too small. This corresponds to the explanation given in section 4.3, that $\varepsilon_0 * \kappa_1$ has to be small enough to produce a reasonable acceptance rate, for otherwise the simulation will be stuck on the left side of the window $[\kappa_0, \kappa_1]$. Hence, the product $\varepsilon_0 * \kappa_1$ determines how fast the switching takes place. Larger values of $\varepsilon_0$ cause the $\Delta F(\kappa)$ to be steeper, but the plateau values are the same. With proper rescaling of the $x$-axis, all curves with different $\varepsilon_0$ would collapse on top of each other. Hence, the choice of $\varepsilon_0$ only affects the intermediate states but not the physical states at $\kappa = 0$ and $\kappa = 1$, provided $\varepsilon_0 \gg 1$.

The fact that the curves are non-monotonic are not surprising after having seen this in the conceptually simpler case in the previous section. However, it is intriguing to examine this closer to see if the reasons are also similar. We proceed analogously by filling both boxes with the same phase so that no interface is formed during the integration. The results are shown in Fig. 4.14 for a solid-solid and a fluid-fluid case.

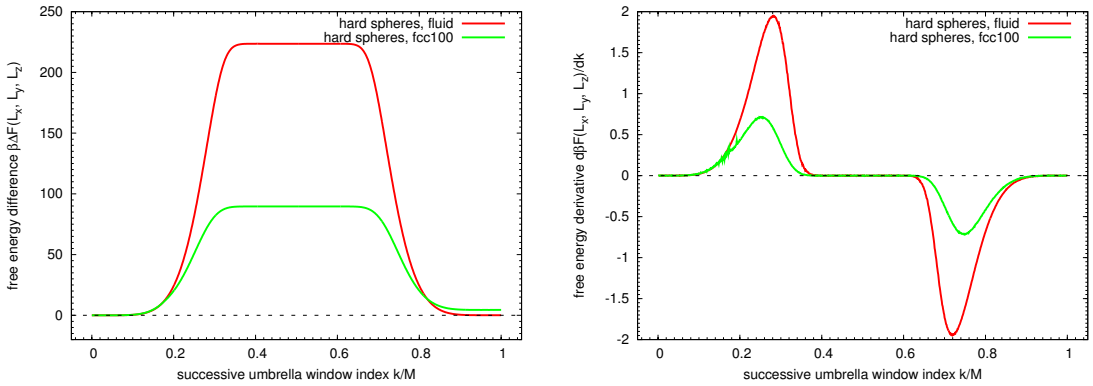


Figure 4.14: Free energy $\Delta F(\kappa)$ versus $\kappa$ for the case where both boxes are filled with the same phase, so that $\Delta F = 0$ as expected. The box dimensions in both cases are $L_x = 8.5, L_y = 8.5$ and $L_z = 33.9$. The curves are perfectly inversion symmetrical around $k/M = 1/2$, except for some fluctuations in the solid-solid case at $k/M = 0.2$, which is discussed in the main text.

We discuss the fluid-fluid case first. The free energy difference is zero, as expected, and the derivative shown in Fig. 4.14(b) is perfectly inversion symmetrical. For the intermediate states, the free energy is of the order of 100 $k_\mathrm{B}T$. The density profiles [Fig. 4.15(a)] show that the effect is the same as discussed in the previous section, i.e. the fluid avoids the boundary region where the two boxes are joint by creating depletion zones. This effect is maximal at $\kappa = 0.5$ and vanishes for $\kappa = 0$ and $\kappa = 1$.

The situation is different for the solid-solid case. Note that in the crystalline case, the free energy $\Delta F(\kappa)$ does not go back to zero but there is a non-vanishing $\Delta F \approx 3\ k_\mathrm{B}T$. Figure 4.14(b) shows where this effect comes from. The derivative is perfectly inversion symmetrical, just like in the fluid-fluid case, but at $k/M \approx 0.2$, there are some fluctuations. The origin of these fluctuations can be seen in Fig. 4.16. At $\kappa$ close to zero, the two crystals do not interact with each other, so the particles can overlap at the box boundaries without penalty. Also, they can translate independently of each other in the $x$- and $y$-directions and thereby create a mismatch. Since there is no interaction between the boxes at $\kappa = 0$, this mismatch is not relevant to the system. However, as the integration proceeds, such a mismatch becomes

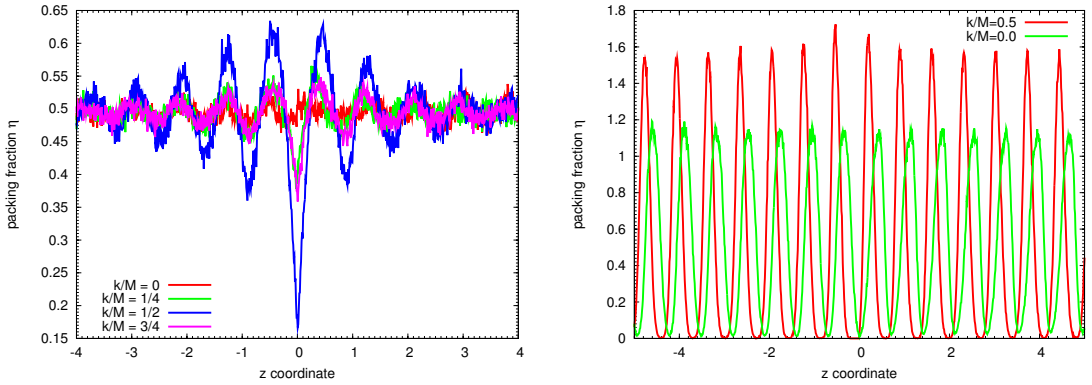


Figure 4.15: (a) Average packing fraction profiles for the fluid-fluid coexistence ($L_x = L_y = 8.5, L_z = 33.9$) at various values $k$ of the successive umbrella window index, as indicated. For $0 < k/M < 1$, there are depletion zones in the boundary regions. The amplitude of this depletion zone is strongest exactly at $k/M = 1/2$ and vanishes for $\kappa \to 0$ or $\kappa \to 1$, where the packing fraction is spatially constant at $\eta_f = 0.494$ throughout the whole system. (b) Average packing fraction profiles for the crystal-crystal coexistence [fcc (100)] in a box of the same size. At $k/M = 0$ the two crystals can move freely within the box, which is why the crystalline layers are smeared out and less high than at $k/M = 0.5$. The height is equal for all layers. At $k/M = 0.5$ however, the peaks are higher because the crystal cannot move in $z$-direction anymore. Furthermore, the two layers surrounding the boundary (at $z = 0$) are more localized, due to the mixing of the periodic boundary conditions.

energetically unfavorable, while at the same time, the interaction is not strong enough to align the two crystals. This is true as soon as the plateau region in Fig. 4.14(a) is reached. There is no depletion zone this time [Fig. 4.15(b)], because the crystalline structure ensures that the configuration of particles on the other side of the same box, interacting with periodic boundary conditions, and in the other box are compatible. However, the crystals are not in equilibrium, as fluctuations within the crystalline matrix and the movement of the combined crystal in the $z$-direction is still constrained, e.g. one can see in density profiles that the particles in the boundary region where the boxes are joint, are more localized. These effects vanish near the end of the integration when the free energy $\Delta F(\kappa)$ drops towards zero again. Since the fluctuations at $k/M = 0.2$ in $\partial \Delta F / \partial k$ are the reason for the non-vanishing $\Delta F$, the ensemble switch method might not be able to compute interfacial tensions between solids and solids. Since we are interested in solid-liquid coexistence, where only one of the two phases is ordered, this is not an issue.

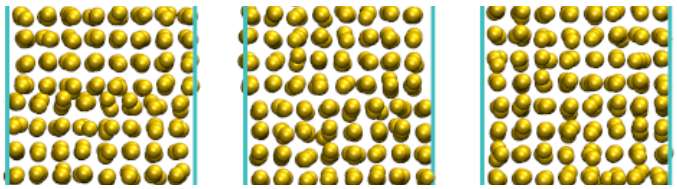

(a) (b) (c)

Figure 4.16: Snapshots of the boundary region where the boxes are combined. In (a), at $k/M = 37/1024$, the mixing is very low, hence the particles in the boundary region can overlap without great penalty. In (b), at $k/M = 186/1024$, the mixing is high enough to prevent overlaps. Due to the low interaction, a misfit in the crystal can occur at the boundary, which influences the result of the integrations. In (c), $k/M = 900/1024$, the misfit has vanished and the two crystals have merged.

Figure 4.17 shows the same packing fraction plots, but for the solid-fluid case. Note that the fluid does not form a depletion zone. Instead, it forms layers compatible with the crystalline structure, as the integration proceeds. At the same time, the crystalline translational freedom is constrained so that the peaks become sharper. This is especially true for the crystalline layers close to the boundaries, which are even more localized. This is the same phenomenon seen for the solid-solid case in Fig. 4.15(b).

In the following, we attempt to interpret the shape of the free energies $\Delta F(\kappa)$ of the solid-fluid case [Fig. 4.13] similarly to the liquid-vapor case discussed in the previous section. Note however, that the situation is more delicate here, so that we can only give a preliminary interpretation. While some details in this interpretation are not fully clear, the application of the method in the solid-liquid case is nevertheless possible and leads to dependable results.

Having discussed the solid-solid and the fluid-fluid cases separately, one could expect that the data seen in Fig. 4.13 are superpositions of two effects. On the one hand, there are two interfaces formed, which is why the total free energy difference is nonzero, and on the other hand, there are reversible effects which occur and vanish during the integration, like the depletion zones or the constrained crystal movement.

Considering Fig. 4.17, where density profiles at various values of $k/M$ are shown, one can see that the crystal shows the same behavior as in the solid-solid case, being more localized in the bulk and especially in the vicinity of the boundaries. On the other hand, the fluid does not form a depletion zone but rather adjusts to the crystal by creating layers next to it which are compatible with the lattice structure. This indicates that the situation is more subtle, as the behavior of the fluid

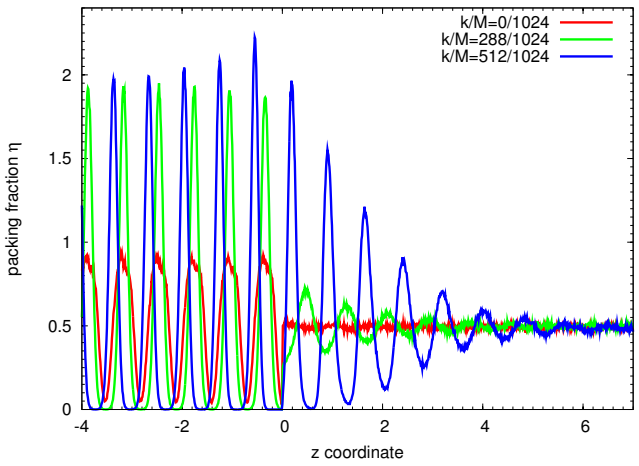


Figure 4.17: Packing fraction profiles for the solid-fluid case. The boundary is situated at $z = 0$. At $k/M = 0$, the crystalline layers appear as broad peaks because the crystal can move freely in $z$-direction, thereby smearing out the peaks. Halfway through the integration, the crystal layers are more localized, especially near the boundary. The fluid does not create a depletion zone but forms layers next to the crystal.

differs depending on whether a crystal is present or not. To illustrate the situation, Fig. 4.18 shows the solid-fluid case along with the solid-solid and the fluid-fluid case. Additionally, there is one curve (labeled K4) where we have subtracted the solid-solid curve from the solid-fluid curve. This is motivated by the fact that the crystal shows the same behavior as in the solid-solid case while the fluid does not. Hence, it looks like the decrease of the free energy at about $k/M = 0.7$ is entirely due to the relaxation of the crystal structure. The corresponding curve K4 seems to support this, as the curve is almost flat after the increase at about $k/M = 0.25$. However, one has to be careful because the solid-fluid case contains only half as much of the crystal phase and hence one should only subtract half of the solid-solid case to correctly account for the relaxation of the crystal. Furthermore, it totally neglects the behavior of the fluid during the integration, e.g. the translational degree of freedom in $z$-direction of the fluid is constrained by the presence of the crystal. Therefore, this interpretation is not entirely convincing.

Figure 4.18 also shows the curve K5, where the interpretation of the liquid-vapor case is adopted literally, namely subtracting half of the solid-solid and half of the fluid-fluid curve. The resulting curve indicates a two-step process. However, this procedure is not convincing either, as the fluid forms a depletion zone in the fluid-fluid case and creates a layering structure in the solid-fluid case. Hence, the contribution

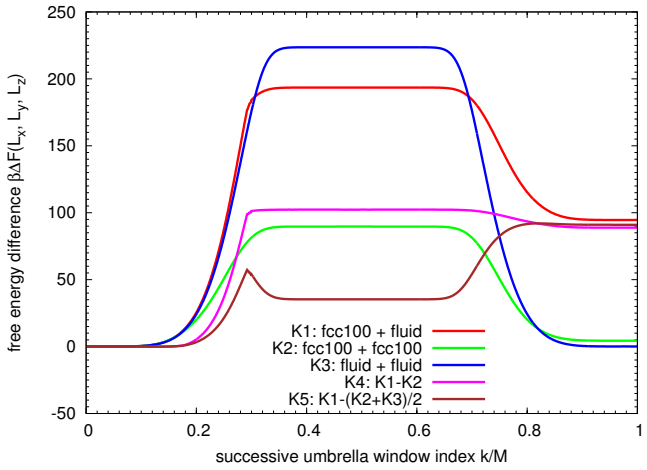


Figure 4.18: Free energy $\Delta F(\kappa)$ versus $\kappa$ for the solid-fluid, solid-solid and fluid-fluid case in a box with $L_x = L_y = 8.5$ and $L_z = 33.9$. The curve K1 shows data from Fig. 4.13 while K2 and K3 are taken from Fig. 4.14(a).The curve K4 is the difference between solid-fluid and solid-solid, while K5 is the difference between solid-fluid and half of the solid-solid and fluid-fluid curves. The decomposition is not as straightforward as in the liquid-vapor case because the fluid behaves differently in the fluid-fluid and solid-fluid case.

of the fluid to the solid-fluid case is not given by K3 and cannot be computed straightforwardly in an independent simulation, which is possible in the liquid-vapor case. Nevertheless, it is plausible that the qualitative behavior is similar to the liquid-vapor case, namely the curves are superpositions of the creation of interfaces on the one hand and additional reversible effects like the localization and relaxation of the crystal. In summary, one can understand the shape of the free energy $\Delta F(\kappa)$ in the case of hard spheres on a phenomenological level. The ensemble switch method is capable of accurately computing interfacial tensions $\gamma(L_x, L_y, L_z)$.

## 4.6 Conclusion

In this chapter, a new Monte Carlo method called ensemble switch method is presented which is capable of computing the interfacial tension for interfaces between liquid and vaporous phases as well as crystalline and liquid phases. The unified treatment of both types of interfaces is an attractive feature of the method. Furthermore, the resulting free energies $\Delta F(\kappa)$ from the state where the two phases are separated (no interfaces) to the state where the two phases are in coexistence (two interfaces) have

been analyzed and interpreted as being a superposition of the process of creating the interfaces and additional effects which have no contribution on the total free energy difference but only on the free energy difference of the intermediate states. The ensemble switch method is a powerful tool and will be used extensively in the following chapters to accurately compute interfacial tensions.

# Chapter 5

# Finite-Size Scaling of the Interfacial Tension for the Ising Model

As presented in chapter 4, there exist quite a few methods to compute the interfacial tensions. However, the discrepancy of the results these methods yield might hint at a more fundamental problem. In this chapter, we show that the interfacial tension $\gamma(L_x, L_y, L_z)$ of a flat interface obtained from simulations depends on the box dimensions $L_x, L_y$ and $L_z$ in a universal fashion. The knowledge of this dependence can be used to gain consistent and precise estimates of the interfacial tension by conducting a proper finite-size scaling.

Section 5.1 motivates and discusses the finite-size scaling ansatz, which takes into account entropic degrees of freedom of the interface(s) like translational entropy and capillary waves. Also, a new mechanism called domain breathing is found. The scaling ansatz is then approved thoroughly in section 5.2 for the two- and three-dimensional Ising model using the ensemble switch method established chapter 4. The chapter closes with a short summary.

Note that parts of the results of this chapter appeared in [Schmitz et al., 2014a,b].

## 5.1 Finite-Size Scaling for Ising Systems

### 5.1.1 Motivation

To understand complex phenomena, it is wise to start at a simple model and use it to detect and understand the fundamental effects. The two-dimensional Ising

(lattice gas) model on a square lattice is attractive for studies concerning interfacial phenomena, because the interfacial tension $\gamma_\infty$ in the thermodynamic limit can be calculated explicitly [Onsager, 1944], namely

$$\beta\gamma_\infty = 2\beta - \ln\left(\frac{1+\exp(-2\beta)}{1-\exp(-2\beta)}\right) . \tag{5.1}$$

Recall that we have set the interaction constant $J$ and the lattice constant $a$ of the Ising model to unity throughout this thesis. Also the results from the ensemble switch method can be compared to the probability distribution method proposed in [Binder, 1982], by which the interfacial tension can be extracted via the probability distribution $P_L(\varrho)$, which can be sampled accurately if the free energy barrier separating the two homogeneous states is small enough so that the simulation can explore both maxima equally often, i.e. if the system size $L$ is small or the temperature is high. In general it is preferable to use advanced simulation methods like Wang-Landau sampling or multicanonical sampling to obtain $P_L(\varrho)$.

Figure 5.1 shows why it is important to do a finite-size scaling. Here, the interfacial tensions on a square lattice of linear dimension $L$ with $L^2$ spins has been calculated using the new ensemble switch method and the existing probability distribution method. According to Eq. (5.1), $\beta\gamma_\infty = 0.2281$ at the chosen temperature $k_\mathrm{B}T/J = 2.0$, but for the chosen $L$, the computed values are not even close to this value. Apparently, they converge to this value for $L \to \infty$, but if one measured only at one finite box size, the systematic error would be impossible to estimate. For most models, an equation like Eq. (5.1) is not available, and hence one cannot straightforwardly estimate the deviation of $\gamma$ for a finite simulation box.

The first question one has to ask is what the leading order correction to the interfacial tension $\gamma$ is, because it dominates the finite-size scaling behavior. Of course, in an infinite system, the interfacial free energy $F_\mathrm{int}$ is infinite because it is proportional to the area of the interface. The interfacial tension, however, is the interfacial free energy per unit area and remains finite and well-defined in the thermodynamic limit. Therefore one can write

$$\gamma_\infty = \lim_{V\to\infty} \frac{F_\mathrm{int}}{A} , \tag{5.2}$$

where $A$ is the total area of all interfaces in the system. Note that all length scales are given in units of some universal length, for example the lattice spacing $a$ for the Ising model or the particle diameter $\sigma$ in off-lattice models, so that the area $A$ and lengths also dimensionless. Since in a computer simulation, one always works with

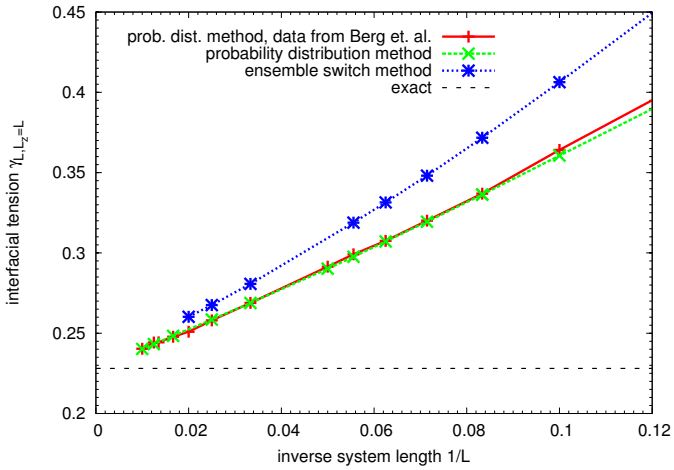


Figure 5.1: The interfacial tension $\gamma$ against $1/L$ for the $d = 2$ Ising model on a square lattice of linear dimension $L$ at $k_{\mathrm{B}}T/J = 2.0$. On the one hand, the plot shows results from the ensemble switch method, and on the other hand two sets of data using the probability distribution method [cf. section 4.2] are also shown, which agree with each other within statistical errors (the data labeled with Berg et. al. is from [Berg et al., 1993a]). The finite values of $\gamma$ differ for both methods [this is discussed in section 5.2.2], but they both converge to the literature value $\beta\gamma_\infty$ given by Eq. (5.1) for $L \to \infty$.

finite boxes, one has to understand how this limiting process behaves in order to extrapolate properly. In other words, one is interested in the leading order terms $r(\{L_i\})$ of the ansatz

$$F_{\mathrm{int}}(\{L_i\}) = A(\gamma_\infty + r(\{L_i\})) \tag{5.3}$$

or

$$\gamma_\infty = \gamma(\{L_i\}) - r(\{L_i\}) \; . \tag{5.4}$$

From this consideration, it is clear that

$$\lim_{V\to\infty} r(\{L_i\}) = 0 \; . \tag{5.5}$$

The leading order correction to the interfacial tension is not a $L^{-1}$ correction but a logarithmic correction. This can be shown by simple means. Consider a one-dimensional Ising model with length $L$ at temperature $T$ with magnetization $m = -1$ and periodic boundary conditions. The energetic cost to create a configuration with a domain of length $l$ of spins of opposite sign is $4J$, since there is no contribution from the inner spins of this domain. There are $L$ positions for the left domain wall, so the probability of the configuration with a domain of length $l < L$ is

$$P_L(l) = cL \exp(-4\beta J) \; , \tag{5.6}$$

where $c$ is a normalization constant. Note that this probability does not depend on the domain length in this one-dimensional case. The probability to create a uniform magnetization across the system can be written as

$$P_L(0) = 1 - \sum_{l=1}^{L-1} P_L(l) \ , \tag{5.7}$$

ignoring configurations with more than one domain, i.e. for small $T$. This yields

$$P_L(0) = 1 - cL(L-1)\exp(-4\beta J) \ . \tag{5.8}$$

The interfacial tension can then be calculated as the free energy difference between the uniform magnetization and a slab-geometry case, where the domain of up and down spins has the same size. This difference is equal to two times the interfacial tension due to the two domain walls, and so one obtains

$$\begin{aligned} 2\beta\gamma_L &= \ln\left(\frac{P_L(0)}{P_L(L/2)}\right) \\ &= \ln\left(\frac{1 - cL(L-1)\exp(-4\beta J)}{cL\exp(-4\beta J)}\right) \\ &= 4\beta J - \ln(cL) + \ln\left(1 - cL(L-1)\exp(-4\beta J)\right) \ , \end{aligned}$$

resulting in

$$\beta\gamma_L = 2\beta - \frac{1}{2}\ln(cL) + \frac{1}{2}\ln\left[1 - cL(L-1)\exp(-4\beta)\right] \ . \tag{5.9}$$

The leading order correction is a logarithmic one, which arises from the fact that the domain has some translational freedom due to the periodic boundary conditions.

The extension to two-dimensional systems is non-trivial. Consider a two-dimensional box with dimension $L, L_z$ with antiperiodic boundary conditions in $z$-direction and periodic boundary conditions in $x$-direction. In such a situation, the system will form a slab configuration with one interface in the middle of the box, separating two domains of opposite magnetization. If $L_z > L$, the one-dimensional interface[1] will be perpendicular to the $z$-direction. On average, each of the domains occupies the volume $LL_z/2$ and their densities are is $\varrho_l$ and $\varrho_g$.

In the grand-canonical ensemble, the interface can move freely within the box. This translational degree of freedom in the $z$-coordinate of the interface gives rise to an entropy contribution

$$\Delta S = k_{\mathrm{B}} \ln(L_z/l_z) \ , \tag{5.10}$$

[1] Although, in a two-dimensional box, the interface is just a one-dimensional object, the terms interface and area are applied here.

where $l_z$ is an unknown constant, denoting a natural length of the system for measuring the properties of the interface. It will be discussed in detail later [see section 5.2.4].

For the case $L = 1$, the system becomes one-dimensional. In the limit $T \to 0$, any fluctuation in the bulk is strongly suppressed, so the magnetization in the two domains is $m_+ = 1$ and $m_- = -1$. The entropy of the interface is strictly zero and the interfacial energy in this trivial case is the energy of the interface $2J$ divided by the length of the interface, which is 1. However, the generalization of this behavior to $L > 1$ is nontrivial. One cannot simply use the equations above for the translational entropy, assuming that the interfacial tension without this correction is simply $\gamma_\infty$ (the interfacial tension in the thermodynamic limit). In $d = 2$, the interfacial energy depends on $L$, for the periodic boundary conditions in $x$-direction only allow capillary wave excitations with wavelengths $\lambda_n = \frac{2L}{n}$, corresponding to wave numbers $k_n = n\lambda_1$. This finite-size effect on the capillary wave spectrum is well-known.

These considerations clearly indicate that the finite-size scaling of the interfacial tension is highly non-trivial. There are many effects, depending on the ensemble, the boundary conditions and the box geometry, which have to be taken into account to accurately extrapolate the interfacial tension $\gamma$ from simulations in finite boxes.

### 5.1.2 Theory of Finite-Size Scaling for the Ising Model

In order to understand the differences between the interfacial tension of a finite interface and of an interface in the thermodynamic limit, it is a good idea to start with a simplistic model. Here, the simplest model is a two-dimensional Ising system, where the interface is only a one-dimensional object. One great advantage of this system is that the interfacial tension $\beta\gamma_\infty$ can be calculated exactly via Eq. (5.1) for any temperature. For simplicity, it is wise to study a situation with only one interface. In a box with periodic boundary conditions in all directions [Fig. 5.2], this is not possible because a slab configuration naturally has two interfaces. However, with antiperiodic boundary conditions in one direction [Fig. 5.2], the system is able to form only one interface perpendicular to this direction. Considering only one interface is a good idea, since the interaction between interfaces can be excluded for the moment. While the slab configuration is unstable (or at least metastable) in the case of periodic boundary conditions unless the magnetization (or density) is conserved, the antiperiodic boundary conditions stabilize inhomogeneous configurations. Therefore we were able to study interfaces in a canonical ensemble with fixed density as well as a grandcanonical situation, where the density is not constrained.

In general, the free energy of a $d$-dimensional system with volume $V$ and any amount

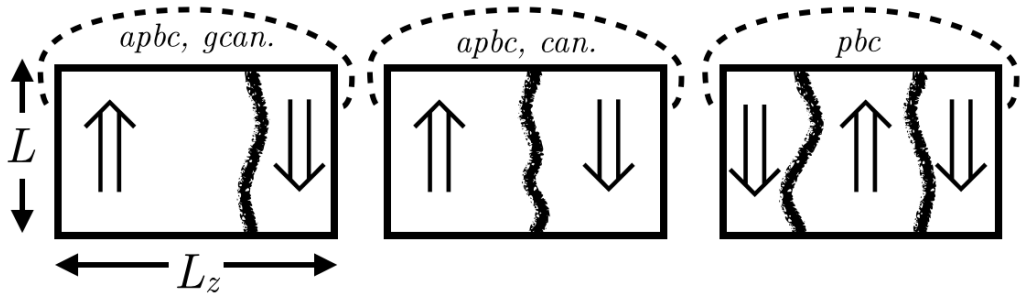


Figure 5.2: Sketch of box geometries considered here. All sides of the boxes have length $L$ except for $L_z$, which can differ In the directions other than $L_z$, periodic boundary conditions are used. On the left and in the center, antiperiodic boundary conditions (APBC) are applied in $z$-direction, so that an interface forms. While on the left, the density is not constrained (grandcanonical), in the middle, the density is kept constant at $\varrho = 0.5$, so that the interface is always in the center of the box. On the right, periodic boundary conditions (PBC) are used in all directions, so that two interfaces occur. In order to stabilize these interfaces, the density is always fixed at $\varrho = 0.5$ in this case.

of interfaces of total ($(d-1)$-dimensional) area $A$, can be written as

$$F = V f_{\text{bulk}} + F_{\text{int}}(\{L_i\}) \tag{5.11a}$$

$$F - V f_{\text{bulk}} = F_{\text{int}}(\{L_i\}) =: A\gamma(\{L_i\}) \,, \tag{5.11b}$$

where $F_{\text{bulk}} = V f_{\text{bulk}}$ is the bulk free energy, and an effective interfacial free energy $\gamma(\{L_i\})$, which in general depends on all box lengths $L_i$, $i = 1, \ldots, d$, has been introduced. In a computer simulation in a finite box, one can only measure $\beta F_{\text{int}}(\{L_i\})$. To obtain $\beta\gamma_\infty$, one has to extrapolate to $V \to \infty$. Therefore, the interfacial tension $\gamma(\{L_i\})$ of the finite geometry can be written as

$$\beta\gamma(\{L_i\}) = \frac{\beta F_{\text{int}}(\{L_i\})}{A} = \beta\gamma_\infty + \frac{\beta\Delta F_{\text{int}}(\{L_i\})}{A} \tag{5.12}$$

where $\Delta F_{\text{int}}$ consists of several contributions depending on the geometry of the box. In the thermodynamic limit, only $\beta\gamma_\infty$ must remain, so that $\Delta F_{\text{int}}/A \to 0$. In the following, various contributions will be discussed and later compared to computer simulations. For sake of simplicity, we restrict ourselves to the rectangular boxes, where all lengths except for the length $L_z$ perpendicular to the interface(s) are equal. Then $\beta\gamma(\{L_i\}) = \beta\gamma(L, L_z)$.

### Translational Freedom of the Interface

Consider first an Ising system in a two-dimensional box of dimension $L, L_z$ with periodic boundary conditions in $L$-direction and antiperiodic boundary conditions in $L_z$-direction. In such a geometry, the system creates two domains of opposite magnetization with an interface in between. If the density is not constrained, the interface may wander around in $L_z$ direction. This corresponds to an entropy gain

$$\Delta S = k_{\mathrm{B}} \ln(L_z/l_z) \,, \tag{5.13}$$

where $l_z$ is an unknown constant. The entropy gain changes the interfacial free energy $F = U - TS$, so that

$$\beta \Delta F_{\mathrm{int}} = -\ln(L_z/l_z) \,. \tag{5.14}$$

As one can see, the enhancement of entropy causes a decrease of the free energy cost to form an interface. This means that for long boxes, i.e. $L_z \gg L$, the system becomes unstable. Hence it can form a new pair of interfaces in order to gain more entropy. So this contribution of translational entropy is the reason for the transition to a multi-domain situation for extremely elongated boxes.

Since in a $d$-dimensional box, one has $(d-1)$-dimensional interfaces which can move along the direction perpendicular to the interface, Eq. (5.14) is valid for all $d$.

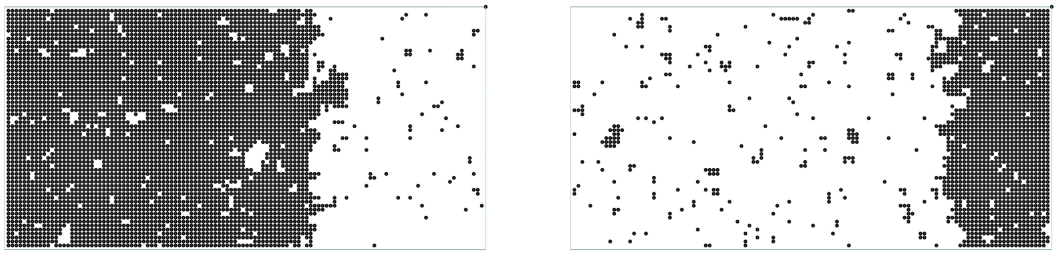

Figure 5.3: Snapshots of two-dimensional systems to visualize the translational freedom of an interface. The snapshots are from a simulation with $L = 60, L_z = 120, k_{\mathrm{B}}T/J = 2.0$ with APBC in $z$-direction and PBC in $x$-direction.

### Constrained Translational Freedom – Domain Breathing

Consider a $d$-dimensional box with volume $L^{d-1}L_z$ using antiperiodic boundary conditions in $z$-direction and periodic boundary conditions in all other directions.

Within the canonical ensemble, if the density $\varrho$ (or magnetization $m$) is fixed within the slab regime (cf. Fig. 2.1), the system will again consist of two domains with an interface of area $L^{d-1}$ between them. However, since the density is conserved, the interface cannot wander around in the box but it can fluctuate around its equilibrium position. If we assume that the liquid is on the left-hand side and the gas on the right-hand side of the box, the average densities in these domains are $\varrho_1 = \varrho_l$ and $\varrho_2 = \varrho_g$, respectively, and the volumes are determined by

$$\varrho L^{d-1} L_z = \varrho_l L^{d-1} L_{z,l} + \varrho_v L^{d-1} L_{z,g} \tag{5.15}$$

so that in equilibrium the length of the domains is given by

$$L_z = L_{z,l} + L_{z,g} \qquad L_{z,l} = \frac{\varrho - \varrho_g}{\varrho_l - \varrho_g} L_z \qquad L_{z,g} = \frac{\varrho_l - \varrho}{\varrho_l - \varrho_g} L_z \; . \tag{5.16}$$

Note that all lengths are given in units of the lattice spacing $a$ of the lattice gas model. At finite temperatures, the densities and volumes of these domains are fluctuating. These fluctuations are uncorrelated with each other, but are correlated with a fluctuation $h$ of the position of the interface. This degree of freedom contributes to the interfacial energy and is of a translational entropy character. The constraint about the density yields

$$\varrho L^{d-1} L_z = \varrho_1 L^{d-1} (L_{z,l} - h) + \varrho_2 L^{d-1} (L_{z,g} + h) \; . \tag{5.17}$$

Hence

$$h = \frac{\varrho_1 L_{z,l} + \varrho_2 L_{z,g} - \varrho L_z}{\varrho_1 - \varrho_2} \; . \tag{5.18}$$

The directions parallel to the interface cancel each other so that $h$ seems to depend only on $L_z$. However, there is a hidden $L$-dependence through the bulk fluctuations. To take these fluctuations into account, write $\varrho_1 = \varrho_l + \delta\varrho_1$ and $\varrho_2 = \varrho_g + \delta\varrho_2$, so that

$$h \approx \frac{L_{z,l}\delta\varrho_1 + L_{z,g}\delta\varrho_2}{\varrho_l - \varrho_g} \; , \tag{5.19}$$

where (5.15) was used. Furthermore, $\delta\varrho_i$ are assumed to be small compared to $\varrho_l$ and $\varrho_g$ and are therefore neglected in the denominator.

From general statistical thermodynamics, it is known that the fluctuations in the bulk are Gaussian distributed with mean $\varrho_l$ or $\varrho_g$ and variance $\sigma_\varrho^2$

$$P_{L_x,L_z}(\delta\varrho) = \frac{1}{\sqrt{2\pi\sigma_\varrho^2}} \exp\left(-\frac{1}{2}\frac{(\delta\varrho)^2}{\sigma_\varrho^2}\right) \qquad , \qquad \sigma_\varrho^2 = \frac{k_\mathrm{B} T \chi_\mathrm{coex}}{L^{d-1} L_z} \; , \tag{5.20}$$

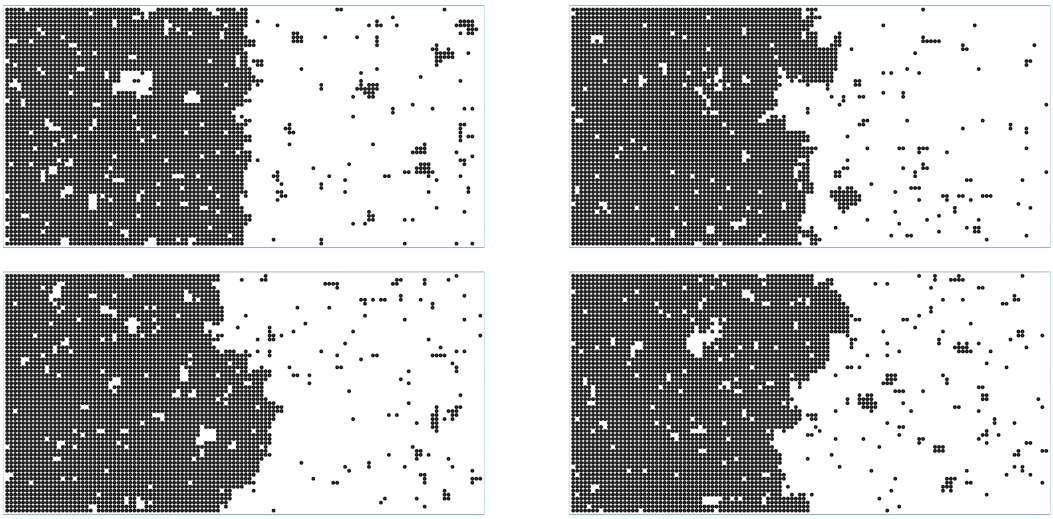

Figure 5.4: Various snapshots of two-dimensional systems to visualize the domain breathing. If the density is conserved, the interface cannot move freely within the interface but stays in the center of the box. Spontaneous fluctuations within the two bulk phases have an effect on the position of the interface. The snapshots are from a simulation with $L = 60, L_z = 120, k_\mathrm{B}T/J = 2.0$ with APBC in $z$-direction and PBC in $x$-direction. The density is fixed at $\varrho = 0.5$. The figure shows the bulk fluctuations. A considerable shift of the interface is not seen here because $L_z$ is too small compared to $L_x$ and hence $\langle h \rangle$ is of the order of one lattice spacing.

where $\chi_\mathrm{coex}$ is the susceptibility at the coexistence curve. The expression for $\sigma_\varrho$ follows from the standard fluctuation relation $\beta\chi_\mathrm{coex} = V\,\langle(\delta\varrho)^2\rangle$. Applying this to (5.19) results in

$$\langle h^2 \rangle = \frac{1}{(\varrho_l - \varrho_g)^2} \left( L_{z,l}^2 \langle \delta\varrho_1^2 \rangle + L_{z,g}^2 \langle \delta\varrho_2^2 \rangle + 2L_{z,l}L_{z,g} \langle \delta\varrho_1 \delta\varrho_2 \rangle \right) \tag{5.21}$$

$$= \frac{1}{(\varrho_l - \varrho_g)^2} \left( L_{z,l}^2 \frac{k_\mathrm{B}T\chi_\mathrm{coex}}{L^{d-1}L_{z,l}} + L_{z,g}^2 \frac{k_\mathrm{B}T\chi_\mathrm{coex}}{L^{d-1}L_{z,g}} \right) \tag{5.22}$$

$$= \frac{k_\mathrm{B}T\chi_\mathrm{coex}}{(\varrho_l - \varrho_g)^2} \frac{L_z}{L^{d-1}} \tag{5.23}$$

Apart from (5.16), it was used that the $\delta\varrho_i$ are uncorrelated and that the first moments vanish. From this, one can conclude the length scale (in units of the lattice spacing $a$) of the fluctuations of the interface between the two domains

$$\sqrt{\langle h^2 \rangle} = \sqrt{\frac{k_\mathrm{B}T\chi_\mathrm{coex}L_z}{L^{d-1}(\varrho_l - \varrho_g)^2}}\,. \tag{5.24}$$

The bulk fluctuations of the two domains therefore give rise to an entropy contribution (similar to (5.13))

$$\Delta S = k_{\mathrm{B}} \ln\left(\sqrt{\langle h^2 \rangle}\right) = \frac{k_{\mathrm{B}}}{2} \ln(L_z) - \frac{k_{\mathrm{B}}(d-1)}{2} \ln(L) + \frac{k_{\mathrm{B}}}{2} \ln(\mathrm{const}) \tag{5.25}$$

and additional correction terms for the surface free energy

$$\beta \Delta F_{\mathrm{int}} = -\frac{1}{2} \ln(L_z) + \frac{d-1}{2} \ln(L) - \frac{1}{2} \ln(\mathrm{const}) \ , \tag{5.26}$$

where the constant depends on temperature. Comparing this result to the unconstrained case (5.14), the prefactor to the $\ln(L_z)$ term is smaller. The contribution parallel to the $L_z$-direction is negative while all others are positive. The interpretation is that the translational entropy becomes smaller if the interface becomes larger and therefore more inert.

### Capillary Waves

The periodic boundary conditions in $x$-direction impose a constraint to the interface structure. The capillary wave spectrum is constrained to capillary wave excitations with wavelengths compatible with the box geometry. In a finite two-dimensional box, the spectrum of wavelengths is discrete with values $\lambda_n = \frac{2L}{n}$ with $n = 1, 2, 3, \ldots$. Compared to an unconstrained interface, the entropy is decreased, resulting in another logarithmic correction to the finite-size scaling, as will be shown in the following. For simplicity, a geometry with only one interface is considered. This can be achieved by fixed-spin-boundary conditions (see also [Svrakic et al., 1988], where a generalization to tilted interfaces is considered), where the spins near box walls are fixed to being positive on the left half of the box and negative on the right half. The interface is therefore clamped at the walls, thereby suppressing translational freedom. However, capillary wave excitations can still occur.

At low temperature, the one-dimensional interface in a two-dimensional box can be seen as a random walk problem, because it corresponds to the solid-on-solid model (SOS model), where all bulk fluctuations in the two coexisting phases (islands, clusters, etc.) are eliminated and overhangs are also neglected, so that the interface can be described in terms of a directed random walk. The interface of a configuration is created by a walker in $x$-direction (the $x$-coordinate plays the role of time in the random walk language), making steps in the $\pm z$-direction with some small probability $p$. Overhangs are neglected in this picture, so interfaces at high temperatures are not modeled correctly. In a finite box, such an interface has to adhere $z(L) = z(0)$.

If a random walk has on average $n = pL/a$ steps, where $p$ is the average number of steps per unit length, the probability of a random walk to return to the origin at the $n$th step is[2]

$$r_n = \frac{1}{\sqrt{2\pi n}} \tag{5.27}$$

The entropy of the constrained interface is therefore decreased by $\Delta S = -k_\mathrm{B} \ln(1/r_n) = -k_\mathrm{B}/2 \ln(2\pi pL/l_x)$, leading to an enhanced free energy

$$\beta \Delta F_\mathrm{int} = \frac{1}{2} \ln(2\pi pL/l) = \frac{1}{2} \ln(L) + \text{const} \,, \tag{5.28}$$

where the constant depends on temperature, but not on $L$. This calculation holds for two-dimensional systems at low temperatures only. However, it shows that simple considerations already yield logarithmic corrections to the interfacial tension.

Actually, this problem of a clamped interface, where none of the aforementioned translational degrees of freedom occur, in two dimensions can be solved explicitly by transfer matrix methods. At low temperatures, the results are equivalent to the above SOS model result, as one expects. One can show that the partition function of the system is [Svrakic et al., 1988]

$$Z_L = \exp(-\beta \gamma_L L) \left( \frac{\beta \kappa_L}{2\pi L} \right)^{1/2} \,, \tag{5.29}$$

with

$$\gamma_L = \gamma_\infty + a/L \tag{5.30}$$

$$\kappa_L = \kappa_\infty + b/L \tag{5.31}$$

where $\gamma_\infty$ and $\kappa_\infty$ are the interfacial free energy and stiffness of the Ising interface for $L \to \infty$. The free energy of the system then is

$$\beta F_L = -\ln Z_L = \gamma_L L + \frac{1}{2} \ln L - \frac{1}{2} \ln \frac{\kappa_L}{2\pi} \tag{5.32}$$

Hence,

$$\beta \Delta F_\mathrm{int} = \frac{1}{2} \ln(L) + \text{const} \,, \tag{5.33}$$

agreeing with (5.28). Capillary waves in two dimensions give rise to a universal enhancement of the interfacial tension. The interpretation of this effect is that finite-size constrains the capillary waves, so the entropy due to the capillary waves is

[2] This result can be found in a paper about drunken Englishmen [Fisher, 1984].

reduced. Due to the fixed-spin boundary condition, for large $L_z$ the $L_z$-dependence of $\gamma_L$ is completely negligible.

To deal with $d$-dimensional system instead of of two-dimensional systems, we refer to [Brézin and Zinn-Justin, 1985], where both a cubic system with volume $L^d$ and periodic boundary conditions in all directions and a quasi-one-dimensional system $L \times L \times L_z$ with $L_z \to \infty$ are considered. They state that the typical distance $\xi_\parallel$ between domain walls is $\xi_\parallel \propto L^{(3-d)/2} \exp(\gamma_\infty L^{d-1})$ and attribute the prefactor to capillary waves. Since the interfacial width due to capillary waves scales as $w \propto L^{(3-d)/2}$, but $w \propto \sqrt{\ln L}$ in $d = 3$, the interpretation can be made that $w$ sets the scale for interfacial translations. Thus, one could speculate that the entropy due to capillary waves, $\ln(L^{x_{cw}})$ with $x_{cw} = (3-d)/2$ could turn into $\ln(\sqrt{\ln L})$ for $d = 3$. As we are only interested in the leading-order corrections to the interfacial tension, such a small correction is probably beyond the precision of current computing power. For more information on this matter, please refer to section A.1 in the appendix.

Hence, the capillary wave contribution of an interface at arbitrary dimension $d$ is given by

$$\beta \Delta F_{\text{int}} = \frac{3-d}{2} \ln(L) \; . \tag{5.34}$$

### Summary

First, we summarize the possible contributions of an interface to the interfacial free energy.

$$\text{full translational freedom: } \beta \Delta F_{\text{int}} = -\ln(L_z) + \text{const} \tag{5.35}$$

$$\text{constrained translational freedom: } \beta \Delta F_{\text{int}} = -\frac{1}{2} \ln L_z + \frac{d-1}{2} \ln L + \text{const} \tag{5.36}$$

$$\text{capillary wave fluctuations: } \beta \Delta F_{\text{int}} = \frac{3-d}{2} \ln(L) + \text{const} \tag{5.37}$$

These results need to be confirmed by computer simulations, but the underlying effects can in most cases only be seen together. We start with an Ising system and use various boundary conditions to verify the conjectures. The simplest variant is a box with antiperiodic boundary conditions (APBC) in the direction perpendicular to the interface and periodic boundary conditions parallel to the interface in a grandcanonical ensemble (gc). The interface has full translational freedom and therefore

$$\beta \Delta F_{\text{int}} = -\ln L_z + \frac{3-d}{2} \ln L + \text{const} \tag{5.38}$$

Using (5.12), one obtains

$$\text{APBC(gc), } d=2: \qquad \beta\gamma(L,L_z) = \beta\gamma_\infty - \frac{\ln L_z}{L} + \frac{1}{2}\frac{\ln L}{L} + \frac{\text{const}}{L} \tag{5.39}$$

$$\text{APBC(gc), } d=3: \qquad \beta\gamma(L,L_z) = \beta\gamma_\infty - \frac{\ln L_z}{L^2} + \frac{\text{const}}{L^2}\ . \tag{5.40}$$

Note that all normalization constants only contribute to const, e.g. via $\ln(L/l) = \ln(L/a) + \ln(a/l)$, where $a$ is the Ising lattice spacing, set to unity. In off-lattice systems, one can take any length scale, since it only modifies the constant.

Another situation is a similar box as above but in a canonical ensemble, where the magnetization is kept at $m = 0$. The interface then gives rise to

$$\beta\Delta F_{\text{int}} = -\frac{1}{2}\ln(L_z) + \frac{d-1}{2}\ln(L) + \frac{3-d}{2}\ln(L) + \text{const} \tag{5.41}$$

and hence

$$\text{APBC(c), } d=2: \qquad \beta\gamma(L,L_z) = \beta\gamma_\infty - \frac{1}{2}\frac{\ln(L_z)}{L} + \frac{\ln(L)}{L} + \frac{\text{const}}{L} \tag{5.42}$$

$$\text{APBC(c), } d=3: \qquad \beta\gamma(L,L_z) = \beta\gamma_\infty - \frac{1}{2}\frac{\ln(L_z)}{L^2} + \frac{\ln(L)}{L} + \frac{\text{const}}{L^2}\ . \tag{5.43}$$

The constrained translational freedom modifies the scaling behavior both parallel and perpendicular to the interface.

The third case to examine is a box with periodic boundary conditions in all directions, for this is the usual case if the interfacial tension is computed. In this case, one has to deal with two interfaces, which interact with each other. For the inhomogeneous state to be stable, the magnetization (or density, respectively) has to be kept constant. With two interfaces, the total area $A$ of the system is $2L^{d-1}$, and the capillary wave fluctuations for both interfaces has to be taken into account separately. One might assume that each interface has full translational entropy through the periodic boundary conditions, but the constant density prevents them from moving independently of each other. Instead, the whole system has full translational freedom, while the average distance between the two interfaces is fixed. Additionally, the position of the second interface relative to the other interface can fluctuate according to the domain breathing effect. In summary, the free energy of the system is

$$\beta\Delta F_{\text{int}} = -\ln(L_z) - \frac{1}{2}\ln(L_z) + \frac{d-1}{2}\ln(L) + 2\cdot\frac{3-d}{2}\ln(L) + \text{const} \tag{5.44}$$

so the interfacial tension behaves like

$$\text{PBC(c), } d=2: \qquad \beta\gamma(L,L_z) = \beta\gamma_\infty - \frac{3}{4}\frac{\ln(L_z)}{L} + \frac{3}{4}\frac{\ln(L)}{L} + \frac{\text{const}}{L} \tag{5.45}$$

$$\text{PBC(c), } d=3: \qquad \beta\gamma(L,L_z) = \beta\gamma_\infty - \frac{3}{4}\frac{\ln(L_z)}{L^2} + \frac{1}{2}\frac{\ln(L)}{L^2} + \frac{\text{const}}{L^2}\ . \tag{5.46}$$

We do not discuss the constant arising in all these equations, because it consists of many (known and unknown) contributions, e.g. the length scales $l, l_z$ and the temperature dependent constant appearing in the discussion of the domain breathing effect. The constant will be treated as a free parameter when data is described by these equations.

All the previous equations can be described by a single equation[3] with universal constants $x_\perp, x_\parallel$:

$$\beta\gamma(L, L_z) = \beta\gamma_\infty - x_\perp \frac{\ln L_z}{L^{d-1}} + x_\parallel \frac{\ln L}{L^{d-1}} + \frac{C}{L^{d-1}} \,. \tag{5.47}$$

Recall that all lengths in this equation are dimensionless, as we use universal lengths (lattice spacing for the Ising model or particle diameter $\sigma$ for off-lattice models) to normalize the box dimensions $L$ and $L_z$.

This is one of the central results of this whole thesis. It implies that the leading-order terms in the finite-size scaling are of order $\ln(L)/L^{d-1}$ and $\ln(L_z)/L^{d-1}$ while the next term is of order $1/L^{d-1}$. The prefactors $x_\perp$ and $x_\parallel$ depend only on the dimensionality, the boundary conditions and the ensemble, but not on the pair interaction or whether one studies liquid-vapor or solid-liquid interfaces. Note that during the derivation, these details have not been of any importance so that Eq. (5.47) is not necessarily restricted to the Ising model.

| $d$ | BC | ensemble | $x_\perp$ | $x_\parallel$ |
|---|---|---|---|---|
| 2 | antiperiodic | grandcanonical | 1 | 1/2 |
| 3 | antiperiodic | grandcanonical | 1 | 0 |
| 2 | antiperiodic | canonical | 1/2 | 1 |
| 3 | antiperiodic | canonical | 1/2 | 1 |
| 2 | periodic | canonical | 3/4 | 3/4 |
| 3 | periodic | canonical | 3/4 | 1/2 |

Table 5.1: Values of the universal constants in 2 and 3 dimensions. The universal constants only depend on the boundary conditions (periodic or antiperiodic) and the ensemble (canonical or grandcanonical). Note that $x_\perp$ is independent of the dimensionality of the interface while $x_\parallel$ depends on $d$ because of capillary wave effects and constrained translational freedom.

[3] The generalization to $L_x \neq L_y$ in three dimensions is straightforward and can be found in section 6.2.

## 5.2 Simulation Results for the Ising Model

The Ising model is very attractive to test the finite-size scaling relation Eq. (5.47) derived above because of the variety of available boundary conditions. While the three effects, namely translational entropy, capillary waves and the domain breathing effect, cannot be considered independently of each other, one can test various combinations of boundary conditions and ensembles to verify that Eq. (5.47) correctly takes them into account. In off-lattice systems, which will be studied in chapter 6, one is restricted to periodic boundary conditions in a canonical ensemble, so it is important to consider the Ising model first in order to understand the interplay of the three effects.

The implementation of the ensemble switch method is straight-forward for the Ising model. Apart from the lattice, one needs to implement a function which can calculate the energy of a lattice point for both types of boundary conditions. There are only two Monte Carlo moves. On the one hand, there are spin flips, which change the system's configuration. Because the magnetization (or in the lattice gas view the density) has to be kept constant, we use spin exchange moves, where we pick two spins of opposite orientation randomly and attempt to flip both at once. This move conserves the magnetization and, at the same time, changes the configuration significantly, because of the nonlocal character of this move. One could also restrict the pairs of spins to be neighbors, but this implementation suffers from hydrodynamic slowing-down [Landau and Binder, 2009; Binder and Heermann, 2010]. If the density is not conserved, the standard single spin flip moves are used. On the other hand, one needs to implement the $\kappa$-move where one attempts to change the current $\kappa = \kappa_i$ of the system to $\kappa' = \kappa_{i\pm1}$. This move is computationally very cheap, as the program keeps track of the total energy $E_0$ and $E_1$ and only needs to calculate the energy difference $\Delta E = E' - E$, where

$$E = \kappa E_1 + (1-\kappa)E_0 \qquad \text{and} \qquad E = \kappa' E_1 + (1-\kappa')E_0 \ .$$

Note that we choose a mapping $k \to \kappa_k$ of the $M = 1024$ successive umbrella windows as given in Eq. (4.17a). This increases the number of windows near $\kappa = 0$ and 1 so that the computing time is used to simulate the important parts of the path with increased accuracy.

### 5.2.1 The two-dimensional Ising Model

In order to test the universal scaling relation given by Eq. (5.47), consider the two-dimensional Ising model first, where the exact result $\beta\gamma_\infty$ is known [Eq. (5.1)].

If one fixes $L$ and only varies the length $L_z$ of the box in the direction perpendicular to the interfaces, the scaling relation reduces to

$$\beta\gamma(L, L_z) = \text{const} - x_\perp \frac{\ln L_z}{L^{d-1}} \,. \tag{5.48}$$

Hence, if plotting the data at constant $L$ against $\ln L_z / L^{d-1}$, the resulting curves should be straight lines with slope $-x_\perp$. Indeed, if plotting the data this way [Fig. 5.5], the data follows straight lines in all considered combinations of boundary conditions and canonical or grandcanonical ensembles. Note that the slope does not depend on temperature and system size although a broad temperature range ($k_\mathrm{B}T/J = 1.2, 1.6, 2.0$) and several box widths ($L = 10, 20, 30, 40$) are considered with $L_z$ ranging from $L$ up to $L_z = 200$. In all cases, the slopes are compatible with the values of $x_\perp$ given in Table 5.1. This shows that the above ansatz reflects the actual behavior of the interfaces regarding translational entropy and domain breathing.

Unfortunately, one cannot extract the interfacial tension from these plots because it is hidden among other constants in the $y$-intercept. To estimate $\gamma_\infty$, one has to vary $L$ also. Therefore, the next step is to keep $L_z$ fixed and vary $L$ to see whether Eq. (5.47) can also correctly explain the data in this case. Indeed, Fig. 5.6 shows that the data are well-represented by the scaling ansatz. Note that this fit contains only one unknown constant, namely the constant $C$ appearing in Eq. (5.47), because for the two-dimensional Ising model, the interfacial tension $\gamma_\infty$ is known beforehand.

As the ansatz is supported very well by the data, one can use the knowledge about the logarithmic corrections to subtract them from the data and extract the interfacial tension $\gamma_\infty$ from a fit as follows:

$$\beta\widetilde{\gamma}(L, L_z) = \beta\gamma(L, L_z) + \frac{x_\perp \ln L_z - x_\parallel \ln L}{L^{d-1}} = \beta\gamma_\infty + \frac{C}{L^{d-1}} \,. \tag{5.49}$$

The constant $C$ for this "reduced" interfacial tension $\widetilde{\gamma}(L, L_z)$ is the same as before. After subtraction of the logarithmic corrections, there are two fit parameters left, namely the interfacial tension $\gamma_\infty$ and the constant $C$, so that the desired quantity $\gamma_\infty$ is obtained from these fits at constant $L_z$. The corresponding fits are shown in Fig. 5.6. As one can see, the exact values $\beta\gamma(k_\mathrm{B}T/J = 1.2) = 1.284$, $\beta\gamma(k_\mathrm{B}T/J = 1.6) = 0.660$ and $\beta\gamma(k_\mathrm{B}T/J = 2.0) = 0.228$ are perfectly reproduced by this procedure. Furthermore, the constant $C$, which must depend on the ensemble, the boundary conditions and the temperature, is roughly the same for different choices of $L_z$ at otherwise equal circumstances. In the thermodynamic limit, the $C$ should no longer depend on $L_z$, so at the chosen values of $L_z$ there is still some higher order correction. It is remarkable that the three combinations of boundary conditions and ensembles (canonical or grandcanonical) give very accurate estimates for the interfacial tension

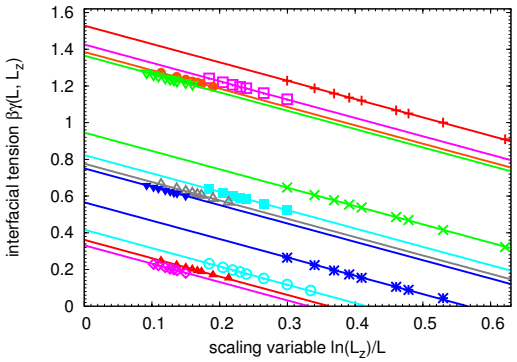


(a) $d = 2$, APBC(gc)

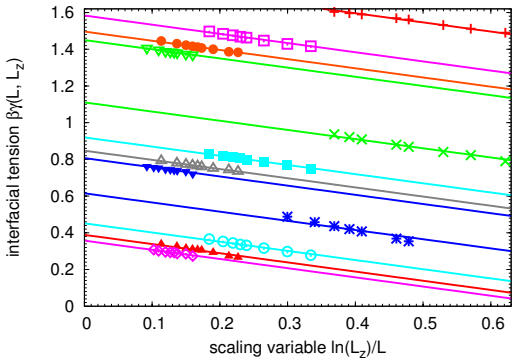


(b) $d = 2$, APBC(c)

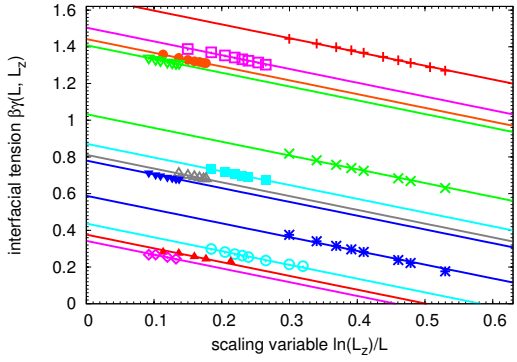


(c) $d = 2$, PBC(c)

Figure 5.5: Finite-size scaling at constant $L$. In each plot, data for three temperatures and four $L$ are shown. The top four lines belong to $k_{\mathrm{B}}T/J = 1.2$, the middle four lines to $k_{\mathrm{B}}T/J = 1.6$ and the bottom four lines to $k_{\mathrm{B}}T/J = 2.0$. In each set of lines, from top to bottom $L = 10, 20, 30, 40$. The lines are fits to the data with constant slope, so that only the y-intercept is a free parameter. The slope is taken to be $x_\perp = 1$ for APBC(gc), $x_\perp = 1/2$ for APBC(c) and $x_\perp = 3/4$ for PBC(c).

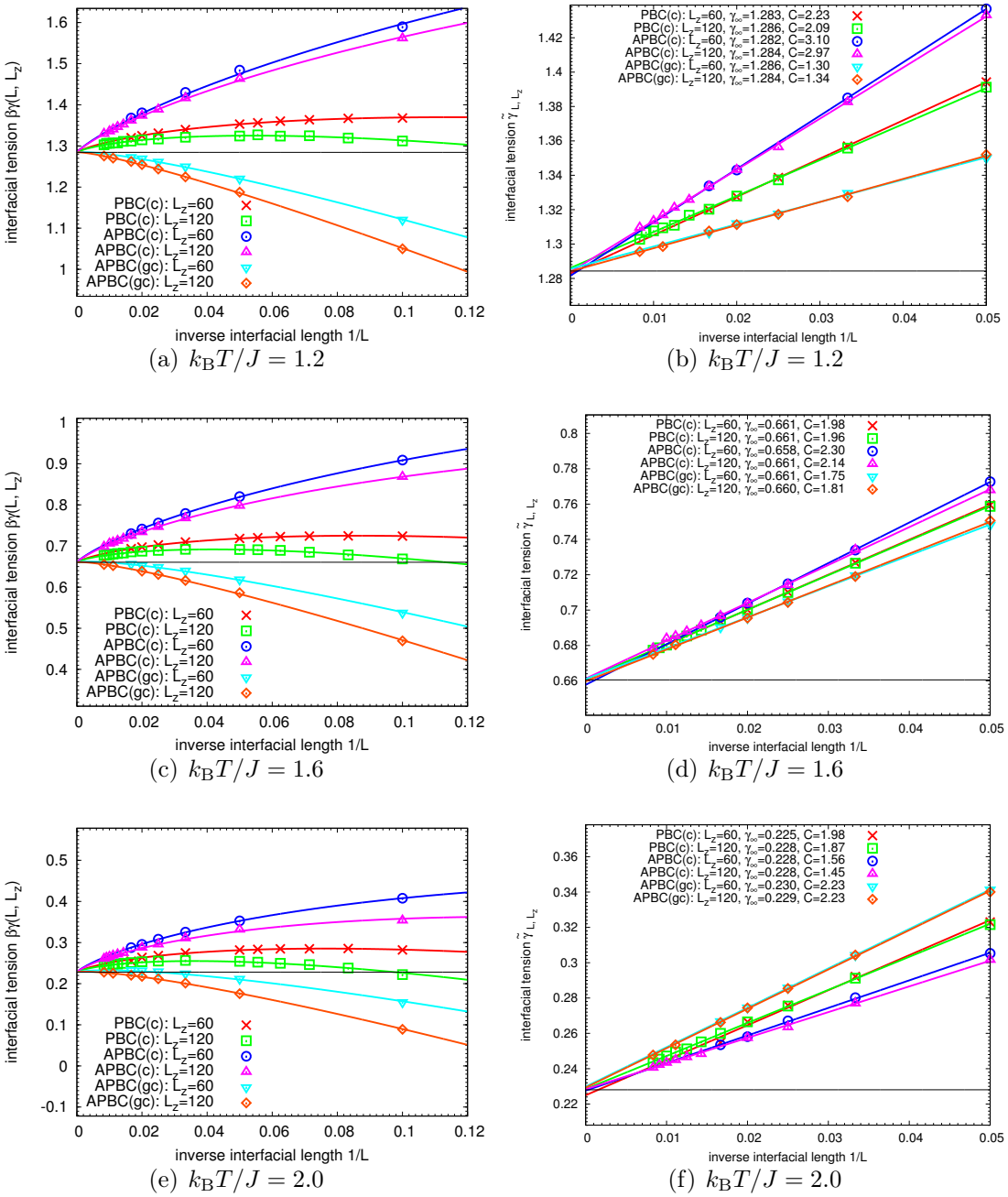


(a) $k_{\mathrm{B}}T/J = 1.2$ (b) $k_{\mathrm{B}}T/J = 1.2$

(c) $k_{\mathrm{B}}T/J = 1.6$ (d) $k_{\mathrm{B}}T/J = 1.6$

(e) $k_{\mathrm{B}}T/J = 2.0$ (f) $k_{\mathrm{B}}T/J = 2.0$

Figure 5.6: Finite-size scaling of the interfacial tension $\beta\gamma(L, L_z)$ and the reduced interfacial tension $\beta\widetilde{\gamma}(L, L_z)$ at constant $L_z$ for $L_z = 60, 120$ and various temperatures and ensembles, as indicated. (a), (c) and (e) show the original data and a fit of the form Eq. (5.47), while in (b), (d) and (f), the same data is shown after the logarithmic corrections have been subtracted. This reduced interfacial tension $\widetilde{\gamma}(L, L_z)$ has only a $1/L$-dependence on $L$ at fixed $L_z$.

$\gamma_\infty$, which are consistent with each other. This shows that the above ansatz is correct and that the ensemble switch method is a valuable tool for this analysis.

### 5.2.2 Comparison to the Probability Distribution Method

Before heading to the three-dimensional Ising model, it is a good idea to take a step back and compare the results from the ensemble switch method to results of other methods. In the original paper about the probability distribution method [Binder, 1982], finite-size scaling is discussed as follows.

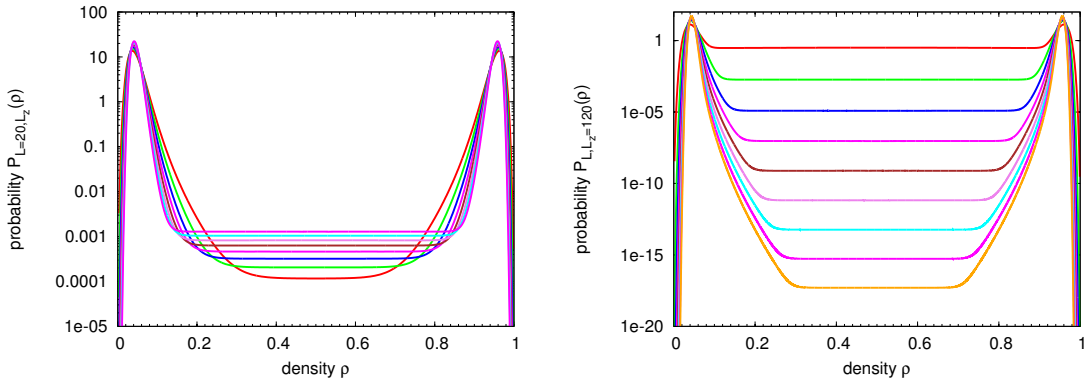


(a) $L = 20$, $L_z = 30, 40, 50, 60, 70, 80, 90, 100$ (from bottom to top at $\varrho = 0.5$)

(b) $L_z = 120$, $L = 10, 20, 30, 40, 60, 70, 80, 90$ (from top to bottom at $\varrho = 0.5$)

Figure 5.7: Probability distributions of a two-dimensional Ising model at $k_\mathrm{B}T/J = 2.0$. At fixed interfacial length $L$, the probability of heterogeneous states ($\varrho = 0.5$) increases. If the box length $L_z$ is fixed and $L$ is increased, the probability decreases. Both effects seen here are of entropical nature.

The probability distribution $P_L(m)$ for an Ising model in a $d$-dimensional cubic box has two peaks at $\pm m_\mathrm{coex}$, corresponding to the two homogeneous (pure) phases, which we call vapor ($-m_\mathrm{coex}$) and liquid ($+m_\mathrm{coex}$). These peaks are well described by Gaussians

$$P_L(m) = \frac{1}{\sqrt{2\pi\sigma_m^2}} \exp\left(-\frac{1}{2}\frac{(m - \langle m\rangle)^2}{\sigma_\varrho^2}\right) \tag{5.50}$$

with variance

$$\sigma_m^2 = \frac{k_\mathrm{B}T\chi}{L^d} \tag{5.51}$$

where $\langle m\rangle = \pm m_\mathrm{coex}$ and $\chi$ denotes the order-parameter susceptibility (in the Ising model $\chi = (\partial m/\partial H)_T$). The probability of a homogeneous state with magnetization

zero is hence given by

$$P_{L,\mathrm{hom}}(m=0) \propto \frac{L^{d/2}}{\sqrt{2\pi k_\mathrm{B} T \chi}} \exp\left(-L^d \frac{m_\mathrm{coex}^2}{2k_\mathrm{B} T \chi}\right) \tag{5.52}$$

i.e. the probability decreases exponentially with the volume, $\exp(L^d)$. On the other hand, the probability of heterogeneous states, consisting of two domains separated by two interfaces (heterogeneous states with flat walls need to have an even number of interfaces, because of the periodic boundary conditions), decreases only exponentially with the area of the interfaces, namely

$$P_L(m=0) \propto \exp\left(-2L^{d-1}\beta\gamma_L\right) \tag{5.53}$$

where $\gamma_L$ is the interfacial tension in the finite box. The preexponential factor is complicated because it is expected to contain a power law dependence on $L$, which is influenced by a number of effects, which are hard to distinguish, such as

- the invariance of the configuration under translation of the interface in one direction (translational entropy),
- deviation of an interface from the planar shape,
- capillary wave fluctuations and the restriction to wavelengths compatible with the boundary conditions.

Therefore, the preexponential factor is simply taken as a power law with an unknown exponent $p$ and a constant $N$:

$$P_L(m=0) = NL^p \exp\left(-2L^{d-1}\beta\gamma_\infty\right) \tag{5.54}$$

Following this ansatz, one can derive two different expressions for the interfacial tension, provided one knows the probability distribution $P_L(m)$, which can be obtained from Monte Carlo simulations (e.g. using multicanonical sampling, see section 2.7.1)

$$\beta\gamma_\infty = \lim_{L\to\infty} \frac{1}{2L^{d-1}} \ln\left(\frac{P_L(m_\mathrm{coex})}{P_L(0)}\right) \tag{5.55a}$$

$$\beta\gamma_\infty = \lim_{L\to\infty} \frac{1}{2L^{d-1}} \ln\left(P_L(0)\right) \ . \tag{5.55b}$$

Using

$$P_L(\pm m_\mathrm{coex}) = \frac{L^{d/2}}{\sqrt{2\pi k_\mathrm{B} T \chi}} \tag{5.56}$$

and equation (5.54), one can calculate

$$\frac{P_L(m_{\text{coex}})}{P_L(0)} = \frac{L^{d/2-p}}{N\sqrt{2\pi k_{\text{B}}T\chi}} \exp\left(+2L^{d-1}\beta\gamma_\infty\right) \tag{5.57}$$

$$2L^{d-1}\beta\gamma_L = \ln\left(\frac{P_L(m_{\text{coex}})}{P_L(0)}\right) = (d/2-p)\ln(L) - \ln(N\sqrt{2\pi k_{\text{B}}T\chi}) + 2L^{d-1}\beta\gamma_\infty \tag{5.58}$$

$$\beta\gamma_L = \beta\gamma_\infty - (p-d/2)\frac{\ln(L)}{2L^{d-1}} - \frac{\ln(N\sqrt{2\pi k_{\text{B}}T\chi})}{2L^{d-1}} \tag{5.59}$$

and obtain the finite-size scaling

$$\beta\gamma_L = \beta\gamma_\infty - \frac{2p-d}{4}\frac{\ln L}{L^{d-1}} - \frac{A}{2L^{d-1}} \tag{5.60}$$

with a prefactor $x = \frac{2p-d}{4}$ for the logarithmic correction. The unknown parameter $p$ has later been found to be $p = d-1$ [Brézin and Zinn-Justin, 1985; Gelfand and Fisher, 1990; Morris, 1992; Wiese, 1992], leading to a finite-size behavior

$$\beta\gamma_L = \beta\gamma - \frac{d-2}{4}\frac{\ln L}{L^{d-1}} - \frac{A}{2L^{d-1}} \tag{5.61}$$

for a cubic box of volume $L^d$.

The scaling ansatz Eq. (5.47) proposed in this work simplifies in the special case of a cubic geometry to

$$\beta\gamma(L) = \beta\gamma_\infty - (x_\perp - x_\parallel)\frac{\ln(L)}{L^{d-1}} + \frac{\text{const}}{L^{d-1}} \tag{5.62}$$

according with (5.61) since $x_\perp - x_\parallel = (-1 - \frac{1}{2} + \frac{d-1}{2} + 2\frac{3-d}{2})/2 = \frac{d-2}{4}$, which is exactly the prefactor in Eq. (5.61). So although the derivation of the scaling behavior is completely different, the leading order behavior agrees. Furthermore, Berg, Hansmann and Neuhaus reported [Berg et al., 1993a,b] that in $d = 2$, the logarithmic dependence vanished, which also agrees with our result $x_\parallel = x_\perp$ in $d = 2$.

Non-cubic geometries have only rarely been considered in the literature. Therefore, we performed simulations using both variants of the probability distribution method Eq. (5.55) and test whether the scaling behavior is equal for all methods. Note that the probability distribution method can only be applied if using periodic boundary conditions in all directions. Therefore, if the results agree, then the ensemble switch method provides a valuable complementary tool to study other boundary conditions where the probability distribution method is not applicable. The results are shown in Fig. 5.8 for fixed $L$ and Fig. 5.9 for fixed $L_z$.

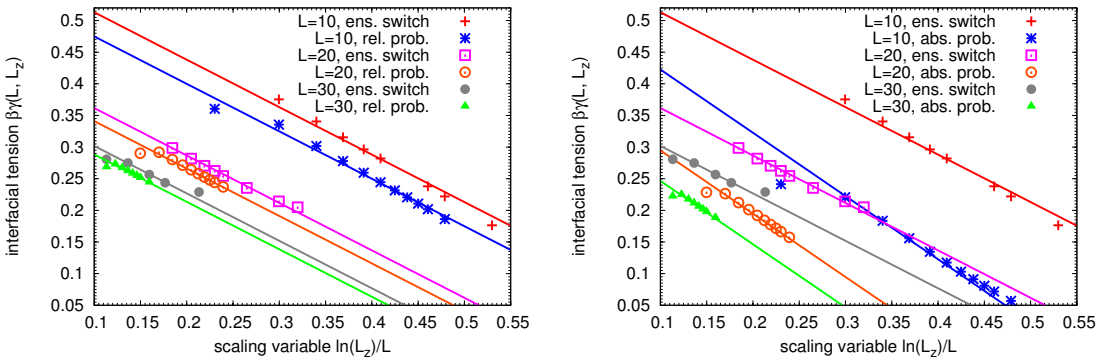


Figure 5.8: Finite-size scaling for $d = 2$ at fixed $L = 10, 20, 30$ for box geometries with PBC in all directions. Both plots show data from the ensemble switch method, for reference. On the left, the data using (5.55a) is shown, having the same slope -3/4 as the results from the ensemble switch method. On the right, data using (5.55b) is included, having a different slope -1, correctly predicted by (5.68).

The constants $x_\perp$ and $x_\parallel$ from table 5.1 for the case of periodic boundary conditions in a canonical ensemble are compatible with the probability distribution method using (5.55a), for both plots. This means that the probability distribution method yields the same finite-size scaling behavior, as expected. It should be noted, however, that the exact values differ, as was already noted in Fig. 5.1. This is due to the non-logarithmic term in Eq. (5.47). The interfacial tension $\gamma_\infty$ from both methods agrees nonetheless.

The scaling behavior for the method (5.55b) is different however, which can be understood as follows. According to Eq. (5.56), $P_L(m_{\text{coex}}) \propto \sqrt{L_z L^{d-1}}$ depends on the box geometry, which implies

$$\beta F_{\text{rel}} = \ln\left(\frac{P_L(m_{\text{coex}})}{P_L(0)}\right) = \ln\left(\frac{\text{const}(L_z L^{d-1})^{1/2}}{P_L(0)}\right) \tag{5.63}$$

$$= \frac{1}{2}\ln L_z + \frac{d-1}{2}\ln L + \ln\left(\frac{1}{P_L(0)}\right) + \ln \text{const} \tag{5.64}$$

$$= \frac{1}{2}\ln L_z + \frac{d-1}{2}\ln L + \beta F_{\text{abs}} + \ln \text{const} \tag{5.65}$$

The interfacial free energies between the two probability methods differ by the

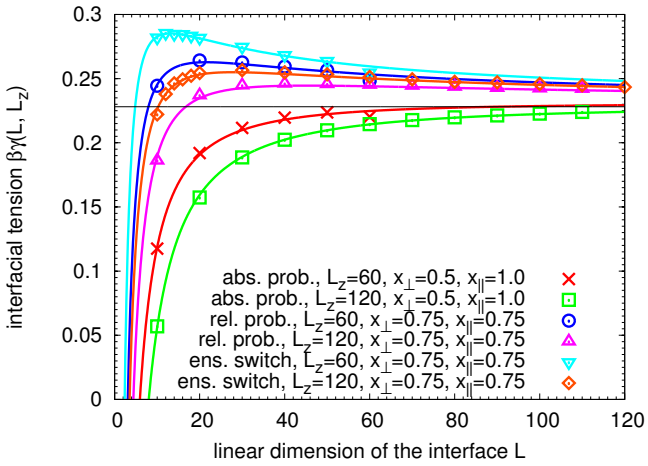


Figure 5.9: Finite-size scaling for $d = 2$ at fixed $L_z = 60, 120$ for box geometries with PBC in all directions. Data from the ensemble switch method is included for reference. The curves are from one-parameter fits where the only free parameter is the constant in the term $C/L$. Note that the absolute probability method converges from below while the other methods converge from above.

dependence of $P_L(m_{\text{coex}})$, so the prefactors $x_\perp$ and $x_\parallel$ change according to

$$\beta\Delta F_{\text{int,abs}} = \beta\Delta F_{\text{int, rel}} - \left(\frac{1}{2}\ln L_z + \frac{d-1}{2}\ln L\right) \tag{5.66}$$

$$= -2\ln(L_z) + (3-d)\ln(L) + \text{const} \ . \tag{5.67}$$

Therefore, the following behavior is to be expected

$$\beta\gamma(L, L_z) = \beta\gamma_\infty - \frac{\ln(L_z)}{L} + \frac{1}{2}\frac{\ln(L)}{L} + \frac{\text{const}}{L} \ . \tag{5.68}$$

Figures 5.8 and 5.9 confirm the above considerations.

### 5.2.3 The three-dimensional Ising Model

After having fully covered the two-dimensional Ising model, where the scaling ansatz Eq. (5.47) has been fully confirmed, the next step is to also test it in three dimensions. Here, the exact value of the interfacial tension is unknown, i.e. an equation like Eq. (5.1) does not exist. There are, however, enough data in the literature for comparison.

In the three-dimensional case, it is also possible to study various combinations of boundary conditions (periodic or antiperiodic) and ensembles (canonical or grand-canonical). Since the simulations in three dimensions require more computing time, we restrict our discussion to one temperature, namely $k_{\mathrm{B}}T/J = 3$, which is well above the roughening temperature $k_{\mathrm{B}}T_R/J \approx 2.454$ [Bürkner and Stauffer, 1983; Mon et al., 1989, 1990; Hasenbusch and Pinn, 1994; Hasenbusch et al., 1996; Hasenbusch and Pinn, 1997] and still far below the critical temperature $k_{\mathrm{B}}T_c/J = 4.5115$ [Ferrenberg and Landau, 1991; Baillie et al., 1992]. As in the two-dimensional case, we consider the dependence on the box length $L_z$ and the length $L$ in the other two directions separately. The results are shown in Fig. 5.10.

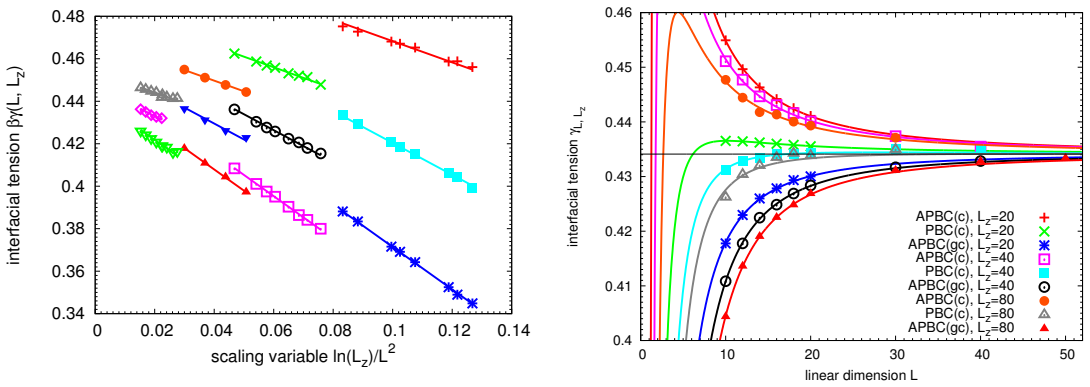


(a) fixed $L$ (b) fixed $L_z$

Figure 5.10: Finite-size scaling of the interfacial tension $\beta\gamma(L, L_z)$ and the reduced interfacial tension $\beta\widetilde{\gamma}(L, L_z)$ for the three-dimensional Ising model at $k_{\mathrm{B}}T/J = 3$. (a) Scaling behavior at constant $L$. The four top sets of points are APBC(c), the middle lines are PBC(c), the bottom lines are APBC(gc) For each case, the four sets of points are for $L = 6, 8, 10, 14$, from right to left. The lines are fits with fixed slope $x_\perp$. (b) Scaling behavior at constant $L_z$, as indicated, plotted against the length $L$. For the fits, the known value $\beta\gamma_\infty = 0.434$ [Hasenbusch and Pinn, 1994] is used so that the only fit parameter is the constant in the term $C/L^2$.

The quality of the results are as gratifying as in the two-dimensional case. Therefore, we proceed analogously and subtract the logarithmic corrections in order to estimate the interfacial tension $\gamma_\infty$. For reasons explained later, we slightly modify the ansatz given by Eq. (5.49) and use

$$\beta\widetilde{\gamma}(L, L_z) = \beta\gamma(L, L_z) + \frac{x_\perp \ln L_z - x_\parallel \ln L}{L^{d-1}} = \beta\gamma_\infty + \frac{C_1}{L} + \frac{C_2}{L^2} \tag{5.69}$$

instead. Note that apart from the term containing $C_2$, we have added a phenomenological term $C_1/L$ which is not predicted by the above considerations. The term

$C_2/L^2$ is taken into account in Eq. (5.47) because it must occur if the arguments of the logarithmic terms are to be dimensionless. Recall from section 5.1.2 that the arguments of the terms $\ln(L_z)$ and $\ln(L)$ must be dimensionless, which is why we introduced an arbitrary[4] length $a$ and used it as a length scale for $L$ and $L_z$. Then, e.g. the translational entropy term becomes $\ln(L_z/l_z) = \ln(L_z/a) - \ln(l_z/a)$, and assuming that the length $l_z$ is independent of the box geometry, the resulting term $\ln(l_z)$ contributes to the constant $C_2$. The same applies for the length $l$ introduced in section 5.1.2. The term $C_1/L$ is added because in the existing literature, it is common to assume a simple fit of the form $A + B/L$ and thereby neglect the logarithmic corrections and the mandatory term $C_2/L^2$. We should therefore investigate the role of such a term in our analysis.

If we take the term $C_1/L$ into account for the fits, as shown in Fig. 5.11(a), the constant $C_1$ is about 100 times smaller than $C_2$, indicating that such a term, if it exists, is very small. At the same time, the data seems to collapse, which was not the case in $d = 2$. It might be a coincidence. The estimated $\gamma_\infty$ from the fits are in perfect agreement to the literature value $\beta\gamma_\infty = 0.434$ [Hasenbusch and Pinn, 1994]. If we ignore a term of the form $C_1/L$ completely [as shown in Fig. 5.11(b)], the quality of the fits is not affected and no systematic error can be detected.

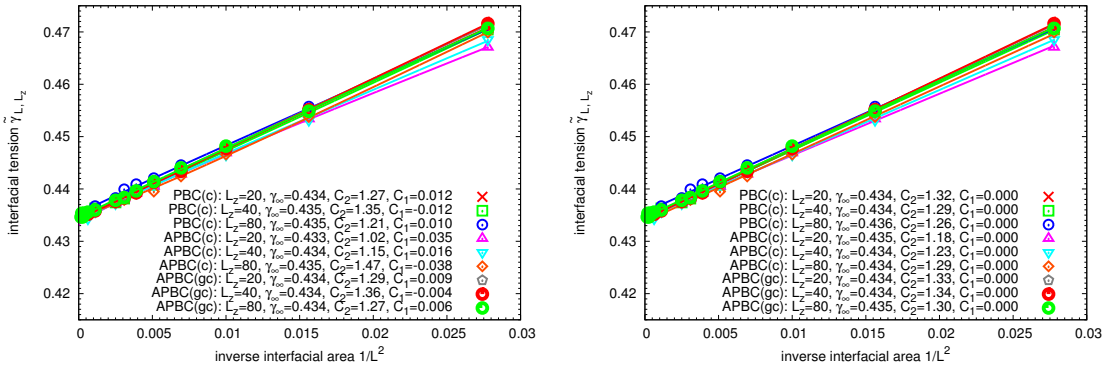


(a) (b)

Figure 5.11: Finite-size scaling of the reduced interfacial tension defined in Eq. (5.69) with fit parameters $\gamma_\infty, C_1$ and $C_2$ for the three-dimensional Ising model at $k_\mathrm{B}T/J = 3$. (a) Various combinations of boundary conditions and ensembles are shown for $L_z = 20, 40, 80$ in each case, as indicated. In (b), the same data is shown but the fits do not include $C_1$.

The existence of a term of the form $C_1/L$ is not supported by the data. Furthermore,

[4]For the Ising model, the lattice spacing is an obvious choice.

from a physical point of view, such a correction is inexplicable: Consider a similar geometry as before, but in the direction parallel to the interfaces, we now use free boundary conditions (which then act as a wall) instead of periodic boundary conditions. In such a situation, one can measure the line tension $\gamma_{\text{line}}$ [Schimmele et al., 2007] as a contribution to the free energy $\Delta F = \gamma A + \gamma_{\text{line}} S$ where $S$ is the length of the contact line between the two phases and a wall. This has been done successfully [Winter et al., 2009a,b]. On the other hand, if a term $C_1/L$ existed, this would imply that there is also some kind of line tension in systems where no walls are present. If this was the case, the simulations in [Winter et al., 2009a,b] could not have yielded sensible results. Therefore, it is important to stress that a term $C_1/L$ does not exist, for it is not detected in our simulations. This is important because while it is obvious from the results for the three-dimensional Ising model, the situation is not so simple if considering more complicated models where the computational cost to do a similarly thorough finite-size scaling is much higher. This will be discussed in chapter 6.

### 5.2.4 Further Remarks

#### Generalization to O(n) Models with n > 1

The Ising model is the special case $n = 1$ of the so-called $O(n)$ models. The characteristic features of these models are an order parameter field with $n$ components and an interaction energy function which depends on the local dynamic variables and is $O(n)$ invariant. Other examples of $O(n)$ models are the XY model ($n = 2$) and the Heisenberg model ($n = 3$).

If one applies antiperiodic boundary conditions in $z$-direction, the $n$-dimensional spins can gradually turn from pointing upwards to downwards across the whole system. This minimizes the energy cost to form an interface. In an Ising-like system, there are only two possibilities for the spins (up or down), hence the interface is always localized. This can also be seen from the Hamiltonian

$$\mathcal{H} = -J \sum_{\langle i,j \rangle} \boldsymbol{S}_i \cdot \boldsymbol{S}_j = -J \sum_{\langle i,j \rangle} cos(\theta_{ij}) \approx -J \sum_{\langle i,j \rangle} \left(1 - \frac{\theta_{ij}^2}{2}\right) \tag{5.70}$$

where the sum ranges over all next neighbors. In this case $|\boldsymbol{S}_i| = 1$ for all $i$. The approximation is only valid for small angles between the spins, which is valid for an elongated system. In the case of a one-dimensional system with antiperiodic boundary conditions, the spin orientation changes by an angle of $\pi$ over the whole linear dimension $L_z$. Hence each pair of spins along this direction will try to minimize

its energetic cost, so that the angles are on average $\theta_{ij} = \pi/L_z$. Hence the energetic cost of the interface is given by

$$E_{\text{interface}} \approx \frac{J}{2} \sum_{\langle i,j \rangle} \frac{\pi^2}{L_z^2} = \frac{J\pi^2}{2L_z} \tag{5.71}$$

Here, we have restricted ourselves to a one-dimensional system. The generalization to higher dimensions is straightforward, as the spins in the planes perpendicular to $L_z$ will be parallel to each other.

While in the ground state of an Ising chain, the cost of a kink (domain boundary) is $2J$ and hence finite, for the XY and Heisenberg chains, the domain boundary energy hence vanishes (for $L_z \to \infty$). Analogously, in higher dimension an interfacial tension does not exist! However, the cost of forming domain walls in isotropic systems then is described by a higher order term (the so-called "helicity modulus" [Fisher et al., 1973]).

### Generalization beyond the Ising model

In the discussion of finite-size effects so far, one always has an additional term of the form to the const $/L^{(d-1)}$ which is weaker than the $\ln(L)/L^{d-1}$ terms. At the same time, this term is very complicated, since its prefactor consists of several unknown factors.

The constant $l_z$ can be interpreted as follows. In a quasi-one-dimensional geometry, the translational entropy of the interfaces leads to a multidomain structure instead of a state with two bulk phases separated by two interfaces. The typical distance $\xi_L$ between domain walls is given by (see equation (6.11) in [Brézin and Zinn-Justin, 1985])

$$\xi_L = A(T) L^{(3-d)/2} \exp(L^{d-1} \beta \gamma_\infty) \tag{5.72}$$

where $A(T)$ is a temperature-dependent constant and $\gamma_\infty$ is the interfacial tension in the thermodynamic limit. This equation coincides with an exact transfer matrix result[5] in $d = 2$, where

$$\xi_L \propto L^{1/2} \exp(L \beta \gamma_\infty) \tag{5.73}$$

Thus, defining

$$\xi_L = \exp(L^{d-1} \beta \gamma_{L,\text{eff}}) \tag{5.74}$$

one obtains

$$\beta \gamma_{L,\text{eff}} = \beta \gamma_\infty + \frac{3-d}{2} \frac{\ln(L)}{L^{d-1}} + \frac{\text{const}}{L^{d-1}} \, . \tag{5.75}$$

[5] See the works of M. N. Barber in chapter 2 of [Domb and Lebowitz, 1983].

Note that this corresponds to (5.34). In a multidomain situation the translational entropy has been taken into account by considering multiple domains in the long strip. The arrangement of all interfaces together has a translational entropy proportional to $\ln L_z$, but per interface this term vanishes with the number of interfaces.

Considering the case of a single interface, stabilized by antiperiodic boundary conditions, the scaling behavior is (compare to (5.41))

$$\beta\gamma_L = \beta\gamma_\infty + \frac{3-d}{2}\frac{\ln L}{L^{d-1}} - \frac{\ln L_z}{L^{d-1}} + \frac{\text{const}}{L^{d-1}} \tag{5.76}$$

If one recalls now how the interfacial width due to capillary waves scales as $w_L^2 \propto L^{3-d}/(\beta\gamma)$, so that

$$\ln w_L = \frac{3-d}{2}\ln L + \text{const} \tag{5.77}$$

then one can write

$$\beta\gamma_L = \beta\gamma_\infty - \frac{\ln(L/w_L)}{L^{d-1}} + \frac{\text{const}}{L^{d-1}}\ . \tag{5.78}$$

This equation suggests that the natural length scale for all distances in $z$-direction is simply the interfacial width $w_L$. This can already be seen from (5.72)

$$\xi_L/w_L \propto \exp(L^{d-1}\beta\gamma\infty) \tag{5.79}$$

that $w_L$ sets the length scale for $\xi_L$. If $\xi_L$ approaches $w_L$, the interfaces start to interact with each other. The quantity $L_z/w_L$ counts the number of possibilities where the interface is located within the box. This interpretation suggests that the generalization to off-lattice systems is possible without any problems, since the natural length scale is provided by the interfaces themselves.

### Generalization of Finite-Size Effects to Spherical Interfaces

In section 5.1.2, the translational entropy of the interface in the box and the domain breathing effect was discussed for planar interfaces. One can also consider the case of a droplet with a compact shape in a box. For simplicity, the Ising language will be used for this discussion.

If one fixes the magnetization $m$ of a cubic box with volume $L^d$ with periodic boundary conditions in all directions in the droplet regime (see section 2.2.2), the phase with positive magnetization $m_l$ will gather into a droplet while the phase with negative magnetization $m_v$ will surround it. In equilibrium, the droplet will on average have a radius $R_{\text{eq}}$ and the magnetization $m_{\text{eq},l} = m_{\text{coex}}$ while the surrounding will have the magnetization $m_{\text{eq},v} = -m_{\text{coex}}$.

Since the position of the droplet is not fixed, the translational degrees of freedom of the droplet in all directions give rise to a translational entropy

$$\Delta S = \ln L^d \tag{5.80}$$

and therefore a free energy difference

$$\beta \Delta F_{\text{int}} = -d \ln L \, . \tag{5.81}$$

Capillary waves also occur on curved interfaces. For a planar surface, recall (5.34), where $\Delta F = \frac{3-d}{2} \ln L = \frac{3-d}{2(d-1)} \ln(L^{d-1})$ so that for a droplet with surface area $A$, one can speculate

$$\Delta F_{\text{int}} = \frac{3-d}{2(d-1)} \ln A \, . \tag{5.82}$$

To discuss the domain breathing effect, first consider the equilibrium, where, assuming the droplet is spherical with radius $R_{\text{eq}}$, volume $V_{\text{drop}}(R_{\text{eq}})$ and surface $S_{\text{drop}}(R_{\text{eq}})$, one can write

$$\left(L^d - V_{\text{drop}}(R_{\text{eq}})\right) m_{\text{eq},v} + V_{\text{drop}}(R_{\text{eq}}) m_{\text{eq},l} = m \, . \tag{5.83}$$

Now if due to bulk fluctuations, the magnetizations $m_l$ and $m_v$ differ from their equilibrium values, the droplet radius changes by $R = R_{\text{eq}} + \Delta R$, so that

$$\left[L^d - V_{\text{drop}}(R_{\text{eq}}) - S_{\text{drop}}(R_{\text{eq}}) \Delta R\right] m_v + \left[V_{\text{drop}}(R_{\text{eq}}) + S_{\text{drop}}(R_{\text{eq}}) \Delta R\right] m_l = m \, . \tag{5.84}$$

Subtracting the equations from each other yields

$$\begin{aligned} 0 = L^3 \left(m_v - m_{\text{eq},v}\right) + V_{\text{drop}}(R_{\text{eq}}) \left[ - m_v + m_{\text{eq},v} + m_l - m_{\text{eq},l}\right] \\ + S_{\text{drop}}(R_{\text{eq}}) \Delta R \left(m_l - m_v\right) \end{aligned} \tag{5.85}$$

or

$$\begin{aligned} S_{\text{drop}}(R_{\text{eq}}) \Delta R \left(m_l - m_v\right) = -L^3 \left(m_v - m_{\text{eq},v}\right) \\ - V_{\text{drop}}(R_{\text{eq}}) \left( [m_l - m_{\text{eq},l}] - [m_v - m_{\text{eq},v}] \right) \end{aligned} \tag{5.86}$$

On the right side, the expressions $m_l - m_v$ and $[m_l - m_{\text{eq},l}] - [m_v - m_{\text{eq},v}]$ are of the same order. Assuming that the droplet's volume is much smaller than the box volume ($R_{\text{eq}}^3 \ll L^3$), which is usually the case, the term with $V_{\text{drop}}(R_{\text{eq}})$ can be neglected against the term with $L^d$. Therefore

$$\Delta R \approx -\frac{L^d}{S_{\text{drop}}(R_{\text{eq}})} \frac{m_v - m_{\text{eq},v}}{m_l - m_v} \approx -\frac{L^d}{S_{\text{drop}}(R_{\text{eq}})} \frac{\delta m_v}{2 m_{\text{coex}}} \tag{5.87}$$

with $\delta m_v = m_v - m_{\mathrm{eq},v}$ and $m_l - m_v \approx 2m_{\mathrm{coex}}$. As this equation shows, the fluctuations in the surrounding vapor cause a fluctuation of the droplet radius. The negative sign means that the magnetization in the vapor has to decrease for the droplet radius to become larger. This equation corresponds to (5.18), where a similar equation was derived for the case of a flat interface. In two and three dimensions, the equation turns into

$$d = 2: \qquad \Delta R \approx -\frac{L^2}{2\pi R_{\mathrm{eq}}} \frac{\delta m_v}{2m_{\mathrm{coex}}} \tag{5.88}$$

$$d = 3: \qquad \Delta R \approx -\frac{L^3}{4\pi R_{\mathrm{eq}}^2} \frac{\delta m_v}{2m_{\mathrm{coex}}} \tag{5.89}$$

The following procedure is analogous to the case of flat interfaces in section 5.1.2: One can approximate the probability distribution $P_L(\delta m)$ by a Gaussian distribution with variance

$$\left\langle (\delta m)^2 \right\rangle = \frac{k_{\mathrm{B}} T \chi}{L^d} \ , \tag{5.90}$$

where $\chi$ is the susceptibility of the system in its current state, and obtain

$$\left\langle (\Delta R)^2 \right\rangle = \frac{k_{\mathrm{B}} T \chi}{\left(2m_{\mathrm{coex}} S_{\mathrm{drop}}(R_{\mathrm{eq}})\right)^2} L^d \ . \tag{5.91}$$

The interface of the droplet can therefore fluctuate by a distance of order $\sqrt{\langle (\Delta R)^2 \rangle}$, which corresponds to an entropy gain ($l_R$ is an unknown constant to make the logarithm dimensionless)

$$\Delta S = k_{\mathrm{B}} \ln \left( \sqrt{\langle (\Delta R)^2 / l_R \rangle} \right) \tag{5.92}$$

and a free energy difference

$$\beta \Delta F_{\mathrm{int}} = -\frac{d}{2} \ln L + \ln(S_{\mathrm{drop}}(R_{\mathrm{eq}})) + \mathrm{const} \ . \tag{5.93}$$

Together with the contributions from translational entropy (5.81) and capillary waves (5.82), the effective interfacial tension is given by

$$\beta \gamma_L = \frac{\beta F_{\mathrm{int}}}{A} = \beta \gamma_\infty - \frac{d}{2} \frac{\ln L}{A} + \frac{\ln A}{A} - d \frac{\ln L}{A} + \frac{3-d}{2(d-1)} \frac{\ln A}{A} + \frac{\mathrm{const}}{A} \tag{5.94}$$

$$= \beta \gamma_\infty - \frac{3d}{2} \frac{\ln L}{A} + \frac{1+d}{2(d-1)} \frac{\ln A}{A} + \frac{\mathrm{const}}{A} \tag{5.95}$$

This equation yields for two and three dimensions the following finite-size scaling

$$d = 2: \qquad \beta\gamma_\infty - 3\frac{\ln L}{A} + \frac{3}{2}\frac{\ln A}{A} + \frac{\text{const}}{A} \tag{5.96}$$

$$d = 3: \qquad \beta\gamma_\infty - \frac{9}{2}\frac{\ln L}{A} + \frac{\ln A}{A} + \frac{\text{const}}{A} \tag{5.97}$$

so the size effects are much more pronounced than for slab configurations.

These corrections have not been taken into account in the studies of curvature corrections to the interfacial tensions of droplets and bubbles done by [Block et al., 2010; Tröster and Binder, 2012; Tröster et al., 2012], since they were unknown at the time of these studies. A re-analysis of the data obtained in these studies in the light of the above results is in progress (A. Tröster, private communication).

## 5.3 Conclusion

In this chapter, we have established a theory to predict the finite-size scaling behavior of the interfacial tension for any model and phase coexistence. The theory was motivated and tested by using the two- and three-dimensional Ising model. Here, the results for two dimensions are interesting because one can compare the results with results from exact calculations. In the three-dimensional Ising model, we found that Eq. (5.47), which is the central result of this chapter, still holds, and that although in the literature, a finite-size scaling using a term $C/L$ was used, there was no evidence found for such a term.

The underlying phenomena of the scaling ansatz given by Eq. (5.47) are independent of the model, as they arise from entropic degrees of freedom. Hence, we can use the values for the universal constants $x_\perp$ and $x_\parallel$ in Table 5.1 to improve predictions of the interfacial tension in the thermodynamic limit. Note that while in this thesis, the ensemble method is used to compute interfacial tensions, the finite-size scaling results are of general validity and can also be used when using alternative methods [cf. section 4.2]. The next step is to apply this ansatz to off-lattice models, especially those where we can examine crystal-liquid coexistence.

# Chapter 6

# Finite-Size Scaling of the Interfacial Tension beyond the Ising Model

In this chapter, the ensemble switch introduced in chapter 4 will be used to compute interfacial tensions for off-lattice models. The main goal is to apply and validate also in this case the finite-size scaling ansatz Eq. (5.47), and the secondary goal is to get accurate predictions for the interfacial tension $\gamma_\infty$ in the thermodynamic limit for certain models. For off-lattice models, there is no analog to the antiperiodic boundary conditions which were very useful in validating Eq. (5.47). Therefore we will focus on the PBC(c) case, i.e. canonical ensembles with periodic boundary conditions in all directions and two interfaces in the system.

To this end, the Lennard-Jones model [cf. section 2.3.1] is considered first, as an example model for liquid-vapor transitions. Since liquid-vapor interfaces are conceptually simpler than solid-liquid interfaces, this model is a good candidate to test the theory of chapter 5 and extend the scope to off-lattice models. This is the topic in section 6.1. After this, section 6.2 applies the same analysis to solid-fluid interfaces in hard sphere systems [cf. section 2.3.3] and the soft effective AO model [cf. section 2.3.4]. The finite-size scaling ansatz presented in chapter 5 depends only on general entropic degrees of freedom of the interface(s). Therefore, one expects that it is valid for any kind of interface between coexisting phases. Finally, in section 6.3, various extensions of the ensemble switch method are discussed to improve performance.

Note that parts of the results of this chapter appeared in [Schmitz et al., 2014b]. A further publication on the results for hard spheres and the soft effective AO model will be prepared.

## 6.1 Liquid-Vapor Interfaces

### 6.1.1 Introduction

The truncated and shifted Lennard-Jones fluid introduced in section 2.3.1 is considered here as a generic off-lattice system. This system has a dense phase denoted as liquid and a less dense phase denoted as vapor. The interfacial tension for the liquid-vapor interfaces can be computed using the probability distribution method [see section 4.2], which makes this method an excellent candidate to test the scaling ansatz given by Eq. (5.47). We work at the temperature $k_\mathrm{B}T/\varepsilon = 0.78$ which is well below the critical point (which is at $k_\mathrm{B}T/\varepsilon = 0.999$, see section 2.3.1). At this temperature, the interfacial tension has been calculated previously for the same model [Block et al., 2010]. Note that we choose $\varepsilon$ and $\sigma$ as the natural energy and length scales for our system, so that $\varepsilon = 1$ and $\sigma = 1$.

As was mentioned in section 4.4, one can either use local or nonlocal moves for the particle movements through the system. For the Ising case, we only considered nonlocal moves, but for the off-lattice systems, we will use both local moves, where a Monte Carlo move consists of moving a particle to a position in the vicinity of its current position, and nonlocal moves, where the new position can be anywhere in the simulation box. We expect the latter to make the algorithm converge much faster, but essentially, the results should agree after sufficient equilibration.

### 6.1.2 Finite-Size Scaling for a Lennard-Jones Fluid

To test the finite-size scaling ansatz Eq. (5.47) for the Lennard-Jones fluid, we proceed as in the previous chapter by checking the dependence on $L$ and $L_z$ independently. Note that contrary to the Ising model, we can only consider periodic boundary conditions in a canonical ensemble, where the predominant Monte Carlo move is the movement of one particle within the box. This can be either a local move, where the new position of a particle is in the vicinity of the current position, or nonlocal moves, where the new position can be anywhere in the simulation box.

Figure 6.1 shows the free energy $\Delta F(\kappa)$ as a function of the successive umbrella window index $k$, where we have used the spacing given by Eq. (4.17a). While Fig. 6.1(a) shows that the interfacial free energy $\Delta F$ depends on the cross-section area of the interface, Fig. 6.1(b) shows the subtle finite-size effects. If there were no finite-size effects, the curves should not depend on $L_z$ at all and lie on top of each other. For a discussion of the shape, please refer to section 4.4.

Consider the dependence on $L_z$ first. Figure 6.2 shows that the data is well represented

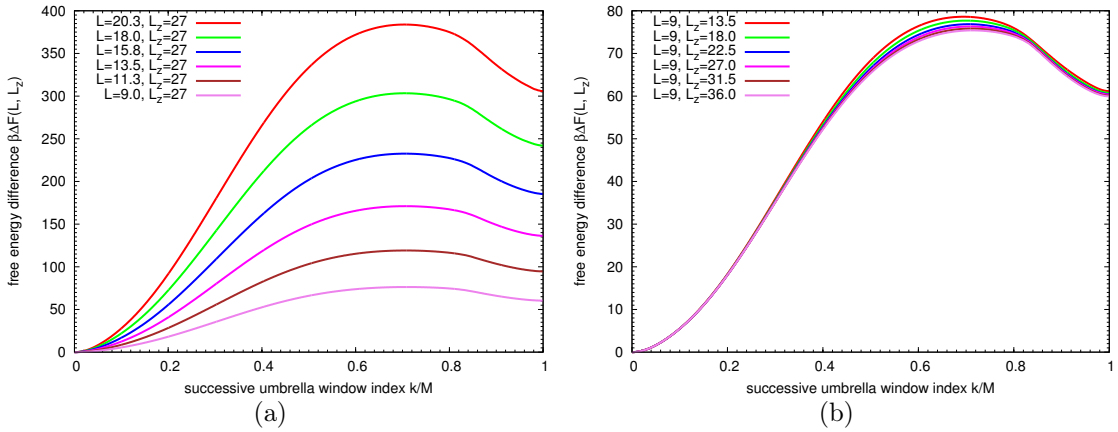


Figure 6.1: Free energy $\Delta F(\kappa)$ versus $\kappa$ for the Lennard-Jones fluid introduced in section 4.3. (a) The box length $L_z$ is kept constant as indicated, while the cross-sectional area $L^2$ is increased linearly. (b) The area $L^2$ is fixed and $L_z$ is varied, as indicated. Note that in (b), the curves are not perfectly equal. This hints at some non-trivial finite-size scaling behavior, which will be discussed in the next chapters.

by straight line fits whose slope is fixed at $-x_\perp = -3/4$, which is the expected value for periodic boundary conditions in a canonical ensemble, as given in Table 5.1. This is true for all three different cross-section areas $L^2$, giving confidence that the ensemble switch method can also be applied to off-lattice systems. Note that these fits do not give an estimate on $\gamma_\infty$ but can only serve to test the scaling ansatz.

Examining Figure 6.2 more closely, one observes that there are preliminary data points included which do not follow the expected dependence but instead seem to approach the fitted straight line from above (they are omitted from the fit). The fact that the convergence is quite slow is a consequence of using local moves. In the previous chapter, the main Monte Carlo move chooses two spins of opposite sign and makes an attempt to flip them simultaneously. As the spins can be anywhere in the simulation box, the system can equilibrate quickly and the interface can explore the whole box by moving in $\pm z$-direction rather fast.

For the Lennard-Jones system, the local moves slow down the movement of the interface significantly. This can also be seen in Fig. 6.3, where the mean squared displacement of the interfaces are shown as a function of "time" $\tau$, where time refers to Monte Carlo steps per particle. Note that the lower set of curves in Fig. 6.3(a) belongs to local moves while the upper set belongs to nonlocal moves. The mobility of the interfaces is about a factor 100 larger if using nonlocal moves, which is a striking result. The diffusion of the interfaces behaves like $\langle (z(\tau) - z(0))^2 \rangle = 2Dt$,

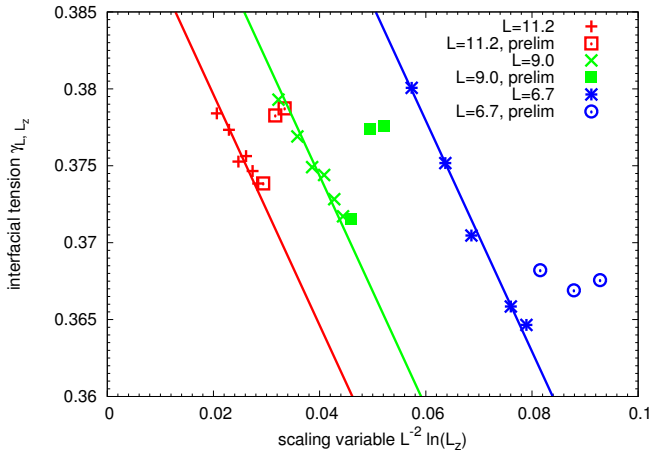


Figure 6.2: Finite-size scaling of the interfacial tension $\beta\gamma(L, L_z)$ at constant $L$ for the Lennard-Jones fluid. The lines are fits to the data with fixed slope $-x_\perp = -3/4$, according to Table 5.1. Local Monte Carlo moves have been used to obtain these data. The figure also shows additional data points which are not taken into account by the fit as they are not fully equilibrated (see discussion in the main text).

since it is a random Brownian motion in one dimension. The diffusion constant $D$ can be extracted from the curves in Fig. 6.3(a) by fitting straight lines. In Fig. 6.3(b) these diffusion constants are plotted against the inverse cross-section area $L^{-2}$ of the system. As is expected, the diffusion constant decreases for larger interfaces, which are more inert than smaller ones. Comparing local and nonlocal moves, the diffusion constant is about a factor 100 larger for nonlocal moves. Hence, it is clear that nonlocal moves[1] are the more favorable choice.

During the simulations, we noticed that it is not so much the fact that the interface has to visit every position in the simulation box. Instead, there are two major types of configurations. On the one hand, there are configurations, where the interfaces are at the positions of the boundaries[2], which is true for small $\kappa$. On the other hand, near the end of the integration, when the system is almost in the state of one combined box with two interfaces, the interfaces can be anywhere in the box

[1] From a conceptual standpoint, the Monte Carlo moves in the Ising model, which conserve magnetization by flipping spins of opposite orientation, are equivalent to nonlocal moves in the Lennard-Jones fluid. Using the lattice gas viewpoint instead of the Ising viewpoint, the flipping of the two spins means a displacement of a liquid particle from one place to another, which is exactly the definition of nonlocal moves in off-lattice models.

[2] Of course the interfaces are created near the boundaries, where the two separate boxes are combined by shifting the periodic boundary conditions. For more information, please refer to section 4.3.

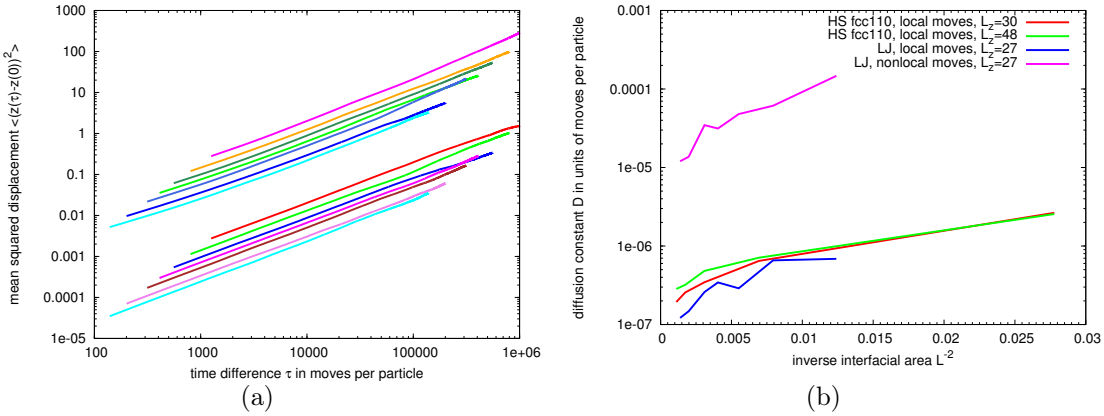


(a) (b)

Figure 6.3: (a) Mean squared displacement of the interface versus Monte Carlo steps per particle for a Lennard-Jones mixture. The top set of curves shows data with nonlocal moves in a box with $L_z = 27$ and $L = 9, 11, 13, 16, 18, 22, 27$ (from top to bottom). The bottom set of curves shows data with local moves for the same box dimensions. (b) Diffusion constant $D$ versus inverse area $L^{-2}$ of the interface. With nonlocal moves, the mobility of the interface is about a factor 100 higher than with local moves. The mobility of an interface between a hard sphere crystal and fluid is similar to the liquid-vapor case.

and do not necessarily stay in the vicinity of the boundaries. While the reaction coordinate $\kappa$ goes from 0 to 1, the former type of configurations is predominant first but becomes less dominant while the latter type occurs more often. Of course, at $\kappa = 0$ and $\kappa = 1$, the box boundaries have no effect on the system whatsoever but act as normal periodic boundary conditions.

On the other hand, the interfaces can be anywhere else in the box so that the system has two interfaces and additionally, the system includes the superposition of periodic boundary conditions at the boundaries. The latter configurations typically occur near the end of the integration, where the system is almost in the state of one combined box and the boundaries have a rather small effect on the system. During the integration, the former type of configurations is predominant first, but as the integration proceeds, becomes less dominant while the latter type occurs more and more often. In Fig. 4.8, one can see how the interface is created near the boundaries. Once it is fully present, it can move away from the boundary and explore the whole simulation box.

The transition between the two can only be accurately sampled if the system can switch often enough between the two types, where “often” is meant in comparison to

the total simulation time. Since the nonlocal moves promote the movement of the interface and allow to traverse phase space more quickly, the transition is sampled with much less effort. However, we shall continue to use both to compare the quality of the results. It is expected that the results using local and nonlocal moves agree once the simulations run long enough.

Ignoring what we know about the scaling ansatz Eq. (5.47) for the moment, the bare results from the ensemble switch method are shown in Fig. 6.4.

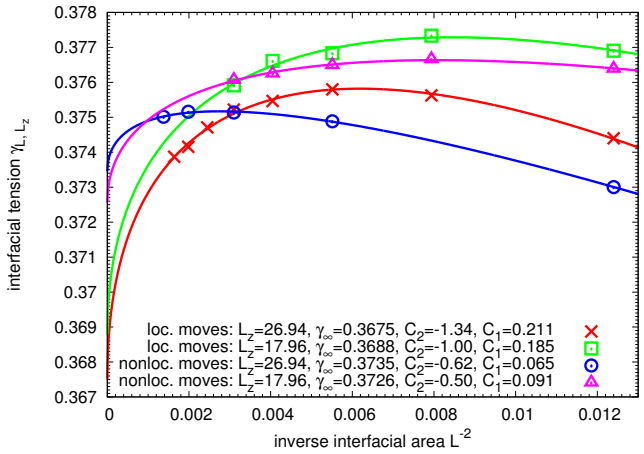


Figure 6.4: Finite-size scaling of the interfacial tension $\beta\gamma(L, L_z)$ at constant $L_z$ for the Lennard-Jones fluid using either local or nonlocal moves, as indicated, and choosing two values of $L_z$ for each kind of move. Note that the logarithmic corrections Eq. (5.47) are ignored here. Instead a fit of the form (6.1) is used.

Note that one cannot rate the quality of the data using local or nonlocal moves by looking at this plot. The figure includes fits of the form

$$\beta\gamma(L, L_z) = \beta\gamma_\infty + \frac{C_1}{L} + \frac{C_2}{L^2} \tag{6.1}$$

including a term $C_1/L$. This is the same ansatz used in section 5.2.3 where similar results for the three-dimensional Ising model are discussed. As stated there, a term $C_1/L$ should not occur but was used for finite-size scaling in the literature nevertheless [Block et al., 2010]. Applying this ansatz to the data in Fig. 6.4, the two sets of data agree in their estimates of $\beta\gamma_\infty$. Furthermore, the data based on local moves do not appear to be irregular, although the predictions on $\beta\gamma_\infty$ for the two types of moves differ significantly. Also, the constants $C_1$ and $C_2$ differ depending on which kind of moves are used. The fact that the convergence using nonlocal moves is much better [cf. Fig. 4.12] indicates that the quality of the data using nonlocal

moves is much more reliable. Note that one would not be able to rate the quality of the data using local moves without the nonlocal data. The term $C_1/L$, which should not occur at all, is more dominant in the case of local moves, which implies that it rather reflects the insufficient equilibration of the simulations.

So far, we did not make use of the logarithmic corrections predicted in chapter 5. The picture becomes much clearer if we now make use of Eq. (5.47) by subtracting the logarithmic corrections, as done in Eq. (5.69), so that the reduced interfacial tension is given by

$$\beta\widetilde{\gamma}(L, L_z) = \beta\gamma(L, L_z) + \frac{x_\perp \ln L_z - x_\parallel \ln L}{L^2} = \beta\gamma_\infty + \frac{C_1}{L} + \frac{C_2}{L^2} \tag{6.2}$$

where we still allow the unphysical contribution $C_1/L$. Fig. 6.5 shows the results.

It is striking that after the subtraction of the logarithmic contributions, the coefficient $C_1$ is much smaller for both kinds of moves. This indicates that in previous analyses, the logarithmic corrections might have been interpreted as corrections of order $L^{-1}$. In the nonlocal case, the coefficient $C_1$ is almost negligibly small and can be omitted from the fit. Then the data are perfectly represented by the scaling ansatz Eq. (5.47) with $C_2$ being the constant $C$ in Eq. (5.47). Also the data at different $L_z$ nicely collapse. The data based on local moves are also compatible with the assumption that $C_1 = 0$. If $C_1/L$ is allowed, the prediction of $\beta\gamma_\infty$ is systematically smaller, which is due to the combined problem of insufficient equilibration and a flawed ansatz for the fit.

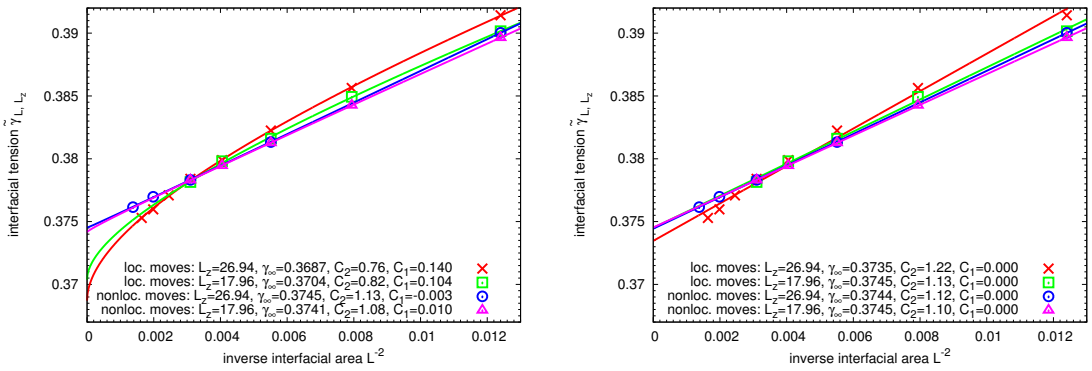


(a) (b)

Figure 6.5: Finite-size scaling of the reduced interfacial tension $\beta\widetilde{\gamma}(L, L_z)$. The same data as in Fig. 6.4 is used, but the logarithmic corrections are subtracted. The fit parameters in (a) are $\gamma_\infty, C_1$ and $C_2$, while in (b), $C_1$ is set to zero.

In summary, using nonlocal moves greatly increases the sampling performance of the method in the context of liquid-vapor interfaces. The data suggest that the interfacial tension at the chosen temperature is $\beta\gamma_\infty = 0.3745 \pm 0.0005$. This result is consistent with an earlier result for the same model [Block et al., 2010].

As the method is now tested and yields reliable information on the interfacial tension, another production run with another $L_z$ could further improve the prediction if necessary. We feel that these data indicate that a valid and versatile approach to study interfacial tensions between coexisting phases in simple and complex fluids and fluid mixtures has been developed, and expect that this approach will be taken up by other research groups in the future. A very interesting question at this point is, however, whether crystal-liquid interfaces can also be covered by Eq. (5.47). This is the main topic of section 6.2.

## 6.2 Solid-Liquid Interfaces

We now focus on the solid-liquid transition. In the case of hard spheres, we will instead use the term fluid since in this model, there is only a fluid phase and no further phase separation into liquid and vaporous phase. As discussed in section 4.2, solid-liquid interfaces are conceptually much more delicate, which is why predictions of the interfacial tensions spread so much [cf. Fig 4.1]. The main goal here is to test whether the finite-size scaling ansatz, which has been established for off-lattice liquid-vapor interfaces, is also valid in the solid-liquid case. An affirmative answer would greatly improve any simulation algorithm, since the finite-size scaling is then much clearer.

Note that the crystal structure makes nonlocal moves inappropriate, as the acceptance probability of removing a particle from the crystal and inserting it somewhere else in the crystal (or in the dense fluid surrounding the crystal) is extremely small. Even if such moves were possible, they would create defects and destroy the crystal structure. Hence we use local moves, which rather mimic typical fluctuations in the crystal, where a particle fluctuates around its equilibrium position, and analyze whether we have a similar effect from the small mobility. A very important complication is that there is not just an unique solid-fluid interface, but one must take the dependence of the interface orientation relative to the crystal lattices axes into account. Here, we focus on the (100), (110) and (111) orientations.

Since the crystalline structure determines the box dimensions, it is in general no longer possible[3] to choose $L_x = L_y = L$. If we instead fix the ratio $L_y/L_x$ in three

[3]For an fcc crystal with (100) orientation, $L_x = L_y$ is compatible with the crystalline structure, but

dimensions, Eq. (5.47) translates into

$$\beta\gamma(L_x, L_y, L_z) = \beta\gamma_\infty - x_\perp \frac{\ln L_z}{L_x L_y} + x_\parallel \frac{\ln L_x}{L_x L_y} + \frac{C}{L_x L_y} \tag{6.3}$$

with the same $x_\perp$ and $x_\parallel$ but a different constant $C$. The reason behind this is that in three dimensions, the only contribution to the term with $x_\parallel$ is the domain breathing effect [see section 5.1.2], where all the $(d-1)$-directions parallel to the interface contribute equally to a term $\ln(L^{d-1})$. Hence we can write in three dimensions

$$\begin{aligned} \ln\left(L^{d-1}\right) \to \ln\left(L_x L_y\right) &= \ln\left(L_x^2\right) + \ln\left(\frac{L_y}{L_x}\right) \\ &= \ln\left(L_x^{d-1}\right) + \text{const} \end{aligned} \tag{6.4}$$

where the second term merely changes the constant $C$. Hence one can define a reduced interfacial tension as

$$\begin{aligned} \beta\widetilde{\gamma}(L_x, L_y, L_z) &= \beta\gamma(L_x, L_y, L_z) + \frac{x_\perp \ln L_z - x_\parallel \ln L_x}{L_x L_y} \\ &= \beta\gamma_\infty + \frac{C}{L_x L_y} \,. \end{aligned} \tag{6.5}$$

We shall now consider hard spheres first and the soft effective AO model afterwards.

### 6.2.1 Finite-Size Scaling for Hard Spheres

For the study of hard spheres, we use the coexistence packing fractions $\eta_s = 0.545$ and $\eta_f = 0.494$ [Hunter and Weeks, 2012] and the particle diameter $\sigma = 0.902875$, as stated in section 4.5. Figure 6.6 shows typical free energies $\Delta F(\kappa)$ for the free energy $F(\kappa)$ along the integration path for the hard sphere case. For a discussion of the shape, please refer to section 4.5.

Proceeding as before, consider the dependence on the linear dimension $L_z$ first. The data is more noisy than for the previous models, especially for the (111) direction. This is due to the limited amount of computing power and the increased demand for computing time necessary for each point. Additionally, as only local moves are possible, the sampling of the translational degrees of freedom of the interfaces requires much more computing time than in the liquid-vapor case. Nevertheless, the data in Fig. 6.7 indicates that the finite-size scaling ansatz Eq. (5.47) [or the

this is an exception.

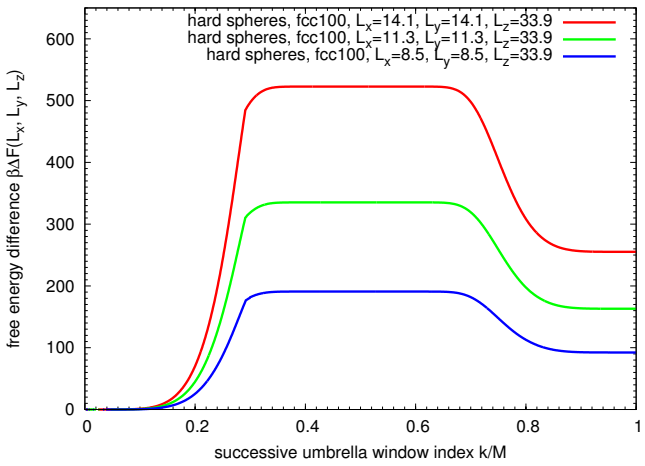


Figure 6.6: Free energy $\Delta F(\kappa)$ versus $\kappa$ for a hard sphere solid-fluid coexistence. The crystal structure is fcc (100). The curves show various cross-section areas $A = L_x L_y$ at constant box length $L_z$, as indicated. Note that the lengths are not given in units of $\sigma = 0.902875$ but in units of the lattice spacing, which is set to 1.

modified version Eq. (6.3), respectively] still holds for solid-liquid interfaces, where the slope is expected to be $-x_\perp = -3/4$ according to Table 5.1. This result had to be expected, since the final system (an elongated simulation box with a crystal slab separated by two interfaces oriented along the $z$-axis) is translationally invariant in $z$-direction due to periodic boundary conditions, and so (in full equilibrium) picks up an entropy contribution due to translation of the slab. The nontrivial question, of course, is whether this translational degree of freedom is actually picked up by the simulation algorithm (or rather stays "quenched" due to the limited investment of computing time).

The next step is to use Eq. (6.5) to determine the interfacial tension for various crystalline orientations. The results using the ensemble switch method are shown in Fig. 6.8. The data is compatible with a fit as predicted by Eq. (6.5), suggesting that indeed, the finite-size scaling analysis developed in chapter 5 is also valid for solid-liquid interfaces. The figure includes two data series for each orientation, each with a different $L_z$. After the subtraction of the logarithmic terms, the reduced interfacial tension should no longer depend on $L_z$, apart from higher order terms. Therefore, the discrepancy between the two sets can serve as an error estimation for the method. The resulting values are

$$\text{fcc (111)}: \ \beta\gamma_\infty = 0.518 \ , \tag{6.6a}$$

$$\text{fcc (110)}: \ \beta\gamma_\infty = 0.562 \ . \tag{6.6b}$$

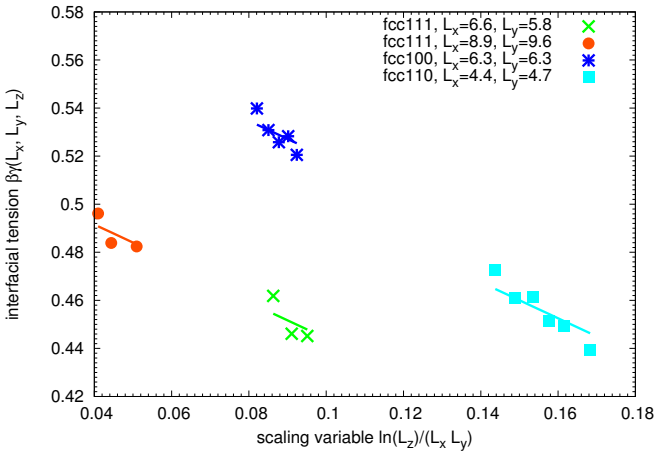


Figure 6.7: Finite-size scaling of the interfacial tension $\beta\gamma(L_x, L_y, L_z)$ at constant $L_x$ and $L_y$. The particle diameter is $\sigma = 0.902875$ and the cross-section areas are $L_x = 6.00\sigma, L_y = 5.20\sigma$ for the (111) orientation, $L_x = 4.00\sigma, L_y = 4.24\sigma$ for the (110) orientation and $L_x = 5.66\sigma, L_y = 5.66\sigma$ for the (100) orientation. The lines are fits with a fixed slope of $-x_\perp = -3/4$.

The fact that the (111) orientation has the lowest interfacial tension is in accordance with previous results, see Table 4.1. It is an interesting task to also compute the interfacial tension for the (100) orientation, but this must be left to future work. In the first place, these results show that the ensemble switch method combined with the finite-size scaling analysis presented in this thesis is a valuable tool to calculate the interfacial tension of solid-liquid interfaces. The results also indicate that finite-size effects have a considerable influence on the results and should not be neglected.

### 6.2.2 Finite-Size Scaling for the Soft Effective AO Model

As the soft effective AO model, which was introduced in section 2.3.4, is of interest for current work within our group, it was one task to produce results about the interfacial tension of the solid-fluid interface and especially the anisotropy. Therefore, three crystalline orientations are discussed here, namely (100), (110) and (111). Similarly to hard spheres, the (111) is expected to have the lowest interfacial tension. This can also be seen in Fig. 4.1.

Due to limited time and resources, the data in Fig. 6.9 does not contain data for two different $L_z$ for all orientations. For future work, it is recommendable to always use at least two different values of $L_z$ to have a consistency check and estimate the

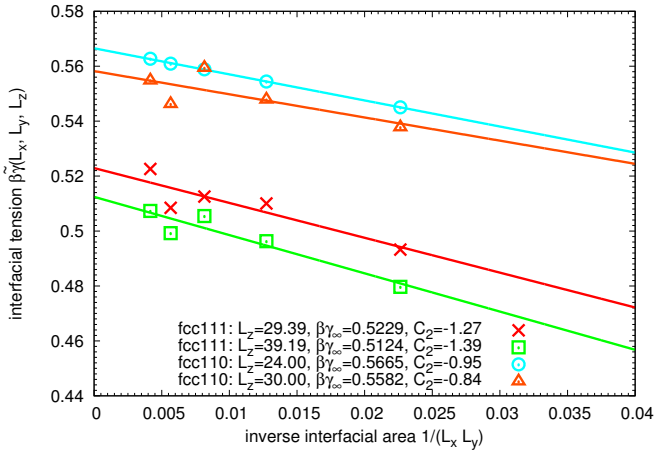


Figure 6.8: Finite-size scaling of the reduced interfacial tension $\beta\widetilde{\gamma}(L_x, L_y, L_z)$ for a hard-sphere solid-fluid coexistence at constant box length $L_z$. Various crystalline orientations are shown, as indicated. Note that the lengths are not given in units of $\sigma = 0.902875$ but in units of the lattice spacing, which is set to 1. Fits of the form as in Eq. (6.5) are included along with the resulting values of the fit parameters.

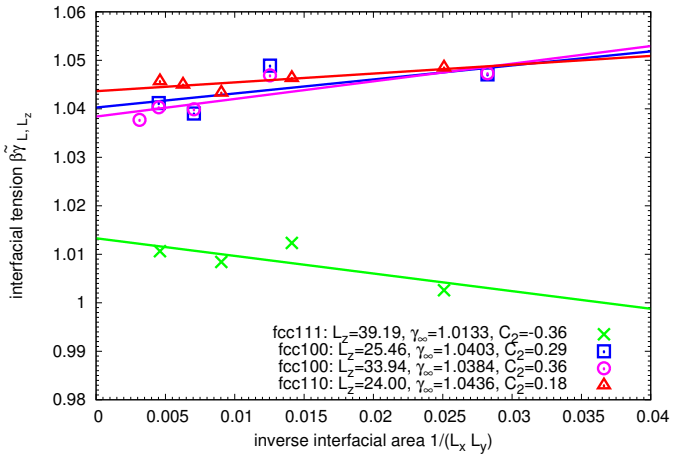


Figure 6.9: Finite-size scaling of the reduced interfacial tension $\beta\widetilde{\gamma}(L_x, L_y, L_z)$ for the soft effective AO model at constant box length $L_z$. Various crystalline orientations are shown, as indicated. Fits of the form as in Eq. (6.5) are included along with the resulting values of the fit parameters.

error. However, the data below is convincing enough to allow first conclusions. It is interesting to see that the two data series for fcc (100) at different $L_z$ agree in their prediction quite nicely, hinting at a dependable result, at least for the (100) orientation. The obtained interfacial tensions are

$$\text{fcc (111): } \beta\gamma_\infty = 1.013 \,, \tag{6.7a}$$
$$\text{fcc (110): } \beta\gamma_\infty = 1.044 \,, \tag{6.7b}$$
$$\text{fcc (100): } \beta\gamma_\infty = 1.039 \,, \tag{6.7c}$$

the (111) orientation is the energetically most favorable orientation, while the interfacial tension of the other two orientations are almost equal.

Since the density gap for the coexisting fluid and solid phases for this model is much wider than for the hard sphere case [cf. Fig. 2.5], and previous data [Zykova-Timan et al., 2010] for the effective AO model had indicated an interfacial stiffness twice as large than for hard spheres, one might speculate that the anisotropy of the interfacial tension is considerably more pronounced than for hard spheres. Indeed, Fig. 6.9 confirms that the interfacial tensions of the soft effective AO model are about twice as large as for hard spheres, but the relative differences due to anisotropy have not increased! This indicates that anisotropy effects on the shape of critical nuclei in this model should be very small, unlike the case of the Ising model at low temperatures [cf. chapter 3].

## 6.3 Further Remarks on Translational Entropy

The convergence of the free energy $\Delta F(\kappa)$ is slowest in the range where the interfaces can explore the whole simulation box and are no longer fixed to the boundaries [see Fig. 4.12]. It would be desirable to somehow get rid of this effect. In fact, many methods make an attempt to prohibit any movement of the interfaces along the $z$-direction, for example the method of Davidchack [cf. section 4.2 and the references given there], where runs are thrown away if the interface has moved "too far". Of course, there is some undesirable arbitrariness in such a procedure. The problem is that all constraints on the interfaces must be gone in the final state. Therefore, all the simulations presented in this thesis take the effects of translational entropy into account.

During the work on off-lattice systems, some new ideas arose on how to possibly enhance the simulation performance. Although the value of these new ideas has not yet been established, they nevertheless are listed here as an inspiration for future work.

### 6.3.1 Collective canonical Moves

A simple approach would be to enhance the translational freedom and help the interface to explore the full box faster. This is especially desired if nonlocal canonical moves are not an option. A straightforward strategy to achieve this is to implement collective canonical moves. Such a move consists of choosing a random vector and translate all particles at the same time by this vector. Note that in an ordinary system with periodic boundary conditions, the energy difference $\Delta E$ is zero, because the distances between the particles are unaltered. However, for the intermediate states in the ensemble switch method, namely those with $0 < \kappa < 1$, the boundary regions, i.e. the volume around the box boundaries of two boxes are glued together, introduce an inhomogeneity into the box so that the collective canonical moves become non-trivial moves, moving the interface through the box much faster than with local canonical moves. Because these moves are attempted and accepted with the standard Metropolis criterion and the random translation vector is chosen randomly, then detailed balance is fulfilled and the move is a valid Monte Carlo move.

While this move is quite expensive, as all particles have to be moved and the total energy has to be recalculated, it is sufficient to use it only with a low frequency. Collective canonical moves have not been used to produce any results in this thesis, but the results of preliminary tests look promising.

### 6.3.2 Introducing a Center-of-Mass Potential

Another idea is to fix the center of mass of the system, which is always situated in the center of the denser of the two phases using some weak potential of the form

$$V_{\mathrm{com}}(R_z) = \frac{A}{V}(R_z - R_{z,0})^2 \tag{6.8}$$

where $A$ is the amplitude, $V$ is the volume and $R_{z,0}$ is the reference position. This potential acts on the $z$-component only and provides a restoring force towards the reference position. Since the interfacial mobility is proportional to the inverse of the area [see also section 6.1.2], the volume $V$ in the denominator ensures that the potential vanishes in the thermodynamic limit, where the mobility of the interface vanishes also.

Unfortunately, when applying this ansatz, the potential changes the scaling behavior in a non-trivial way. Since no systematic dependence on $A$ was found, this idea was abandoned.

### 6.3.3 Freezing

A straightforward method to suppress movement in $z$-direction is to fix (or "freeze") some layers of particles in the system, e.g. a few crystal layers in the center of the crystalline region. The term freezing means that these particles are never taken into account for canonical moves. Instead they remain at their respective initial positions. Naively, one would assume that this is an elegant way to solve the problem.

However, the use of this approach is doubtable. The frozen planes act like additional interfaces in the system, and although their contribution to excess free energies presumably is very small, it still could be comparable to other finite-size corrections.

### 6.3.4 Using Walls

One can think of geometries where one uses walls and thereby create a situation where the interface is in the center of the box on average, similarly to antiperiodic boundary conditions or fixed-spin boundary conditions. Although this reduces the number of interfaces from two to one, adding walls introduces additional parameters to the system which themselves are not known very well. While the wall excess free energies can be obtained by independent simulations for both phases [Deb et al., 2012a], it is not obvious that in the end, the accuracy would be better than reached in Figs. 6.8 and 6.9.

## 6.4 Conclusion

In this chapter, the finite-size scaling ansatz was verified to be applicable to liquid-vapor and solid-liquid interfaces. As an example system for the liquid-vapor case, a truncated and shifted Lennard-Jones fluid was used, while for the solid-liquid case, hard spheres are considered, for they are of special interest as a reference system to test new methods. The ensemble switch method successfully confirms that the scaling ansatz still works for off-lattice models. Unfortunately, the results for the hard spheres and the soft effective AO model have only preliminary character. More definite results will require additional large scale simulations, and such an effort must be left to future work.

# Chapter 7

# Summary & Outlook

The main goal of this thesis was the study of the interfacial tension. This involved two parts. First, a preliminary examination of anisotropy effects was undertaken. Within the Ising model, it was found that macroscopic droplets below the roughening temperature have facets and assume a more and more cubic shape if the temperature is lowered. Above the roughening temperature, the facets disappear and the shape becomes rather spherical, but a closer examination shows that the shape is still anisotropic up to about 85% of the critical temperature. Since classical nucleation theory (CNT) always assumes perfectly spherical droplets, the deviation of the shape in the simulation leads to an underestimation of the nucleation barrier by CNT. Another result of this examination is that it is possible to distinguish at each lattice site between the droplet and its surroundings by taking into account the definition of physical clusters. It was shown that the presented definition correctly predicts the volume of droplets in the thermodynamic limit. However, in finite systems, there is still a deviation left due to surface excess particles. In contrast to the physical clusters, the geometrical cluster definition tremendously overestimates the droplet volume at high temperatures. Therefore, the use of the physical cluster definition is more sensible and highly recommended in the future.

The second part of this thesis focused on the accurate prediction of the interfacial tension, especially for solid-liquid interfaces, where current methods face difficulties and disagree with each other within their respective error bars. The investigation of this thesis to approach this problem consists of two components. First, a new simulation scheme called ensemble switch method is introduced which can be used to estimate the interfacial tension of liquid-vapor interfaces and solid-liquid interfaces. The second ingredient is a systematic finite-size scaling, for only then one can accurately predict the interfacial tension via extrapolation to the thermodynamic limit. In this context, a universal finite-size scaling ansatz has been proposed,

which is motivated by taking into account the entropic degrees of freedom of the interface(s) in the system. From the effects we have discussed, including a new mechanism called domain breathing, two logarithmic corrections arise, featuring universal prefactors which only depend on the chosen boundary conditions, ensemble and the dimensionality $d$ of the box.

These two ingredients have been combined to predict the interfacial tension for solid-liquid interfaces. Prior to that, the ensemble switch method and the finite-size scaling ansatz are thoroughly tested

1. for the two-dimensional Ising model, where the interfacial tension is known exactly,
2. for the three-dimensional Ising model, in order to test the ansatz in three dimensions,
3. for the three-dimensional Lennard-Jones model to validate the method and the ansatz in case of an off-lattice liquid-vapor interface and finally
4. for hard spheres as a prototype of a system with solid-liquid interfaces.

As has been demonstrated for the example of hard spheres [Table 4.1 and Fig. 4.1], previous methods to compute interfacial tensions may lead to results that systematically (far outside the error bars) disagree with each other, and the sources of these errors are not understood. Even for the much simpler case of the Ising model, a comprehensive analysis of systematic errors due to finite-size effects (simulations always deal with finite systems!) does not exist in the literature. Therefore, it was an inevitable and useful task for this thesis to try to fill this gap, and it can be said that for the Ising model, the situation is now fully understood, and also for interfaces between liquid and vaporous phases, a practically useful well-validated methodology has been developed. Also for the more difficult problem of solid-liquid interfaces, promising first steps for hard spheres and the soft effective AO model have been taken. The corresponding sections contain preliminary results, but it is clear that more work on the problem of solid-liquid interfaces is desirable, although a substantial investment of additional computer resources will be needed. Thus, this task must be left for future work. The machinery consisting of the ensemble switch method and the finite-size scaling ansatz is now well tested and ready to be applied to arbitrary interfaces between bulk phases. Of course, there is some room for conceptual improvement, and possible extensions have been discussed. Currently, the Monte Carlo program is highly parallelized, so it is very flexible for any architecture on supercomputers, making it a valuable and performant tool to predict interfacial tensions.

One immediate application of the results for the soft effective AO model is the shape of crystalline colloidal nuclei [Statt, 2015], which is completely determined by the anisotropy of the interfacial tension. Of course, compared to the Ising model droplets in this thesis, crystalline nuclei are more complicated and their shape is the result of the interplay of the interfacial tensions in different directions. The scope of this thesis allows to expect an anisotropy between the minimal and the maximal interfacial tension of up to 5%, where the (111) orientation is much more favorable compared to the (110) and (100) directions.

# Appendix A

# Supplementary Information

## A.1 The Capillary Wave Contribution to Finite-Size Scaling of the Interfacial Tension

In section 5.1.2, when discussing capillary waves and their influence on the finite-size scaling behavior, the contribution from capillary waves was motivated in two dimensions. An alternative treatment of the problem, which is not limited to two dimensions, starts with the capillary wave Hamiltonian. The capillary wave Hamiltonian of a two-dimensional interface in three-dimensional space is (see also section 2.5)

$$\mathcal{H} = \int_0^L \mathrm{d}x \int_0^L \mathrm{d}y \frac{\kappa}{2} \left|\boldsymbol{\nabla} h(x,y)\right|^2 \ . \tag{A.1}$$

The Hamiltonian for a one-dimensional interface in two-dimensional space is

$$\mathcal{H}_{cw} = \frac{\kappa}{2} \int_0^L \mathrm{d}x \left|\frac{\mathrm{d}h(x)}{\mathrm{d}x}\right|^2 \ . \tag{A.2}$$

In both cases, $\kappa$ is the interfacial stiffness and the function $h(x)$ or $h(x,y)$ parametrizes the interface. In this picture, there cannot be any overhangs. However, this can always be fulfilled after proper coarse-graining. By introducing the Fourier transform $h_q$ of $h(x,y)$ or $h(x)$, respectively, one obtains the capillary wave Hamiltonian

$$\mathcal{H}_{cw} = \frac{\kappa}{2} \left(\frac{L}{2\pi}\right)^{d-1} \int \mathrm{d}^{d-1}q \; q^2 h_q^* h_q \tag{A.3}$$

Since this Hamiltonian is harmonic, its partition function can be computed exactly. Note that $h_q$ and $h_q^*$ are independent variables corresponding to independent modes.

The partition function $\ln Z_{cw}$ and hence the free energy $\beta F_{cw} = -\ln Z_{cw}$ in the thermodynamic limit can be written in terms of path integrals

$$Z_{cw} = \int \mathcal{D}h_q \int \mathcal{D}h_q^* \exp\left(\frac{\beta\kappa}{2}\left(\frac{L}{2\pi}\right)^{d-1} \int \mathrm{d}^{d-1}q\, q^2 h_q^* h_q\right) \tag{A.4}$$

We consider the two-dimensional case first. Being interested in the effects on a finite interface in a box of size $L \times L_z$ with periodic boundary conditions parallel to the interface, it is convenient to introduce a lattice structure (with lattice spacing $a$) which provides a cutoff at large wavelengths. Write $L = Na$ with lattice spacing $a$ and an even number $N$. Of course, for the Ising model, such a lattice structure is provided by the model itself. In a finite box with a finite lattice spacing, the spectrum of possible wavenumbers $q$ is discrete. The Hamiltonian (A.3) is replaced by

$$\mathcal{H}_{cw} = \frac{\kappa}{2} \sum_{\nu} q_\nu^2 h_\nu^* h_\nu \tag{A.5}$$

with wavenumbers $q_\nu = \frac{2\pi\nu}{N}, \nu = 1, 2, \ldots, N$. The mode $q_0 = 0$ is excluded, because it reflects translation of the interface as a whole. The partition function (A.4) then becomes

$$Z_N = \prod_{\nu=1}^{N} \int_{-\infty}^{\infty} \mathrm{d}h_\nu \int_{-\infty}^{\infty} \mathrm{d}h_\nu^* \exp\left(-\frac{\beta\kappa}{2} q_\nu^2 h_\nu^* h_\nu\right) . \tag{A.6}$$

To solve the integral, write $h_\nu = X + \mathrm{i}Y$ and $h_\nu^* = X - \mathrm{i}Y$ and use

$$\int_{-\infty}^{\infty} \mathrm{d}h_\nu \int_{-\infty}^{\infty} \mathrm{d}h_\nu^* \exp\left(-\alpha h_\nu^* h_\nu\right) = \int_{-\infty}^{\infty} \mathrm{d}X \int_{-\infty}^{\infty} \mathrm{d}Y \exp\left(-\alpha(X^2 + Y^2)\right)\big) = \frac{\pi}{\alpha} \tag{A.7}$$

so that

$$Z_N = \prod_{\nu=1}^{N} \frac{2\pi}{\beta\kappa q_\nu^2} = \left(\frac{1}{2\pi\beta\kappa}\right)^N \prod_{\nu=1}^{N} \frac{N^2}{\nu^2} \tag{A.8}$$

and the free energy is

$$\beta F_N = -\ln Z_N = N \ln(2\pi\beta\kappa) + 2 \sum_{\nu=1}^{N} \ln\left(\frac{\nu}{N}\right) \tag{A.9}$$

The capillary wave contribution to the interfacial tension can then be written in the limit of an infinitely fine lattice as

$$\beta\Delta\gamma_{cw} = \lim_{N\to\infty} \frac{\beta F_N}{N} = \ln(2\pi\beta\kappa) - 2 \tag{A.10}$$

having used

$$\lim_{N\to\infty}\frac{1}{N}\sum_{\nu=1}^{N}\ln\left(\frac{\nu}{N}\right)=\int_0^1\ln(s)\mathrm{d}s=[s\ln s-s]_0^1=-1\ . \tag{A.11}$$

The finite-size behavior of the interfacial tension is determined by the way in which the limit $N\to\infty$ of this sum is approached. Therefore consider

$$S_2(N)=\frac{1}{N}\sum_{\nu=1}^{N}\ln\left(\frac{\nu}{N}\right) \tag{A.12}$$

The dependence of $S_2(N)$ of the discretization $N$ is expected to be of the form [see also Eqs. (5.28) and (5.33)]

$$S_2(N)=A+B\frac{\ln N}{N}+\frac{C}{N} \tag{A.13}$$

with $A=-1$ as shown in (A.11). To test this, it is easier to consider the first derivative

$$N^2\frac{\mathrm{d}S_2}{\mathrm{d}N}=B-C-B\ln(N) \tag{A.14}$$

and plot the result against $\ln(N)$. Fig. A.1 shows that the derivative becomes linear for large $N$ with slope $-1/2$, yielding $B=1/2$ and $C=0.919489$. The fact that the logarithmic correction has a prefactor $B=1/2$ agrees with Eqs. (5.28) and (5.33).

Now, the case $d=3$ will be discussed briefly, as the calculation is similar to $d=2$. The capillary wave Hamiltonian after Fourier transformation is

$$\mathcal{H}_{cw}=\frac{\kappa}{2}\sum_{\substack{\nu_x\\ \nu_x+\nu_y\neq 0}}\sum_{\nu_y}\boldsymbol{q}_{\nu_x,\nu_y}^2|h_{\nu_x,\nu_y}|^2 \tag{A.15}$$

where $\boldsymbol{q}_{\nu_x,\nu_y}=(q_{\nu_x},q_{\nu_y})^\top$ with $q_{\nu_x}=\frac{2\pi\nu_x}{N},\nu_x=0,1,2,\ldots,N$ and $q_{\nu_y}=\frac{2\pi\nu_y}{N},\nu_y=0,1,2,\ldots,N$. Note that the wave vector $\boldsymbol{q}_{0,0}=(0,0)^\top$ has to be excluded. The partition function is

$$Z_N=\prod_{\substack{\nu_x=1\\ \nu_x+\nu_y\neq 0}}^{N}\prod_{\nu_y=1}^{N}\int_{-\infty}^{\infty}\mathrm{d}h_{\nu_x,\nu_y}\int_{-\infty}^{\infty}\mathrm{d}h^*_{\nu_x,\nu_y}\exp\left(-\frac{\beta\kappa}{2}q^2_{\nu_x,\nu_y}h^*_\nu h_\nu\right)\ . \tag{A.16}$$

The computation of the integrals can be calculated as in $d=2$, resulting in

$$Z_N=\prod_{\substack{\nu_x=1\\ \nu_x+\nu_y\neq 0}}^{N}\prod_{\nu_y=1}^{N}\frac{2\pi}{\beta\kappa q^2_{\nu_x,\nu_y}}=\prod_{\substack{\nu_x=1\\ \nu_x+\nu_y\neq 0}}^{N}\prod_{\nu_y=1}^{N}\frac{2\pi N^2}{4\pi^2\beta\kappa\left(\nu_x^2+\nu_y^2\right)}=\left(\frac{1}{2\pi\beta\kappa}\right)^{N^2}\prod_{\substack{\nu_x=1\\ \nu_x+\nu_y\neq 0}}^{N}\prod_{\nu_y=1}^{N}\frac{N^2}{\nu_x^2+\nu_y^2} \tag{A.17}$$

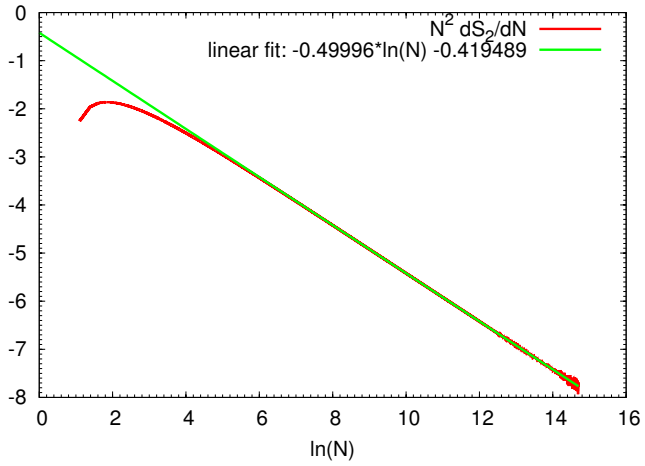


Figure A.1: Plot of $N^2 \mathrm{d}S_2(N)/\mathrm{d}N$ in (A.12) against $\ln(N)$. The linear fit uses data between $\ln N \geq 10$. For $\ln N \geq 14$, one can see noise arising from rounding errors. To increase precision, the summands were sorted from small to large and double precision was used. The derivative at one point is done numerically by taking the average of the slopes between the point and both neighboring points.

and the free energy

$$\beta F_N = -\ln Z_N = N^2 \ln(2\pi\beta\kappa) + \sum_{\substack{\nu_x=1 \\ \nu_x+\nu_y\neq 0}}^{N} \sum_{\nu_y=1}^{N} \ln\left(\frac{\nu_x^2+\nu_y^2}{N^2}\right) . \tag{A.18}$$

The limit $N \to \infty$ can be calculated explicitly

$$\begin{aligned} \lim_{N\to\infty} \frac{1}{N^2} \sum_{\substack{\nu_x=1 \\ \nu_x+\nu_y\neq 0}}^{N} \sum_{\nu_y=1}^{N} \ln\left(\frac{\nu_x^2}{N^2}+\frac{\nu_y^2}{N^2}\right) &= \int_0^1 \mathrm{d}u \int_0^1 \mathrm{d}v \ln\left(u^2+v^2\right) \\ &= \frac{\pi}{2} + \ln(2) - 3 \end{aligned}$$

Hence

$$\beta\gamma_{cw} = \lim_{N\to\infty} \frac{\beta F_N}{N^2} = \ln(2\pi\beta\kappa) + \frac{\pi}{2} + \ln(2) - 3 \tag{A.19}$$

To study the finite-size behavior, consider

$$S_3(N) = \frac{1}{N^2} \sum_{\substack{\nu_x=0 \\ \nu_x+\nu_y\neq 0}}^{N} \sum_{\nu_y=0}^{N} \ln\left(\frac{\nu_x^2}{N^2}+\frac{\nu_y^2}{N^2}\right) . \tag{A.20}$$

Note that the mode $\boldsymbol{q} = (0, 0)$ has to be excluded in this sum. Motivated by the considerations preceding Eq. (5.34), one expects the asymptotic dependence of $N$ to be of the form

$$S_3(N) = A + B\frac{\ln(\ln(N))}{N^2} + \frac{C}{N^2} \tag{A.21}$$

where $A = \frac{\pi}{2} + \ln(2) - 3$ and the $1/N^2$ comes from the division by $L^{d-1}$. The results are shown in Fig. A.2. Contrary to the expectation, the dominant term is a $C/N$-contribution. The appearance of such a term indicates that the above treatment is flawed. A possible reason is the dominant role of short wavelengths in $S_3(N)$. In capillary wave theory in three dimensions, a short wavelength cutoff has to be introduced [cf. Eq. (2.61b)], but the cutoff length is arbitrary. Therefore, in the above calculation, one has to exclude large wave vectors. Indeed, we found that the exponent $\alpha$ in the term $C/N^\alpha$ varies from 1 to about 1.8 as we restrict the integration to wave vectors $\boldsymbol{q}$ with $|\boldsymbol{q}| < q_{\max}$ with different values of $q_{\max}$.

In face of such a contribution, we cannot expect to unambiguously identify a subtle $\ln(\ln(N))$-term. If it exists, it is beyond the current level of accuracy, and we are safe to assume that the considerations given in section 5.1.2 are valid.

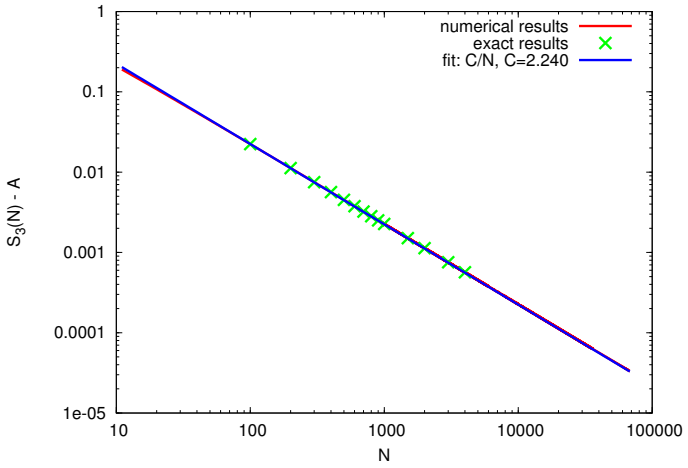


Figure A.2: Plot of $S_3(N) - A$ from (A.20) against $N$, where $A = \frac{\pi}{2} + \ln(2) - 3$. Apart from numerical results, the finite-size residual has been calculated analytically using Mathematica 7 to check whether the numerical results suffer from numerical inaccuracies. The data are well represented by a fit of the form $C/N$.

# Acknowledgments

# Bibliography


Abraham, F. F. (1974). *Homogeneous nucleation theory; the pretransition theory of vapor condensation*. Academic Press, New York.

Acharyya, M. and Stauffer, D. (1998). Nucleation and hysteresis in ising model: classical theory versus computer simulation. *Eur. Phys. J. B*, 5:571.

Asakura, S. and Oosawa, F. (1958). Interaction between particles suspended in solutions of macromolecules. *J. Polym. Sci.*, 33(126):183–192.

Baillie, C. F., Gupta, R., Hawick, K. A., and Pawley, G. S. (1992). Monte carlo renormalization-group study of the three-dimensional ising model. *Phys. Rev. B*, 45:10438–10453.

Balibar, S. and Villain, J., editors (2006). *Nucleation*, volume 7. Elsevier, special issue edition.

Becker, R. and Döring, W. (1935). Kinetische Behandlung der Keimbildung in übersättigten Dämpfen. *Ann. Phys. (Leipzig)*, 416(8):719–752.

Berg, B., Hansmann, U., and Neuhaus, T. (1993a). Properties of interfaces in the two and three dimensional ising model. *Zeitschrift für Physik B Condensed Matter*, 90(2):229–239.

Berg, B. A., Hansmann, U., and Neuhaus, T. (1993b). Simulation of an ensemble with varying magnetic field: A numerical determination of the order-order interface tension in the $d = 2$ ising model. *Phys. Rev. B*, 47:497–500.

Berg, B. A. and Neuhaus, T. (1992). Multicanonical ensemble: A new approach to simulate first-order phase transitions. *Phys. Rev. Lett.*, 68:9–12.

Bier, M., Harnau, L., and Dietrich, S. (2005). Free isotropic-nematic interfaces in fluids of charged platelike colloids. *J. Chem. Phys.*, 123(11):114906.

Binder, K. (1980). Percolation effects in the kinetics of phase separation. *Solid State Commun.*, 34(3):191 – 194.

Binder, K. (1982). Monte carlo calculation of the surface tension for two- and three-dimensional lattice-gas models. *Phys. Rev. A*, 25:1699–1709.

Binder, K. (1984). Nucleation barriers, spinodals, and the ginzburg criterion. *Phys. Rev. A*, 29:341–349.

Binder, K. (1987). Theory of first-order phase transitions. *Rep. Prog. Phys.*, 50(7):783.

Binder, K. (2003). Theory of the evaporation/condensation transition of equilibrium droplets in finite volumes. *Physica A*, 319:99–114.

Binder, K., Block, B., Das, S. K., Virnau, P., and Winter, D. (2011). Monte carlo methods for estimating interfacial free energies and line tensions. *J. Stat. Phys.*, 144(3):690–729.

Binder, K., Block, B. J., Virnau, P., and Tröster, A. (2012). Beyond the van der waals loop: What can be learned from simulating lennard-jones fluids inside the region of phase coexistence. *Am. J. Phys.*, 80(12):1099–1109.

Binder, K., Bowker, M., Inglesfield, J. E., and Rous, P. J. (1995). *Cohesion and Structure of Interfaces*. Elsevier, North Holland, 1st edition.

Binder, K. and Heermann, D. W. (2010). *Monte Carlo Simulation in Statistical Physics*. Springer, Heidelberg, Dordrecht, London New York, 5th edition.

Binder, K. and Kalos, M. H. (1980). "critical clusters" in a supersaturated vapor: Theory and monte carlo simulation. *J. Stat. Phys.*, 22:363–396. 10.1007/BF01014648.

Binder, K., Müller, M., Schmid, F., and Werner, A. (2001). 'intrinsic' profiles and capillary waves at interfaces between coexisting phases in polymer blends. *Adv. Colloid Interface Sci.*, 94(1–3):237 – 248.

Binder, K. and Müller-Krumbhaar, H. (1974). Investigation of metastable states and nucleation in the kinetic ising model. *Phys. Rev. B*, 9:2328–2353.

Binder, K. and Stauffer, D. (1972). Monte carlo study of the surface area of liquid droplets. *J. Stat. Phys.*, 6:49–59. 10.1007/BF01060201.

Binder, K. and Stauffer, D. (1976). Statistical theory of nucleation, condensation and coagulation. *Adv. Phys.*, 25:343–396.

Bittner, E., Nussbaumer, A., and Janke, W. (2009). Anisotropy of the interface tension of the three-dimensional ising model. *Nuclear Physics*, B(820):694–706.

Bizjak, A., Urbič, T., and Vlachy, V. (2009). Phase diagram of the lennard-jones system of particles from the cell model and thermodynamic perturbation theory. *Acta Chim. Slov.*, 56:166–171.

Block, B., Deb, D., Schmitz, F., Statt, A., Tröster, A., Winkler, A., Zykova-Timan, T., Virnau, P., and Binder, K. (2014). Computer simulation of heterogeneous nucleation of colloidal crystals at planar walls. *Eur. Phys. J. Special Topics*, 223(3):347–361.

Block, B. J., Das, S. K., Oettel, M., Virnau, P., and Binder, K. (2010). Curvature dependence of surface free energy of liquid drops and bubbles: A simulation study. *J. Chem. Phys.*, 133(15):154702.

Bonn, D. and Ross, D. (2001). Wetting transitions. *Rep. Prog. Phys.*, 64(9):1085.

Boulougouris, G. C., Economou, I. G., and Theodorou, D. N. (1999). On the calculation of the chemical potential using the particle deletion scheme. *Molecular Physics*, 96(6):905–913.

Brézin, E. and Zinn-Justin, J. (1985). Finite size effects in phase transitions. *Nuclear Physics B*, 257(0):867 – 893.

Broughton, J. Q. and Gilmer, G. H. (1986). Molecular dynamics investigation of the crystal–fluid interface. vi. excess surface free energies of crystal–liquid systems. *J. Chem. Phys.*, 84(10):5759–5768.

Buff, F. P., Lovett, R. A., and Stillinger, F. H. (1965). Interfacial density profile for fluids in the critical region. *Phys. Rev. Lett.*, 15:621–623.

Bürkner, E. and Stauffer, D. (1983). Monte carlo study of surface roughening in the three-dimensional ising model. *Zeitschrift für Physik B Condensed Matter*, 53:241–243.

Cahn, J. W. and Hilliard, J. E. (1958). Free energy of a nonuniform system. i. interfacial free energy. *J. Chem. Phys.*, 28(2):258–267.

Caillol, J. M. (1998). Critical-point of the lennard-jones fluid: A finite-size scaling study. *J. Chem. Phys.*, 109(12):4885–4893.

Colot, J. and Baus, M. (1985). The freezing of hard spheres ii. a search for structural (f.c.c.-h.c.p.) phase transitions. *Molecular Physics*, 56(4):807–824.

Coniglio, A. (1975). Percolation problems and phase transitions. *J. Phys. A: Math. Gen.*, 8(11):1773.

Coniglio, A. and Klein, W. (1980). Clusters and ising critical droplets: a renormalisation group approach. *J. Phys. A: Math. Gen.*, 13(8):2775.

Coniglio, A., Peruggi, F., Nappi, C., and Russo, L. (1977). Percolation points and critical point in the ising model. *J. Phys. A*, 10:205.

Das, S. K. and Binder, K. (2011). Universal critical behavior of curvature-dependent interfacial tension. *Phys. Rev. Lett.*, 107:235702.

Davidchack, R. L. (2010). Hard spheres revisited: Accurate calculation of the solid–liquid interfacial free energy. *J. Chem. Phys.*, 133(23):234701.

Davidchack, R. L. and Laird, B. B. (2000). Direct calculation of the hard-sphere crystal /melt interfacial free energy. *Phys. Rev. Lett.*, 85:4751–4754.

Davidchack, R. L. and Laird, B. B. (2003). Direct calculation of the crystal–melt interfacial free energies for continuous potentials: Application to the lennard-jones system. *J. Chem. Phys.*, 118(16):7651–7657.

Davidchack, R. L. and Laird, B. B. (2005). Crystal structure and interaction dependence of the crystal-melt interfacial free energy. *Phys. Rev. Lett.*, 94:086102.

Davidchack, R. L., Morris, J. R., and Laird, B. B. (2006). The anisotropic hard-sphere crystal-melt interfacial free energy from fluctuations. *J. Chem. Phys.*, 125(9):094710.

de Gennes, P.-G., Brochard-Wyart, F., and Quere, D. (2003). *Capillarity and Wetting Phenomena: Drops, Bubbles, Pearls, Waves*. Springer, New York.

De Meo, M. D., Heermann, D. W., and Binder, K. (1990). Monte carlo study of the ising model phase transition in terms of the percolation transition of “physical clusters". *J. Stat. Phys.*, 60:585–618. 10.1007/BF01025984.

Deb, D., Wilms, D., Winkler, A., Virnau, P., and Binder, K. (2012a). Methods to compute pressure and wall tension in fluids containing hard particles. *Int. J. Mod. Phys. C*, 23(08):1240011.

Deb, D., Winkler, A., Virnau, P., and Binder, K. (2012b). Simulation of fluid-solid coexistence in finite volumes: A method to study the properties of wall-attached crystalline nuclei. *J. Chem. Phys.*, 136(13):134710.

Deb, D., Winkler, A., Yamani, M. H., Oettel, M., Virnau, P., and Binder, K. (2011). Hard sphere fluids at a soft repulsive wall: A comparative study using monte carlo and density functional methods. *J. Chem. Phys.*, 134(21):214706.

Dietrich, S., Rauscher, M., and Napiorkowski, M. (2013). *Nanoscale Liquid Interfaces - Wetting, Patterning and Force Microscopy at the Molecular Scale*. Pan Stanford, Stanford.

Dijkstra, M., Brader, J. M., and Evans, R. (1999). Phase behaviour and structure of model colloid-polymer mixtures. *J. Phys.: Condens. Matter*, 11(50):10079.

Dijkstra, M., van Roij, R., Roth, R., and Fortini, A. (2006). Effect of many-body interactions on the bulk and interfacial phase behavior of a model colloid-polymer mixture. *Phys. Rev. E*, 73:041404.

Dillmann, A. and Meier, G. E. A. (1989). Homogeneous nucleation of supersaturated vapors. *Chem. Phys. Lett.*, 89:71.

Domb, C. and Green, M. S., editors (1972). *Phase Transitions and Critical Phenomena*, volume 2. Academic Press, London.

Domb, C. and Lebowitz, J. L., editors (1983). *Phase Transitions and Critical Phenomena*, volume 8. Academic Press, London.

Domb, C. and Lebowitz, J. L., editors (1988). *Phase Transitions and Critical Phenomena*, volume 12. Academic Press, London.

Evans, R. (1979). The nature of the liquid-vapour interface and other topics in the statistical mechanics of non-uniform, classical fluids. *Adv. Phys.*, 28(2):143–200.

Feder, J., Russell, K. C., Lothe, J., and Pound, G. M. (1966). Homogeneous nucleation and growth of droplets in vapours. *Adv. Phys.*, 15(111).

Feller, W. (1968). *An Introduction to Probability Theory and Its Applications, Vol. 1, 3rd Edition*. Wiley, 3 edition.

Fernandez, L. A., Martin-Mayor, V., Seoane, B., and Verrocchio, P. (2012). Equilibrium fluid-solid coexistence of hard spheres. *Phys. Rev. Lett.*, 108:165701.

Ferrenberg, A. M. and Landau, D. P. (1991). Critical behavior of the three-dimensional ising model: A high-resolution monte carlo study. *Phys. Rev. B*, 44:5081–5091.

Fisher, M. E. (1984). Walks, walls, wetting, and melting. *J. Stat. Phys.*, 34(5-6):667–729.

Fisher, M. E., Barber, M. N., and Jasnow, D. (1973). Helicity modulus, superfluidity, and scaling in isotropic systems. *Phys. Rev. A*, 8:1111–1124.

Fisher, M. P. A. and Wortis, M. (1984). Curvature corrections to the surface tension of fluid drops: Landau theory and a scaling hypothesis. *Phys. Rev. B*, 29:6252.

Fladerer, A. and Strey, R. (2006). Homogeneous nucleation and droplet growth in supersaturated argon vapor: The cryogenic nucleation pulse chamber. *J. Chem. Phys.*, 124:164710.

Fortuin, C. and Kasteleyn, P. (1972). On the random-cluster model: I. introduction and relation to other models. *Physica*, 57(4):536 – 564.

Frenkel, D. and Smit, B. (2001). *Understanding Molecular Simulation, Second Edition: From Algorithms to Applications (Computational Science)*. Academic Press, 2nd edition.

Gelb, L. D., Gubbins, K. E., Radhakrishnan, R., and Sliwinska-Bartkowiak, M. (1999). Phase separation in confined systems. *Rep. Prog. Phys.*, 62(12):1573.

Gelfand, M. P. and Fisher, M. E. (1990). Finite-size effects in fluid interfaces. *Physica A*, 166(1):1 – 74.

Goodstein, D. (1985). *States of matter*. Dover books on physics and chemistry. Dover Publications, Incorporated.

Hamley, I. W. (1998). *The Physics of Block Copolymers*. Oxford Univ. Press, Oxford.

Härtel, A., Oettel, M., Rozas, R. E., Egelhaaf, S. U., Horbach, J., and Löwen, H. (2012). Tension and stiffness of the hard sphere crystal-fluid interface. *Phys. Rev. Lett.*, 108:226101.

Hasenbusch, M., Meyer, S., and Pütz, M. (1996). The roughening transition of the three-dimensional ising interface: A monte carlo study. *J. Stat. Phys.*, 85:383–401.

Hasenbusch, M. and Pinn, K. (1993). Surface tension, surface stiffness, and surface width of the 3-dimensional ising model on a cubic lattice. *Nuclear Physics B - Proceedings Supplements*, 30:857 – 860. Proceedings of the International Symposium on.

Hasenbusch, M. and Pinn, K. (1994). Comparison of monte carlo results for the 3d ising interface tension and interface energy with (extrapolated) series expansions. *Physica A*, 203(2):189 – 213.

Hasenbusch, M. and Pinn, K. (1997). Computing the roughening transition of ising and solid-on-solid models by bcsos model matching. *J. Phys. A*, 30:63.

Hayward, S., Heermann, D. W., and Binder, K. (1987). Dynamic percolation transition induced by phase separation: a monte carlo analysis. *J. Stat. Phys.*, 49:1053.

Hoshen, J., Berry, M. W., and Minser, K. S. (1997). Percolation and cluster structure parameters: The enhanced hoshen-kopelman algorithm. *Phys. Rev. E*, 56:1455–1460.

Hoshen, J. and Kopelman, R. (1976). Percolation and cluster distribution. i. cluster multiple labeling technique and critical concentration algorithm. *Phys. Rev. B*, 14(8):3438–3445.

Hoyt, J. J., Asta, M., and Karma, A. (2001). Method for computing the anisotropy of the solid-liquid interfacial free energy. *Phys. Rev. Lett.*, 86:5530–5533.

Hunter, G. L. and Weeks, E. R. (2012). The physics of the colloidal glass transition. *Rep. Prog. Phys.*, 75(6):066501.

Hunter III, J. E. and Reinhardt, W. P. (1995). Finite-size scaling behavior of the free energy barrier between coexisting phases: Determination of the critical temperature and interfacial tension of the lennard-jones fluid. *J. Chem. Phys.*, 103(19):8627–8637.

Iland, K., Wölk, J., Strey, R., and Kashchiev, D. (2007). Argon nucleation in a cryogenic nucleation pulse chamber. *J. Chem. Phys.*, 127:154506.

Ilett, S. M., Orrock, A., Poon, W. C. K., and Pusey, P. N. (1995). Phase behavior of a model colloid-polymer mixture. *Phys. Rev. E*, 51:1344–1352.

Jasnow, D. (1984). Critical phenomena at interfaces. *Rep. Prog. Phys.*, 47(9):1059.

Jones, J. E. (1924). On the determination of molecular fields. ii. from the equation of state of a gas. *Proceedings of the Royal Society of London. Series A*, 106(738):463–477.

Kashchiev, D. (2000). *Nucleation, Basic Theory with Applications*. Butterworth-Heinemann, Oxford.

Kasteleyn, P. W. and Fortuin, C. M. (1969). Phase transitions in lattice systems with random local properties. *J. Phys. Soc. Japan*, 26 (Suppl):11.

Laaksonen, A., Talanquer, V., and Oxtoby, D. W. (1995). Nucleation: Measurements, theory, and atmospheric applications. *Ann. Rev. Phys. Chem.*, 46:489.

Landau, D. P. and Binder, K. (2009). *A Guide to Monte Carlo Simulations in Statistical Physics*. Cambridge Univ. Press, 3 edition.

Landau, D. P., Tsai, S.-H., and Exler, M. (2004). A new approach to monte carlo simulations in statistical physics: Wang-landau sampling. *American Journal of Physics*, 72(10):1294–1302.

Langer, J. (1974). Metastable states. *Physica*, 73(1):61 – 72.

Langer, J. S. (1969). Statistical theory of the decay of metastable states. *Ann. Phys.*, 54:258.

Lebowitz, J. L. and Penrose, O. (1966). Rigorous treatment of the van der waals-maxwell theory of the liquid-vapor transition. *J. Math. Phys.*, 7(1):98–113.

Lee, T. D. and Yang, C. N. (1952). Statistical theory of equations of state and phase transitions. ii. lattice gas and ising model. *Phys. Rev.*, 87(3):410–419.

Lekkerkerker, H. N. W., Poon, W. C.-K., Pusey, P. N., Stroobants, A., and Warren, P. B. (1992). Phase behaviour of colloid + polymer mixtures. *EPL (Europhysics Letters)*, 20(6):559.

MacDowell, L. G., Virnau, P., Müller, M., and Binder, K. (2004). The evaporation/condensation transition of liquid droplets. *J. Chem. Phys.*, 120(11):5293–5308.

Mau, S.-C. and Huse, D. A. (1999). Stacking entropy of hard-sphere crystals. *Phys. Rev. E*, 59:4396–4401.

Mecke, K. R. and Dietrich, S. (1999). Effective hamiltonian for liquid-vapor interfaces. *Phys. Rev. E*, 59:6766–6784.

Metropolis, N., Rosenbluth, A. W., Rosenbluth, M. N., Teller, A. H., and Teller, E. (1953). Equation of state calculations by fast computing machines. *J. Chem. Phys.*, 21(6):1087–1092.

Meyer-Ortmanns, H. (1996). Phase transitions in quantum chromodynamics. *Rev. Mod. Phys.*, 68:473–598.

Milchev, A. and Binder, K. (2002). Momentum-dependent interfacial tension in polymer solutions. *EPL (Europhysics Letters)*, 59(1):81.

Mon, K. K., Landau, D. P., and Stauffer, D. (1990). Interface roughening in the three-dimensional ising model. *Phys. Rev. B*, 42:545–547.

Mon, K. K., Wansleben, S., Landau, D. P., and Binder, K. (1989). Monte carlo studies of anisotropic surface tension and interfacial roughening in the three-dimensional ising model. *Phys. Rev. B*, 39:7089–7096.

Morris, J. J. (1992). Finite-size scaling of the interfacial tension. *J. Stat. Phys.*, 69(3-4):539–571.

Mu, Y., Houk, A., and Song, X. (2005). Anisotropic interfacial free energies of the hard-sphere crystal-melt interfaces. *The Journal of Physical Chemistry B*, 109(14):6500–6504. PMID: 16851729.

Müller-Krumbhaar, H. (1974). Percolation in a lattice system with particle interaction. *Phys. Lett. A*, 50(1):27 – 28.

Murch, G. and Thorn, R. (1978). Petit and grand ensemble monte carlo calculations of the thermodynamics of the lattice gas. *Journal of Computational Physics*, 29(2):237 – 244.

Narayanan, R., editor (2008). *Interfacial Processes and Molecular Aggregation of Surfactants*. Springer, Heidelberg.

Nijmeijer, M. J. P., Bakker, A. F., Bruin, C., and Sikkenk, J. H. (1988). A molecular dynamics simulation of the lennard-jones liquid-vapor interface. *J. Chem. Phys.*, 89(6):3789–3792.

Onsager, L. (1944). Crystal statistics. i. a two-dimensional model with an order-disorder transition. *Phys. Rev.*, 65(3-4):117–149.

Oosawa, F. and Asakura, S. (1954). Surface tension of high-polymer solutions. *J. Chem. Phys.*, 22(7):1255–1256.

Oxtoby, D. W. (1992). Homogeneous nucleation: theory and experiment. *J. Phys.: Condens. Matter*, 4:7627.

Oxtoby, D. W. and Evans, R. (1988). Nonclassical nucleation theory for the gas–liquid transition. *J. Chem. Phys.*, 89:7521.

Pan, A. C. and Chandler, D. (2004). Dynamics of nucleation in the ising model. *J. Phys. Chem. B*, 108:19681.

Parry, A. O. and Boulter, C. J. (1994). Fluctuation theory for the wavevector expansion of the excess grand potential of a liquid-vapour interface and the theory of interfacial fluctuations. *J. Phys.: Condens. Matter*, 6(36):7199.

Penrose, O. and Lebowitz, J. (1971). Rigorous treatment of metastable states in the van der waals-maxwell theory. *J. Stat. Phys.*, 3(2):211–236.

Potoff, J. J. and Panagiotopoulos, A. Z. (2000). Surface tension of the three-dimensional lennard-jones fluid from histogram-reweighting monte carlo simulations. *J. Chem. Phys.*, 112(14):6411–6415.

Powles, J. G., Holtz, B., and Evans, W. A. B. (1994). New method for determining the chemical potential for condensed matter at high density. *J. Chem. Phys.*, 101(9):7804–7810.

Prestipino, S., Laio, A., and Tosatti, E. (2013). A fingerprint of surface-tension anisotropy in the free-energy cost of nucleation. *J. Chem. Phys.*, 138(6):064508.

Privman, V. (1988). Finite-size properties of the angle-dependent surface tension of rough interfaces. *Phys. Rev. Lett.*, 61:183–186.

Privman, V. (1992). fluctuating interfaces, surface tension, and capillary waves: an introduction. *International Journal of Modern Physics C*, 03(05):857–877.

Pronk, S. and Frenkel, D. (1999). Can stacking faults in hard-sphere crystals anneal out spontaneously? *J. Chem. Phys.*, 110(9):4589–4592.

Puri, S. and Wadhavan, V., editors (2009). *Kinetics of Phase Transitions*. CRC Press, Boca Raton.

Ramos, R. A., Rikvold, P. A., and Novotny, M. A. (1999). Test of the kolmogorov-johnson-mehl-avrami picture of metastable decay in a model with microscopic dynamics. *Phys. Rev. B*, 59:9053.

Reiss, H., Katz, J. L., and Cohen, E. R. (1968). Translation–rotation paradox in the theory of nucleation. *J. Stat. Phys.*, 2:83.

Reiss, H., Tabazadeh, A., and Talbot, J. (1990). Molecular theory of vapor phase nucleation: the physically consistent cluster. *J. Chem. Phys.*, 92:1266.

Rowlinson, J. S. and Widom, B. (1982). *Molecular Theory of Capillarity*, volume 8. Oxford Univ. Press, Oxford.

Rozas, R. E. and Horbach, J. (2011). Capillary wave analysis of rough solid-liquid interfaces in nickel. *EPL (Europhysics Letters)*, 93(2):26006.

Ryu, S. and Cai, W. (2010). Validity of classical nucleation theory for ising models. *Phys. Rev. E*, 81(3):030601(R).

Schimmele, L., Napiórkowski, M., and Dietrich, S. (2007). Conceptual aspects of line tensions. *J. Chem. Phys.*, 127(16):164715.

Schmitz, F., Virnau, P., and Binder, K. (2013). Monte carlo tests of nucleation concepts in the lattice gas model. *Phys. Rev. E*, 87:053302.

Schmitz, F., Virnau, P., and Binder, K. (2014a). Determination of the origin and magnitude of logarithmic finite-size effects on interfacial tension: Role of interfacial fluctuations and domain breathing. *Phys. Rev. Lett.*, 112:125701.

Schmitz, F., Virnau, P., and Binder, K. (2014b). Logarithmic finite-size effects on interfacial free energies: Phenomenological theory and monte carlo studies. *Phys. Rev. E*, 90:012128.

Schrader, M., Virnau, P., and Binder, K. (2009a). Simulation of vapor-liquid coexistence in finite volumes: A method to compute the surface free energy of droplets. *Phys. Rev. E*, 79:061104.

Schrader, M., Virnau, P., Winter, D., Zykova-Timan, T., and Binder, K. (2009b). Methods to extract interfacial free energies of flat and curved interfaces from computer simulations. *The European Physical Journal - Special Topics*, 177:103–127. 10.1140/epjst/e2009-01170-y.

Severance, F. L. (2001). *System Modeling and Simulation*. Wiley.

Shell, M. S., Debenedetti, P. G., and Panagiotopoulos, A. Z. (2002). Generalization of the wang-landau method for off-lattice simulations. *Phys. Rev. E*, 66:056703.

Shneidman, V. A., Jackson, K. A., and Beatty, K. M. (1999a). Nucleation and growth of a stable phase in an ising-type system. *Phys. Rev. B*, 59:3579.

Shneidman, V. A., Jackson, K. A., and Beatty, K. M. (1999b). On the applicability of the classical nucleation theory in an ising system. *J. Chem. Phys.*, 11:6932.

Smit, B. (1992). Phase diagrams of lennard-jones fluids. *J. Chem. Phys.*, 96(11):8639–8640.

Statt, A. (2015). *Monte Carlo simulations of colloidal crystals (working title)*. PhD thesis, Johannes Gutenberg-Universität Mainz.

Svrakic, N., Privman, V., and Abraham, D. (1988). Finite-size corrections for inclined interfaces in two dimensions: Exact results for ising and solid-on-solid models. *J. Stat. Phys.*, 53(5-6):1041–1059.

Swendsen, R. H. and Wang, J. S. (1987). Nonuniversal critical dynamics in Monte Carlo simulations. *Phys. Rev. Lett.*, 58(2):86–88.

ten Wolde, P. R. and Frenkel, D. (1998). Computer simulation study of gas–liquid nucleation in a lennard-jones system. *J. Chem. Phys.*, 109:9901.

Tolman, R. C. (1948). Consideration of the gibbs theory of surface tension. *J. Chem. Phys.*, 16(8):758–774.

Tolman, R. C. (1949). The effect of droplet size on surface tension. *J. Chem. Phys.*, 17(3):333–337.

Tröster, A. and Binder, K. (2012). Microcanonical determination of the interface tension of flat and curved interfaces from monte carlo simulations. *J. Phys.: Condens. Matter*, 24(28):284107.

Tröster, A., Oettel, M., Block, B., Virnau, P., and Binder, K. (2012). Numerical approaches to determine the interface tension of curved interfaces from free energy calculations. *J. Chem. Phys.*, 136(6):064709.

Turnbull, D. (1950a). Formation of crystal nuclei in liquid metals. *J. Appl. Phys.*, 21(10):1022–1028.

Turnbull, D. (1950b). Kinetics of heterogeneous nucleation. *J. Chem. Phys.*, 18(2):198–203.

Vehkamaki, H. and Ford, I. J. (1999). Nucleation theorems applied to the ising model. *Phys. Rev. E*, 59:6483.

Vilsanen, Y., Strey, R., and Reiss, H. (1993). Homogeneous nucleation rates for water. *J. Chem. Phys.*, 99:4680.

Vink, R. L. C., Horbach, J., and Binder, K. (2005). Capillary waves in a colloid-polymer interface. *J. Chem. Phys.*, 122(13):134905.

Virnau, P. (2003). *Monte-Carlo-Simulationen zum Phasen- und Keimbildungsverhalten von Polymerlösungen*. PhD thesis, Johannes Gutenberg-Universität Mainz.

Virnau, P. and Müller, M. (2004). Calculation of free energy through successive umbrella sampling. *J. Chem. Phys.*, 120(23):10925–10930.

Virnau, P., Müller, M., MacDowell, L. G., and Binder, K. (2004). Phase behavior of n-alkanes in supercritical solution: A monte carlo study. *J. Chem. Phys.*, 121(5):2169–2179.

Volmer, M. (1929). Über Keimbildung und Keimwirkung als Spezialfälle der heterogenen Katalyse. *Zeitschrift für Elektrochemie*, 35:555.

Volmer, M. and Weber, A. (1926). Keimbildung in übersättigten Gebilden. *Z. phys. Chem.*, 119:277.

Vrij, A. (1976). Polymers at Interfaces and the Interactions in Colloidal Dispersions. *Pure and Applied Chemistry*, 48(4):471–483.

Walton, J., Tildesley, D., Rowlinson, J., and Henderson, J. (1983). The pressure tensor at the planar surface of a liquid. *Molecular Physics*, 48(6):1357–1368.

Wang, F. and Landau, D. P. (2001a). Determining the density of states for classical statistical models: A random walk algorithm to produce a flat histogram. *Phys. Rev. E*, 64:056101.

Wang, F. and Landau, D. P. (2001b). Efficient, multiple-range random walk algorithm to calculate the density of states. *Phys. Rev. Lett.*, 86:2050–2053.

Weeks, J. D. (1977). Structure and thermodynamics of the liquid–vapor interface. *J. Chem. Phys.*, 67(7):3106–3121.

Widom, B. (1963). Some topics in the theory of fluids. *J. Chem. Phys.*, 39(11):2808–2812.

Widom, B. (1982). Potential-distribution theory and the statistical mechanics of fluids. *J. Phys. Chem.*, 86(6):869–872.

Wiese, U. (1992). Capillary waves in Binder's approach to the interface tension. *arXiv:hep-lat/9209006*.

Winter, D., Virnau, P., and Binder, K. (2009a). Heterogeneous nucleation at a wall near a wetting transition: a monte carlo test of the classical theory. *J. Phys.: Condens. Matter*, 21(46):464118.

Winter, D., Virnau, P., and Binder, K. (2009b). Monte carlo test of the classical theory for heterogeneous nucleation barriers. *Phys. Rev. Lett.*, 103(22):225703.

Wolff, U. (1989). Collective monte carlo updating for spin systems. *Phys. Rev. Lett.*, 62:361.

Wonczak, S., Strey, R., and Stauffer, D. (2000). Confirmation of classical nucleation theory by monte carlo simulations in the 3-dimensional ising model at low temperature. *J. Chem. Phys.*, 113(5):1976–1980.

Wulff, G. V. (1901). Zur Frage der Geschwindigkeit des Wachstums und der Auflösung der Kristallflächen. *Z. Kristallogr. Mineral.*, 34:449–530.

Young, T. (1805). An Essay on the Cohesion of Fluids. *Philosophical Transactions of the Royal Society of London*, 95:65–87.

Zeldovich, Y. B. (1943). On the theory of new phase formation; cavitation. *Acta Physicochim. USSR*, 18:1.

Zykova-Timan, T., Horbach, J., and Binder, K. (2010). Monte carlo simulations of the solid-liquid transition in hard spheres and colloid-polymer mixtures. *J. Chem. Phys.*, 133(1):014705.